# Simulating Noise Assisted Quantum Transport Mechanisms with cold Atoms

by

Andrew David White

A thesis submitted to
The University of Birmingham
for the degree of
DOCTOR OF PHILOSOPHY

Ultracold Atoms Group
School of Physics and Astronomy
College of Engineering and Physical Sciences
The University of Birmingham

November 2019

UNIVERSITY OF BIRMINGHAM

**University of Birmingham Research Archive**

**e-theses repository**

This unpublished thesis/dissertation is copyright of the author and/or third parties. The intellectual property rights of the author or third parties in respect of this work are as defined by The Copyright Designs and Patents Act 1988 or as modified by any successor legislation.

Any use made of information contained in this thesis/dissertation must be in accordance with that legislation and must be properly acknowledged. Further distribution or reproduction in any format is prohibited without the permission of the copyright holder.

**Abstract**

A strong interplay between quantum coherence and a noisy protein environment was used to explain the high efficiency of exciton transport through the photosynthetic Fenna-Matthews-Olson (FMO) complex. Aspects of this transport process were simulated experimentally using a three-site system composed of RF coupled magnetic sub-states of the $F = 1$ state of rubidium 87. The effect of a noisy environment was modelled by a noisy pure dephasing classical field that perturbed the site energies. An optimum noise power for efficient transport in a linear network was observed and in addition, the theoretically predicted localisation, environmental noise assisted quantum transport (ENAQT) and Zeno-like regimes were identified. Transport through the system was also found to be strongly dependent on the frequency components of the applied perturbation. Low frequency perturbations, below the dressed state splitting of the system, were found to induce transport using sub-resonance transfer paths. Dephasing assisted transport (DAT, modelled using a broadband noise source), and vibration assisted transport (VAT, modelled as a structured noisy environment with a Lorentzian centred on the dressed state energy splitting) were compared. It was found that VAT was a faster transport mechanism than DAT.

# ACKNOWLEDGEMENTS

I would like to thank the following people. My supervisor Dr Vincent Boyer for all his help and support, and for giving me the opportunity to undertake this PhD. The Ultracold Atoms department of the School of Physics and Astronomy, University of Birmingham for providing the laboratory facilities and EPSRC for funding my PhD (award number 1658685). Dr Plamen Petrov and Dr Chris Gill who designed and built the original experiment and with who I have had many profitable discussions. My friends in the cold atoms group for providing a constructive and entertaining atmosphere. All my friends and family particularly my parents and Lizzy.

# CONTENTS

**1 Introduction and Motivation for the study of Noise Assisted Quantum Transport** **1**

1.1 Introduction . . . . . 1

1.2 Quantum processes in biological systems . . . . . 3

1.2.1 The Fenna-Matthews-Olson Complex . . . . . 3

1.2.2 Two-dimensional spectroscopy of the FMO complex . . . . . 6

1.3 Modelling of the FMO complex . . . . . 6

1.3.1 Introduction to open quantum systems . . . . . 8

1.3.2 Experimental modelling of a noisy environment . . . . . 10

1.4 Key models for transport mechanisms . . . . . 10

1.4.1 Dephasing assisted transport . . . . . 11

1.4.2 Vibration Assisted Transport . . . . . 13

1.5 Experimental investigations of noise assisted quantum transport (NAQT) . . 13

1.5.1 Optical systems . . . . . 15

1.5.2 Superconducting qubit systems . . . . . 16

1.5.3 Ion systems . . . . . 18

1.5.4 Summary . . . . . 20

1.6 Review of modulated quantum systems . . . . . 21

1.6.1 Landau-Zener transitions . . . . . 21

1.6.2 Landau-Zener-Stuckelberg Interferometry . . . . . 22
1.6.3 Multi-photon transitions and Floquet theory . . . . . 24
1.7 Applications of noise assisted quantum transport . . . . . 26
1.8 Our approach to simulating NAQT processes . . . . . 27
1.9 Structure of the thesis . . . . . 28

**2 Evolution of Quantum Systems: Elements of Theory 31**

2.1 Introduction . . . . . 31
2.2 Dynamics of a three level system with harmonic coupling . . . . . 32
2.2.1 Construction of the Hamiltonian . . . . . 33
2.2.2 Applying the rotating wave approximation . . . . . 34
2.2.3 Diagonalising the Hamiltonian . . . . . 36
2.2.4 Rabi oscillations . . . . . 37
2.3 Mapping a three level system to the Bloch Sphere . . . . . 39
2.4 Dephasing and decoherence . . . . . 47
2.5 Modelling pure dephasing using the master equation . . . . . 51
2.6 Perturbation theory . . . . . 53
2.7 Incoherent transfer and the width of the energy distribution . . . . . 60
2.8 The relationship between measurement and dephasing . . . . . 62
2.9 Conclusions . . . . . 63

**3 Experimental Set-up 65**

3.1 Introduction . . . . . 65
3.2 The experimental set-up . . . . . 66
3.2.1 Cooling the atoms . . . . . 66
3.2.2 The Laser Set-up . . . . . 70
3.3 Preparation of the initial excitation . . . . . 70

3.3.1 Depumping procedure . . . . . 72
3.3.2 F1 polarisation procedure . . . . . 73
3.4 Measuring the state of the system . . . . . 75
3.4.1 Optical pumping to the $F = 2$ $m_F = +2$ state . . . . . 76
3.4.2 Absorption imaging . . . . . 79
3.5 RF coupling . . . . . 81
3.5.1 Theoretical description . . . . . 81
3.5.2 Adiabatic following . . . . . 82
3.5.3 Inhomogeneous broadening . . . . . 83
3.6 Raman coupling . . . . . 86
3.6.1 Theoretical description . . . . . 88
3.6.2 Determining the optimum detuning . . . . . 90
3.6.3 Light shifts . . . . . 92
3.6.4 Initial experimental results . . . . . 93
3.7 Perturbation generation . . . . . 96
3.8 Analysis . . . . . 98
3.9 Summary . . . . . 100

**4 Single Frequency Modulation: Experimental Results and Discussion 101**
4.1 Introduction . . . . . 101
4.2 Theory of coupling between the dressed states . . . . . 101
4.3 Single frequency coupling between dressed states . . . . . 103
4.3.1 Experimental procedure . . . . . 104
4.3.2 Evolution under resonant modulation . . . . . 105
4.3.3 Varying the generalised Rabi frequency . . . . . 108
4.4 Sub-harmonic resonances . . . . . 109
4.5 Floquet theory . . . . . 112

4.6 The dependence of the fundamental and 1st mode resonances on the modulation amplitude . . . 116
4.6.1 Experimental procedure . . . 117
4.6.2 On-resonance Rabi frequency dependence on modulation amplitude . 117
4.6.3 Widths of the Fundamental and Sub-resonances . . . 123
4.6.4 Inhomogeneous broadening . . . 124
4.6.5 Bloch-Siegert effect . . . 126
4.6.6 Summary . . . 131
4.7 High amplitude modulation: the sideband model . . . 132

**5 Experimental Investigation into Noisy Perturbation 139**

5.1 Introduction . . . 139
5.2 Experimental modelling of the environment . . . 140
5.3 Measurement of population transport . . . 141
5.4 Experimental method . . . 141
5.4.1 Generation of the perturbation . . . 141
5.4.2 Determining the required number of realisations . . . 142
5.5 The system response to white noise perturbation . . . 144
5.5.1 Experimental method . . . 144
5.5.2 The response of the system to rms noise amplitude . . . 148
5.5.3 The density of states interpretation . . . 148
5.5.4 System behaviour at low rms amplitudes . . . 150
5.5.5 The effect of the resonances . . . 151
5.5.6 Distribution and spread of the resultant magnetisation . . . 151
5.5.7 Summary of the system response to white noise perturbation . . . 153
5.6 The response of the system to spectrally shaped perturbations . . . 153
5.6.1 Experimental procedure . . . 154

5.6.2 Experimental results for shaped perturbations . . . . . 156
5.6.3 Conclusions . . . . . 165
5.6.4 Sideband interpretation of the effect of shaped perturbations . . . . . 166
5.7 Effect of the spectral width of the noisy Lorentzian perturbation . . . . . 169
5.8 The effect of Static Disorder . . . . . 170

**6 Conclusions and Further Work** **175**
6.1 Principal conclusions . . . . . 175
6.2 Future work . . . . . 178
6.2.1 Implementing a multiply connected network . . . . . 178
6.2.2 Implementing a sink . . . . . 179
6.2.3 Realising a 'genuine' three-level system . . . . . 180
6.2.4 Making the perturbation of the energy levels independent . . . . . 184
6.2.5 Implementation of the glass cell . . . . . 185
6.2.6 Expanding the system to more sites . . . . . 187
6.2.7 Non-Markovian dynamics . . . . . 187
6.3 Final Conclusions . . . . . 188

**List of References** **I**

# LIST OF FIGURES

1.1 **The FMO complex:** The FMO complex is comprised of 8 BChl molecules that make up the excitation sites. A chromophore absorbs a photon forming an exciton that is transferred to the nearest site (in this case site 8) in the FMO. The exciton is then transferred between sites to the molecule that is closest to the reaction centre (site 3), from where it is incoherently transferred to the reaction centre. Figure adapted from Jia [1] and Lambert [2]. . . . . 4

1.2 **The principle of 2D spectroscopy:** The $x$ axis corresponds to the coherence frequency, that represents the frequency of the initial excitation, and the $y$ axis the re-phasing frequency, that represents the subsequent re-emission frequency. The off-diagonal peaks are cross peaks, where the absorption and re-emission frequencies differ, and correspond to transfer of population between sites of the system. Figure from Scholes et al [3]. . . . . 7

1.3 **Open quantum systems:** The open quantum system comprises the system, environment and the system-environment interaction. The environment is larger and has many more degrees of freedom than the system. . . . . 9

1.4 **Overlap of states:** As the width of the energy distribution of the states is increased the states overlap increasing the coupling/entanglement between the states and thus the transport. Black signifies the base states and red the dressed states. Dephasing introduces low frequency noise into the system increasing the width of the states. Figure from Caruso et al [4]. . . . . 12

1.5 **Vibration assisted transport:** The frequency components of the environment causes transitions between dressed states. Figure from Huelga et al [5]. 14

1.6 **Modified Mach-Zender interferometer:** a) the four site network; sites 1 and 2 are fiber Bragg gratings (FBG) and sites 0 and 3 are 50/50 beam splitters. b) Schematic representation showing the arrangement of the Mach-Zender interferometer; mirrors (M1 and M2) reflect the empty ports of the 50/50 back into the system entangling the cavities. The detector (D3) is the sink state where the excitation is destroyed. c) The optical fiber set-up; the laser produces the initial excitation that travels through the fiber network. Figure from Viciani et al [6]. . . . . 17

1.7 **Landau-Zener-Stuckelberg interference diagram:** a) the avoided crossing of the energy eigenstates of the system, due to the coupling. b) the perturbation of the detuning. Figure adapted from Shevchenko et al [7]. . . . . 23

1.8 **Landau-Zener-Stuckelberg interference:** For low frequency perturbations small proportions of the population are transferred each time the resonance of the system is crossed. The figure is simulated using QuTip [8,9] for a two-level system. . . . . 24

1.9 **Fully connected network (FCN):** a) The initial excitation is formed by pumping all the atoms to the $m_F$=+1 state and the target site is the $m_F$=-1 state. The RF field couples the nearest neighbour states together ($m_F$=1 to $m_F$=0 and $m_F$=0 to $m_F$=-1), and the Raman transitions couple the next nearest neighbour states together ($m_F$=1 to $m_F$=-1), b) The three sites are the magnetic sub-states of the F=1 level of rubidium 87. . . . . 28

2.1 **The co-rotating and counter-rotating cases:** The co-rotating cases are; 1a) where a photon is absorbed and the state is excited to the higher energy state, and 1b) the case where the state is de-excited to the lower energy state and a photon is emitted. The counter-rotating cases are; 2a) that the state absorbs a photon and transmits to the lower energy state, and 2b) that the state is excited from the lower energy to the higher energy state with the emission of a photon. . . . . 35

2.2 **Rabi oscillations for a three level system:** The evolution of the populations in the system states, for $40kHz$ RF coupling and initial state $|+1\rangle$, dependency on the detuning; a) the evolution of state $|-1\rangle$, b) the evolution of state $|0\rangle$, c) the evolution of state $|+1\rangle$, and d) the evolution of the magnetisation of the system $(p_{+1} - p_{-1})$. . . . . 40

2.3 **Bloch sphere:** Representation of a state of the system ($\psi$) on a Bloch sphere. The state is defined by 2 parameters; the angle of rotation around the x axis ($\theta$) and the angle of rotation around the z axis ($\phi$) . . . . . 41

2.4 **Evolution represented on a Bloch sphere:** The precession of the $|+1\rangle$ state on the Bloch sphere for a coupling frequency ($\Omega_{RF}/2\pi$) of $40kHz$ for different detunings; a) the Bloch sphere representation showing the precession of the initial state around the precession axis for different detunings, b) the change in the angle $\phi$, the rotation angle around the $z$ axis defined in figure 2.3, for different detunings, c) the change in the angle $\theta$, the rotation angle around the $x$ axis defined in figure 2.3, for different detunings, and d) the evolution of the magnetisation, the projection of the state on the z axis, for different detunings. . . . . 46

2.5 **Dephasing and decoherence:** a) the interaction of a system with a fluctuating environment causes dephasing, b) the average of the density matrix of an ensemble of systems dephases due to interactions with a fluctuating environment. Each system of the ensemble interacts with a slightly different environment that has the same spectral shape, c) decoherence can result from the entanglement of system states with the states of a bath. The bath's states cannot support long term coherence and therefore are constantly being traced over destroying the superposition between the system and the bath and thus the state of the system partially collapses to a mixed state. . . . . 49

2.6 **Dephasing of a two level system under coupling and pure dephasing:** a)$\gamma_\phi = 0$, no dephasing; only the coherent part of the evolution is observed, b) $\gamma_\phi = 1$, medium dephasing; the coherent oscillation is damped and the state tends to the thermalised state (equal population), and c) $\gamma_\phi = 20$, strong dephasing; the coherent oscillation is no longer observed and the state takes longer to decay to the thermalised state. $\tau_{\Omega_{gen}}$ is the period of the generalised Rabi frequency. The results were simulated using QuTip [8, 9]. . . . . 54

2.7 **Measurement and dephasing:** The evolution of the population in the excited state of a two level atom. a) For 1 realisation the evolution of the system collapses multiple times due to the effect of the measurement. b) For the average of 100 realisations the response is very similar to that of a dephasing process. . . . . 63

3.1 **The system network:** a) representation of the fully connected network (FCN) with nearest neighbour radio frequency (RF) coupling and next nearest neighbour Raman coupling. The initial excitation (full population in the $m_F = +1$ state) transfers between the sites to reach the target site ($m_F = -1$ state). b) the energy level structure of the system. A magnetic bias field (B) splits the energy levels (Zeeman effect) and an RF field couples the nearest neighbour sites. Noise is introduced into the system by perturbing the bias field, 'shaking' the energies of the sites. . . . . 66

3.2 **The full pumping procedure:** Initially the atoms are cooled using laser cooling followed by molasses cooling. This results in the majority of the atoms being in the $F = 2$ state. The atoms are then pumped to the $F = 1$ state using the de-pump beam and then polarised into the $F = 1$ $m_F = +1$ state using the F1 polarisation beam. The couplings and perturbations under investigation are then applied and the resulting distribution between the $F = 1$ $m_F$ states is measured. The measurement involves a Stern-Gerlach pulse that spatially separates the atoms depending upon their $m_F$ state. The F1 pumping beam then pumps the atoms to the $F = 2$ state from where they are polarised into the $F = 2$ $m_F = 2$ substate. Finally the three atomic clouds are measured using absorption imaging to obtain an optical density profile of the three clouds. This profile is then fitted to determine the distribution of the population between the three $m_F$ states. . . . . 67

3.3 **Molasses temperature measurement:** The cold atomic cloud is allowed to expand for varying times in order to determine the temperature. The cloud profiles are fitted using a 2D Gaussian function and the horizontal (x) and vertical (y) widths of the clouds are determined. For this particular measurement the number of atoms was determined to be ≈10 million atoms at ≈10$\mu$K. Over the measurement time the cloud can be observed to fall due to gravity. . . . 69

3.4 **The experimental set-up:** The arrangement of the coils around the vacuum system and the resulting fields imparted on the atoms in the the cloud. . . . 69

3.5 **Beam frequencies:** The multiple frequencies of the beams used in this study in relation to the atomic energy levels. The $F'$ states represent the excited states. This figure was adapted from Steck Alkali D data [10]. . . . . 71

3.6 **Depumping:** a) The $F = 1$ state is populated using the $F = 2$ to $F' = 1$ depump beam, b) the population left in the $F = 2$ state for varying depump irradiation times. . . . . 73

3.7 **Optical pumping:** a) The $F = 1$ $m_F$=+1 state is populated using a $\sigma_+$ polarised beam, b) the change in the relative fraction of the population between the three states with varying F1 polarisation pumping time. . . . . 75

3.8 **Measurement procedure:** The Stern-Gerlach field spatially separates the cloud dependent upon the $m_F$ state. The clouds are then pumped to the $F = 2$ $m_F = +2$ state and imaged using absorption imaging. . . . . 76

3.9 **F1 repumping:** a) The $F = 2$ state is populated using the F1 polarisation pumping beam, b) the measured dependence of the atom population in the $F = 2$ state on the pumping time. . . . . 78

3.10 **F2 pumping:** a) pumping the atoms to the $F = 2$ $m_F$=+2 state using a $\sigma^+$ beam, b) the dependence of the measured population in the $F = 2$ state on the pumping time. The measured population is dependent upon the distribution of the atoms between the $F = 2$ $m_F$ states. . . . . 80

3.11 **The dependence of the amplitude of the RF field on time for an applied square pulse:** The RF field amplitude asymptotically approached a maximum with a shape of the form $(1 - e^{-t/\tau})$, where $\tau$ is the time constant. This non-instantaneous behaviour results from the resonance response of the coil. . . . . 83

3.12 **Adiabatic following**: a) The dependence of the amplitude of the RF coupling pulse on time, b) as the pulse time is varied for a 0.01ms power on/off time the amplitude of the off-resonance response is reduced compared with the instantaneous pulse, c) the response of the system for an on-resonant $0.1ms$ pulse showing the state of the system during the evolution, d) the response of the system for an off-resonant $0.1ms$ pulse showing the state of the system during the evolution. A slow increase/decrease in the amplitude of the RF field results in adiabatic following of the state. For an instantaneous pulse the distribution between the states does not evolve after the pulse is powered off. 84

3.13 **The experimentally determined dependence of the Rabi oscillations on the magnetic field:** a) Example Rabi oscillation for off-resonant coupling (magnetic field= 990 $kHz$), b) example Rabi oscillation for on-resonant coupling (magnetic field= 1017 $kHz$), c) the dependence of the amplitude of the Rabi oscillations on the magnetic field (detuning), d) the dependence of the frequency of the Rabi oscillations on the magnetic field (detuning). At the resonance the Zeeman splitting is equal to the RF field frequency and this was used to calibrate the magnetic field. . . . . 85

3.14 **The dependence of the Rabi oscillations on the amplitude of the RF field:** a) example on-resonance Rabi oscillation for $0.4mW$ of RF power, b) example on-resonance Rabi oscillation for $1.26mW$, c) the dependence of the frequency of the on-resonance Rabi oscillations measured experimentally on the amplitude of the RF field, d) the dependence of the amplitude of the on-resonance Rabi oscillations on the amplitude of the RF field. The on-resonance Rabi frequency increases linearly with RF amplitude but the amplitude of the on-resonance Rabi oscillation asymptotically approaches a maximum due to inhomogeneous broadening. The amplitude of the RF field is the amplitude of the output from the frequency generator, which is proportional to the amplitude of the RF field at the atoms. . . . . 87

3.15 **Energy levels of the Raman transition:** The energy levels for the D1 line of rubidium 87 showing the ground states (1,2) and the excited states (a,b,c,d) that interact with the Raman beams. From K.C.Wright et al [11] . . . . . 88

3.16 **Quantisation axis:** The geometrical relationship between the Raman beams and the bias field (quantisation axis). From K.C.Wright et al [11] . . . . . 89

3.17 **Finding the optimum detuning:** a) Raman coupling frequency, b) scattering rate and c) modulus of the ratio dependence upon the detuning of the Raman laser for the D1 transition in rubidium 87 at an intensity of $10mW/cm^2$ for each beam. The detuning of the Raman laser is taken relative to the transition frequency corresponding to the $F = 1$ to $F' = 1$ transition. The second resonance corresponds to the $F = 1$ to $F' = 2$ transition frequency (detuning $= 814.5MHz$). The red line corresponds to the total, the blue is the contribution from the $F = 1$ to $F' = 1$ transition and the green is the contribution from the $F = 1$ to $F' = 2$ transition. . . . . 91

3.18 **The scalar light shift:** Single photon dressing results in light shifts moving the energy of the outer states. The antisymmetric shifts can be compensated using the frequency difference between the Raman beams and altering the resonance frequency of the RF field. The scalar light shift however cannot be compensated for as it is effectively moving the central state and creating a difference in the energy between the central state and the outer 2 states. . . 93

3.19 **Scalar light shift:** The dependence of the scalar light shift ($\frac{\tilde{\alpha}}{2}$) on the detuning for a beam intensity of $10mW/cm^2$ ($I_+ = I_- = 10mW/cm^2$). . . . . 94

3.20 **The dependence of the scalar light shift on the intensity:** A comparison of the light shift and the Raman-Rabi frequency at the optimum point ($252MHz$) for different intensities ($I_+ = I_-$). The modulus of the Rabi frequency and the light shift is shown to allow for direct comparison, the value of the light shift is negative. . . . . 94

3.21 **Schematic for the Raman transition experimental set-up:** Two beams were generated with opposite circular polarisation and shifted by the frequency splitting between the $m_F = 1$ and $m_F = -1$ states. The laser was locked using a DAVLL lock. . . . . 96

3.22 **Raman-Rabi oscillation:** A damped Rabi oscillation (frequency=$3.25 \pm 0.32kHz$, amplitude=$0.66 \pm 0.10$ and damping rate=$0.11 \pm 0.01ms$) was observed for different Raman pulse times. . . . . 97

3.23 **Characterisation of the response of the perturbation coil driver:** a) shows the response of the current for a 50kHz sine wave, b) shows the response to changing frequency. . . . . 98

3.24 **Example absorption image:** An example image of the calibration shot, showing the three fitted 2D Gaussians. . . . . 99

4.1 **Modulation on the Bloch sphere:** a) Oscillation of the bias field in the base state basis due to the modulation, showing the modulation (green), the precession axis (blue) and the quantisation axis (red) b) the oscillating bias field is decomposed into both a perpendicular and parallel modulation on the precession axis, and c) the resulting perpendicular and parallel coupling in the dressed basis arising from the modulation. . . . . 103

4.2 **Fundamental on-resonance response:** Experimental results showing an $8kHz$ ($Freq_{low}$) Rabi oscillation for the fundamental response, where the modulation frequency was equal to the generalised Rabi frequency ($\omega_m = \tilde{\Omega}$). . . 106

4.3 **The effect of varying the generalised Rabi frequency:** The frequency of the measured Rabi oscillations plotted against the generalised Rabi frequency. 109

4.4 **Spectroscopy:** a) Rabi oscillation for $\omega_m = 30kHz$, b) Rabi oscillation for $\omega_m = 60kHz$, c) experimental results for the dependence of the amplitude of the Rabi oscillations on the modulation frequency, showing the fundamental and sub-resonances. . . . . 110

4.5 **Possible photon transition paths:** a) a 1 photon transition resulting from the absorption of a $\sigma^+$ photon, b) a 2 photon transition resulting from the absorption of a $\sigma^+$ and $\pi$ photon, c) a 3 photon transition resulting from the absorption of a $\sigma^+$, and two $\pi$ photons, d) a 3 photon transition can also result from the absorption of a $\sigma^+$, $\sigma^-$ and $\sigma^+$ photon. . . . . 112

4.6 **Rabi frequency for the fundamental and 1st mode:** The coupling frequency dependence on the modulation amplitude for the fundamental and 1st mode. . . . . 119

4.7 **Resonance width:** The dependence of the width of the resonance of the fundamental and 1st mode on the modulation amplitude. The width of the fundamental had a linear response, whereas the width of the 1st mode was smaller and had a quadratic response. . . . . 125

4.8 **The on-resonance minimum magnetisation response of the atoms:** The dependence of the on-resonance minimum of the magnetisation (that is related to the amplitude of the Rabi response) on the modulation amplitude. 127

4.9 **Bloch-Siegert shift:** Experimental data showing the dependence of the shift of the fundamental and 1st mode resonance frequencies on the modulation amplitude. . . . . 131

4.10 **High amplitude response:** The dependence of the fundamental frequency response on the amplitude of the modulation. . . . . 133

4.11 **Sidebands on the Bloch sphere:** Green is the Bloch vector that corresponds to the un-modulated dressing of the system by the RF (detuning of $\Delta$), blue is the Bloch vector for the 1st order sideband (detuning of $\Delta - \omega_m$), and red is the Bloch vector for the 2nd order sideband that is on-resonance ($\Delta - 2\omega_m = 0$). . . . . 138

4.12 **Sidebands:** a) The dependence of the strength of the different sidebands on the modulation amplitude. As in the case of the Floquet theory, the 1st sideband frequency increases linearly, the 2nd quadratically and the 3rd cubically. b) An example of the Fourier transform of the coupling frequencies. The 1st sideband frequency corresponds to the single photon, the 2nd to the two photon and the 3rd to the three photon transition. . . . . 138

5.1 **Average of the system response to a fluctuating environment:** To determine the response of the system to a fluctuating environment the distribution of the population between the system states was measured for different realisations that had the same spectral shape but different individual components. . . . . 140

5.2 **Generating and shaping the perturbation** (sequential processing is shown in a) to e)): a) Randomly distributed points that have a Gaussian distribution of width 1.00 are generated at discrete points in time, b) this signal is Fourier transformed and has a flat white noise spectrum, c) the spectrum is then shaped by multiplying the spectrum by a filter function that has the desired spectral feature, d) the final shaped white noise spectrum, and e) the normalised realisation is generated by applying the inverse Fourier transform to the shaped spectrum, and normalising the resultant signal. This normalised signal (that contains the desired spectral features) is amplified to produce the final signal. . . . . 143

5.3 **The dependence of the distribution of the moving average on the numbers of realisations:** 100 realisations of a white noise ($0 - 100kHz$, noise rms $= 59kHz$) perturbation were applied to the system for $60\mu s$ and the resultant responses averaged using the moving average method where the number of realisations (bin size) was altered. . . . . 144

5.4 **The dependence of the final state on the rms noise amplitude:** The rms amplitude of the noisy perturbation ($0 - 50kHz$ flat spectral shape) was varied for a $60\mu s$ evolution time and the average of the population in the different $m_F$ states for 25 realisations measured. The rms amplitude is in units of frequency in order to provide comparison with the energy separation of the magnetic sub-states ($\approx 1MHz$). The vertical histograms show the population distribution of the 25 realisations for each value of the noise field amplitude. The colour in the key corresponds to the fraction of the 25 realisations that were in the final state (e.g for an amplitude of $0kHz$ the probability that the magnetisation ($p_{+1} - p_{-1}$) of the final state will have a value of between 0.8 and 1.0 is 100%). . . . . 146

5.5 **3D representation of the dependence of the probability distribution on the rms perturbation amplitude:** 3D representation of the vertical histograms in figure 5.4 showing the dependence of the probability distribution on the rms perturbation amplitude. . . . . 147

5.6 **Overlap of the RF field and the energy distribution of the state:** Pictorial representation of the overlap between two adjacent energy levels, where the distribution of the energy of the upper state has a broadening of its energy distribution, overlapping with the frequency of the coherent coupling field. . . . . 149

5.7 **Shaping the perturbation:** Shaping the spectrum of the perturbation allows different resonances to be targeted. For the $0 - 50kHz$ band the system response is dependent on the contributions from all the resonances. For the $20 - 40kHz$ band only the fundamental resonance contributes toward the system response. . . . . 152

5.8 **Filter functions used in this study:** The shape of the filter functions used to generate the perturbations in this study (from top to bottom); $0-100kHz$ band, $0-50kHz$ band, $0-20kHz$ band, $20-40kHz$ band and Lorentzian band of width $10kHz$ centred at the generalised Rabi frequency. . . . . 155

5.9 **The magnetisation of the system in response to the $0-100kHz$ perturbation:** a) The dependence of the system magnetisation on the rms amplitude applied for an evolution time of $60\mu s$ (the rms amplitude is in units of frequency in order to provide comparison with the energy separation of the magnetic sub-states ($\approx 1MHz$)). b) The dependence of the system magnetisation on evolution time for fixed rms amplitudes of $44kHz$, $59kHz$ and $73kHz$. The vertical histograms show the population distribution of the 25 realisations and the colour in the key corresponds to the fraction of the 25 realisations that were in the final state. The histogram in b) only displays data from the $59kHz$ response. . . . . 157

5.10 **The magnetisation of the system in response to the $0-50kHz$ perturbation:** a) The dependence of the system magnetisation on the rms amplitude applied for an evolution time of $60\mu s$ (the rms amplitude is in units of frequency in order to provide comparison with the energy separation of the magnetic sub-states ($\approx 1MHz$)). b) The dependence of the system magnetisation on evolution time for fixed rms amplitudes of $34kHz$, $45kHz$ and $56kHz$. The vertical histograms show the population distribution of the 25 realisations and the colour in the key corresponds to the fraction of the 25 realisations that were in the final state. The histogram in b) only displays data from the $45kHz$ response. . . . . 158

5.11 **The magnetisation of the system in response to the $0 - 20kHz$ perturbation:** a) and b) The dependence of the system magnetisation on the rms amplitude applied for an evolution time of $70\mu s$ and $120\mu s$ respectively (the rms amplitude is in units of frequency in order to provide comparison with the energy separation of the magnetic sub-states ($\approx 1MHz$)). c) The dependence of the system magnetisation on evolution time for fixed rms amplitudes of $26kHz$, $33kHz$, $44kHz$ and $55kHz$. The vertical histograms show the population distribution of the 25 realisations and the colour in the key corresponds to the fraction of the 25 realisations that were in the final state. The histogram in c) only displays data from the $44kHz$ response. . . . . 159

5.12 **The magnetisation of the system in response to the $20 - 40kHz$ perturbation:** a) The dependence of the system magnetisation on the rms amplitude applied for an evolution time of $70\mu s$ (the rms amplitude is in units of frequency in order to provide comparison with the energy separation of the magnetic sub-states ($\approx 1MHz$)). b) The dependence of the system magnetisation on evolution time for fixed rms amplitudes of $22kHz$, $39kHz$ and $51kHz$. The vertical histograms show the population distribution of the 25 realisations and the colour in the key corresponds to the fraction of the 25 realisations that were in the final state. The histogram in b) only displays data from the $39kHz$ response. . . . . 160

5.13 **The magnetisation of the system in response to the $10kHz$ width Lorentzian perturbation:** a) The dependence of the system magnetisation on the rms amplitude applied for an evolution time of $40\mu s$ (the rms amplitude is in units of frequency in order to provide comparison with the energy separation of the magnetic sub-states ($\approx 1MHz$)). b) The dependence of the system magnetisation on evolution time for fixed rms amplitudes of $22kHz$, $37kHz$ and $59kHz$. The vertical histograms show the population distribution of the 25 realisations and the colour in the key corresponds to the fraction of the 25 realisations that were in the final state. The histogram in b) only displays data from the $37kHz$ response. . . . . 161

5.14 **Response of the magnetisation of the system to different perturbation spectral shapes:** The response of the magnetisation to the different spectral shapes is shown. The behaviour of the system for no perturbation is included in order to provide comparison. . . . . 163

5.15 **An example of the modulus of the Fourier transform of $A(t)e^{i\omega_0 t}$:** The Fourier transform of $A(t)e^{i\omega_0 t}$ plotted for a rms perturbation amplitude of $50kHz$ for different perturbation shapes. . . . . 167

5.16 **The dependence of the strength of the on-resonance Fourier component, $c$, on the rms amplitude of the perturbation of different perturbation shapes:** The strength of the on-resonance Fourier component, $c$, is in arbitrary units. . . . . 168

5.17 **The response of the magnetisation of the system to the $5kHz$ width Lorentzian perturbation frequency band:** The dependence of the magnetisation of the system on the evolution time for a fixed rms amplitude of $36kHz$. . . . . 170

5.18 **Computational simulation of static disorder:** a) pictorial representation of the two level system under investigation. The distribution of the energy of the upper state has static disorder. The coupling between the states is resonant when $\omega_{RF}$ is equal to $\omega_0$. b) The probability distribution of the detunings for different widths of static disorder. c) The average population response in the lower energy state for different static disorder widths. d),e) and f) the frequency components of the average population response in the lower energy state for the $5kHz$, $28kHz$ and $50kHz$ width bands respectively. 173

6.1 **The transitions require to implement a sink state:** a) diagram of the multiply connected network showing the three sites (composed of the magnetic sub-states) and the target state (sink state) that is connected to the network by an irreversible transition, b) the energy level structure and the transitions required to implement a sink state; atoms are excited from the $F = 1$ $m_F = -1$ state to the $F = 2$ $m_F = -2$ where they spontaneously decay to the sink state. 181

6.2 **Scattering ratio:** The dependence of the ratio of the scattering of the transition, $F = 1$ $m_F = -1$ to $F = 2$ $m_F = -2$, relative to the transition, $F = 1$ $m_F = 0$ to $F = 2$ $m_F = -1$, on the detuning of the sink beam for magnetic fields from 0-10 Gauss. The detuning is taken relative to the transition $F = 1$ $m_F = -1$ to $F = 2$ $m_F = -2$. . . . . 182

6.3 **The non-linear Zeeman effect:** a) The dependence of the energy of the $m_F$ states on the magnetic field for the range $0 - 1T$, b) The dependence of the energy of the $m_F$ states on the magnetic field for the range $0 - 20G$, c) the dependence of the difference in the resonant frequencies between adjacent $m_F$ states on the magnetic field. . . . . 183

6.4 **Glass cell:** The glass cell that is used in the enhanced set-up to remove the influence of eddy currents and provide more optical access. The cold atomic cloud is formed in the square part of the chamber and the flat surfaces of the cell (windows) have an anti-reflection coating. . . . . 186

6.5 **An example of non-Markovian feedback to the noisy perturbation:** a) the evolution of the population in the target state, b) the amplitude of the noise is altered for the next stage of the evolution depending on the measurement of the population in the target state (the multiplier in this case is one minus the population fraction in the target state). . . . . 189

# LIST OF TABLES

5.1 **Summary of the optimum rms amplitudes:** The optimum rms amplitudes for the different perturbations under investigation. . . . . 156

CHAPTER 1

# INTRODUCTION AND MOTIVATION FOR THE STUDY OF NOISE ASSISTED QUANTUM TRANSPORT

## 1.1 Introduction

Highly efficient processes may unexpectedly have both quantum and classical characteristics. Quantum mechanics accurately describes simple situations involving a limited number of atoms or molecules at relatively small distance and short times. As the complexity of the system increases it is generally thought that, due to the interaction with an environment, the system reverts to classical behaviour. In this study the hypothesis is that quantum behaviour, when combined with the interaction of the environment, can lead to situations where processes are more efficient than can be explained by either purely classical or quantum behaviour.

Understanding developed in this study will provide insight into how key mechanisms in complex biological systems are enhanced by exploiting quantum processes. A particular focus will be on how the rate and efficiency of exciton transport is enhanced in biological photosynthetic structures; indeed natural selection may have favoured the development of

quantum behaviour to enhance certain processes over purely classical evolution. In addition the work may have implications for the development of quantum computers [12, 13] and networks where full isolation from the environment is not possible. Efficient transport in solar cells may also be enhanced by similar hybrid processes, thus influencing the design of future devices.

Quantum coherence at room temperature has been detected in the Fenna Matthews Olson (FMO) photosynthetic complex [14] leading to theories that the combination of the quantum coherence and noisy environment produces highly efficient exciton transport. This is a counter-intuitive result as at room temperature it was previously believed that the system could not support quantum behaviour due to high levels of thermal noise that would de-cohere the quantum states. The FMO complex is a well-studied, simple structure making it the ideal candidate to investigate quantum processes in biological systems [2]. The dynamics of exciton transport in the FMO will be modelled in this study using the open quantum system approach that incorporates the system-environment interactions by including non-unitary dynamics between the states of the system, thus removing the large number of degrees of freedom introduced by the environment.

The role that the individual frequency modes of the environment have on the evolution of the system will also be investigated to gain insight into the effect that a resonant structure has on the system response, with emphasis on the role of multi-photon resonances. Many experiments have reported on the features of resonant quantum systems particularly those utilising the technique of nuclear magnetic resonance (NMR) [15–17]. More recently, superconducting qubit [18] and diamond nitrogen vacancy (NV) [19] systems have also been studied. The approach taken in this study will be to investigate a range of quantum processes using a simple three level cold atomic system that allows precise control of the energies and couplings of the states in an isolated environment. The interaction of the environment with

the system can thus be explored in a controlled manner.

## 1.2 Quantum processes in biological systems

Initially examples are given of quantum mechanisms that occur in biological systems. Following this the FMO complex, which is the key biological system that is being emulated in this study, is explained and the evidence surrounding the detection of coherence is discussed.

Quantum mechanisms are at the root of some of the most complex processes in biological systems; an example is found in birds, which use magnetic field sensing for navigational purposes [2, 20, 21]. A possible mechanism to describe this phenomenon involves pairs of free radicals in the cryptochrome proteins in the bird's retina [2]. Photons excite pairs of free radicals that have correlated unpaired electron spin. The evolution of the free radical pair is dependent on the orientation of the earth's magnetic field and thus the recombination decay ratio between the singlet and triplet states is altered; this is detected by the bird. For quantum processes to have an effect, long coherence times between the spins of the electron pairs are required, which is unexpected in a noisy thermal environment [2]. This suggests the presence of some unknown process that protects the coherent evolution of the states. Mammalian sense of smell has also been theorised to have a fundamental quantum basis where the vibrational modes of the molecules are thought to influence the quantum tunnelling processes that lead to a sensing signal. This is interpreted by the mammal to identify the molecule [22].

### 1.2.1 The Fenna-Matthews-Olson Complex

The photosynthetic Fenna-Matthews-Olson (FMO) complex is found in green sulphur bacteria in low light environments [14]. Chromophores absorb photons, forming excitons that

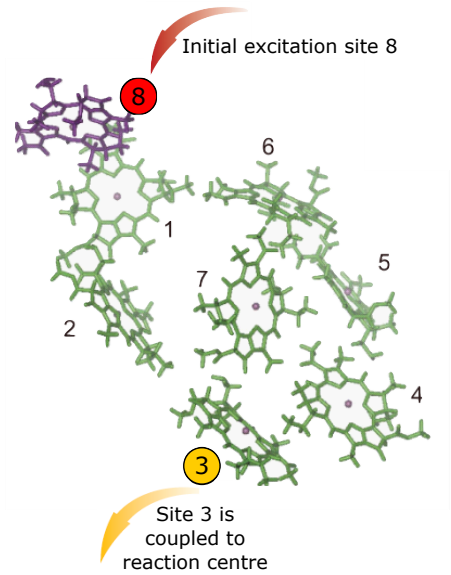


Figure 1.1: **The FMO complex:** The FMO complex is comprised of 8 BChl molecules that make up the excitation sites. A chromophore absorbs a photon forming an exciton that is transferred to the nearest site (in this case site 8) in the FMO. The exciton is then transferred between sites to the molecule that is closest to the reaction centre (site 3), from where it is incoherently transferred to the reaction centre. Figure adapted from Jia [1] and Lambert [2].

are transferred through the FMO complex to the reaction centre, where the photon's energy is chemically stored. The FMO complex is composed of eight sites that are coupled together in the presence of a noisy protein environment [2]. The observed high efficiency of exciton transport through the complex is thought to be due to the interplay between the quantum mechanical coupling and the noisy environment.

The FMO is most commonly modelled theoretically as a collection of energy levels that represent the sites in the FMO system. The interaction between sites in the FMO is represented by coupling these energy levels together. The interaction of the noisy environment can be simulated in these models by perturbing the energy of the levels. Key features of the FMO system are modelled in this study using a network of atomic energy levels, discussed further in section 1.8.

Measurements of the FMO have revealed the process of exciton transport through the FMO in more detail. The number of sites and the structure of the FMO are well understood through crystallographic studies [23] and the site energies have been determined using charge density coupling methods, measurements of the optical spectra and two-dimensional spectroscopy [14, 23]. Based on these measurements the following description of exciton dynamics has developed. A photon causes a charge separation event, an exciton, in the light harvesting chromophore. This exciton is transferred to the nearest site in the FMO complex, as shown in figure 1.1. The exciton is then transported internally through the FMO complex reaching the nearest site to the reaction centre from where it is irreversibly transferred to the reaction centre and absorbed. The lifetime of the exciton is of the order of $1ns$ and it decays due to recombination and fluorescence relaxations [24]. The transfer time of the exciton through the FMO is very fast, of the order of $10 - 100ps$ [25], therefore a strong quantum component is hypothesised. The Coulomb interaction between the sites allows for coherent transfer and consequently it is postulated that quantum mechanical wave-like transfer through the FMO occurs [14]. The transport process takes place at room temperature leading to incoherent variation of the energies of the sites. The combination of many path interference effects and the interplay between coherence and the incoherent noise is believed to explain the highly efficient exciton transfer [26].

The protein scaffolding that holds the FMO [2] is responsible for introducing classical noise into the system. The amplitude of the vibrational modes of the environmental noise is $10 - 100$ times lower than the coupling between the sites [5], therefore the major effect of the environment is to perturb the energies of the sites rather than directly coupling the sites.

### 1.2.2 Two-dimensional spectroscopy of the FMO complex

Coherent transport has been observed in the FMO complex at 77K using the technique of 2D Fourier transform electronic spectroscopy [14, 27, 28]. Two-dimensional spectroscopy observes how the absorption spectrum, measured using a local oscillator, is altered when the FMO complex is excited by a laser that can be tuned to the excitation energy of specific sites in the FMO complex [29–31]. If coherent transfer occurs between sites, the distribution of excited sites (and thus the amplitude of the absorption peaks) will oscillate and cross peaks will emerge, as shown in figure 1.2. Cross peaks are a result of the absorption of a photon by one of the states and the coherent transfer of the absorbed energy to another site [3]. The variation in time of the amplitude of these cross peaks leads to the conclusion that coherent transport is occurring between sites. Additionally it is found that there is correlation between the behaviour of the diagonal peaks and cross peaks that provides further support for this conclusion [14]. The oscillation of the cross peak amplitude lasts for greater than $660fs$ which is generally thought to be long enough to have a significant impact on the exciton transport dynamics [14]. Furthermore, analysis of the frequency components of this oscillation reveals beating corresponding to interference effects resulting from the different coherent transfer paths in the FMO complex. This result supports the concept of coherent wavelike transfer between sites as opposed to a classical hopping model [14, 32, 33].

## 1.3 Modelling of the FMO complex

This section describes the theoretical structures that are applied to model exciton transport through the FMO system. Initially there is a discussion of Forster and Redfield theory and the regimes in which they describe the system dynamics. Following this the open quantum system approach is discussed and finally the experimental application, used in this study, of the noise is described.

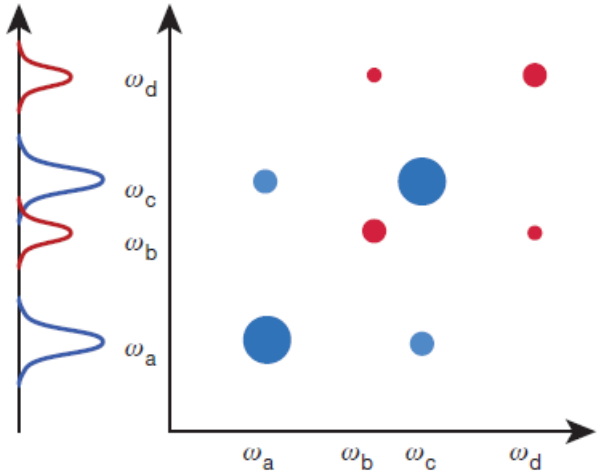


Figure 1.2: **The principle of 2D spectroscopy:** The $x$ axis corresponds to the coherence frequency, that represents the frequency of the initial excitation, and the $y$ axis the re-phasing frequency, that represents the subsequent re-emission frequency. The off-diagonal peaks are cross peaks, where the absorption and re-emission frequencies differ, and correspond to transfer of population between sites of the system. Figure from Scholes et al [3].

The modelling of the FMO can be split into two broad cases; situations where the coupling is weak therefore the environment directly causes transport, and instances where the coupling is strong and the interaction with the environment is treated perturbatively [34]. In the first case transport through the network is described using a Forster theory approach where the exciton hops between states incoherently due to the interaction with the environment [27, 34] , therefore no phase information is retained as the exciton is transported through the system. The second case is described using Redfield theory where the coupling is strong and therefore the environment is treated as a perturbation [34, 35]. Prior to the discovery of long lived quantum coherence in the FMO [14] it was believed that a classical hopping Forster theory best represented transport through the FMO. However the theory was not able to explain the high efficiency of exciton transport, consistent with measured properties of the FMO, and therefore it was theorised that quantum superpositions and coherences, allowing for constructive and destructive interference, play a greater role [36]. In addition the amplitude of

the vibrations of the environment in the FMO are a factor of 10 less than the coupling between the sites [5], thus this study will focus on the regime covered by the Redfield theory. [2,33,37]

### 1.3.1 Introduction to open quantum systems

The key features emerging from experiments with the FMO are that 1) there is clear evidence of wavelike transfer with interference effects observed between competing paths, 2) the system functions with large levels of environmental noise, and 3) there is unidirectional flow to the reaction centre [33]. Due to the presence of quantum effects and the large number of degrees of freedom (due to the environment) the theories of open quantum systems are needed to model the interaction of the system with a noisy classical environment [38–41]. The interaction is typically modelled as perturbations of the energies of the sites; this is referred to as pure dephasing noise [4, 42–44].

An open quantum system is a system where interactions with the environment influence the evolution of the system. The elements of the full system include the system (composed of the sites), the states of the environment and the interactions with the environment [38], as shown in figure 1.3. However in most practical cases full knowledge of the system is not possible and the interactions with the environment have to be approximated. Non-unitary evolution due to non-Hermitian interactions are therefore possible between the states of the system in interaction with the environment. Key processes that are modelled using open quantum systems are dissipation and dephasing [25, 44–46]. Dissipation is the process by which excitons are exchanged with the environment, dissipating energy from the molecular complex into the larger environment. Dephasing is used to describe any loss of phase between the sites of the system. This can be due to, for example, quantum mechanical decoherence processes resulting from the entanglement of the system with a bath that does not support long term entanglement or by classical variation of the system parameters over the evolution

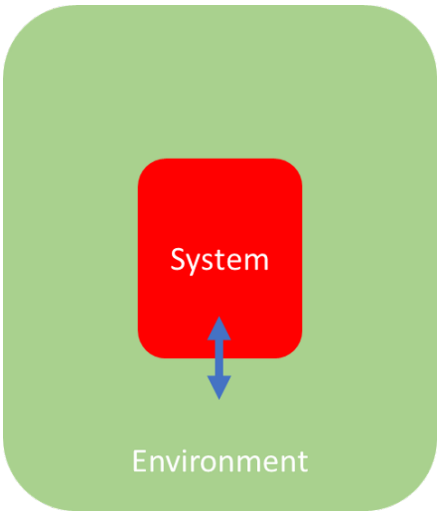


Figure 1.3: **Open quantum systems:** The open quantum system comprises the system, environment and the system-environment interaction. The environment is larger and has many more degrees of freedom than the system.

of the system [38].

An open quantum system master equation approach describing the evolution of the system's density matrix with Lindblad equations has been used in the literature to model the system and the interactions between sites due to the environment [47, 48]. The Lindblad equations represent the non-unitary terms governing the evolution of the system that arise due to the interaction with the environment [49]. A series of approximations about the environment are used in order to represent the system in a Lindblad form [45]. The first approximation is the Born approximation where the environment is considered to be very large and does not significantly change due to interactions with the system; in this case the interaction with the system can be treated as a perturbation and no correlations with the environment evolve. The second approximation is the Markov approximation where the evolution of the system is dependent only upon the current state and not on past interactions, thus in this case the correlation function of the environment is short compared with the evolution time (this is described as the environment having no memory). A structured

environment has non-Markovian characteristics where environment-system correlations can evolve [50]. The final approximation used to generate Lindblad equations is the secular approximation where the fast rotating terms in the Hamiltonian are neglected, similar to the rotating wave approximation (RWA) [38, 51].

### 1.3.2 Experimental modelling of a noisy environment

In this study the environment will be modelled as noisy perturbations of the site energies. The effects of a noisy classical environment can be modelled by averaging multiple quantum trajectories that have evolved under the influence of perturbations which have similar noisy spectral shapes [52]. Each trajectory is a unitary evolution however the average of all the trajectories can have non-unitary properties [53]. Spontaneous emission results from the coupling of a site to a quantum bath (quantum vacuum fluctuations) that causes incoherent decay [54–56]. Therefore, if a site in the system is coupled to a site that has spontaneous emission processes, the quantum bath will effect the evolution of the system.

## 1.4 Key models for transport mechanisms

A lot of theoretical interest [24, 26, 33, 37, 57, 58] has been generated since the discovery of coherence in the FMO [14]. Over time this theoretical understanding has been furthered by improved measurements of both the FMO and the structure of the environment generated from the protein scaffolding [59, 60]. Initially dephasing assisted transport [24, 26, 44] was thought of as the most likely candidate to explain the high efficiency of transport within the FMO complex, however as refinements were made to the measurement of the spectrum of the environment, vibration assisted transport [5, 61, 62] was suggested as a more likely mechanism.

### 1.4.1 Dephasing assisted transport

Dephasing destroys the coherence between sites; this, counter-intuitively, leads to increased transport in cases where the localisation of an exciton is due to destructive interference [56]. As the dephasing is increased, destructive interference is reduced and thus the overlap with the target site (the site that is coupled to the reaction centre) is increased [4]. For low levels of dephasing the sites are in a coherent superposition with a small overlap with the target site, the role of dephasing is to destroy this superposition and thus the transport rate is increased [26].

Alternatively dephasing can be interpreted as broadening of the distribution of the site energy, figure 1.4, which increases the overlap between the sites that have different energies (static disorder), and thus increases the rate of transport [4, 24]. The broadening due to dephasing can also be thought of as introducing low frequency noise into the system that can combine with a weak coherent coupling field, opening new strong transfer paths. For very large dephasing, the widths of the energy distribution of the sites are very large and consequently the overlap between the sites and the coupling field is small. This is equivalent to the watchdog (quantum Zeno) [63–68] effect where the system partially or completely collapses to the base site basis at a rate of $1/\gamma$ [26] due to a measurement process, where $\gamma$ is defined as the dephasing rate and is related to the width of the energy distribution of the state. This acts to reduce transport by rapidly destroying all coherences and hence the system does not evolve, localising the initial excitation. The increase in the transport rate due to the addition of dephasing is small in systems where the static disorder (where the energy difference between the states is very disordered) is large and consequently it does not fully explain the enhanced rate of transport observed in the FMO. [44].

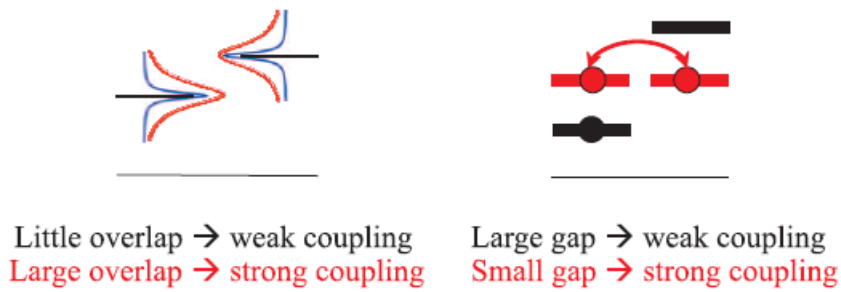


Figure 1.4: **Overlap of states:** As the width of the energy distribution of the states is increased the states overlap increasing the coupling/entanglement between the states and thus the transport. Black signifies the base states and red the dressed states. Dephasing introduces low frequency noise into the system increasing the width of the states. Figure from Caruso et al [4].

Rebentrost et al. [26] suggest that the effect of dephasing can be treated as diffusion on a Bloch sphere. Bloch spheres are a 3D representation of the state of a system and Rebentrost et al. model diffusion as a biased random walk on the surface of the Bloch sphere. This random walk has a step size dependent upon the Hamiltonian acting on the system and an evolution time dependent on the decoherence rate (that is related to the strength of the dephasing). The result of this intepretation is that, for a large decoherence rate, the evolution time is short and consequently the quantum Zeno effect slows the evolution of the system state (due to the initial quadratic response of the system evolution under the Hamiltonian). For a small decoherence rate, on the other hand, the system state evolution is dominated by the effect of the Hamiltonian and the system's state remains localised for a long time. In-between these extremes the optimum decoherence rate causes the system state to delocalise and diffuse around the Bloch sphere.

### 1.4.2 Vibration Assisted Transport

The energy spectrum of the protein structure that is responsible for the environment surrounding the FMO reveals a complex noisy structure that could influence the transport [59,60]. The spectrum has a continuous smooth background that reaches a maximum, as well as discrete peaks corresponding to long-lived vibrational modes [5]. The sites in the FMO are weakly coupled together and therefore interactions of the environment with the system can no longer be considered independent of the coupling, the new states (eigenstates) of the coupled system are referred to as dressed states. The long lived vibrational modes present in the environment are able to cause transitions between the dressed states thus enhancing transport, as shown in figure 1.5. Frequencies that resonate with the energy splitting of the dressed states strongly contribute to the transport [5]. Consequently it has been suggested that the FMO complex may have naturally evolved quantum coherence in order to use the noisy power of the vibrational modes in the environment to enhance transport [5]. This could also provide an explanation for the robust nature of the transport rate in the FMO in response to variations of the environment. The vibrational assisted transport mechanism is effective in cases where the static disorder is large, in contrast to dephasing assisted transport.

## 1.5 Experimental investigations of noise assisted quantum transport (NAQT)

Various experiments have investigated the dynamics of quantum systems that are interacting with an environment in both the dephasing and vibrational regimes. The key features of the FMO that experiments try to replicate are; 1) there is an initial excitation, 2) there is control of the static and dynamic disorder of the energy states of the sites, 3) there is coupling between the sites and 4) there is an excitation sink. In the following section the

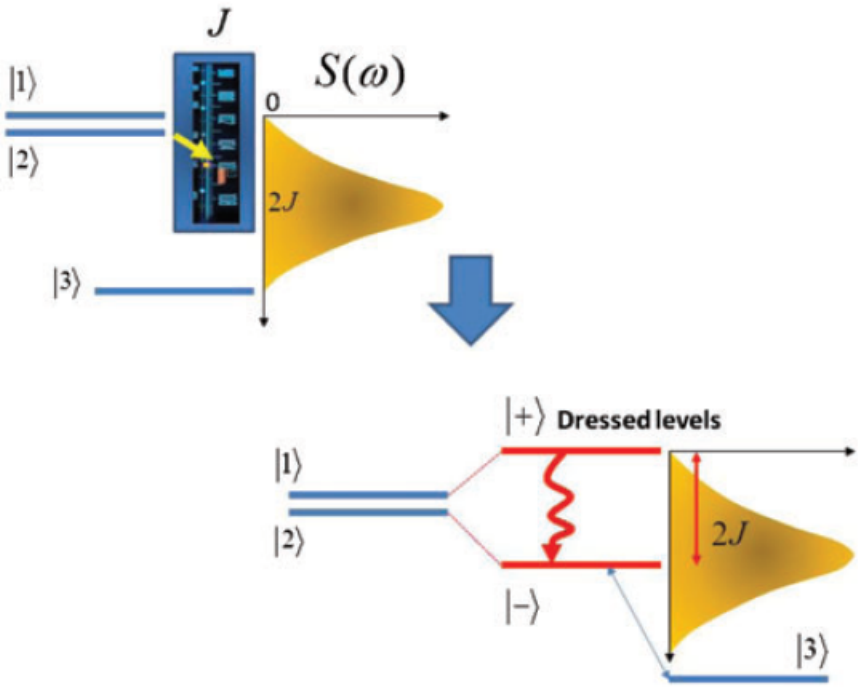


Figure 1.5: **Vibration assisted transport:** The frequency components of the environment causes transitions between dressed states. Figure from Huelga et al [5].

approach taken by these different experiments will be critically evaluated.

### 1.5.1 Optical systems

Optical systems using coupled cavities have been developed to examine noise assisted quantum transport processes [6,58]. One such experiment conducted by Viciani et al. [6] examined the efficiency of transfer through coupled cavities in a modified Mach-Zender interferometer, as shown in figure 1.6. In this experiment the initial excitation is provided by a laser, the excitation sink is provided by an optical detector and an individual cavity is a site in the network which is excited when a photon is present. The coupling between the cavities is provided by reflecting the empty ports of the interferometer back into the system. The cavities are fibre Bragg gratings with resonant frequencies that are controlled using piezoelectric transducers, this allows the simulation of both static disorder and dynamic noise (dephasing noise).

The system is initialised so that the relative phase between the two interferometer arms produces destructive interference at the detector when the cavities are both on-resonance. In the case of the non-modified Mach-Zender interferometer a large static disorder (large detuning of one of the cavities) leads to a cancelling of this destructive interference and thus high transmission across the network. However for the case of the modified Mach-Zender interferometer there is additional destructive interference between different paths, due to the coupling between the cavities, which produces a reduced transmission compared with the non-modified Mach-Zender interferometer. Viciani et al. found that as dephasing noise increased this destructive interference was reduced increasing transmission until it reached a maximum. For higher levels of dephasing noise the response reverted to the non-modified Mach-Zender interferometer case and the transmission reduced due to increased destructive interference resulting from the cavity becoming less opaque because of the presence of dephasing noise.

This was the first experimental evidence of the transport peak theoretically predicted by dephasing assisted transport mechanisms [4, 24, 26]. A major extension of Viciani's et al. work would be to investigate the effect that the frequency distribution of the dephasing noise might have on the system.

Optical methods of investigating transport mechanisms have the drawback that no information about the dynamic evolution of the system is accessible. Such systems, therefore, can only give information on the efficiency and not the rate that an excitation is transferred across the network. It is also not possible using this approach to examine the effect that quantum noise might have on transport due to the classical nature of the sites in the system.

### 1.5.2 Superconducting qubit systems

In another approach taken to investigate light harvesting models, Potocnik et al. [18] used three capacitatively coupled superconducting transmon qubits. The initial site is excited using microwave fields and the environment is simulated by perturbing the energy of one of the qubits through control of the local magnetic field. This control allows both static disorder and dynamic noise (dephasing noise) to be investigated. The transmission through the system is measured in continuous mode. The sink is generated by a Purcell like effect [69, 70], incoherently coupling the target qubit to a transmission line resonator.

In this experiment the system is initialised by creating an energy mismatch between the qubits generating a bright and a dark state. The bright state has a large overlap with the first two qubits and is excited by the incoming radiation. The dark state has a large overlap with the final qubit that is coupled to the sink. The perturbation is able to cause transitions between the bright and dark states thus enhancing transmission through the network.

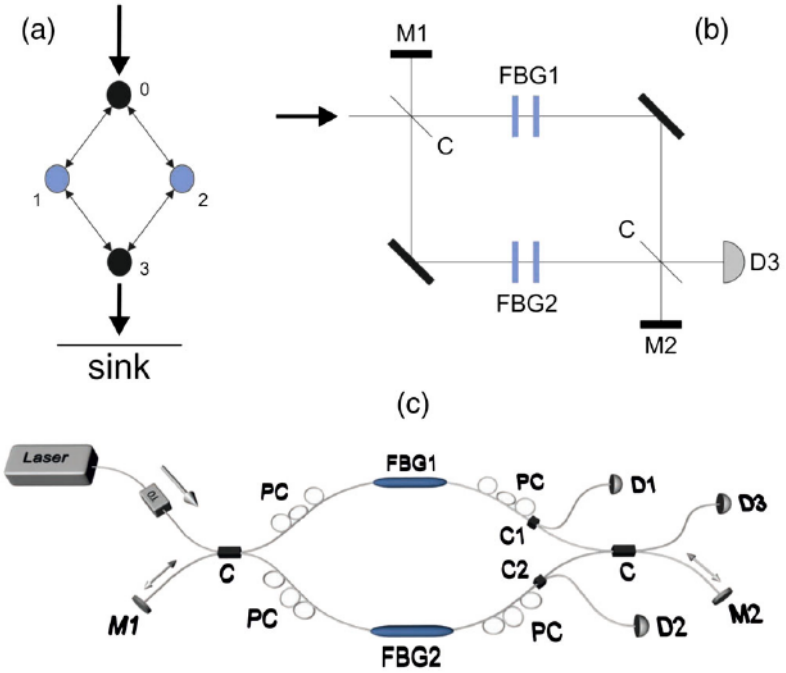


Figure 1.6: **Modified Mach-Zender interferometer:** a) the four site network; sites 1 and 2 are fiber Bragg gratings (FBG) and sites 0 and 3 are 50/50 beam splitters. b) Schematic representation showing the arrangement of the Mach-Zender interferometer; mirrors (M1 and M2) reflect the empty ports of the 50/50 back into the system entangling the cavities. The detector (D3) is the sink state where the excitation is destroyed. c) The optical fiber set-up; the laser produces the initial excitation that travels through the fiber network. Figure from Viciani et al [6].

Transmission through the system was found to be dependent upon the amplitude of the noisy dephasing perturbation as well as the structure of the applied spectral distribution. The dependence of the transmission on the amplitude of dephasing noise showed an optimum level of dephasing for which transmission was maximised for both a white and Lorentzian shaped noisy spectrum. This dependence showed the theoretically predicted de-localisation, ENAQT and Zeno regimes [37]. It was also found that the peak efficiency for the Lorentzian was larger than that for the white noise spectrum. Finally it was observed that there was limited transmission through the network when the perturbation did not contain frequencies that could cause resonant transitions between the bright and dark states.

This superconducting qubit system could be extended to include more sites allowing a more precise simulation of the FMO system to be experimentally realised. However, as this system works in continuous mode, it is not possible for the time evolution of the individual qubits to be measured and consequently only the efficiency and not the rate at which an excitation is transported across the system can be measured.

### 1.5.3 Ion systems

Ions are an ideal candidate to investigate transport in quantum networks of coupled qubits as they are long-lived and can be easily manipulated using electric fields, magnetic fields and light. The study of Maier et al. [52] uses a chain of 10 ions representing 10 qubits. The energy of each qubit is individually controlled using the AC Stark shift produced by an independent laser beam generated by an acoustic optical reflector. The energy of each qubit is perturbed to simulate the interaction with a noisy environment. Using light to control the energy of the qubits allows a high bandwidth of perturbation to be investigated. A global laser pulse fully couples all the sites together with different coupling strengths between individual pairs of qubits. The initial excitation is provided by exciting the spin of one of the sites. Transport

through the network is determined by measuring the probability of excitation in one of the ions far from the initial excitation site. The full response of the system to a noisy spectrum is determined by averaging the effect of multiple realisations, that have the same spectral form, on the probability distribution. The probability distribution between the sites of the system is determined by repeating the measurement a large number of times using the same perturbation field.

It was found that for large static disorder between the energies of the ions, low levels of dephasing noise had the effect of reducing localisation thus increasing the transport. As dephasing increased the probability of population transported reached a maximum until, for very large levels of dephasing noise, the efficiency reduced due to the quantum Zeno effect; this is consistent with the theoretical predictions of dephasing assisted transport [37]. In addition the time dynamics of the states were investigated for different amplitudes of dephasing noise. From the dependence of the width of the wavepacket on time it was found that as the amplitude of the dephasing noise increased the system transitioned from ballistic to diffusive transport in the region of ENAQT. For larger amplitudes of dephasing noise the system further transitioned to sub-diffusive transport. Maier et al. also investigated Markovian and non-Markovian noise spectra and found that transport was highly dependent on the frequency distribution of the dephasing noise. For a non-Markovian narrow band Lorentzian frequency distribution, covering only a few resonances, coherence between local qubits was maintained for a longer time than that observed using a white noise source.

Key extensions to ion system experiments could include; 1) the incorporation of a population sink, 2) the determination of the dependence of the rate of transfer through the network (not just the efficiency) on the spectral distribution of the dephasing noise and 3) the investigation of more noise spectral distributions and amplitudes. The drawback of this system is that there are only single ions at each site and therefore a large number of measurements is

required to determine the probability distribution.

### 1.5.4 Summary

A key feature of all these alternative experiments has been good quantum control over the network and the applied environment. Cold atomic systems, as used in this study, achieve comparable levels of control of the quantum state. The alternative experiments have also observed the predicted theoretical behaviour of the dependence of the transport on the amplitude of dephasing noise and furthermore experiments with superconducting qubits have demonstrated this same behaviour for a Lorentzian noise shape. The cold atoms approach taken in this study will aim initially to replicate these results.

The time dynamics of each individual state has been investigated using ion experiments allowing the rate of transport dependence on the dephasing noise source to be determined. This will also be a key measurement parameter investigated in the cold atomic system. Additionally a cold atomic system has the benefit of easier measurement of the population distribution between sites compared with the ion experiment. This is because the large number of atoms used in the cold atoms experiment all experience the same couplings and perturbations and hence the probability distribution between the sites is able to be determined in one shot without the undesirable repetition required in the ion experiment. The cold atoms experiment will be able to generate a much larger data-set and examine a more extensive parameter space, verifying and building on the work of the ion experiment.

A desirable feature of both the superconducting qubits and the optical assembly experiments is the presence of a sink state. It is possible to incorporate a sink state into the cold atoms system and this is discussed in section 6.2.2. It is also possible to increase the size of the network in cold atom systems by using alternative atomic energy levels, this is discussed

in section 6.2.6. Comparable experiments to the 10 site ion experiment can therefore be performed in the cold atoms system.

The cold atoms system is therefore able to reproduce all the aspects of the optical, superconducting qubit and ion systems, but with the ability to generate a much larger data-set and examine a more extensive parameter space.

## 1.6 Review of modulated quantum systems

To understand the mechanisms driving transport in coupled quantum systems it is important to investigate the effect that different perturbation frequencies, that constitute the environment, have on the evolution of the system. The environment is modelled as a pure dephasing perturbation where the transition frequency is varied periodically. The Hamiltonian for a coupled spin $\frac{1}{2}$ system with a single tone pure dephasing perturbation is

$$H = \hbar \begin{pmatrix} +\frac{\Delta}{2} + \frac{A}{2}\sin(2\pi f_m) & \Omega_{RF} \\ \Omega_{RF} & -\frac{\Delta}{2} - \frac{A}{2}\sin(2\pi f_m) \end{pmatrix} \tag{1.1}$$

where $\Delta$ is the detuning, $\Omega_{RF}$ is the coupling and $A\sin(2\pi f_m)$ is the pure tone modulation, where $A$ is the amplitude and $f_m$ is the frequency of the modulation. At low frequencies Landau-Zener adiabatic following and Landau-Zener-Stuckelberg interference effects dominate. As the perturbation frequency is increased, further resonances from multi-photon transitions are observed.

### 1.6.1 Landau-Zener transitions

Coupling between the base states produces an avoided crossing of the energy eigenstates that are the solutions to the Hamiltonian, as shown in figure 1.7a. The splitting of the

system's energy levels is determined by the coupling strength. Sweeping across the resonance with no coupling results in the system remaining in the initial state, with coupling, however, adiabatic transitions between the states is possible. Landau-Zener transitions result from the slow sweeping of the detuning across the avoided crossing [71]. If this happens slowly enough adiabatic following occurs and the population is transferred entirely between the two states [72]. If the transfer is too fast, however, diabatic transitions occur and no population is transferred. The population transferred ($p$) due to the Landau-Zener transition [71] is equal to

$$p = e^{-2\pi \frac{|V|^2}{\hbar(dE/dt)}} \tag{1.2}$$

where $v$ is the coupling strength and $dE/dt$ is the the rate of change of the detuning. For a fast rate of change of the detuning the population remains in the initial state and for a slow rate the majority of the population is transferred.

### 1.6.2 Landau-Zener-Stuckelberg Interferometry

Landau-Zener-Stuckelberg interference (LZS) [7,73–79] occurs by low frequency oscillation of the detuning across the avoided crossing as shown in figure 1.7. Transfer can slowly build up with a proportion of the population being transferred with each oscillation [76]. The rate of transfer is dependent upon the rate of change of the sweep of the detuning, which is dependent upon the amplitude and the frequency of the perturbation. The response of a two-level system is simulated in figure 1.8 where the frequency of the measured population is shown to change as the perturbation sweeps through the transition and the population transfer slowly builds up. The LZS method can be applied to interferometry where interference occurs due to the difference in the phase evolution between the two energy levels [7]. The Landau-Zener effect requires the perturbation to have a strong phase dependence and therefore for a noisy perturbation the presence of the high frequency components will stop the appearance of

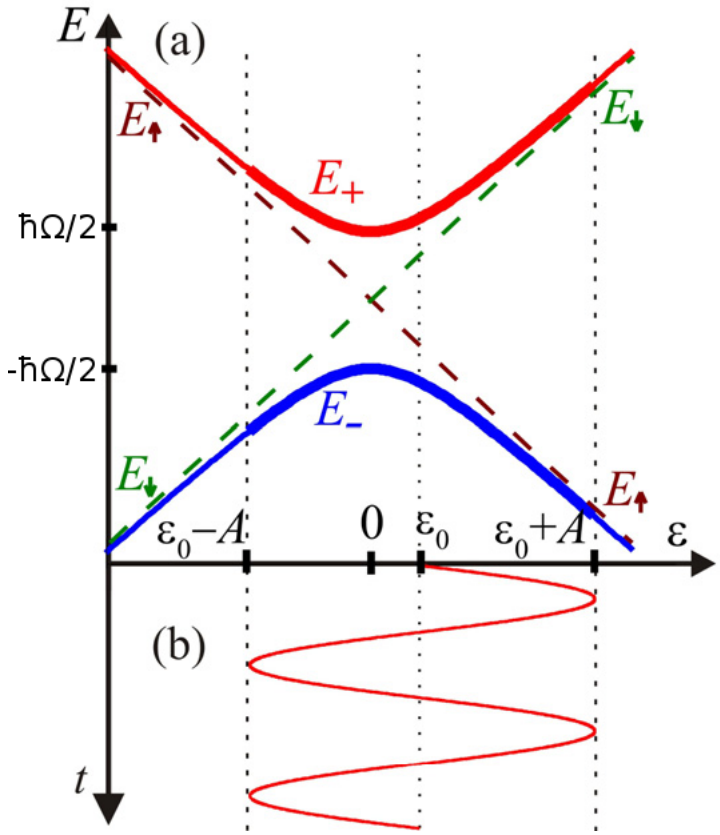


Figure 1.7: **Landau-Zener-Stuckelberg interference diagram:** a) the avoided crossing of the energy eigenstates of the system, due to the coupling. b) the perturbation of the detuning. Figure adapted from Shevchenko et al [7].

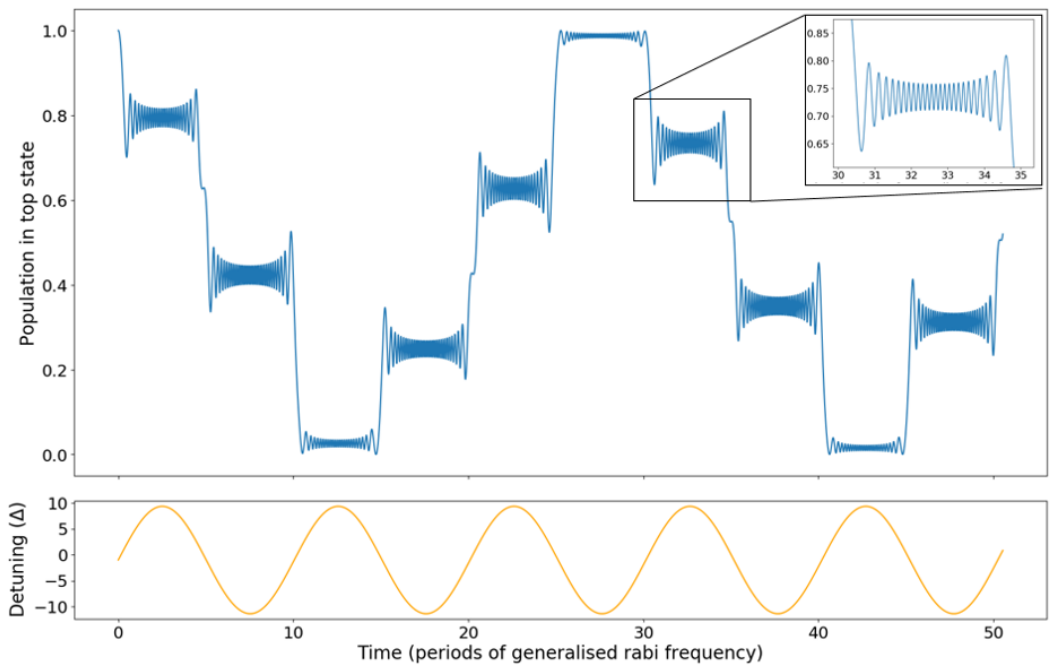


Figure 1.8: **Landau-Zener-Stuckelberg interference:** For low frequency perturbations small proportions of the population are transferred each time the resonance of the system is crossed. The figure is simulated using QuTip [8, 9] for a two-level system.

Landau-Zener effects.

### 1.6.3 Multi-photon transitions and Floquet theory

For higher perturbation frequencies the Landau-Zener transitions do not contribute to the population transfer, adiabatic following no longer occurs and the main processes driving the transfer operate at discrete frequencies. The frequencies in this case can be calculated using Floquet theory [80, 81] where the time dependence of the Hamiltonian is incorporated into discrete Floquet modes. Shirley [82, 83] introduced the idea that these Floquet modes were photon transitions; this interpretation allows the resonant response of the system to be described using concepts such as multi-photon transitions and Bloch-Siegert shifts.

Floquet modes can be used to investigate the breakdown of the rotating wave approximation (RWA) [51, 84, 85]. The breakdown of the RWA requires a coupling strength that produces a resonant Rabi frequency that is comparable to the splitting of the coupled energy levels. In traditional experiments, such as NMR, this requires high power, however, for the resonant Rabi frequency of the Floquet modes to become comparable to the energy splitting of the Floquet modes, fields that have a much lower and thus more achievable power are required.

Techniques to investigate coherent dynamics in quantum systems have been developed from the NMR technique [15–17, 86, 87]. NMR requires a very large magnetic field to be applied to the sample in order to align the spins of the electrons in the material. Additionally the magnetic field causes a small population imbalance between the spin states that is dependent upon the field strength. The system can then be perturbed using an RF field that resonates with the magnetic spin sub-states. This resonance is detected using a pickup coil that detects the re-emission of the RF field. The frequencies at which the NMR transitions occur depend upon the atomic structure of the atoms in the material. Quantum superposition and Rabi oscillations are observed in NMR that allow coherent quantum processes to be investigated; these include multi-photon resonances [88–91] and Bloch-Siegert effects [88, 92–97].

Recently nitrogen vacancy (NV) centres in diamonds have been used [19] to investigate pure tone perturbations with a microwave field, that dresses the system, and a perturbation RF field. The NV centres are long-lived and the energy levels have a small resonant linewidth; this makes these systems excellent for investigating coherent quantum dynamics. This set-up uses fluorescence response to detect the resonances between states in the system [16, 81]. Results have been presented showing the multi-photon transitions, but no phase information about the system state can be retained.

## 1.7 Applications of noise assisted quantum transport

In this section the applications of NAQT will be discussed. Initially the understanding of how transport through the FMO system occurs is presented. Following this, more general implications for quantum computing, solar cells and transport through a quantum network are considered. Finally the use of the experiment as a quantum simulator to investigate open quantum systems, quantum thermodynamics, and incoherent transfer processes arising from environmental interactions.

There is debate over whether similar processes to quantum algorithms (e.g. the Grover algorithm) take place in the FMO complex. The concept advocated by Engel et al. [14] among others is that the exciton is able to sample many paths to the reaction centre simultaneously, using quantum coherence/superpositions, and then pick the most efficient path. However Mohseni et al. [37] argues that it cannot explain the high transport rate in the FMO and the transport is instead governed by a directed quantum random walk process [37], where the excitation diffuses through the system in a stochastic manner until it reaches the target state. This experiment could provide insights into which mechanism occurs in transport through a network and therefore what may occur in the FMO complex.

Quantum computing relies on the data being encoded in superposition states and therefore requires good isolation from the environment and any measurement sources that could collapse the system state. The existence of coherence in the noisy FMO suggests however that it is possible, using the structure of the environment, to protect coherence. This may have wide ranging applications in quantum computing where the system could be made less sensitive to the effect of noise [13]. It has been argued, however, that whilst classical transport across a network is enhanced by the presence of quantum coherence, the transport of a quantum superposition state across a noisy network is degraded [24]. In addition, understanding how

plants photosynthesise so efficiently could enable solar devices to be optimised by adding a quantum aspect to their operation and enhancing performance.

Knowledge gained from this investigation will also impact on the understanding of the transmission of information in quantum networks in the presence of noise, particularly the effect that noise, and different noise shapes, has on the fidelity of the information transferred. In addition the present investigation will have implications for quantum simulation of open quantum systems where the noisy environment has numerous degrees of freedom. This would usually be a computationally intense process however, by using an experimental quantum simulator, it can be done faster and more accurately. The investigation of incoherent transfer processes could also provide knowledge of spontaneous emission processes, the nature of measurement and quantum baths. Furthermore aspects of quantum thermodynamics and how energy is exchanged between a system and the environment may have possible application in heat engines [98–101]. Finally insights into the understanding of how other biophysical processes that involve transport mechanisms occur may be obtained.

## 1.8 Our approach to simulating NAQT processes

In this study a network of sites is formed from the magnetic sub-states of the $F = 1$ ground state of an ensemble of rubidium 87 atoms. The atoms are laser cooled in a high vacuum system isolating them from the environment. The sub-states are controlled using magnetic and electromagnetic fields. A bias field lifts the energy degeneracy of the magnetic sub-states of the $F = 1$ ground state. An off-resonant RF field weakly couples the states together, as shown in figure 1.9. The energy levels are perturbed by modulating the bias field to simulate the environmental interaction, and the spectrum of the perturbation is shaped to investigate the basic features of vibrational and dephasing assisted transport. The initial excitation is produced by polarising the distribution of population between the magnetic sub-states using

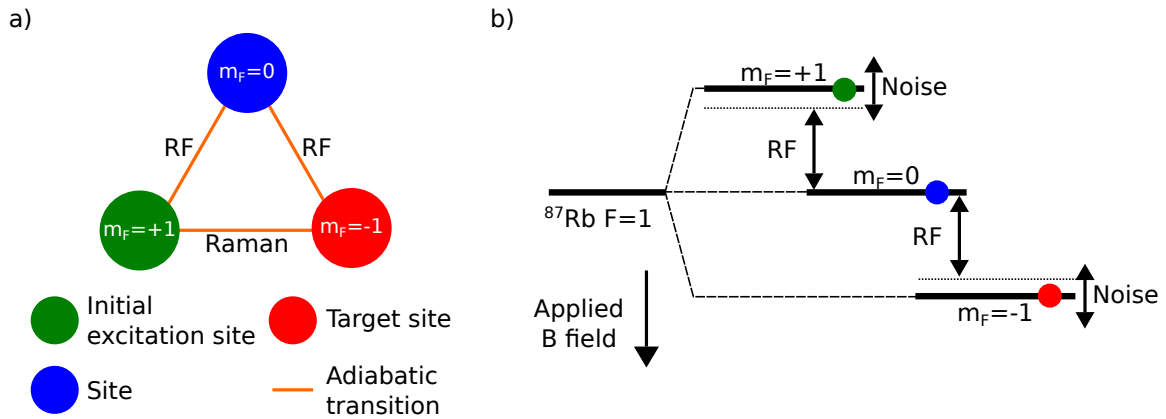


Figure 1.9: **Fully connected network (FCN):** a) The initial excitation is formed by pumping all the atoms to the $m_F$=+1 state and the target site is the $m_F$=-1 state. The RF field couples the nearest neighbour states together ($m_F$=1 to $m_F$=0 and $m_F$=0 to $m_F$=-1), and the Raman transitions couple the next nearest neighbour states together ($m_F$=1 to $m_F$=-1), b) The three sites are the magnetic sub-states of the F=1 level of rubidium 87.

optical pumping. Transport through the coupled network is determined by the population in the magnetic sub-state furthest from the initial excitation state, similar to Maier et al. [52]. The effect of the noisy spectrum is determined by averaging the effect of multiple noisy realisations with the same spectral features, as discussed in section 1.3.2. The population distribution between the states is measured using a Stern-Gerlach type approach combined with absorption imaging. Interference effects can be realised using next-nearest neighbour Raman coupling and a sink can be simulated by irreversible transfer of the population to the $F = 2$ state.

## 1.9 Structure of the thesis

This section outlines the approaches taken in this thesis and the key features of each remaining chapter.

**Chapter 2: Evolution of Quantum Systems: Elements of Theory:** The basic theory and key principles that are required to understand and interpret the findings of this study are outlined. The solution for a coupled system with no perturbation is presented for a three level system. The correspondence between two level systems and symmetrical three level systems is discussed using the Bloch sphere representation. The Lindblad form of the master equation is presented and key terms such as coherence and measurement are defined.

**Chapter 3: Experimental Set-up** The detail of the experimental set-up outlined in section 1.8 is described. Calibration measurements are discussed and the limitations of the experimental set-up are considered. The preparation of the cold atoms, the measurement procedure and couplings (radio frequency and Raman) are discussed with reference to simple examples. The generation of perturbations is analysed to determine the limits on the characteristics of the perturbation that can be imparted on the system.

**Chapter 4: Single Frequency Modulation: Experimental Results and Discussion:** The effect of different frequencies that compose the perturbation, is analysed and the theoretical Floquet approach is used to understand the response of the system. Multi-photon processes are observed with corresponding Bloch-Siegert shifts of the resonant frequencies. Finally the sideband model is discussed and data for the coherent destruction of tunnelling is presented. Insights are given into the processes underlying the effect of a noisy spectrum on the system.

**Chapter 5: Experimental Investigation into Noisy Perturbation:** The effect of various noisy frequency distributions is analysed and discussed within a theoretical framework. Initially the effect of white noise is analysed and discussed, concentrating on the role of the amplitude of the noisy perturbation. Different noise spectral density distributions are then investigated, with reference to the photon and sideband model, to simulate vibration assisted

transport and dephasing assisted transport.

**Chapter 6: Conclusions and Further Work:** The concluding chapter gives a brief summary of the work undertaken and the key results that may improve understanding of noise assisted transport mechanisms. Finally possible extensions for the work are discussed including the implementation of a glass cell and how a sink might be incorporated into the system.

CHAPTER 2

# EVOLUTION OF QUANTUM SYSTEMS: ELEMENTS OF THEORY

## 2.1 Introduction

As discussed in the previous chapter, this study simulates the interaction of a noisy environment with a network of weakly coupled sites. The system under investigation is a three site network with off-resonant RF ($\Omega_{RF}$) nearest neighbour coupling as outlined in the introductory chapter. The sites that form the network are the three magnetic sub-states of the $F = 1$ rubidium 87 ground state. The splitting of the energy states is implemented using a magnetic bias field ($B_b$) that separates the states in energy by $\mu_B g_F B_b$ where $\mu_B$ is the Bohr magneton and $g_F$ is the Landau factor for the F state [10]. The magnetic field is modulated, perturbing the energy of the magnetic sub-states, to simulate the pure dephasing effect of the environment.

This theoretical discussion will begin by investigating the dynamics of the state of a weakly coupled three level system and representing it's evolution using the Bloch sphere formalism. Key concepts required to understand the response of the system to a fluctuating environment will then be evaluated. Finally measurement-like processes and the similarities between the

effect of a wide-band fluctuating environment and incoherent transport processes, such as spontaneous emission, will be discussed.

## 2.2 Dynamics of a three level system with harmonic coupling

The Schrodinger equation will be used to calculate the evolution of the three site system under investigation. The wave function, $\psi(t)$, fully describes the state of a quantum system and, using the Schrodinger equation

$$i\hbar\frac{d}{dt}\left|\psi(t)\right\rangle = H(t)\left|\psi(t)\right\rangle \tag{2.1}$$

the Hamiltonian ($H(t)$) determines its evolution. The solution for a time independent Hamiltonian is

$$\left|\psi(t)\right\rangle = e^{\frac{-iHt}{\hbar}}\left|\psi(0)\right\rangle \tag{2.2}$$

where the initial state, $|\psi(0)\rangle$, evolves a phase that is dependent upon the energy eigenvalue ($E$) of the state.

To model the evolution of the system under harmonic coupling, the system is transformed to a basis where the Hamiltonian is diagonalised and time independent. The time dependency of the Hamiltonian is removed using a unitary transformation and the application of the rotating wave approximation (RWA). The Hamiltonian matrix is diagonal in the dressed state basis, where the evolution of the dressed states is dependent upon the time independent energy eigenvalues of the dressed states.

### 2.2.1 Construction of the Hamiltonian

The interaction of magnetic and electromagnetic fields with the system is symmetrical across the three magnetic sub-states [10]. The Hamiltonian, representing the states' energies and the couplings between the three states, can be constructed from the three level spin matrices [102]

$$J_z = \begin{bmatrix} 1 & 0 & 0 \\ 0 & 0 & 0 \\ 0 & 0 & -1 \end{bmatrix}, \; J_x = \frac{1}{\sqrt{2}} \begin{bmatrix} 0 & 1 & 0 \\ 1 & 0 & 1 \\ 0 & 1 & 0 \end{bmatrix}, \; J_y = \frac{1}{\sqrt{2}} \begin{bmatrix} 0 & -i & 0 \\ i & 0 & -i \\ 0 & i & 0 \end{bmatrix} \tag{2.3}$$

The application of the bias field is represented in the system Hamiltonian as $\mu_B g_F B_b \; J_z$ and defines the quantisation axis of the system. The RF coupling is perpendicular to the quantisation axis and therefore acts as a coupling field between the states. The contribution to the Hamiltonian from the coupling is $2\hbar\Omega_{RF}\cos(\omega_{RF}t) \; J_x$, where $\Omega_{RF}$ is the strength of the coupling and $\omega_{RF}$ is the angular frequency. A perpendicular static field could be applied to couple the states together, however experimentally this is not possible due to the significant amount of adiabatic following that would occur when the coupling field is turned on and off (adiabatic following is discussed in section 3.5). Therefore the total Hamiltonian H=$\mu_B g_F B_b$ $J_z$ + $2\hbar\Omega_{RF}\cos(\omega_{RF}t) \; J_x$ for a coupled three level system is

$$H = \begin{bmatrix} \mu_B g_F B_b & \sqrt(2)\hbar\Omega_{RF}\cos(\omega_{RF}t) & 0 \\ \sqrt(2)\hbar\Omega_{RF}\cos(\omega_{RF}t) & 0 & \sqrt(2)\hbar\Omega_{RF}\cos(\omega_{RF}t) \\ 0 & \sqrt(2)\hbar\Omega_{RF}\cos(\omega_{RF}t) & -\mu_B g_F B_b \end{bmatrix} \tag{2.4}$$

where the energy of the $m_F = +1$ ($|+1\rangle$ ) state is the top left matrix element, the energy of the $m_F = 0$ ($|0\rangle$) state is the central matrix element and the energy of the $m_F = -1$ ($|-1\rangle$)

state is the bottom right matrix element. The off-diagonal terms correspond to the nearest neighbour coupling between the states arising from the application of the RF field.

### 2.2.2 Applying the rotating wave approximation

As described previously, the time dependence of the Hamiltonian is removed by changing the basis of the system to a frame that is rotating at the frequency of the RF coupling field, using a time dependent unitary transformation, and then applying the rotating wave approximation. To apply the rotating wave approximation the oscillating terms of the Hamiltonian are initially expanded using the Euler relation, as shown in

$$H = \begin{bmatrix} \mu_B g_F B_b & \frac{\hbar\Omega_{RF}}{\sqrt{(2)}}(e^{i\omega_{RF}t} + e^{-i\omega_{RF}t}) & 0 \\ \frac{\hbar\Omega_{RF}}{\sqrt{(2)}}(e^{i\omega_{RF}t} + e^{-i\omega_{RF}t}) & 0 & \frac{\hbar\Omega_{RF}}{\sqrt{(2)}}(e^{i\omega_{RF}t} + e^{-i\omega_{RF}t}) \\ 0 & \frac{\hbar\Omega_{RF}}{\sqrt{(2)}}(e^{i\omega_{RF}t} + e^{-i\omega_{RF}t}) & -\mu_B g_F B_b \end{bmatrix} \tag{2.5}$$

The terms containing $+\omega_{RF}$ relate to a photon being absorbed and those with $-\omega_{RF}$ to an emitted photon. Co-rotating terms follow physical intuition e.g. when a photon is absorbed and the state of the atom is promoted to a higher energy level. On the other hand counter-rotating terms represent, for example, the case where a photon is emitted and the state of the atom is transferred to a higher energy level. A pictorial representation of both these cases is shown in figure 2.1. The co-rotating case is energetically the more favourable, but in cases where the amplitude of the coupling ($\Omega_{RF}$) is large or the frequency of the coupling ($\omega_{RF}$) is small, the counter-rotating terms can have a significant effect on the system dynamics. This can result in multi-photon resonances and Bloch-Seigert shifts of the energies of the states; this is discussed further in chapter 4.

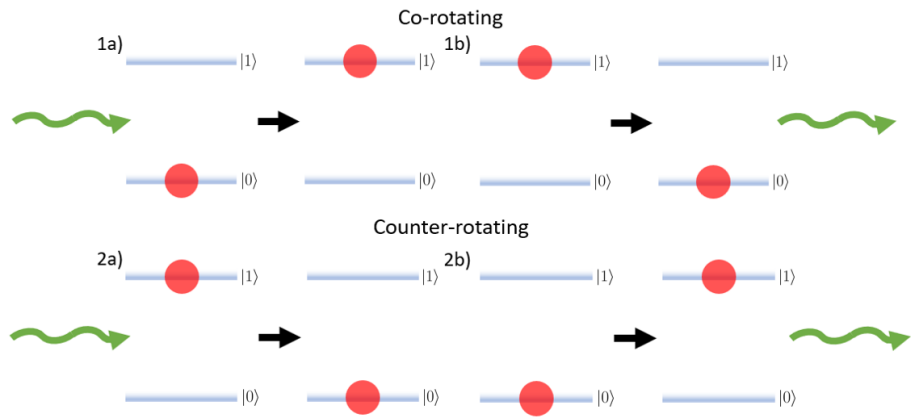


Figure 2.1: **The co-rotating and counter-rotating cases:** The co-rotating cases are; 1a) where a photon is absorbed and the state is excited to the higher energy state, and 1b) the case where the state is de-excited to the lower energy state and a photon is emitted. The counter-rotating cases are; 2a) that the state absorbs a photon and transmits to the lower energy state, and 2b) that the state is excited from the lower energy to the higher energy state with the emission of a photon.

The basis of the system is changed to a frame rotating at the frequency of the coupling field using the unitary transformation

$$u(t) = \begin{bmatrix} e^{i\omega t} & 0 & 0 \\ 0 & 1 & 0 \\ 0 & 0 & e^{-i\omega t} \end{bmatrix} \tag{2.6}$$

This unitary transformation is then applied to the Hamiltonian in the base state basis, equation 2.5, to determine the Hamiltonian in the rotating basis

$$H' = \hbar \begin{bmatrix} \Delta & \frac{\Omega_{RF}}{\sqrt{(2)}}(1 + e^{-2i\omega_{RF}t}) & 0 \\ \frac{\Omega_{RF}}{\sqrt{(2)}}(e^{2i\omega_{RF}t} + 1) & 0 & \frac{\Omega_{RF}}{\sqrt{(2)}}(1 + e^{-2i\omega_{RF}t}) \\ 0 & \frac{\Omega_{RF}}{\sqrt{(2)}}(e^{2i\omega_{RF}t} + 1) & -\Delta \end{bmatrix} \tag{2.7}$$

In the rotating basis the detuning ($\hbar\Delta$) is equal to the difference between the energy of the RF photon and the energy separation of the levels ($\frac{\mu_B g B_b}{\hbar} - \omega_{RF}$). The RF field has been transformed to a static coupling and a fast rotating component ($2\omega_{RF}$), as shown in equation 2.7. After this transformation the RWA is applied, removing the fast rotating terms ($2\omega_{RF}$) as they are far off-resonance and have a negligible effect on the evolution of the system. The time independent Hamiltonian, after the rotating wave approximation has been applied is therefore

$$H' = \hbar \begin{bmatrix} \Delta & \frac{\Omega_{RF}}{\sqrt{2}} & 0 \\ \frac{\Omega_{RF}}{\sqrt{2}} & 0 & \frac{\Omega_{RF}}{\sqrt{2}} \\ 0 & \frac{\Omega_{RF}}{\sqrt{2}} & -\Delta \end{bmatrix} = \hbar\Delta J_z + \hbar\Omega_{RF} J_x \tag{2.8}$$

It is in this basis that the system most closely resembles the biological system simulated in this study. There is a static coupling component ($\Omega_{RF}/\sqrt{2}$) and the environment can be simulated by modulating the detuning (equivalent to perturbing the site energies in the biological system) by perturbing the magnetic field as shown in

$$H' = \hbar \begin{bmatrix} \Delta + \delta(t) & \frac{\Omega_{RF}}{\sqrt{2}} & 0 \\ \frac{\Omega_{RF}}{\sqrt{2}} & 0 & \frac{\Omega_{RF}}{\sqrt{2}} \\ 0 & \frac{\Omega_{RF}}{\sqrt{2}} & -\Delta - \delta(t) \end{bmatrix} \tag{2.9}$$

where $\delta(t) = \mu_B g B_p/\hbar$ is the modulation of the detuning due to the perturbation of the magnetic field ($B_p$).

### 2.2.3 Diagonalising the Hamiltonian

For the case of no perturbation the time independent Hamiltonian (equation 2.8) is diagonalised by changing the basis of the system to the dressed state basis. The dressed states

are eigenvectors of the Hamiltonian, as shown in

$$H_{Dressed}\psi_{Dressed} = E_{dressed}\psi_{Dressed} \tag{2.10}$$

The eigenvalues of this equation are $E = 0$, $E = +\hbar\sqrt{\Delta^2 + \Omega_{RF}^2}$, $E = -\hbar\sqrt{\Delta^2 + \Omega_{RF}^2}$ determined from the characteristic equation of the matrix in equation 2.8. The rotation matrix to convert the base states, $|+1\rangle$, $|0\rangle$ and $|-1\rangle$, which correspond to the states $m_F = +1, 0, -1$, to the dressed states is

$$\begin{pmatrix} |+\tilde{\Omega}\rangle \\ |\tilde{0}\rangle \\ |-\tilde{\Omega}\rangle \end{pmatrix} = \begin{bmatrix} \cos^2(\theta/2) & -\sin(\theta)/(\sqrt{2}) & \sin^2(\theta/2) \\ \sin(\theta)/\sqrt{2} & \cos(\theta) & -\sin(\theta)/\sqrt{2} \\ \sin^2(\theta/2) & \sin(\theta)/\sqrt{2} & \cos^2(\theta/2) \end{bmatrix} \begin{pmatrix} |+1\rangle \\ |0\rangle \\ |-1\rangle \end{pmatrix} \tag{2.11}$$

where $\tan(\theta) = \Omega_{RF}/\Delta$ and $|+\tilde{\Omega}\rangle$, $|\tilde{0}\rangle$ and $|-\tilde{\Omega}\rangle$ are the dressed states corresponding to the eigenvalues $E = +\tilde{\Omega}$, $E = 0$ and $E = -\tilde{\Omega}$ respectively and the generalised Rabi frequency $(\tilde{\Omega})$ is equal to $\sqrt{\Delta^2 + \Omega_{RF}^2}$. Using equations 2.2 and 2.10, the time evolution of the dressed states can be determined and therefore the time dependency of the evolution of the base states can be derived by projecting the dressed states back onto the undressed basis.

### 2.2.4 Rabi oscillations

The time evolution of the dressed states leads to interference between the base states. To investigate this effect the time variation of the populations of the base states will be examined when the system is initially prepared in the $|+1\rangle$ state. The $|+1\rangle$ state can be written as a superposition of the dressed states

$$|+1\rangle = \sin^2(\theta/2)\,|-\tilde{\Omega}\rangle - \sin(\theta)/\sqrt{2}\,|\tilde{0}\rangle + \cos^2(\theta/2)\,|+\tilde{\Omega}\rangle \tag{2.12}$$

derived from the inverse of the rotation matrix used in equation 2.11. Equation 2.2 is applied to determine the evolution of the initial state specified in equation 2.12. The dressed state components, that are eigenvectors of the Hamiltonian, evolve depending on the corresponding eigenvalues, resulting in

$$|\psi(t)\rangle = \sin^2(\theta/2)\,|-\tilde{\Omega}\rangle e^{+i\hbar\sqrt{\Delta^2+\Omega_{RF}^2}t} - \sin(\theta)/\sqrt{2}\,|\tilde{0}\rangle + \cos^2(\theta/2)\,|+\tilde{\Omega}\rangle e^{-i\hbar\sqrt{\Delta^2+\Omega_{RF}^2}t} \quad (2.13)$$

Projecting the state described by equation 2.13 onto the base states basis results in

$$|\psi(t)\rangle = \sin^2(\theta/2)\begin{pmatrix}\sin^2(\theta/2)\\ \frac{\sin(\theta)}{\sqrt{2}}\\ \cos^2(\theta/2)\end{pmatrix} e^{+i\hbar\sqrt{\Delta^2+\Omega_{RF}^2}t} - \frac{\sin(\theta)}{\sqrt{2}}\begin{pmatrix}\frac{\sin(\theta)}{\sqrt{2}}\\ \cos(\theta)\\ -\frac{\sin(\theta)}{\sqrt{2}}\end{pmatrix} + \cos^2(\theta/2)\begin{pmatrix}\cos^2(\theta/2)\\ -\frac{\sin(\theta)}{\sqrt{2}}\\ \sin^2(\theta/2)\end{pmatrix} e^{-i\hbar\sqrt{\Delta^2+\Omega_{RF}^2}t} \quad (2.14)$$

from which the time evolution of the populations of the base states can be extracted. The evolution of the populations in the base states is derived from equation 2.14 in equations 2.15 to 2.17, where $\tilde{\Omega}$ is the generalised Rabi frequency and equal to $\sqrt{\Delta^2+\Omega_{RF}^2}$.

**State $|-1\rangle$:**

$$\begin{aligned}\langle\psi(t)\,|-1\rangle\,\langle-1\,|\psi(t)\rangle &= \sin^4(\theta)\sin^4(\tilde{\Omega}t/2)\\ |\langle-1\,|\psi(t)\rangle\,|^2 &= \frac{\Omega_{RF}^4}{\tilde{\Omega}^4}\sin^4(\tilde{\Omega}t/2)\end{aligned} \quad (2.15)$$

**State $|0\rangle$:**

$$\begin{aligned}\langle\psi(t)\,|0\rangle\,\langle 0\,|\psi(t)\rangle &= \frac{\sin^2(\theta)}{2}(\sin^2(\tilde{\Omega}t) + 4\cos^2(\theta)(\sin^4(\tilde{\Omega}t/2)))\\ |\langle 0\,|\psi(t)\rangle\,|^2 &= \frac{\Omega_{RF}^2}{2\tilde{\Omega}^2}(\sin^2(\tilde{\Omega}t) + 4\frac{\Delta^2}{\tilde{\Omega}^2}(\sin^4(\tilde{\Omega}t/2)))\end{aligned} \quad (2.16)$$

**State $|+1\rangle$:** As the system is closed, the total population is conserved and the population in state $|+1\rangle$ is determined from one minus the populations in states $|0\rangle$ and $|-1\rangle$ hence

$$|\langle 1|\psi(t)\rangle|^2 = 1 - |\langle 0|\psi(t)\rangle|^2 - |\langle -1|\psi(t)\rangle|^2 = 1 - \frac{2\Omega_{RF}^2}{\tilde{\Omega}^4}(\Delta^2 + \frac{\Omega_{RF}^2}{2})(\sin^4(\tilde{\Omega}t/2))) - \frac{\Omega_{RF}^2}{2\tilde{\Omega}^2}(\sin^2(\tilde{\Omega}t) \tag{2.17}$$

The difference in the population between states $|+1\rangle$ to state $|-1\rangle$ is a measure of the population transfer through the system. It is referred to as the magnetisation of the system, which is the spin projection onto the z axis of the Bloch sphere, this is discussed in section 2.3. For Rabi oscillations this results in

$$|\langle\psi_1(t)||1\rangle|^2 - |\langle\psi_{-1}(t)||-1\rangle|^2 = 1 - \frac{2\Omega_{RF}^2}{\tilde{\Omega}^2}(\sin^2(\tilde{\Omega}t/2)) \tag{2.18}$$

that has the same form for Rabi oscillations as it does in a 2 level system. These equations are plotted in figure 2.2 showing the evolution of the populations of the three states with time, for the initial state $|+1\rangle$ and a coupling frequency of $\Omega_{RF} = 40kHz$. As the detuning increases, the frequencies of the populations of all the states increases and their oscillation amplitudes reduce. The evolutions of the populations of the states have a modified sinusoidal response due to the $\sin^4$ dependence. As shown in figure 2.2b the frequency of the central state is twice that of the outer states. The maximum population in the central state is 50% of the total population. As shown in figure 2.2d the magnetisation of the state varies from $-1$ to $+1$, with $+1$ corresponding to the system being fully in the initial $|+1\rangle$ state and $-1$ the system fully in the $|-1\rangle$ state.

## 2.3 Mapping a three level system to the Bloch Sphere

The state and evolution of the system can be represented pictorially using a Bloch sphere. This also gives an intuitive explanation of the effect of the perturbation that will be discussed in chapter 4. Initially the Bloch sphere representation for a two level system will be described

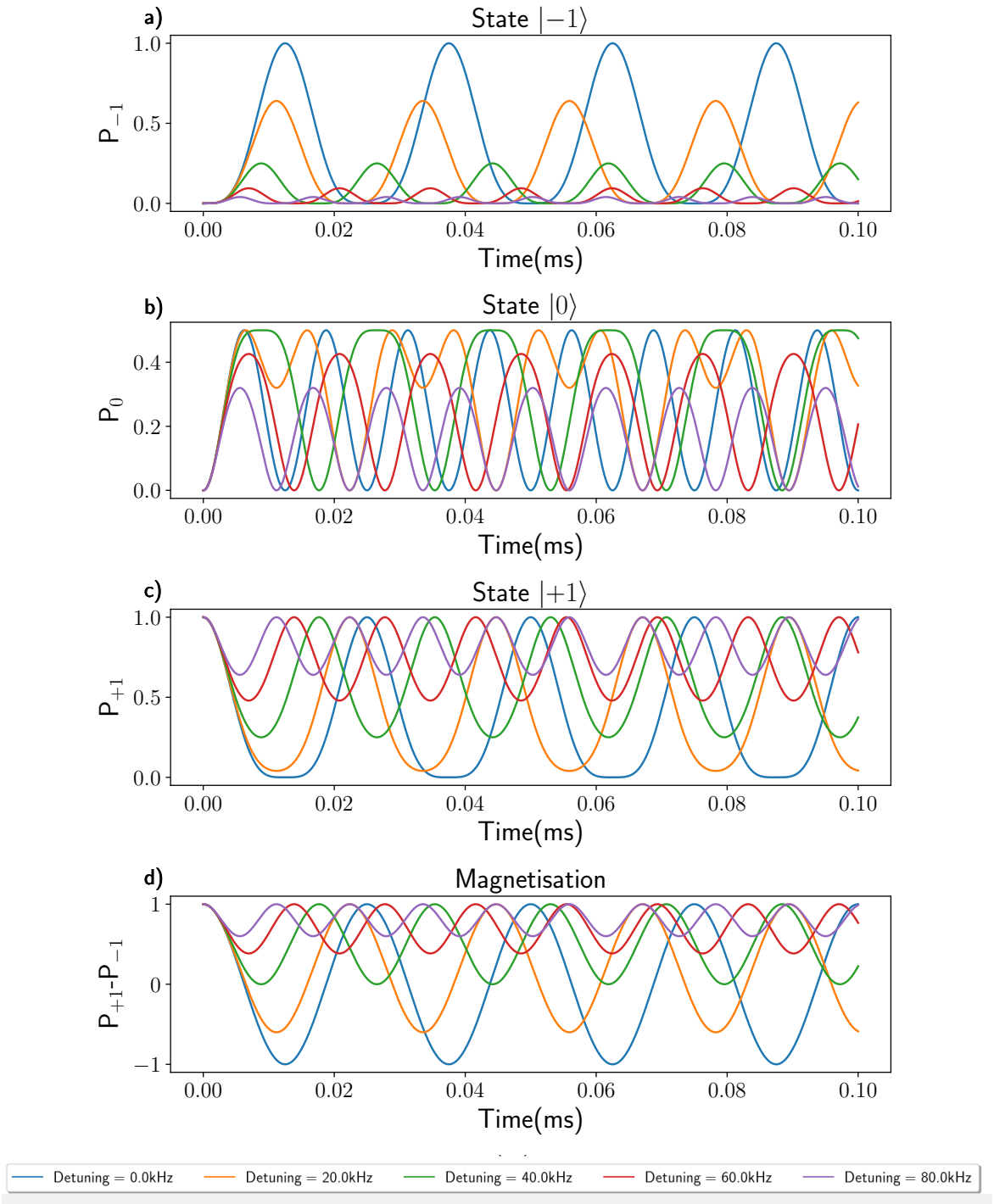


Figure 2.2: **Rabi oscillations for a three level system:** The evolution of the populations in the system states, for $40kHz$ RF coupling and initial state $|+1\rangle$, dependency on the detuning; a) the evolution of state $|-1\rangle$, b) the evolution of state $|0\rangle$, c) the evolution of state $|+1\rangle$, and d) the evolution of the magnetisation of the system $(p_{+1} - p_{-1})$.

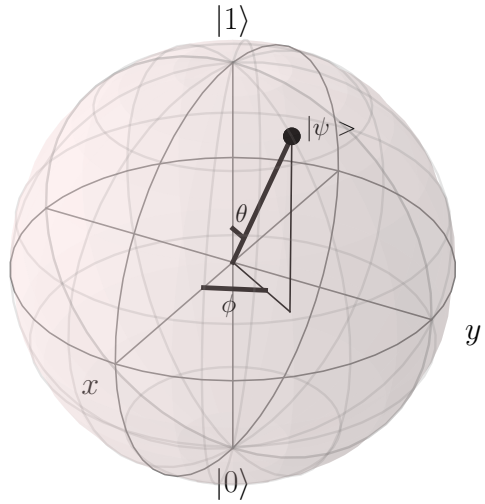


Figure 2.3: **Bloch sphere:** Representation of a state of the system ($\psi$) on a Bloch sphere. The state is defined by 2 parameters; the angle of rotation around the x axis ($\theta$) and the angle of rotation around the z axis ($\phi$)

and from this the three level case will be developed for the system in this study.

**The two level system.** Figure 2.3 shows a pure state represented on a Bloch sphere. The state is confined to the surface of the Bloch sphere if it remains in a pure state. The state is described by three variables $\theta$, $\phi$ and r that in Cartesian coordinates are $(r\sin(\theta)\cos(\phi), r\sin(\theta)\sin(\phi), r\cos(\theta)) = (u, v, w)$ on the 3 dimensional Bloch sphere. The angle $\theta$ corresponds to a rotation about the y axis that is related to the magnetisation of the state. The angle $\phi$ corresponds to the rotation about the z axis and is related to the phase difference between the system states. The amplitude r is normalised to 1 for a pure state system, but for a system decaying into a mixed state it can be less. The density matrix of the system can be determined from

$$\rho = \frac{1}{2}(I + \vec{a}.\vec{\sigma}) \tag{2.19}$$

where $\vec{\sigma}$ is composed of the two level Pauli matrices

$$\sigma_x = \begin{bmatrix} 0 & 1 \\ 1 & 0 \end{bmatrix}, \sigma_y = \begin{bmatrix} 0 & -i \\ i & 0 \end{bmatrix}, \sigma_z = \begin{bmatrix} 1 & 0 \\ 0 & -1 \end{bmatrix} \tag{2.20}$$

and $I$ is the identity matrix. Resulting in the density matrix

$$\rho(t) = \frac{1}{2} \begin{bmatrix} 1+w & u-iv \\ u+iv & 1-w \end{bmatrix} \tag{2.21}$$

In the case where there are no coupling terms between the levels $|0\rangle$ and $|1\rangle$ of the system, the state, that is on the Bloch sphere, will precess around the quantisation axis (in this case the z axis). The rate of precession is dependent upon the change in the phase difference between the two system states, which is dependent upon the energy difference. If coupling is present in the system, the precession axis and the quantisation axis no longer overlap and the evolution can be described by a rotation of the precession axis on the Bloch sphere. Equivalently this can be represented in the dressed state basis, where the dressed basis is rotated relative to the base state basis. The $z$ axis for the dressed state basis overlaps with the precession axis. The initial state, $|1\rangle$, in the dressed state basis is a combination of dressed states and will precess around the $z$ axis of the dressed state basis at the rate of the generalised Rabi angular frequency, as derived in section 2.2. The generalised Rabi frequency is the energy difference between the dressed states.

**Holomorphism to the 3 level case.** The three level system under investigation can also be represented on a Bloch sphere. The evolution of the initial state $\phi_0$ is determined by the solution of the time independent Schrodinger equation [102]

$$\phi(t) = e^{-\frac{iHt}{\hbar}} \phi_0. \tag{2.22}$$

In this study for three level coupling the Hamiltonian ($H$) in equation 2.22 is equal to $\hbar\Delta\ J_z + \hbar\Omega\ J_x$, as discussed in section 2.2.1. The states produced by this Hamiltonian are

$$\phi = e^{-i(\Delta J_z + \Omega J_x)t}\phi_0 \tag{2.23}$$

Due to the symmetries of the implemented Hamiltonian, and thus the symmetries of the evolution of the state, the state of the 3 level system can be represented on a Bloch sphere. The magnetisation of the system is represented along the z axis, with the north pole corresponding to the system in the $|{+1}\rangle$ state and the south pole to the $|{-1}\rangle$ state. The states corresponding to the equator of the Bloch sphere are of the form

$$\frac{1}{2}e^{i\phi}\,|{+1}\rangle + \frac{1}{\sqrt{2}}\,|0\rangle + \frac{1}{2}e^{-i\phi}\,|{-1}\rangle \tag{2.24}$$

where $\phi$ is the angle of rotation around the z axis on the Bloch sphere. The Hamiltonian shown in equation 2.23 results in a precession of the state around the vector $(\Omega, 0, \Delta)$ on the Bloch sphere, as in the 2 level case, as shown in figure 2.4a. If the initial state $|+1\rangle$ evolves due to a combination of Hamiltonians, constructed from the three level matrices $(J_x, J_y, J_z)$, the states will remain on the Bloch sphere. This is not true in general and is only possible because the Hamiltonian is constructed from the operators $J_x, J_y, J_z$ that are generators of SU(2) [102]. The states that are generated from this Hamiltonian can be described by the vector that corresponds to the state $|+1\rangle$ being rotated by $\theta_x$ around the $x$ axis (component of $J_x$), followed by a rotation by $\theta_z$ around the $z$ axis (component of $J_z$). This is shown in

$$\phi = u_z u_x \begin{bmatrix} 1 \\ 0 \\ 0 \end{bmatrix} \tag{2.25}$$

where the unitary transformations that correspond to the rotation of the state around the z axis are defined as

$$u_z = e^{-i\theta_z J_z} = \begin{bmatrix} e^{-i\theta_z} & 0 & 0 \\ 0 & 1 & 0 \\ 0 & 0 & e^{i\theta_z} \end{bmatrix} \tag{2.26}$$

and the rotation of the state around the x axis as

$$u_x = e^{-i\theta_x J_x} = \begin{bmatrix} \cos^2(\theta/2) & -\sin(\theta)/(\sqrt{2}) & \sin^2(\theta/2) \\ \sin(\theta)/\sqrt{2} & \cos(\theta) & -\sin(\theta)/\sqrt{2} \\ \sin^2(\theta/2) & \sin(\theta)/\sqrt{2} & \cos^2(\theta/2) \end{bmatrix} \tag{2.27}$$

The combined rotation matrix is therefore

$$u_z u_x = \begin{bmatrix} \cos^2(\theta/2)e^{-i\theta_z} & -\sin(\theta)/(\sqrt{2})e^{-i\theta_z} & \sin^2(\theta/2)e^{-i\theta_z} \\ \sin(\theta)/\sqrt{2} & \cos(\theta) & -\sin(\theta)/\sqrt{2} \\ \sin^2(\theta/2)e^{+i\theta_z} & \sin(\theta)/\sqrt{2}e^{+i\theta_z} & e^{+i\theta_z}\cos^2(\theta/2) \end{bmatrix} \tag{2.28}$$

and thus

$$\begin{bmatrix} \cos^2(\theta/2)e^{-i\theta_z} & -\sin(\theta)/(\sqrt{2})e^{-i\theta_z} & \sin^2(\theta/2)e^{-i\theta_z} \\ \sin(\theta)/\sqrt{2} & \cos(\theta) & -\sin(\theta)/\sqrt{2} \\ \sin^2(\theta/2)e^{+i\theta_z} & \sin(\theta)/\sqrt{2}e^{+i\theta_z} & e^{+i\theta_z}\cos^2(\theta/2) \end{bmatrix} \begin{bmatrix} 1 \\ 0 \\ 0 \end{bmatrix} = \begin{bmatrix} \cos^2(\theta/2)e^{-i\theta_z} \\ \sin(\theta)/\sqrt{2} \\ \sin^2(\theta/2)e^{+i\theta_z} \end{bmatrix} \tag{2.29}$$

is the wave function of the state produced from the application of this transformation, described by the 2 rotation angles. This is only true for cases where the system has evolved from the $|+1\rangle$ state due to the Hamiltonians composed of the three level spin matrices (equation

2.3). The density matrix for the wave functions produced by these rotations is

$$\begin{bmatrix} \sin^4(\theta/2) & \frac{i\sin(\theta)}{\sqrt{2}}\sin^2(\theta/2)e^{i\phi} & \sin^2(\theta/2)\cos^2(\theta/2)e^{2i\phi} \\ \frac{i\sin(\theta)}{\sqrt{2}}\sin^2(\theta/2)e^{i\phi} & \frac{\sin^2(\theta)}{2} & \frac{i\sin(\theta)}{\sqrt{2}}\cos^2(\theta/2)e^{i\phi} \\ \sin^2(\theta/2)\cos^2(\theta/2)e^{i\phi} & \frac{i\sin(\theta)}{\sqrt{2}}\cos^2(\theta/2)e^{i\phi} & \cos^4(\theta/2) \end{bmatrix} \tag{2.30}$$

From the density matrix, it can be seen that, as the state evolves by a rotation around the x axis, the coherence builds up between the first 2 states and is then transferred to the final 2 states.

The evolution of the 3 level coupled state on the Bloch sphere for various detunings is shown in figure 2.4 [15, 16]. The coupling frequency ($\Omega_{RF}/2\pi$) is $40kHz$. The rotated precession axis that the state precesses around is shown in figure 2.4a. The value of $\phi$ is the angle of rotation around the $z$ axis and $\theta_x$ is the angle of rotation around the $x$ axis. As can be seen in figure 2.4b, $\phi$ evolves from zero to $\pi$ and as the detuning increases the rate of change becomes larger. As can be seen in figure 2.4c, $\theta_x$ evolves from zero and reaches a maximum of $\pi$ that corresponds to the system being fully in the $|-1\rangle$ state, for the on-resonance case. As the detuning of the coupling increases, the maximum reduces and the response is smoother. Figure 2.4d plots the change in magnetisation for one oscillation and, as derived in section 2.2, this shows the expected sinusoidal relationship consistent with Rabi oscillations.

The rest of this chapter focuses on the effects that can result from the interaction of an environment with quantum systems. The theoretical models used to describe the non-unitary evolution resulting from this are also presented and discussed. The discussion begins with an overview of dephasing and decoherence and then the master equation approach is used to describe the evolution of the density matrix. The effect of a wide-band environment interacting with two level quantum systems is then derived using perturbation theory and

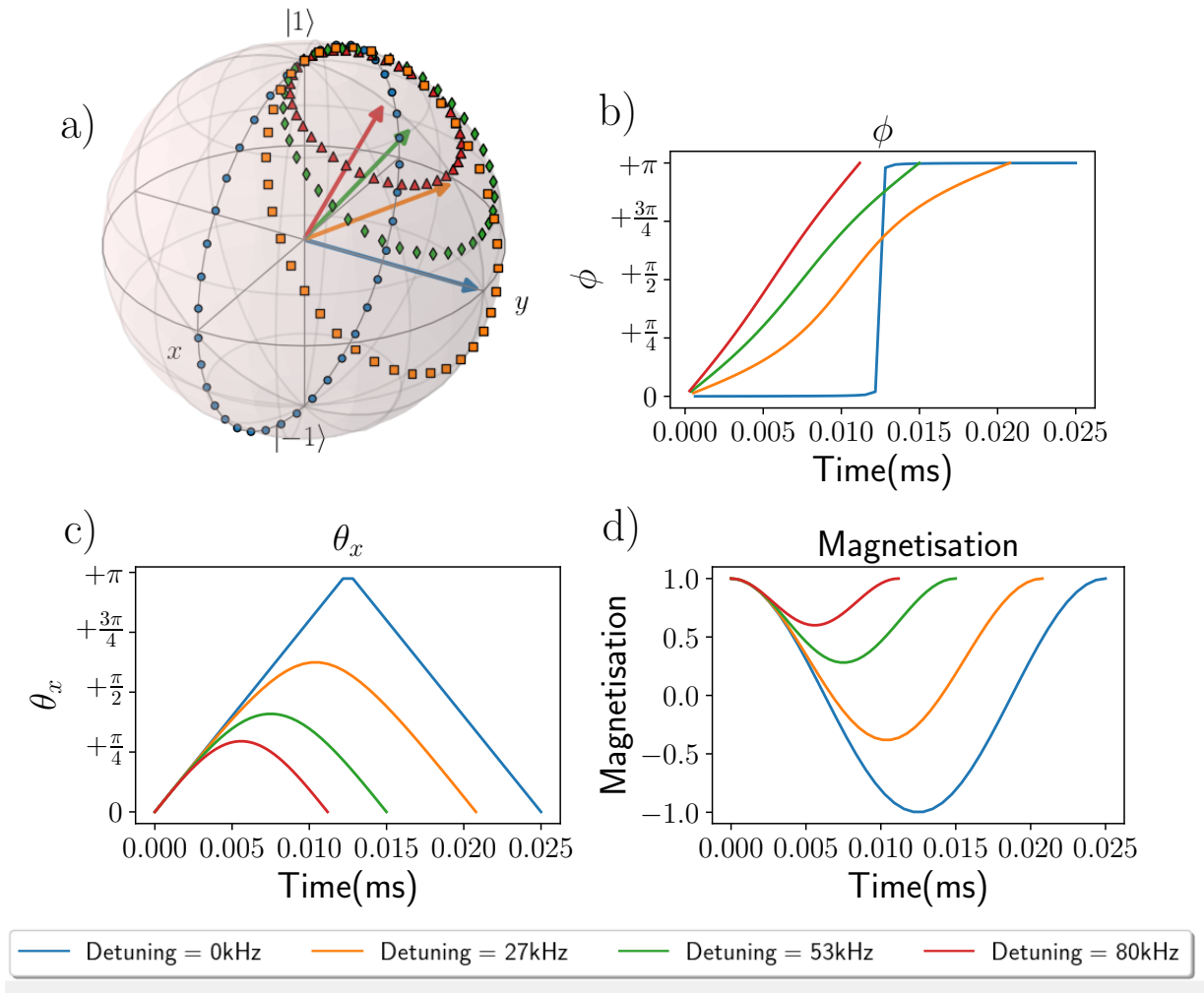


Figure 2.4: **Evolution represented on a Bloch sphere:** The precession of the $|+1\rangle$ state on the Bloch sphere for a coupling frequency ($\Omega_{RF}/2\pi$) of $40kHz$ for different detunings; a) the Bloch sphere representation showing the precession of the initial state around the precession axis for different detunings, b) the change in the angle $\phi$, the rotation angle around the $z$ axis defined in figure 2.3, for different detunings, c) the change in the angle $\theta$, the rotation angle around the $x$ axis defined in figure 2.3, for different detunings, and d) the evolution of the magnetisation, the projection of the state on the z axis, for different detunings.

parallels are made with incoherent transfer processes such as spontaneous emission. Finally there is a discussion of the relationship between measurement and dephasing.

## 2.4 Dephasing and decoherence

To describe the state of a system that is on the classical-quantum boundary it is necessary to have a formalism that can be applied to describe the system in both regimes. An ensemble of base quantum states can form a classical statistical mixture (mixed states), or a linear combination (pure quantum state). Density matrices are used to represent statistical mixtures, pure quantum states and intermediate states and are therefore the formalism used in this study. This section begins with a discussion of pure quantum states and mixed states, then dephasing and decoherence phenomenon is defined and finally an illustrative example of how decoherence can result from the entanglement of a system with a bath is presented.

**Pure quantum states and mixed states.** A pure state is a superposition of base states that have a defined phase relationship, an example is

$$|\psi\rangle = \frac{1}{\sqrt{2}}(|0\rangle + e^{-i\phi(t)}\,|1\rangle) \tag{2.31}$$

where $\phi(t)$ is the phase difference (that can have a time dependency) between the two states. The state described by equation 2.31 can be equivalently represented as the density matrix

$$|\psi\rangle\,\langle\psi| = \frac{1}{2}\begin{bmatrix} 1 & e^{-i\phi(t)} \\ e^{+i\phi(t)} & 1 \end{bmatrix} \tag{2.32}$$

The coherence of the state is defined by the off-diagonal elements in the density matrix and the probability density in each of the base states corresponds to the diagonal terms. The trace of the density matrix is equal to 1 due to probability conservation. Density matrices can

also be used to represent mixed states that are a statistical distribution of pure states with off-diagonal elements equal to zero. For cases where the coherence between the base states is destroyed the system will decay to a mixed state. A measurement of the system, in the basis of the base states, collapses the state of the system to one of its base states destroying any coherence. For an ensemble of systems a measurement will lead to the average of the density matrices collapsing to a mixed state.

**Dephasing and decoherence:** Dephasing and decoherence processes randomise the phase difference between the base states and thus lead to decay of the off-diagonal terms in the density matrix. They result however from different physical processes. Dephasing results from an ensemble of systems interacting with a fluctuating environment where each individual system component of the ensemble evolves slightly differently due to the interaction with a slightly different environment. The different environments have the same spectral form but different components, as shown pictorially in figure 2.5a. The ensemble average of the system can be calculated from taking the average of the response of the system components, as shown in figure 2.5b. The average of the ensemble is decohered, but the individual components of the ensemble may still have coherent properties. Decoherence is a quantum mechanical process where the system becomes entangled with an external bath that does not support long term entanglement between the bath states and therefore leads to a partial decay of the coherences in the system, as shown in figure 2.5c. This is mathematically interpreted as tracing over the bath's states. The greater the coupling to the environment, or the bath, the faster the decay occurs [3].

**Example of decoherence resulting from the entanglement of a system with a bath.** The effect of the coupling of a system with a bath that does not support long term entanglement can lead to destruction of the entanglement between the system states. The system states, in this example, are $|a\rangle$ and $|b\rangle$ that become entangled with each other due to

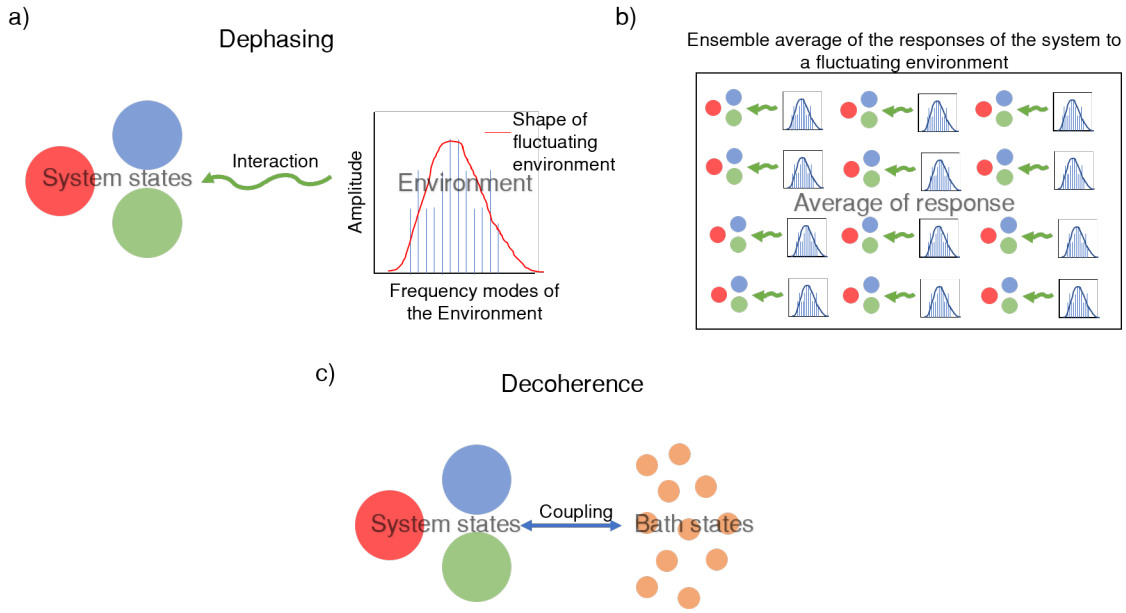


Figure 2.5: **Dephasing and decoherence:** a) the interaction of a system with a fluctuating environment causes dephasing, b) the average of the density matrix of an ensemble of systems dephases due to interactions with a fluctuating environment. Each system of the ensemble interacts with a slightly different environment that has the same spectral shape, c) decoherence can result from the entanglement of system states with the states of a bath. The bath's states cannot support long term coherence and therefore are constantly being traced over destroying the superposition between the system and the bath and thus the state of the system partially collapses to a mixed state.

the interaction with the bath that has spin $|\uparrow\rangle$ and $|\downarrow\rangle$. An example of an entangled system bath state is

$$\phi = |a\uparrow\rangle + |b\downarrow\rangle \tag{2.33}$$

where system state $|a\rangle$ and bath state $|\uparrow\rangle$ have become entangled with system state $|b\rangle$ and bath state $|\downarrow\rangle$. The state, $\phi$, could occur as a result of transfer from states $|a\rangle$ to $|b\rangle$ causing a spin flip of one of the bath states. This can be represented using the density matrix

$$\begin{array}{c} \\ |a\uparrow\rangle \\ |b\uparrow\rangle \\ |a\downarrow\rangle \\ |b\downarrow\rangle \end{array} \begin{array}{c} \begin{array}{cccc} \langle a\uparrow| & \langle b\uparrow| & \langle a\downarrow| & \langle b\downarrow| \end{array} \\ \begin{bmatrix} 1 & 0 & 0 & 1 \\ 0 & 0 & 0 & 0 \\ 0 & 0 & 0 & 0 \\ 1 & 0 & 0 & 1 \end{bmatrix} \end{array} \tag{2.34}$$

If the bath does not support entanglement the states that correspond to the entanglement between $|\uparrow\rangle$ and $|\downarrow\rangle$ (the top right 2x2 matrix and the bottom left 2x2 matrix) are traced over [38]. This results in the density matrix, which describes the system states, collapsing to the mixed state with no entanglement, as shown in

$$\begin{array}{c} \\ |a\rangle \\ |b\rangle \end{array} \begin{array}{c} \begin{array}{cc} \langle a| & \langle b| \end{array} \\ \begin{bmatrix} 1 & 0 \\ 0 & 1 \end{bmatrix} \end{array} \tag{2.35}$$

The entanglement between states $|a\rangle$ and $|b\rangle$ has been demonstrated to be destroyed by the effect of the bath.

## 2.5 Modelling pure dephasing using the master equation

The environment (or bath) that interacts with the system can often produce classical incoherent processes which randomise the phases between the states and collapse the state of the system to a mixed state. Master equations which describe the evolution of the density matrices are used to describe this complex evolution. This section will begin by describing the master equation approach and then describe how dephasing is modelled. Finally the relevance to dephasing assisted transport will be discussed.

**The master equation approach.** The Liouville-von Neumann master equation (equation 2.36) [38], which can be derived from the Schrodinger equation, describes the evolution of the density matrix, $\rho$, interacting with a Hamiltonian $\mathrm{H}_T$. The time derivative of the density matrix is

$$\frac{d\rho}{dt} = \frac{1}{i\hbar}[H_T, \rho] \tag{2.36}$$

The full Hamiltonian $H_T$ is a combination of the system states (S), the bath states (B) and the coupling between the system and bath (SB-int) as shown in

$$H_T = H_S + H_B + H_{SB-int} \tag{2.37}$$

Usually the bath states are not accessible and only the system states can be measured. Hence the interaction of the bath with the system is approximated in the master equation using Lindblad equations. Lindblad equations model the non-unitary evolution of the system states, such as decay processes and dephasing, which can result from interactions with the bath. The evolution of the density matrix in the master equation can be split into a coherent part, determined from the evolution under just the system Hamiltonian $H_s$ that represents

the evolution of the system without the bath, and an operator that models the effect on the system of the interaction with the bath.

**Pure dephasing Lindblad equations.** As discussed previously, the effect of the environment in this study is modelled by modulating the energies of the system states. The modulation of the system states leads to dephasing, referred to as pure dephasing. Pure dephasing is incorporated into the master equation as a Lindblad super operator, $L_\phi$

$$\frac{d\rho}{dt} = \frac{1}{i\hbar}[H, \rho] + L_\phi(\rho(t)) \tag{2.38}$$

where $L_\phi$.is the pure dephasing Lindblad super operator [26] as determined from the Lindblad equation

$$L_\phi(\rho(t)) = \gamma_\phi \sum [A_m \rho(t) A_m^* - \frac{1}{2} A_m A_m^* \rho(t) - \frac{1}{2} \rho(t) A_m A_m^*] \tag{2.39}$$

where $A$ is the collapse operator for pure dephasing, which has the following form for a two level system

$$A = \sqrt{\gamma_\phi} \begin{pmatrix} 1 & 0 \\ 0 & -1 \end{pmatrix} \tag{2.40}$$

and results in the pure dephasing Lindblad operator for a two level system

$$L_\phi(\rho(t)) = \gamma_\phi \begin{pmatrix} 0 & -2\rho_{12} \\ -2\rho_{12} & 0 \end{pmatrix} \tag{2.41}$$

This leads to the decay of the coherence terms in the density matrix (determined by the off-diagonal components of the density matrix, $\rho_{12}/\rho_{21}$). The strength of the interaction with the environment, $\gamma_\phi$, sets the rate of decay of the coherence terms in the density matrix.

The evolution of a coupled two level system under the action of pure dephasing has been numerically modelled in this study using $QuTiP$ and the results are shown in figure 2.6 for different values of $\gamma_\phi$. As can be seen there is an oscillating component that corresponds to the coherent part of the evolution (unitary evolution) and a damping component that corresponds to the non-unitary part of the evolution (pure dephasing operator). For no interaction ($\gamma_\phi = 0$, figure 2.6a), the system evolves according to only the coherent part of the master equation and low amplitude Rabi oscillations are observed. For a medium strength interaction ($\gamma_\phi = 1$, figure 2.6b) the coherent part is still observed, but is highly damped, and the system tends to a state where there is an equal distribution between the system states (described as the system being thermalised). This is referred to as the environment assisted quantum transport regime because the environment enhances transport to the state that is initially not populated. For a very strong interaction ($\gamma_\phi = 20$, figure 2.6c) with the environment, the coherent contribution is negligible and the decay is over-damped resulting in the suppression of the evolution of the system. This is referred to as the quantum Zeno effect and will be discussed in the next section. It should be noted that without the coherent part of the evolution the state would not evolve under just pure dephasing.

## 2.6 Perturbation theory

The evolution of the system arising from the interaction with the environment can be determined using perturbation theory. The model of the environment is composed of a broad range of electromagnetic field modes that perturb the energies of the states, as discussed in section 1. This perturbation, when combined with a coupling field, causes transitions between the base states. This is understood to be the result of individual frequency components within the perturbation causing transitions between the dressed states (the combination of the base states and the coupling field) and this is discussed in more detail in section 4. The

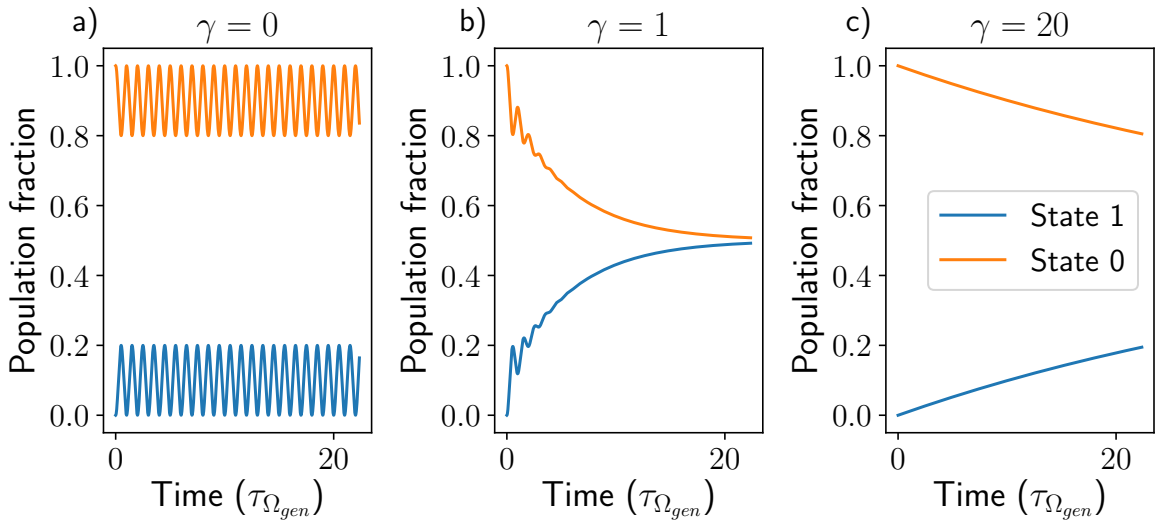


Figure 2.6: **Dephasing of a two level system under coupling and pure dephasing:** a)$\gamma_\phi = 0$, no dephasing; only the coherent part of the evolution is observed, b) $\gamma_\phi = 1$, medium dephasing; the coherent oscillation is damped and the state tends to the thermalised state (equal population), and c) $\gamma_\phi = 20$, strong dephasing; the coherent oscillation is no longer observed and the state takes longer to decay to the thermalised state. $\tau_{\Omega_{gen}}$ is the period of the generalised Rabi frequency. The results were simulated using QuTip [8, 9].

perturbative solution for the interaction of a two level system, dressed with a coupling field, with a single electromagnetic mode representing a component of the environment, is initially derived by considering the coupling between the dressed states. The result is then applied to the case of a wide band environment, deriving the response for different time regimes. At long times the perturbation theory approach is no longer valid and as such, using parallels with spontaneous emission, the wideband environment has to be treated as inducing incoherent transfer between the dressed states.

It should be noted that the time regimes derived are for the case where the environment only acts as a coupling field between the dressed states, however there is also a pure dephasing term (oscillating diagonal component of the Hamiltonian) in the dressed state basis that is not accounted for, discussed in chapter 4. The mapping from the dressed basis to the base state basis might also distort the response. These results, therefore, provide an indication of the expected behaviour but the exact dynamics are not well understood.

**Derivation for a single electromagnetic mode.** A single electromagnetic mode that couples the dressed states of a system can be treated perturbatively. To investigate the effect of population transfer only two dressed states are considered ($\left|\tilde{1}\right\rangle$ and $\left|\tilde{0}\right\rangle$). In this case transfer from the initial state $\left|\tilde{1}\right\rangle$ ($a_{\tilde{1}} = 1$) to the state $\left|\tilde{0}\right\rangle$ is studied. The perturbative solution of the population transferred is equal to

$$p_{\tilde{0}} = \hbar^2 |a_{\tilde{0}}|^2 = 4| \left\langle \tilde{0} \right| H \left| \tilde{1} \right\rangle |^2 \frac{sin^2(\frac{\omega t}{2})}{\hbar^2 \omega^2} \tag{2.42}$$

which is derived using perturbation theory [103]. $\omega$ is equal to the difference in frequency between the splitting of the dressed states ($\omega_0$) and the frequency of the perturbation, $\omega_p$. $H$ is the Hamiltonian which corresponds to the coupling between the dressed states due to

the perturbation. The rate of transfer from state $\left|\tilde{1}\right\rangle$ is given by

$$\frac{dp_{\tilde{1}}}{dt} = -2|\left\langle\tilde{0}\right| H \left|\tilde{1}\right\rangle|^2 t \frac{sinc(\omega t)}{\hbar^2} \tag{2.43}$$

calculated by differentiating equation 2.42 with respect to time. The rate of transfer has a *sinc* dependence, peaking at frequencies that correspond to the transition between the initial state $\left|\tilde{1}\right\rangle$ and the state $\left|\tilde{0}\right\rangle$, ($\omega_p = \omega_0$, $\omega = 0$). The width of the response is dependent on time; at long times, only frequencies close to the resonant frequency will contribute producing a narrow response, but for short times, the width of the response is very large. The effect of a perturbation that contains a wideband range of frequencies on the transfer rate in different time regimes will be discussed in the remainder of this section.

**Interactions with a flat wideband electromagnetic field.** As discussed previously the wideband flat electromagnetic field is used to model the effect of dephasing assisted transport. From the derivation for the response of the system to a single perturbation frequency, the response of the system to an environment composed of many frequencies can be derived. The contribution from the different frequency components of the perturbation do not interfere with each other and therefore can be summed [103], as shown in

$$\frac{dp_{\tilde{1}}}{dt} = -\sum_{\omega} 2|\left\langle\tilde{0}\right| H_\omega \left|\tilde{1}\right\rangle|^2 t \frac{sinc(\omega t)}{\hbar^2} \tag{2.44}$$

where $H_\omega$ is the amplitude corresponding to the detuning frequency $\omega$. For a continuous wideband perturbation this summation becomes an integral over frequency

$$\frac{dp_{\tilde{1}}}{dt} = -\int_{-\infty}^{+\infty} 2|\left\langle\tilde{0}\right| H_\omega \left|\tilde{1}\right\rangle|^2 \frac{sin(\omega t)}{\hbar\omega} \rho(\omega)\ d\omega \tag{2.45}$$

where $\rho(\omega)$ is the energy density of frequency states and the number of frequency modes ($n$) is equal to

$$n = \int_{-\infty}^{+\infty} \hbar\rho(\omega)\ d\omega \tag{2.46}$$

For a flat spectrum $H_\omega$ is equal to $H_{amp}/n$, where $H_{amp}$ is the sum of the effect of all the frequency components. Using equations 2.45 and 2.46 the theoretical response in different time regimes can be derived as detailed in the remainder of this section.

**Short time regime.** For short times relative to the period associated with the coupling frequency ($t < 1/\omega$), the transfer has a wide frequency response due to the presence of the sinc function in the transfer equation. The sinc function for each of the modes can therefore be approximated to one in this regime. For a flat spectrum this results in

$$\frac{dp_1}{dt} = -\frac{2|\left\langle\tilde{0}\right| H_\omega \left|\tilde{1}\right\rangle|^2 t}{\hbar^2} \int_{-\infty}^{+\infty} \hbar\rho(\omega)\ d\omega \tag{2.47}$$

Using equation 2.46 this simplifies to

$$\frac{dp_1}{dt} = -\frac{2|\left\langle\tilde{0}\right| H_{amp} \left|\tilde{1}\right\rangle|^2 t}{\hbar^2} \tag{2.48}$$

where $H_{amp}$ is equal to the number of modes multiplied by the coupling for each mode ($nH_\omega$). Equation 2.48 is integrated with respect to time to give the time dependence of the population in the initial state $\left|\tilde{1}\right\rangle$

$$p_{\tilde{1}} = 1 - \frac{|\left\langle\tilde{0}\right| H_{amp} \left|\tilde{1}\right\rangle|^2 t^2}{\hbar^2} \tag{2.49}$$

For short times, therefore, perturbation theory predicts a quadratic time dependency of the population in the initial state.

The quantum Zeno effect can be applied in this regime because of the quadratic time dependency. The quantum Zeno effect is the suppression of transport due to a fast rate of measurement of a system and occurs because the effect of measurement, in the basis of the initial state, collapses the state of the system, stopping the evolution. In the case of a system evolving under a quadratic dependency a fast measurement thus results in less evolution between successive measurements and therefore for a very fast rate of measurement the system will not evolve from the initial state.

**Intermediate regime: Fermi's golden rule.** At intermediate times the rate of population transferred has a linear dependence on time, consistent with Fermi's golden rule, and can be derived from equation 2.42. The transfer can be calculated by considering that, due to the presence of the sinc function, only the frequencies close to resonance will contribute to transport, and as such the integral limits are altered. The population in the state $\left|\tilde{1}\right\rangle$ is thus equal to

$$P_{\tilde{1}}(t) = 1 - \frac{t^2}{\hbar}\int_{-\Delta\omega/2}^{\Delta\omega/2} |\left\langle\tilde{0}\right| H_\omega \left|\tilde{1}\right\rangle|^2 sinc^2(\omega t/2)\rho(t)d\omega \tag{2.50}$$

where $\Delta\omega$ is the frequency width of the sinc response and is dependent upon time. The density of states, $\rho$, and the coupling, $|\left\langle\tilde{0}\right| H_\omega \left|\tilde{1}\right\rangle|^2$, are constants of the wideband perturbation field under investigation. Therefore equation 2.50 can be simplified to

$$P_{\tilde{1}}(t) = 1 - \frac{2t|\left\langle\tilde{0}\right| H_\omega \left|\tilde{1}\right\rangle|^2\rho(t)}{\hbar}\int_{w_i-\Delta\omega/2}^{w_i+\Delta\omega/2} sinc^2(y)dy \tag{2.51}$$

To solve the integral in equation 2.51 the parameter $y$, which is equal to $\omega t/2$, is used. The integral can be approximated by considering that the integral over the small range close to the resonance frequency is approximately equal to the result of the integral from $-\infty$ to $+\infty$. Under these conditions the equation reduces to Fermi's golden rule, and the transfer is found

to be linear with time as shown in the following equation

$$P_{\tilde{1}}(t) = 1 - \frac{2\pi |\langle \tilde{0} | H_\omega | \tilde{1} \rangle|^2 \rho(t)}{\hbar} t = 1 - \Gamma t \tag{2.52}$$

where the transfer rate, $\Gamma$, is dependent on the strength of the transition ($H_\omega$) and the density of states ($\rho(t)$). In chapter 5 both $\rho$ and $H_\omega$ are experimentally varied in order to evaluate the influence of the shape of the environment on transport.

**Long time regime.** At long evolution times the perturbative approach is no longer valid ($a_{\tilde{1}} \neq 1$) and the transfer rate due to a wideband environment has to be modelled as being entirely incoherent [55]. From comparisons with the origin of the incoherent process of spontaneous emission the validity of this approach will now be discussed.

**Spontaneous emission.** An atom that is in an excited state will decay to the ground state due to spontaneous emission. Spontaneous emission is the result of the dressing of the atom by the electromagnetic vacuum states. The vacuum background is flat at frequencies close to the transition frequency [55, 104] (similar to the system under investigation). The preceding derivation for the perturbation solution can also be applied to spontaneous emission and also leads to the short time quadratic and intermediate time linear responses. At long times the effect of spontaneous emission is calculated using optical Bloch equations [54]. The similarities between the spontaneous emission and the wideband field under investigation at short times suggests that a similar approach to the long time regime using the optical Bloch equations may be appropriate.

The response of the wideband field in the long time regime is thus modelled as being incoherent, as is the case for spontaneous emission; the key difference between the two is that spontaneous emission is a one way process and the wideband field is a two way transfer

between the states. The rate equations that are used for the wideband long time regime are therefore

$$\frac{d(n_{\tilde{1}} - n_{\tilde{0}})}{dt} = -\Gamma(n_{\tilde{1}} - n_{\tilde{0}}) \tag{2.53}$$

where $n_{\tilde{1}} - n_{\tilde{0}}$ is the difference in population between the two states. This results in an exponential decay of the difference in population

$$n_1 - n_0 = (n_1 - n_0)(t = 0)e^{-\Gamma t} \tag{2.54}$$

similar to the approach used by Wigner and Weisskopf [54]. The three response regimes derived in this section will be used in this study to analyse the experimentally determined response of the system to a wideband field. This is reported in chapter 5.

## 2.7 Incoherent transfer and the width of the energy distribution

As discussed the interaction of a wideband coupling field over long times is treated as inducing incoherent transport between the dressed states. The effect of incoherent transitions can also be expected to have an effect on the width of the energy distribution of the state. In this section this effect will be examined, again using parallels with the incoherent transfer process of spontaneous emission. Finally the relationship between incoherent transfer, the Heisenberg uncertainty principle and the width of the energy distribution of the state will be discussed.

**Spectroscopy of spontaneous emission.** To understand the effect of incoherent transfer between states, spontaneous emission between the excited state and ground state of an atom

will be studied. For the case of coherent transitions between states as well as spontaneous emission, the steady state solution of the optical Bloch equations [10], for the population in the excited state ($\rho_{ee}$), is shown in

$$\rho_{ee} = \frac{(\Omega/\Gamma)^2}{1 + 4(\Delta/\Gamma)^2 + 2(\Omega/\Gamma)^2} \tag{2.55}$$

where $\Delta$ is the detuning of the coherent transition field relative to the transition frequency between the ground and excited state of the atom, $\Omega$ is the frequency corresponding to the strength of the coherent coupling field and $\Gamma$ is the frequency corresponding to the spontaneous emission rate. Equation 2.55 shows that the population in the excited state, $\rho_{ee}$, has a frequency dependence with a width that is dependent upon the spontaneous emission rate $\Gamma$ and the power broadening $\Omega^2$. Without spontaneous emission the maximum excited population is 50% of the total population. As the rate of spontaneous emission increases, and thus the width of the energy distribution of the excited state increases, the population in the excited state becomes dependent on $\frac{\Omega^2}{\Gamma^2}$. Thus for very high rates of spontaneous emission the population in the excited state will be negligible. In the present study, the energy distribution of the states is broadened using a noisy field. This is analogous to the broadening of the energy distribution of the states seen in spontaneous emission [103, 104].

**Incoherent transitions.** The preceding discussion noted that the interaction of an incoherent decay process broadens the energy distribution of a state. This can also be thought of as the incoherent transfer process determining the lifetime of the state and therefore the broadening of the state is proportional to the inverse of the lifetime, as determined from the Heisenberg uncertainty principle

$$\Delta E \Delta T > \hbar/2 \tag{2.56}$$

where $\Delta E$ is the width of the energy distibution of the state and $\Delta T$ is the lifetime of the state. Incoherent transfer processes also take place in the FMO system [2]. A sink state is present in the FMO and is the state where ultimately the exciton is transferred to and absorbed. The sink mechanism in the FMO is usually modelled as incoherent transfer from a site in the system to the sink state. This incoherent transfer can broaden the energy of the site and thus increase the transport rate through the system; sinks are discussed in more detail in the future work section (section 6.2.2).

## 2.8 The relationship between measurement and dephasing

Incoherent transitions have been shown to arise from processes that both destroy the phase coherence between the states and transfer population between the states. Measurements are strongly related to the destruction of the phase coherence between the states that can result from the interaction with a wide-band noisy field. The terminology, therefore, surrounding measurement is commonly interchanged with that of incoherent transfer. In this section a discussion of the relationship between measurement and dephasing will be presented.

A measurement, in the base state basis, is a quantum operation that collapses the state of a system to its' base states that destroys any superposition between those base states (removing the coherence terms in the density matrix). To determine the probability distribution between the states a large collection of identical systems can be studied. A measurement results in the average of the ensemble of systems decaying from a pure state to a mixed state.

The response of systems to measurement is similar to the effect of high levels of dephasing [26, 105]. As mentioned the measurement in the base state basis collapses the system to

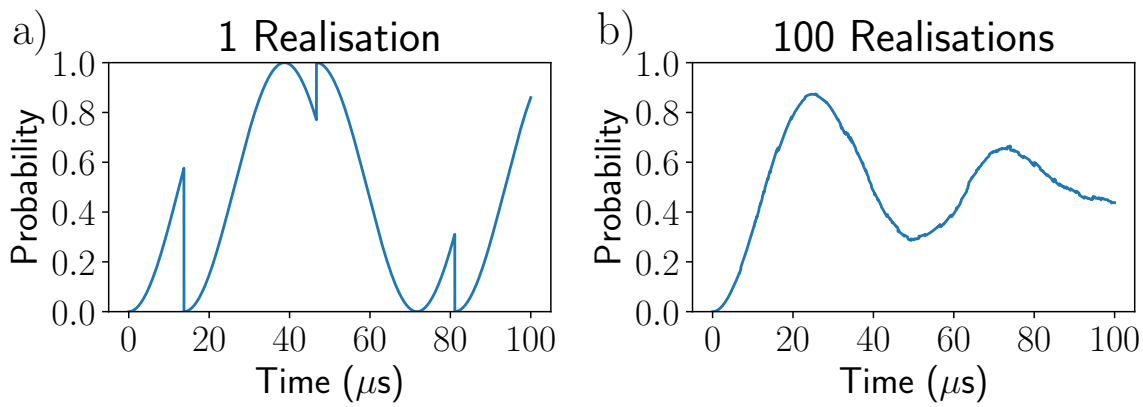


Figure 2.7: **Measurement and dephasing:** The evolution of the population in the excited state of a two level atom. a) For 1 realisation the evolution of the system collapses multiple times due to the effect of the measurement. b) For the average of 100 realisations the response is very similar to that of a dephasing process.

a base state of the system weighted by the relative probability distributions between the base states (the diagonal terms in the density matrix), destroying the off-diagonal coherence terms in the density matrix. Figure 2.7 shows a numerical simulation of this process for 1 and 100 averaged realisations. The rate of measurement follows a probability distribution where there is a probability that the system will be measured that increases with time between measurements. As can be seen in figure 2.7a for a single component of the ensemble there are discontinuities in the evolution of the state that correspond to the state of the system collapsing to the base states. Figure 2.7b is the average of the response of the system for 100 realisations. Damping behaviour is observed consistent with the effect of dephasing. For very high rates of measurement the transport is suppressed. This is referred to as the quantum Zeno effect [106].

## 2.9 Conclusions

This chapter began by constructing the Hamiltonian that determines the evolution of the three level system used in this study. The inclusion of the environment by the perturbation

of the magnetic field was then presented. The evolution of the system for no perturbation was derived showing the expected Rabi oscillation and the Rabi oscillations were mapped using the Bloch sphere representation. Typical effects that result from the interaction of the environment were investigated in the rest of the chapter. Initially there was a discussion of the similarities and differences between dephasing and decoherence, with dephasing resulting from the ensemble average and decoherence resulting from the interaction with a bath. In order to model the effect of the pure dephasing field, master equations using Lindblad equations were used and the three expected responses (localisation, ENAQT and Zeno-like) were found for increasing levels of pure dephasing. The effect of a wideband field that is used to model the environment associated with dephasing assisted transport was discussed. Three regimes were identified for the time evolution of the system; an intial quadratic response, a linear response and an exponential response, these will be used for analysis of experimental results in chapter 5. The quadratic and linear responses were derived using perturbation theory and the exponential response was determined from drawing parallels with the incoherent process of spontaneous emission. The influence of an incoherent process was discussed with reference to the Heisenberg uncertainty principle. Finally, using an approach similar to that of quantum trajectories, it was demonstrated that there is a strong link between dephasing and measurement processes.

# CHAPTER 3

# EXPERIMENTAL SET-UP

## 3.1 Introduction

The key mechanisms and features of systems that exhibit noise assisted quantum transport can be replicated using a three site system. Figure 3.1a shows a fully connected network (FCN) that contains both nearest neighbour and next nearest neighbour couplings. The competing coherent paths between these two couplings allows interference effects to be investigated.

The energy levels of the magnetic substates ($m_F$) of the $F = 1$ ground state of rubidium 87 are used to model the sites in the system, as shown in figure 3.1b. The energies of the sites are set using an applied magnetic bias field (using the Zeeman effect). The site energies are then perturbed to simulate environmental effects, by perturbing the magnetic bias field. The nearest neighbour coupling is provided by an RF field and the next nearest neighbour coupling by Raman transitions. It is possible to increase the complexity of the system further by increasing the number of sites in the network.

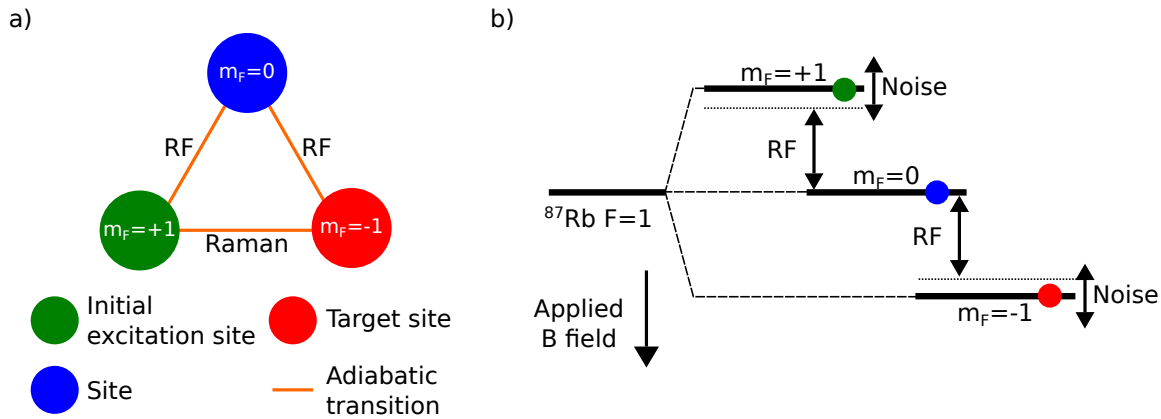


Figure 3.1: **The system network:** a) representation of the fully connected network (FCN) with nearest neighbour radio frequency (RF) coupling and next nearest neighbour Raman coupling. The initial excitation (full population in the $m_F = +1$ state) transfers between the sites to reach the target site ($m_F = -1$ state). b) the energy level structure of the system. A magnetic bias field (B) splits the energy levels (Zeeman effect) and an RF field couples the nearest neighbour sites. Noise is introduced into the system by perturbing the bias field, 'shaking' the energies of the sites.

The following chapter outlines how the state of the system was prepared in order to model the initial site of the excitation in the biological system, how the transfer through the network was measured and finally gives details on the couplings and perturbations used. An earlier review of the experimental set-up can be found in C. Gill, PhD thesis [107]. The full experimental procedure is shown schematically in figure 3.2.

## 3.2 The experimental set-up

### 3.2.1 Cooling the atoms

To precisely control the couplings and the perturbations of the energy levels it is necessary to isolate the sites from the environment. Cold atoms are used for this purpose because of the good isolation from environmental noise and the relatively easy control of the couplings and energy levels of the atoms using magnetic fields and light. In addition the low velocities of

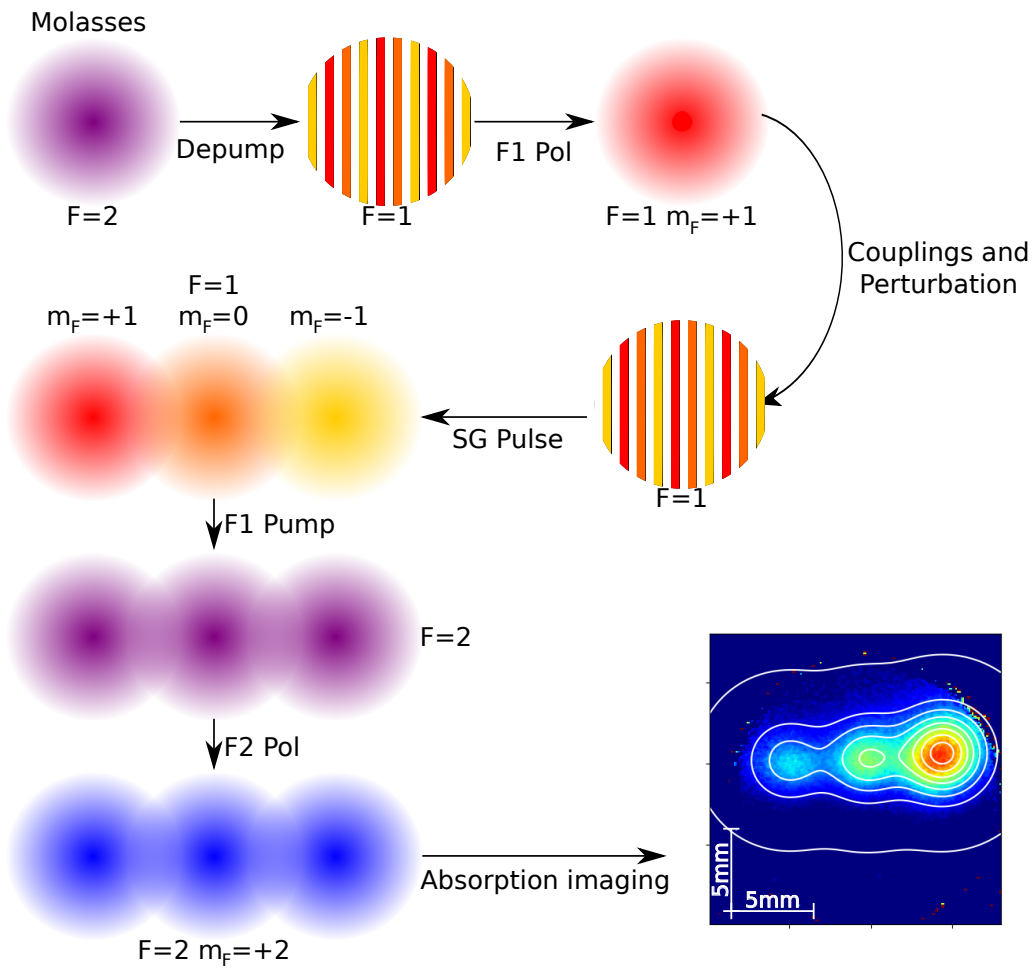


Figure 3.2: **The full pumping procedure:** Initially the atoms are cooled using laser cooling followed by molasses cooling. This results in the majority of the atoms being in the $F = 2$ state. The atoms are then pumped to the $F = 1$ state using the de-pump beam and then polarised into the $F = 1$ $m_F = +1$ state using the F1 polarisation beam. The couplings and perturbations under investigation are then applied and the resulting distribution between the $F = 1$ $m_F$ states is measured. The measurement involves a Stern-Gerlach pulse that spatially separates the atoms depending upon their $m_F$ state. The F1 pumping beam then pumps the atoms to the $F = 2$ state from where they are polarised into the $F = 2$ $m_F = 2$ substate. Finally the three atomic clouds are measured using absorption imaging to obtain an optical density profile of the three clouds. This profile is then fitted to determine the distribution of the population between the three $m_F$ states.

the cold atoms increases the available interaction time with the atoms compared with using room temperature vapours, and reduces the Doppler shift contribution to the broadening of the energy levels.

Rubidium 87 was chosen for this study because the structure of rubidium is simple and well studied, and the techniques for laser cooling rubidium are well known and understood [108–110]. The atoms are initially cooled in a 6 beam magneto optical trap (MOT), followed by sub-Doppler molasses cooling [111, 112], producing a localised dense group of ≈10 million atoms at ≈10 $\mu$K. An example of the temperature measurement for the molasses cooled cold atoms is presented in figure 3.3. The temperature of the atoms is determined by allowing the atomic cloud to expand for set times and measuring the dimensions of the cloud at each time step. The rate of expansion of the cloud of atoms is dependent upon the velocity distribution within the cloud and thus the temperature can be calculated from fitting the equation [113]

$$\sigma(t) = \sqrt{\sigma_0^2 + \frac{kT}{m}t^2} \tag{3.1}$$

where $\sigma$ is the width of the cloud at time $t$, $\sigma_0$ is the initial width, $k$ is the Boltzmann constant, $T$ is the temperature of the cloud, $m$ is the atomic mass of rubidium and $t$ is the time of flight.

Figure 3.4 shows a schematic of the full vacuum system and the arrangement of the magnetic coils. There are 3 pairs of compensation coils that act to cancel out the effect of the earth's magnetic field. Without the compensation coils the residual background magnetic field would reduce the effectiveness of the molasses cooling leading to higher temperatures. The MOT coils produce a field gradient of ≈ 10 G/cm.

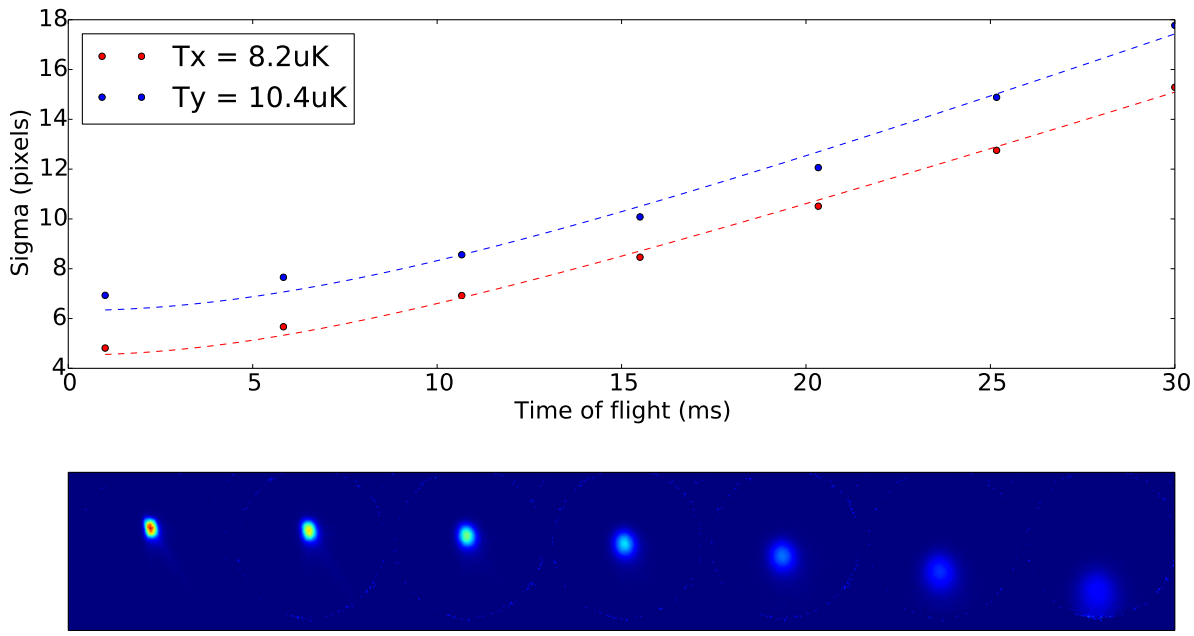


Figure 3.3: **Molasses temperature measurement:** The cold atomic cloud is allowed to expand for varying times in order to determine the temperature. The cloud profiles are fitted using a 2D Gaussian function and the horizontal (x) and vertical (y) widths of the clouds are determined. For this particular measurement the number of atoms was determined to be ≈10 million atoms at ≈10$\mu$K. Over the measurement time the cloud can be observed to fall due to gravity.

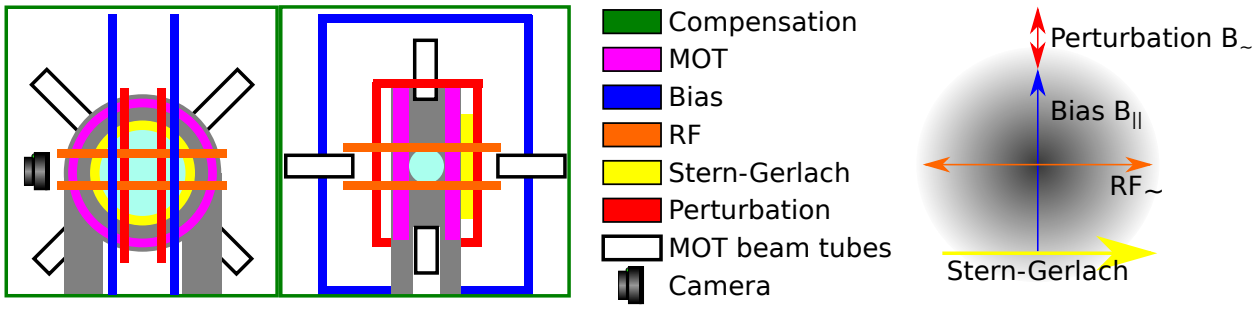


Figure 3.4: **The experimental set-up:** The arrangement of the coils around the vacuum system and the resulting fields imparted on the atoms in the the cloud.

### 3.2.2 The Laser Set-up

The beams in the experiment are derived from two main lasers; the master laser ($F = 2$ to $F' = 3$ cooling transition), from where the imaging, depump and cooling beams are derived, and the repump laser ($F = 1$ to $F' = 2$ transition) that generates the repump and the $F = 1$ to $F' = 1$ polarising beam. Part of the master laser is injection locked into a slave laser that amplifies the beam and splits it into the six beams required for the laser cooling. The cooling beams are detuned by $\approx -12MHz$ relative to the $F = 2$ to $F' = 3$ transition. The master laser is locked using polarisation spectroscopy [114] to the $F = 2$ to $F' = 3$ cooling transition resulting in a linewidth of $\approx$ 400kHz. The repump laser ($F = 1$ to $F' = 2$ transition) is locked relative to the master laser using a beat lock [115], with a shift of $6.568GHz$, producing a linewidth of $\approx 1-2MHz$ as determined from the spectral width of the beat lock signal [116].

The depump beam is derived from the master laser using a double pass 200MHz acoustic optical modulator (AOM) that yields a beam resonant with the $F = 2$ to $F' = 1$ transition (shift of $424MHz$ from the cooling beam). The imaging beam is passed through two double pass configuration AOMs, which first increases the frequency and then reduces it by a set amount, this is in order to precisely control the frequency. The $F = 1$ to $F' = 1$ polarisation pumping beam is generated from the repump laser ($F = 1$ to $F' = 2$) using an 80MHz double pass AOM (shift of $157MHz$). A diagram detailing the frequencies used in the experiment is shown in figure 3.5.

## 3.3 Preparation of the initial excitation

The sites of the network are modelled by the magnetic substates ($m_F$) of the $F = 1$ ground state. A depump beam is used to transfer the states of the atoms to the $F = 1$ ground state. The initial excitation is prepared by pumping the atoms to the $F = 1$ $m_F = +1$ state. This

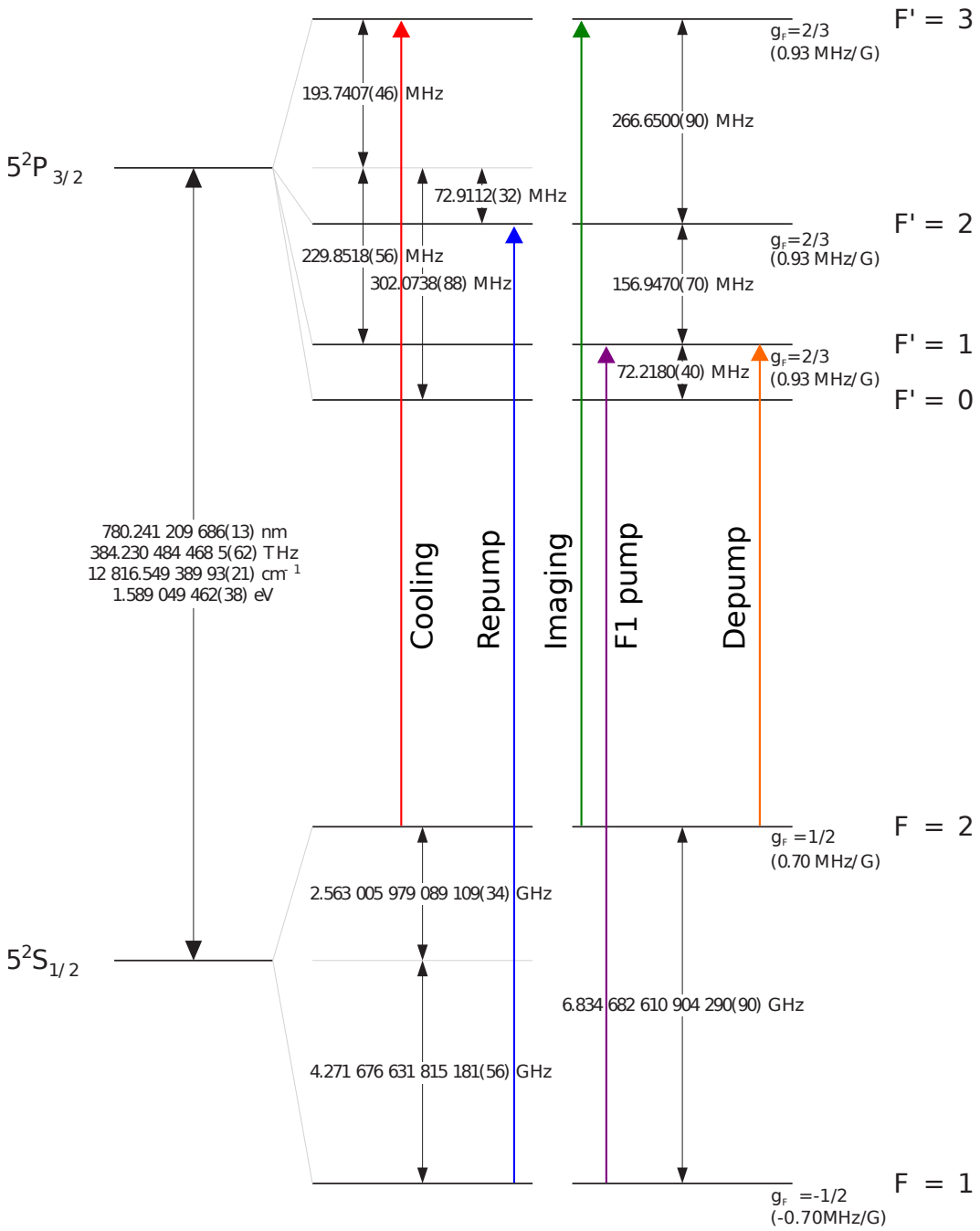


Figure 3.5: **Beam frequencies:** The multiple frequencies of the beams used in this study in relation to the atomic energy levels. The $F'$ states represent the excited states. This figure was adapted from Steck Alkali D data [10].

section discusses the experimental details of these processes and presents the results used to determined the experimental parameters.

### 3.3.1 Depumping procedure

The depumping beam transfers the atoms to the $F = 1$ state. After the atoms are cooled, using the molasses laser cooling technique, a large proportion of the atoms are in the $F = 2$ ground state. To transfer the atoms from the $F = 2$ to the $F = 1$ state a depump beam stimulates transition from the $F = 2$ state to the $F' = 1$ excited state. This state then decays spontaneously, either back to the $F = 2$ ground state or, with a higher probability, to the $F = 1$ ground state due to the larger value of the Clebsch-Gordon coefficients for this transition [10]. This process is shown in figure 3.6a and continually repeats until all the atoms are transferred to the $F = 1$ ground state. The depump beam is composed of all transition polarisations in order to fully depopulate every $F = 2$ $m_F$ state because, in the case of a single polarisation, dark states (where atoms in that state cannot interact with the beam) would exist. For instance, as shown in figure 3.6a, atoms in the $F = 2$ $m_F = +2$ state can only interact with a $\sigma_-$ polarised beam, thus if the depump beam was $\sigma_+$ polarised the $F = 2$ $m_F = +2$ state would be a dark state.

To determine the required depumping time to fully transfer atoms from the $F = 2$ to the $F = 1$ state, the atoms were initially cooled, as discussed in the preceding section, and then the population in the $F = 2$ state was measured, using the absorption imaging technique (section 3.4.2), for set irradiation times of the depump beam. Figure 3.6b shows the atom population in the $F = 2$ state versus depump time measured in this study. As observed the population decay has an exponential form but does not tend to zero as would be expected; this could be because the polarisation of the depump beam was not well mixed between $\sigma_+$, $\sigma_-$ and $\pi$. The residual population in the $F = 2$ state after depumping was removed ('blown

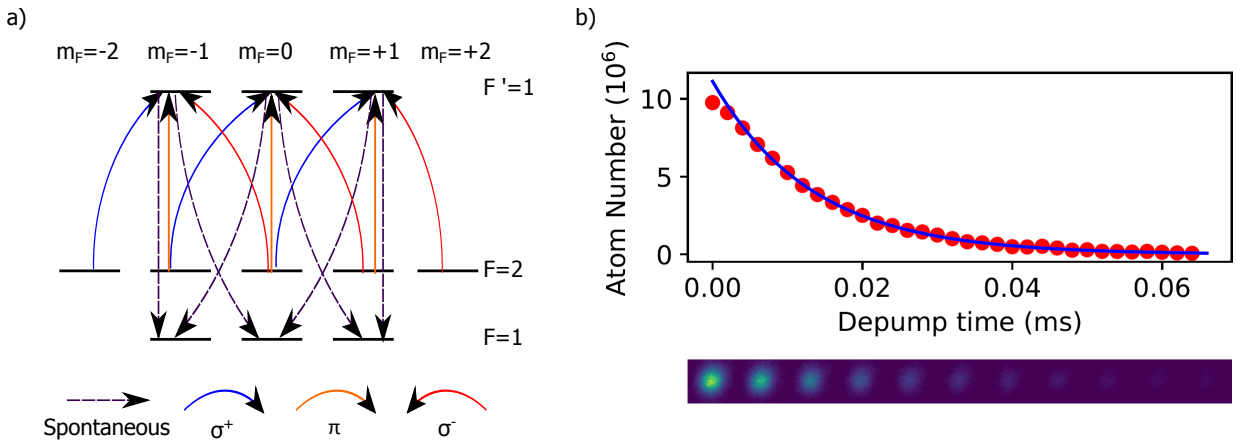


Figure 3.6: **Depumping:** a) The $F = 1$ state is populated using the $F = 2$ to $F' = 1$ depump beam, b) the population left in the $F = 2$ state for varying depump irradiation times.

away') by de-balancing and pulsing the cooling beams. The exponential decay constant for the decay of the population in the $F = 2$ state due to the application of the depump beam was found to be $13.3 \pm 0.1\mu s$ and therefore a long depump time of $1ms$ was chosen to ensure that all of the population was transferred. The choice of this long time is discussed in relation to the F1 polarisation time in the next section.

### 3.3.2 F1 polarisation procedure

The initial excitation is established by polarising the sample into the $F = 1$ $m_F = +1$ state. This is achieved using a circularly polarised resonant $F = 1 \rightarrow F' = 1$ beam parallel to the bias field that drives $\sigma_+$ transitions (henceforth referred to as the F1 polarisation pumping beam). The atoms are initially excited into the $F' = 1$ $m_{F'} = m_F + 1$ state and then spontaneously decay to either the $F = 1$ $m_F = m_F$, $m_F + 1$ or $m_F + 2$ states, as shown in figure 3.7a. The $F = 1$ $m_F = +1$ state cannot interact with the $F = 1$ to $F' = 1$ $\sigma_+$ beam and is therefore referred to as a dark state. Eventually all of the atoms will decay to the $m_F = +1$ dark state.

The efficiency and optical pumping rate of the F1 polarisation beam procedure was experimentally determined by measuring the relative populations of the constituent $m_F$ states for set F1 polarisation pumping times, as shown in figure 3.7b. The measurement procedure is discussed in section 3.4. It was observed that after the depumping procedure the population was initially distributed between the three $m_F$ states. The population in the $m_F = +1$ state asymptotically approached a maximum with increasing pumping time and simultaneously the population in the other two states reduced. The experimentally determined rate of change of the population in the three states was similar with an exponential time constant of $70.7 \pm 2.1\mu s$ for $m_F = +1$, $66.1 \pm 1.6\mu s$ for $m_F = 0$ and $76.1 \pm 3.2\mu s$ for $m_F = -1$. The observation of similar rates is due to the Clebsch-Gordon coefficients being the same for every possible transition [10] resulting in the same transition rate to the target state. Based on this an F1 polarisation pumping time of $1.01ms$ was chosen as the standard for the experimental procedure.

The F1 polarisation pumping and depump beams are applied at the same time so that any population loss resulting from decay which occurs from the $F' = 1$ excited state to the $F = 2$ state, due to the F1 polarisation pumping procedure, can be depumped back to the $F = 1$ state and therefore not lost from the system. The F1 polarisation beam is applied for a longer time in order that the 'purity' (the relative population in the $F = 1$ $m_F = +1$ to the other $F = 1$ $m_F$ states) is maintained.

The effectiveness of the pumping is strongly dependent on the polarisation of the F1 pumping beam. This is because, if the polarisation is mixed, the $F = 1$ $m_F = +1$ state is no longer a dark state and therefore the system would reach a steady-state where the final state of the system after pumping is not localised to the $F = 1$ $m_F = +1$ state, destroying the 'purity' of the initial excitation. An impure state could, however, be useful to investigate theoretical models where the initial excitation is not localised to a single state.

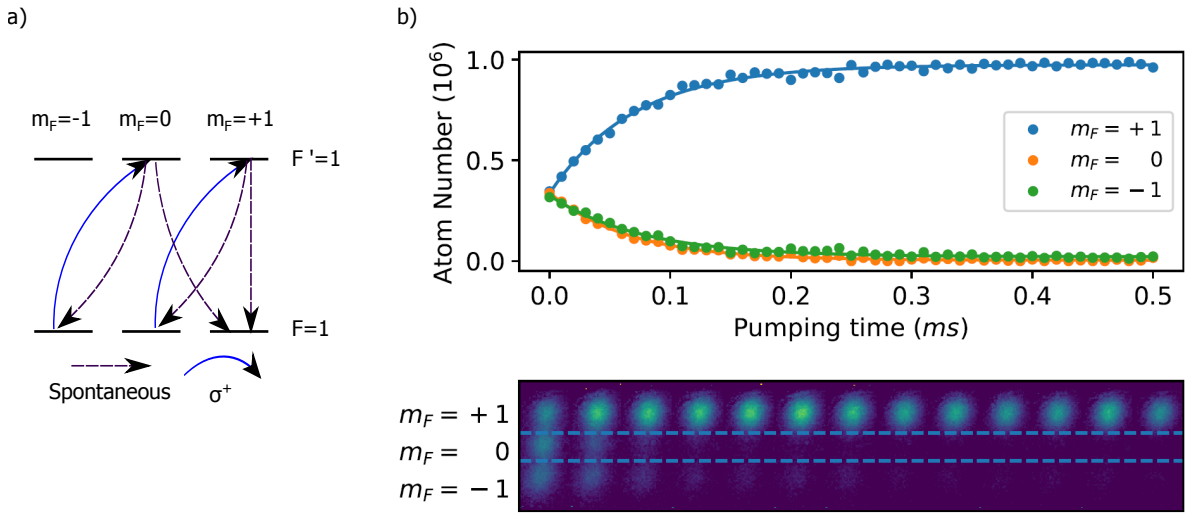


Figure 3.7: **Optical pumping:** a) The $F = 1$ $m_F$=+1 state is populated using a $\sigma_+$ polarised beam, b) the change in the relative fraction of the population between the three states with varying F1 polarisation pumping time.

## 3.4 Measuring the state of the system

Once the quantum state of the system is initialised and the perturbations and coupling fields under investigation are applied, the resulting population distribution between the sub-states is measured. A schematic of the measurement procedure is shown in figure 3.8.

**Stern-Gerlach field** The atoms are spatially separated to an extent dependent upon the magnetic substate ($m_F$) of the atoms [117]. The large magnetic gradient provided by the Stern-Gerlach coil produces a force

$$F = -m_F \mu_b g \frac{dB}{dz}, \tag{3.2}$$

where $\mu_b$ is the Bohr magneton, g is the Landau factor and the force on the atoms is proportional to the gradient of the magnetic field. The Stern-Gerlach coil produces a small magnetic field across the atoms that provides a quantisation axis that is perpendicular to

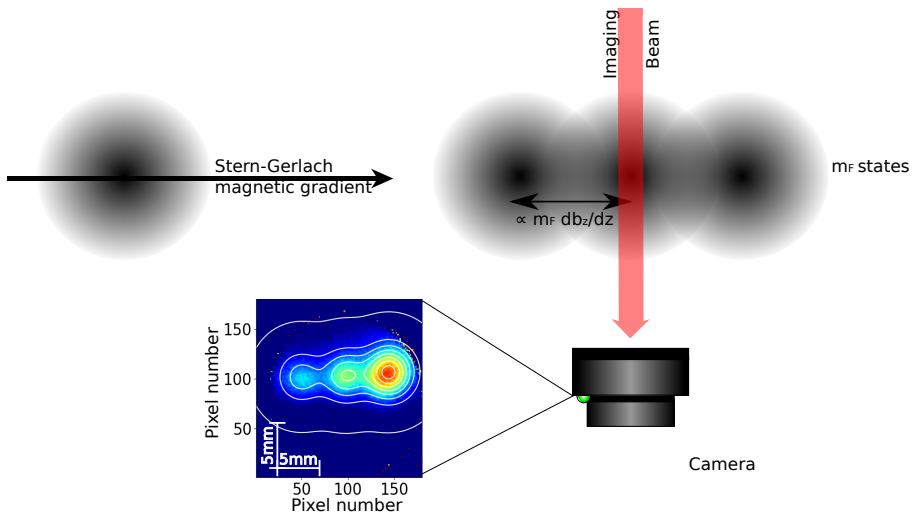


Figure 3.8: **Measurement procedure:** The Stern-Gerlach field spatially separates the cloud dependent upon the $m_F$ state. The clouds are then pumped to the $F = 2$ $m_F = +2$ state and imaged using absorption imaging.

the z axis (imaging axis). The populations in the different $m_F$ states are maintained by applying the small magnetic field slowly; allowing adiabatic following of the populations in the different $m_F$ states. If the field was applied too quickly then population would be exchanged between the $m_F$ states. In addition the magnetic field providing the quantisation axis has to be minimised in order to reduce the influence of the non-linear Zeeman effect, section 6.2.3, that would lead to a non-uniform separation of the clouds.

### 3.4.1 Optical pumping to the $F = 2$ $m_F = +2$ state

The population distribution of the $F = 1$ $m_F$ states is determined from the measurement of the optical density profile of the Stern-Gerlach spatially separated clouds. The optical density profile is measured using an absorption imaging technique that uses the closed $F = 2$ $m_F = +2$ to $F = 3$ $m_F = +3$ $\sigma_+$ transition and therefore the atoms, which are initially in the $F = 1$ state after the Stern-Gerlach field is applied, need to be pumped to the $F = 2$ $m_F = +2$ state.

**F1 pumping procedure** The first phase of pumping transfers the atoms to the $F = 2$ state using the F1 polarisation pumping beam. The F1 polarisation pumping beam causes transitions from the $F = 1$ state to the $F' = 1$ state from where the atom spontaneously decays, either back to the $F = 1$ state or the desired $F = 2$ state, as shown in figure 3.9a. Note that to populate the $F = 2$ state it would be better to use the beam resonant with the $F = 1$ to $F' = 2$ transition. This is because the pumping efficiency from the $F = 1$ state via the $F' = 2$ state is greater than via the $F' = 1$ state due to the higher decay rate from the $F' = 2$ to the $F = 2$ state compared with that from the $F' = 1$ to the $F = 2$ state. The experimental set-up, however, cannot pulse the beam resonant with the $F = 1$ to $F' = 2$ transition reliably for short times.

As already noted, for a single polarisation of the pumping beam there would be dark states within the $F = 1$ $m_F$ states, this is because $\pi$ does not interact with the $F = 1$ $m_F = 0$ state, $\sigma_+$ does not interact with the $F = 1$ $m_F = +1$ state and $\sigma_-$ does not interact with the $F = 1$ $m_F = -1$ state. The transition polarisation of the F1 polarisation pumping beam is therefore mixed in order to depopulate all the $m_F$ states in the $F = 1$ manifold. The F1 polarisation pumping beam is circularly polarised but the application of the perpendicular quantisation axis, provided by the Stern-Gerlach field, mixes the interaction polarisations.

To evaluate the optical pumping rate due to the F1 pumping beam the population in the $F = 2$ state was measured for varying pumping times and the results are shown in figure 3.9b. The graph confirms the theoretical asymptotic approach to a maximum ($\approx 5$ million) of the population in the $F = 2$ state as the pumping time is increased consistent with the general theory of pumping processes. The asymptotic growth time constant, defined as $\tau$ in equations of the form $(1 - e^{-t/\tau})$, was measured as $0.336 \pm 0.038ms$ and therefore a pumping time of $4.75ms$ was chosen as the standard for the ongoing experiments, the reason for selecting a much longer time is discussed in the next part of this section.

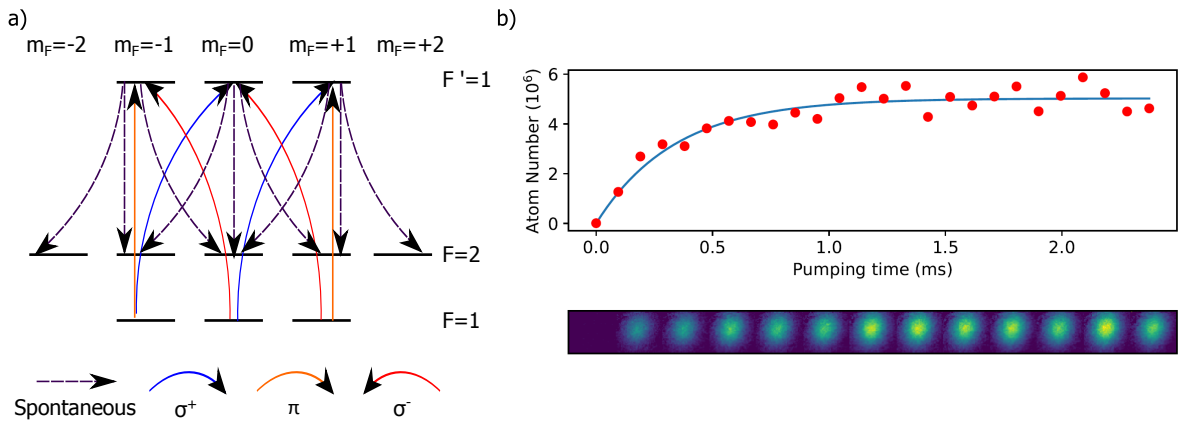


Figure 3.9: **F1 repumping:** a) The $F = 2$ state is populated using the F1 polarisation pumping beam, b) the measured dependence of the atom population in the $F = 2$ state on the pumping time.

**F2 polarisation procedure** The second stage of pumping transfers the atoms from a distribution across the $F = 2$ $m_F$ states to a majority in the $F = 2$ $m_F = +2$ state. The three separate clouds, corresponding to the populations in the three $m_F$ states, are all in the $F = 2$ state after the F1 pumping stage. There is initially an unequal distribution of the $F = 2$ $m_F$ state populations between the three clouds. Different $m_F$ states however interact differently with the imaging beam and therefore, in order to make an accurate measurement of the population in each cloud, the atoms are pumped to the $F = 2$ $m_F = +2$ state. The transfer to the $F = 2$ $m_F = +2$ state is done using the $F = 2$ to $F' = 3$ circularly polarised imaging beam parallel to the bias field that drives $\sigma^+$ transitions from the $F = 2$ state to the $F = 3$ $m_{F'} = m_F + 1$ state. The atoms then decay either to the $F = 2$ $m_F = m_F$, $m_F = m_F + 1$ or $m_F = m_F + 2$ states, as shown in figure 3.10a, this increases the mean $m_F$ state that the atoms are in. Eventually all of the atoms in the clouds are transferred to the $F = 2$ $m_F = 2$ state, where further transitions to a lower $m_F$ state are no longer possible because the $F = 2$ $m_F = 2$ to $F = 3$ $m_{F'} = 3$ transition is cyclic.

To evaluate the optical pumping rate of the transfer to the $F = 2$ $m_F = +2$ state the pumping time of the imaging beam was varied and an absorption image of the resultant clouds taken. The magnitude of the optical density was found to be dependent on the strength of the transition and the distribution of the atoms between the $m_F$ states, with the highest value of the optical density and thus the highest measured population corresponding to all the atoms being in the $F = 2$ $m_F = +2$ state. The results are shown in figure 3.10b. The graph confirms the theoretical asymptotic approach to a maximum ($\approx 4$ million) of the population in the $F = 2$ state as the pumping time is increased and is consistent with the general theory of pumping processes. The asymptotic growth time constant for the population measured in the $F = 2$ state, due to the application of the F2 pumping beam, is $0.533 \pm 0.124ms$ therefore a pumping time of $2.75ms$ was chosen as the standard for the F2 pumping beam.

The F1 pumping beam and the F2 pumping beam are operated simultaneously so that any population transferred using the F1 pumping beam to the $F = 2$ state during the application of the F1 pumping beam is transferred to the $F = 2$ $m_F = +2$ state. In addition the bias magnetic field (parallel to the imaging axis) is ramped up during the pumping so that, as the Stern-Gerlach field reduces, a new quantisation axis is introduced, reducing the effect of the F1 pumping beam but increasing the effectiveness of the F2 polarisation procedure.

### 3.4.2 Absorption imaging

After the atoms are pumped to the $F = 2$ $m_F = +2$ state, absorption imaging is used to generate an optical density profile of the clouds allowing the populations in each of the $F = 1$ $\mathrm{m}_F$ states to be determined. Figure 3.8 shows a diagram of the absorption imaging technique. The imaging beam is resonant with the $F = 2$ to $F' = 3$ transition and drives the cycling $\sigma^+$ transition (the imaging beam is circularly polarised and parallel to the applied bias field).

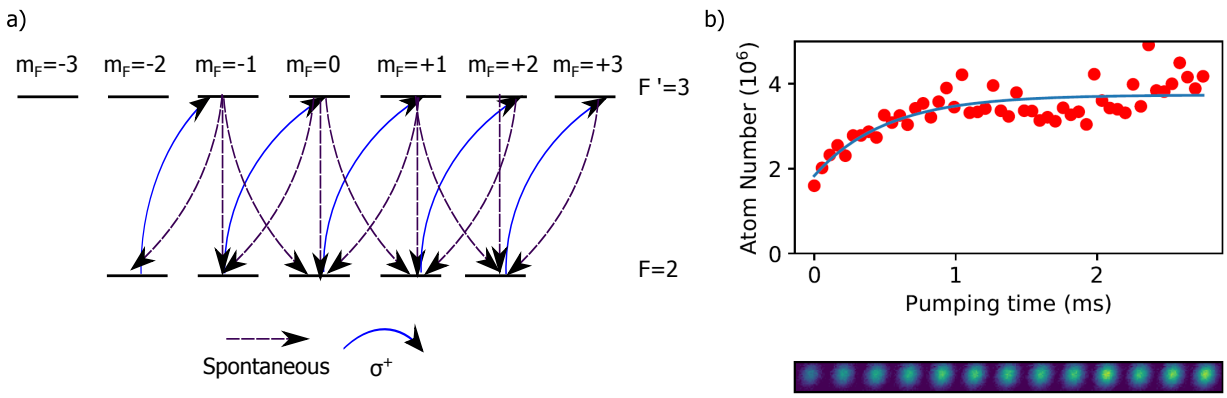


Figure 3.10: **F2 pumping:** a) pumping the atoms to the $F = 2$ $m_F$=+2 state using a $\sigma^+$ beam, b) the dependence of the measured population in the $F = 2$ state on the pumping time. The measured population is dependent upon the distribution of the atoms between the $F = 2$ $m_F$ states.

A 2D profile of the optical density beam absorption due to the atomic clouds is recorded on a CCD camera. Two images are taken, one that shows the absorption of the imaging beam by the cloud under investigation (absorption image) and one of the background with just the imaging beam present (background image). The profile of the optical density is obtained using the equation

$$od(x, y) = ln(\frac{I_0}{I}) \tag{3.3}$$

where $I$ is the intensity profile of the absorption image and $I_0$ is the intensity profile of the background image. The profile is then decomposed into multiple 2D Gaussians and the population in each of the $m_F$ states is calculated using the equation

$$n = \frac{1}{\sigma_0} \int_{-\infty}^{+\infty} \int_{-\infty}^{+\infty} od(x, y)\, dxdy \tag{3.4}$$

where $n$ is the number of atoms and $\sigma_0$ is the absorption cross-section for circularly polarised beams. A small cloud size is desirable (preferably $\approx 4mm$ after the cloud has expanded during the measurement time), this is achieved by ensuring that the temperature of the

atoms is as low as possible. This is because in this experimental set-up the size of the imaging region is limited by the size of the access window to the vacuum chamber ($16.5mm$) and this determines the maximum size of the imaging beam.

The optical frequency of the imaging beam is adjusted to determine the frequency shift, relative to the master locking frequency, required to place the imaging beam precisely on resonance with the $F = 2$ to $F' = 3$ transition. This is achieved by measuring the dependence of the attenuation of the imaging beam, caused by the molasses cooled atoms, on the imaging beam frequency and selecting the frequency that corresponds to the highest optical density.

## 3.5 RF coupling

The full theoretical description of the effect of nearest neighbour coupling on the evolution of a three level system is derived in section 2.2, however there are some practical implications that will be discussed in the following section. Initially the theoretical description of the nearest neighbour RF coupling will be discussed, adiabatic following will then be investigated using both computational models and experimental data, and finally the effect of inhomogeneous broadening will be investigated experimentally.

### 3.5.1 Theoretical description

Nearest neighbour coupling is provided by an RF field that induces magnetic dipole transitions between the adjacent magnetic sub-levels. The Rabi frequency ($\Omega$) of the nearest neighbour RF coupling is proportional to the amplitude of the oscillating RF field ($B$) and the magnetic dipole moment ($\mu$). As shown in

$$\Omega = \frac{\mu B}{\hbar} \tag{3.5}$$

### 3.5.2 Adiabatic following

Adiabatic following results from the slow power on/off time of the RF coupling field. The power of the RF field is increased by using a resonant circuit and this increases the Rabi frequency, it has, however, the negative effect of increasing the time the field takes to power on/off as shown in figure 3.11. Figure 3.11 was produced by measuring the amplitude of the magnetic field generated by the RF coil, using a hall probe. The asymptotic growth time constant was measured as $\approx 5\mu s$. When the field was applied, the amplitude and thus the coupling slowly increased, resulting in partial adiabatic following of the state. Adiabatic following is where the spin dynamics of the atoms follow the changing precession axis; the state of the atom will precess around this changing precession axis leading to damping of the amplitude of the precession. This happens in the case of both static coupling and coupling in the rotating frame [118]. Usually RF fields are used to reduce adiabatic following because in the rotating frame the coupling can be applied nearly instantaneously, much faster than in the case of a static coupling field.

To investigate the influence of the slow power-on time of the coupling field, the response of a two-level system was simulated using QuTiP [8,9] for a $10\mu s$ power-on time and an instantaneous power-on time. Figure 3.12a shows the time dependence of the coupling strength that was used for the QuTip simulations. Figure 3.12b shows the evolution of the system for varying pulse times for an off-resonant coupling field. Figure 3.12c shows the evolution of the state of the system for an on-resonance $0.1ms$ pulse and figure 3.12d for an off-resonant pulse. These figures show that the state of the system precesses around the changing precession axis during the evolution. This has no effect on the final state of the system for an on-resonant pulse, but for an off-resonant pulse the final state of the system is significantly different from the instantaneous case; a slow power-on time maintains the frequency of the Rabi oscillation but changes the amplitude, as observed in figure 3.12b.

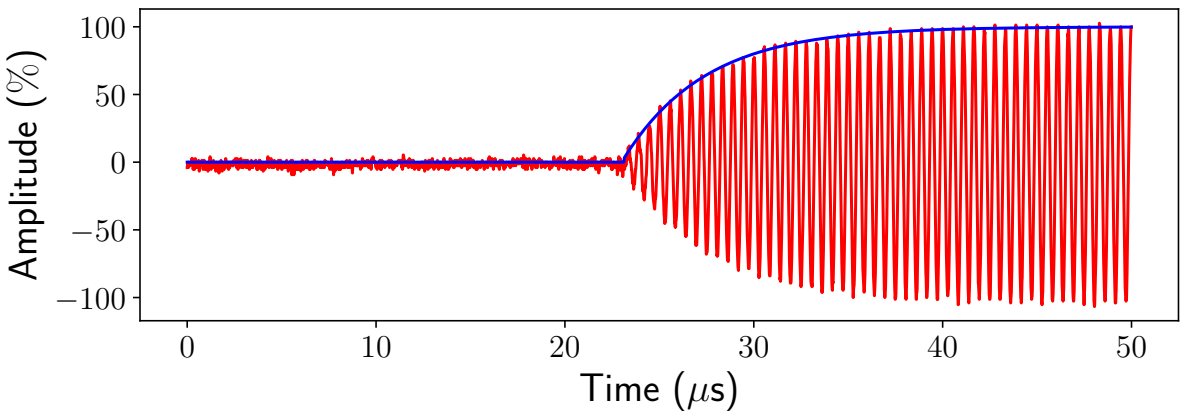


Figure 3.11: **The dependence of the amplitude of the RF field on time for an applied square pulse:** The RF field amplitude asymptotically approached a maximum with a shape of the form $(1 - e^{-t/\tau})$, where $\tau$ is the time constant. This non-instantaneous behaviour results from the resonance response of the coil.

To experimentally investigate the effect of adiabatic following the magnetic field was varied and the amplitude and frequency of the Rabi oscillation was recorded. Figure 3.13a and b show the example fitted Rabi oscillations when the system is off-resonance and on-resonance respectively. Figure 3.13c shows a Lorentzian dependence of the experimentally measured amplitude of the Rabi oscillations on the applied magnetic field. In the off-resonant case, the amplitude of the Rabi oscillations were lower than theoretically expected, which is consistent with the effect of adiabatic following. In contrast it was observed that there was no effect of adiabatic following when the system was on-resonance, this is because reducing the RF field power does not change the angle of the precession axis for an on-resonance coupling field. Figure 3.13d shows the $\sqrt{\Omega_{RF}^2 + \Delta^2}$ frequency response of the experimentally measured Rabi oscillations and shows good agreement with the theoretical values.

### 3.5.3 Inhomogeneous broadening

This section investigates the dependence of the on-resonance Rabi oscillation on the amplitude of the RF field. Figure 3.14c shows that the frequency of the on-resonance RF Rabi

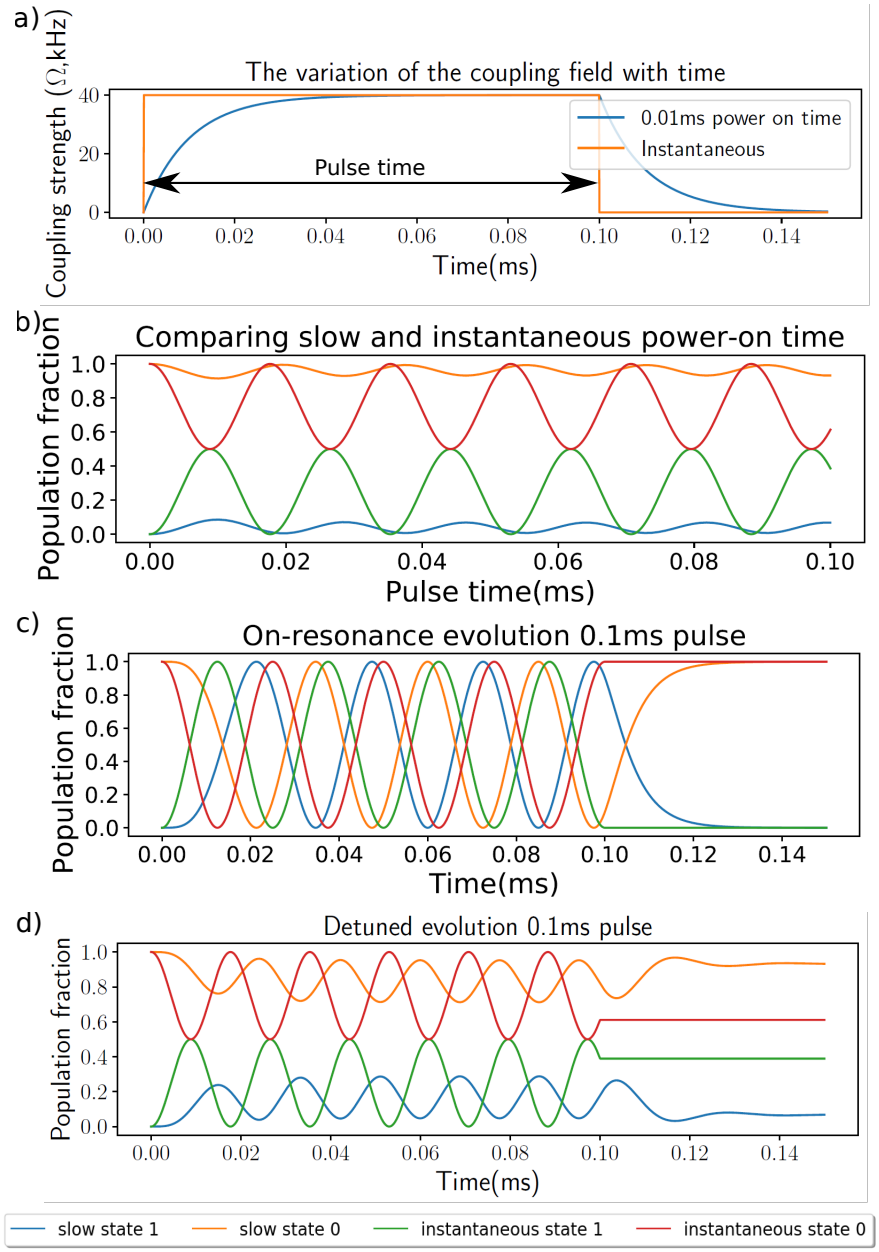


Figure 3.12: **Adiabatic following**: a) The dependence of the amplitude of the RF coupling pulse on time, b) as the pulse time is varied for a 0.01ms power on/off time the amplitude of the off-resonance response is reduced compared with the instantaneous pulse, c) the response of the system for an on-resonant $0.1ms$ pulse showing the state of the system during the evolution, d) the response of the system for an off-resonant $0.1ms$ pulse showing the state of the system during the evolution. A slow increase/decrease in the amplitude of the RF field results in adiabatic following of the state. For an instantaneous pulse the distribution between the states does not evolve after the pulse is powered off.

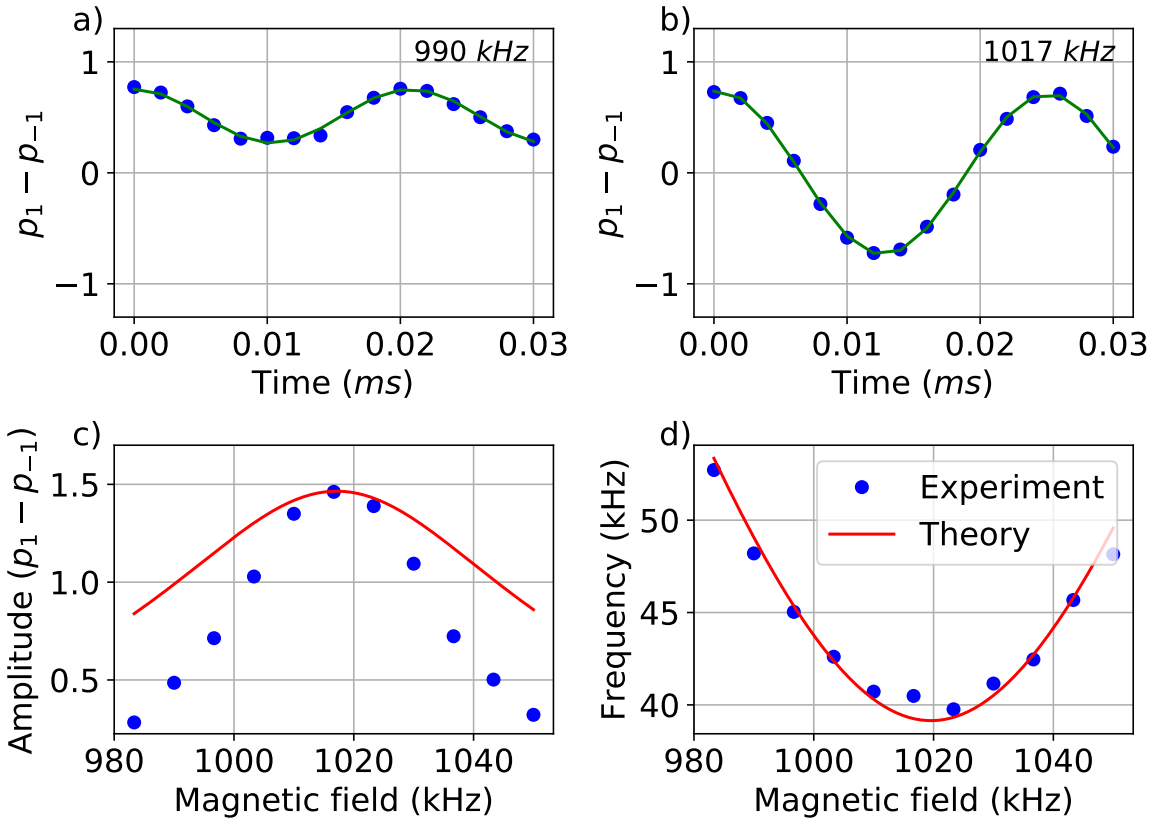


Figure 3.13: **The experimentally determined dependence of the Rabi oscillations on the magnetic field:** a) Example Rabi oscillation for off-resonant coupling (magnetic field= 990 $kHz$), b) example Rabi oscillation for on-resonant coupling (magnetic field= 1017 $kHz$), c) the dependence of the amplitude of the Rabi oscillations on the magnetic field (detuning), d) the dependence of the frequency of the Rabi oscillations on the magnetic field (detuning). At the resonance the Zeeman splitting is equal to the RF field frequency and this was used to calibrate the magnetic field.

oscillation has a linear dependence on the amplitude of the RF field, strongly agreeing with the theory discussed in section 2.2. Figure 3.14d shows that as the RF field amplitude increased the amplitude of the on-resonance RF Rabi oscillation asymptotically approaches a maximum, in contradiction with the theory presented in section 2.2. Theoretically, the amplitude of the on-resonance Rabi oscillations should be independent of the amplitude of the RF field. In practice, however, experimental systems exhibit inhomogeneous broadening of the frequency response due to the spatial extent of the cloud and the inhomogeneity of the bias field. At low amplitude, this results in only a small part of the cloud being on-resonance and thus a reduced amplitude of the Rabi oscillation. As the RF field power increases, the frequency response of the system broadens due to the power broadening effect [103] and consequently more of the cloud will contribute to the system response.

The amount of inhomogeneous broadening can be estimated from the data presented in figure 3.14d by analysing the overlap integral between the frequency distribution of the states of the atoms (the inhomogeneous broadening) and the power broadening. Based on this the inhomogeneous broadening in this study was found to be of the order of $\approx 5kHz$. This is attributable to the inhomogeneity in the bias field (that determines the resonant frequencies of the atoms) across the spatial extent of the atomic cloud. The inhomogeneity of the RF field power across the atomic cloud only contributes towards the dephasing of the Rabi oscillation; this is because the RF power only affects the frequency of the response of the system and not the amplitude.

## 3.6 Raman coupling

To investigate interference effects between competing coherent paths, next nearest neighbour coupling is implemented using two-photon Raman transitions, between the $m_F = -1$ and $m_F = +1$ states, allowing the dynamics of a fully connected network (FCN) to be re-

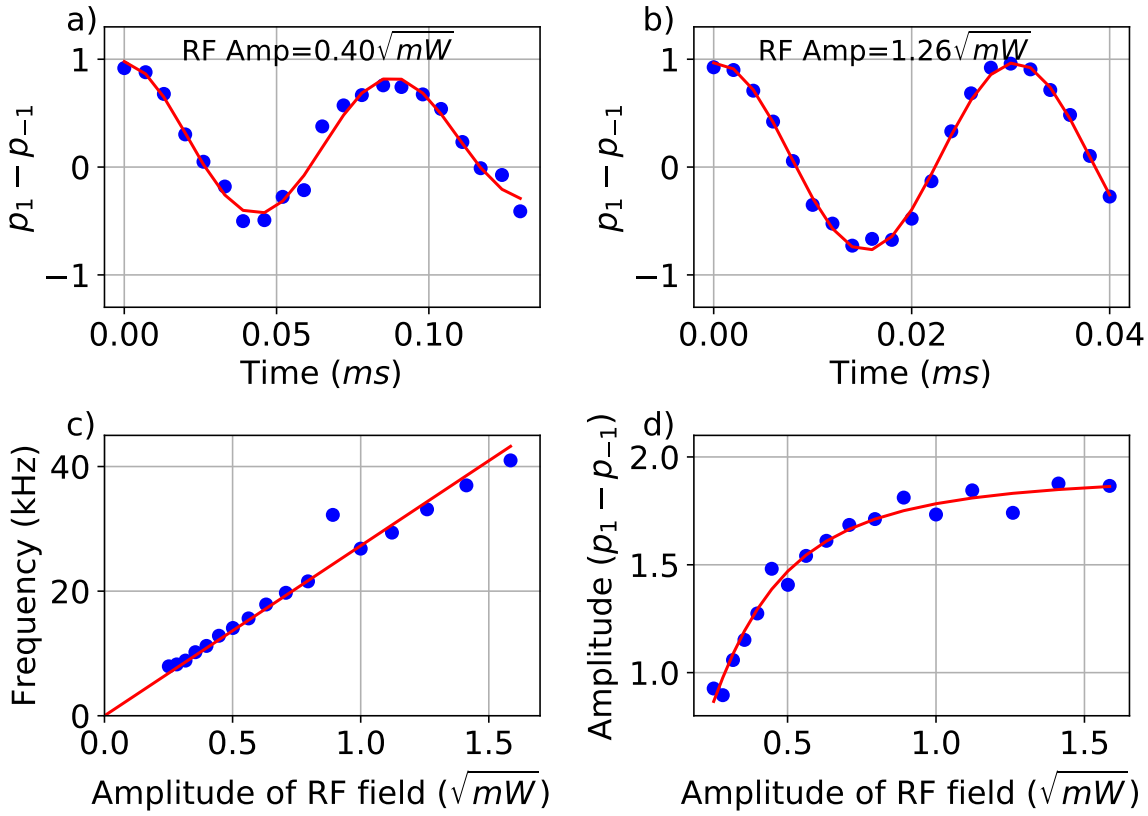


Figure 3.14: **The dependence of the Rabi oscillations on the amplitude of the RF field:** a) example on-resonance Rabi oscillation for $0.4mW$ of RF power, b) example on-resonance Rabi oscillation for $1.26mW$, c) the dependence of the frequency of the on-resonance Rabi oscillations measured experimentally on the amplitude of the RF field, d) the dependence of the amplitude of the on-resonance Rabi oscillations on the amplitude of the RF field. The on-resonance Rabi frequency increases linearly with RF amplitude but the amplitude of the on-resonance Rabi oscillation asymptotically approaches a maximum due to inhomogeneous broadening. The amplitude of the RF field is the amplitude of the output from the frequency generator, which is proportional to the amplitude of the RF field at the atoms.

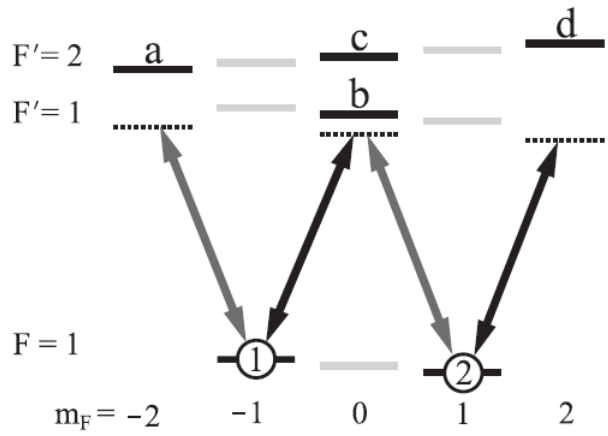


Figure 3.15: **Energy levels of the Raman transition:** The energy levels for the D1 line of rubidium 87 showing the ground states (1,2) and the excited states (a,b,c,d) that interact with the Raman beams. From K.C.Wright et al [11]

alised. Presented in the next section is a theoretical study of the Raman transition adapted from a paper by K.C.Wright et al [11] entitled "Raman coupling of Zeeman sub-levels in an alkali metal Bose-Einstein condensate". The discussion begins with a theoretical description of the Raman transitions, then the optimum frequency of the Raman beams is discussed with reference to the two-photon Raman-Rabi frequency and the single photon scattering rate. Finally the additional complication of light shifts resulting from the application of the Raman beams is discussed. Initial experimental results are also presented illustrating the key experimental difficulties associated with the implementation of Raman transitions.

### 3.6.1 Theoretical description

The Raman transitions used in this study are realised using intermediate states near the D1 transition of rubidium 87. The energy level diagram in figure 3.15 shows the states involved in the two-photon Raman transition. Two opposite handed ($\sigma_+$ and $\sigma_-$) beams coherently couple states that have $\Delta m_F = 2$ via an intermediate excited state. The bias field sets the

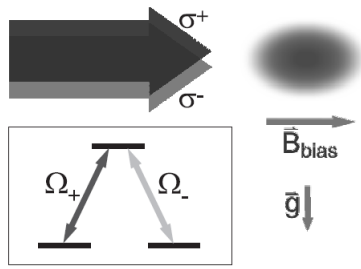


Figure 3.16: **Quantisation axis:** The geometrical relationship between the Raman beams and the bias field (quantisation axis). From K.C.Wright et al [11]

quantisation axis of the circularly polarised Raman beams, as shown in figure 3.16. The $\sigma_+$ beam coherently couples the levels $m_F = -1$ and $m_{F'} = 0$ and the $\sigma_-$ beam couples the $m_F = 1$ and $m_{F'} = 0$ levels. The Raman beams are significantly detuned resulting in negligible population in the excited states and therefore negligible single photon scattering.

The Raman transitions between the $m_F = -1$ and $m_F = +1$ states can be represented in a Hamiltonian by initially including the highly detuned intermediate state $m_{F'} = 0$. The rotating wave approximation is then applied removing the oscillating terms and finally adiabatic elimination is used to remove the $m_{F'} = 0$ intermediate state [119]. The resulting Hamiltonian for coupling between the $m_F = -1$ and $m_F = +1$ levels is thus

$$H = \hbar \begin{bmatrix} \frac{\delta}{2} & \eta_{12}^{bc}\sqrt{I_- I_+} \\ \eta_{12}^{bc}\sqrt{I_- I_+} & -\frac{\delta}{2} \end{bmatrix} \tag{3.6}$$

where $\delta$ is the detuning between the 2 Raman beams and is defined as

$$\delta = (E_1 - E_2)/\hbar - (\omega_+ - \omega_-) \tag{3.7}$$

where $\omega_+$ is the angular frequency of the $\sigma_+$ Raman beam and $\omega_-$ is the angular frequency of the $\sigma_-$ Raman beam. $I_+$ is the intensity of the $\sigma_+$ Raman beam and $I_-$ is the intensity

of the $\sigma_-$ Raman beam. The coefficient $\eta_{12}^{bc}$ is the sum of the strength of the two-photon coupling between the different paths connecting the ground states (1,2) via the two excited states, and is defined as

$$\eta_{12}^{bc} = -\frac{d_{D1}^2}{2c\epsilon_0}\left(\frac{c_1^b c_2^b}{\Delta^{(b)}} + \frac{c_1^c c_2^c}{\Delta^{(c)}}\right) \tag{3.8}$$

where $d_{D1}$ is the transition dipole matrix element for the D1 line, c is the speed of light, $\epsilon_0$ is the electric constant, $\Delta^{(n)}$ is the detuning for the level $n$, $c_x^y$ are the hyperfine dipole matrix elements between state '$x$' and '$y$' that are defined in figure 3.15. The two-photon Rabi frequency of the coherent Raman coupling is

$$\bar{\Omega} = 2\eta_{12}^{bc}\sqrt{I_+ I_-} \tag{3.9}$$

### 3.6.2 Determining the optimum detuning

To determine the optimum detuning relative to the intermediate state of the Raman beams, the two-photon Raman-Rabi frequency and the one-photon scattering rate is plotted for frequencies close to the $F = 1$ to $F' = 1$ and $F = 1$ to $F' = 2$ transitions. Figure 3.17a shows interference due to contribution to the Raman-Rabi frequency from state b ($F = 1$ to $F' = 1$) and state c ($F = 1$ to $F' = 1$). Between the transitions the contributions interfere constructively and outside this region destructively. For large detunings the dependence of the Raman-Rabi frequency on the detuning has a $1/\Delta^2$ dependence. Figure 3.17b shows the dependency of the scattering rate on the detuning. The scattering rate has a $1/\Delta^2$ dependency for large detunings. Figure 3.17c shows the ratio of the Raman-Rabi frequency to the scattering rate. There are two maxima, one at $\approx 252MHz$ and the other at $-661Mhz$. For large detunings, far from the transitions, the ratio is a constant due to the $1/\Delta^2$ dependency for the Raman-Rabi frequency and scattering rate. The peak at $252MHz$ is chosen for this

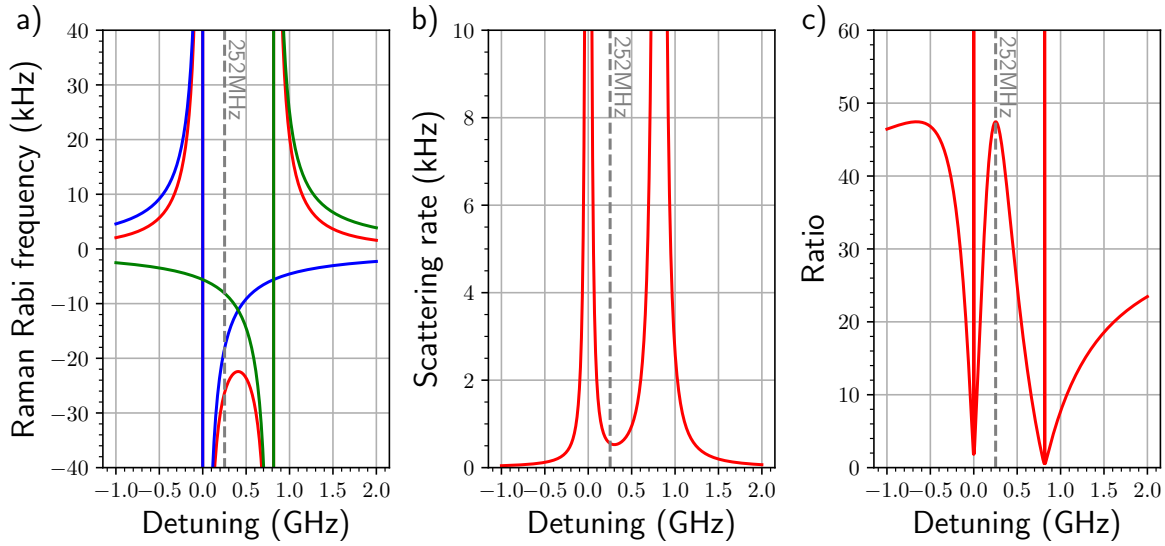


Figure 3.17: **Finding the optimum detuning:** a) Raman coupling frequency, b) scattering rate and c) modulus of the ratio dependence upon the detuning of the Raman laser for the D1 transition in rubidium 87 at an intensity of $10mW/cm^2$ for each beam. The detuning of the Raman laser is taken relative to the transition frequency corresponding to the $F = 1$ to $F' = 1$ transition. The second resonance corresponds to the $F = 1$ to $F' = 2$ transition frequency (detuning $= 814.5MHz$). The red line corresponds to the total, the blue is the contribution from the $F = 1$ to $F' = 1$ transition and the green is the contribution from the $F = 1$ to $F' = 2$ transition.

experiment because it has a much higher Raman-Rabi frequency for a given power input and thus requires more manageable laser power. The optimum detuning ($\approx 252MHz$) is shifted towards the $F = 1$ to $F' = 1$ state due to the larger scattering rate from the $F = 1$ to $F' = 2$ state.

The calculated optimum detuning varies by $\approx 40kHz$ over a range of Raman beam power from $1mW/cm^2$ to $50mW/cm^2$. In addition the ratio of the Raman-Rabi frequency to the scattering rate near the optimum detuning does not significantly vary if the laser frequency drifts by a small amount (therefore reducing the effect of laser frequency instabilities).

### 3.6.3 Light shifts

The energies of the $m_F$=+1 and $m_F$=-1 states are also changed (light shifted) as a result of the single photon coupling of the Raman beams. The light shift lifts the degeneracy of the nearest neighbour resonant transition frequencies, as shown in figure 3.18, and thus makes the RF coupling field no longer resonant. The light shift is equivalent to shifting the central state by $\frac{\tilde{\alpha}}{2}$ where

$$\tilde{\alpha} = I_-(\chi_1^a + \chi_2^{bc}) + I_+(\chi_1^{bc} + \chi_2^d) \tag{3.10}$$

where $I_-$ is the intensity of the $\sigma_-$ beam, $I_+$ is the intensity of the $\sigma_+$ beam and

$$\begin{aligned}
\chi_1^a &= -\frac{d_{D1}^2}{2c\epsilon_0}(\frac{(c_1^a)^2}{\Delta^{(a)}}) \\
\chi_1^{bc} &= -\frac{d_{D1}^2}{2c\epsilon_0}(\frac{(c_1^b)^2}{\Delta^{(b)}} + \frac{(c_1^c)^2}{\Delta^{(c)}}) \\
\chi_2^{bc} &= -\frac{d_{D1}^2}{2c\epsilon_0}(\frac{(c_2^b)^2}{\Delta^{(b)}} + \frac{(c_2^c)^2}{\Delta^{(c)}}) \\
\chi_2^d &= -\frac{d_{D1}^2}{2c\epsilon_0}(\frac{(c_2^d)^2}{\Delta^{(ad}})
\end{aligned} \tag{3.11}$$

and the detunings are equal to

$$\begin{aligned}
2\Delta^{(a)} &= (2E_a - E_1 - E_2)/\hbar - (3\omega_- - \omega_+) \\
2\Delta^{(b)} &= (2E_b - E_1 - E_2)/\hbar - (\omega_- + \omega_+) \\
2\Delta^{(c)} &= (2E_c - E_1 - E_2)/\hbar - (\omega_- + \omega_+) \\
2\Delta^{(d)} &= (2E_d - E_1 - E_2)/\hbar - (3\omega_+ - \omega_-)
\end{aligned} \tag{3.12}$$

These equations can be used to determine the value of the light shift for different detunings (figure 3.19). The value of the light shift is zero midway between the transitions, therefore to minimise the effect of the light shift it is advantageous for the detuning of the Raman beams to be close to the frequency of this zero point.

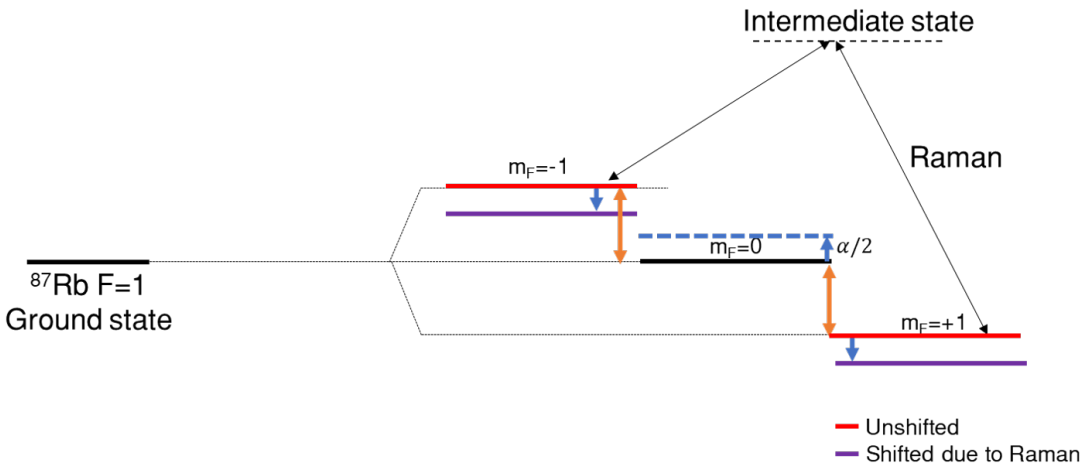


Figure 3.18: **The scalar light shift:** Single photon dressing results in light shifts moving the energy of the outer states. The antisymmetric shifts can be compensated using the frequency difference between the Raman beams and altering the resonance frequency of the RF field. The scalar light shift however cannot be compensated for as it is effectively moving the central state and creating a difference in the energy between the central state and the outer 2 states.

The comparison between the light shift and the Raman-Rabi frequency with changing Raman beam power at the optimum detuning is shown in figure 3.20. The light shift at the optimum detuning has a linear dependence on the intensity of the Raman beams and is always less than the Rabi frequency but of the same order. In addition the ratio between the scattering rate and the Raman-Rabi frequency at the optimum point does not have a dependency on the intensity, for the range $0 - 50mW/cm^2$.

### 3.6.4 Initial experimental results

Preliminary data was taken for the Raman transitions and showed promising results. This section will begin by discussing the experimental set-up required to investigate the Raman transition and then present a preliminary result for the measurement of the Rabi-Raman oscillation. Finally key experimental issues that arose from these initial experiments will be discussed.

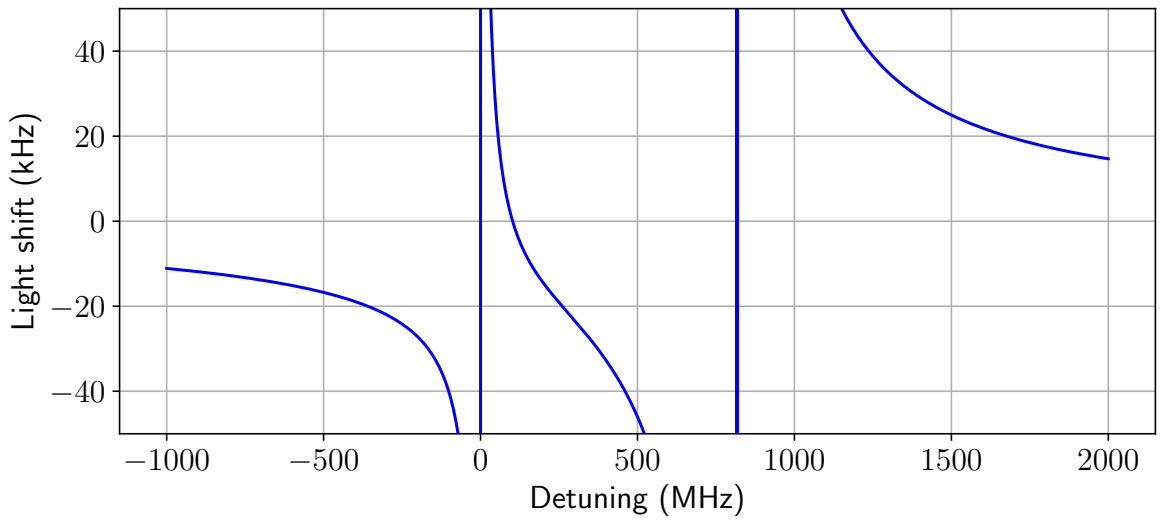


Figure 3.19: **Scalar light shift:** The dependence of the scalar light shift ($\frac{\tilde{\alpha}}{2}$) on the detuning for a beam intensity of $10mW/cm^2$ ($I_+ = I_- = 10mW/cm^2$).

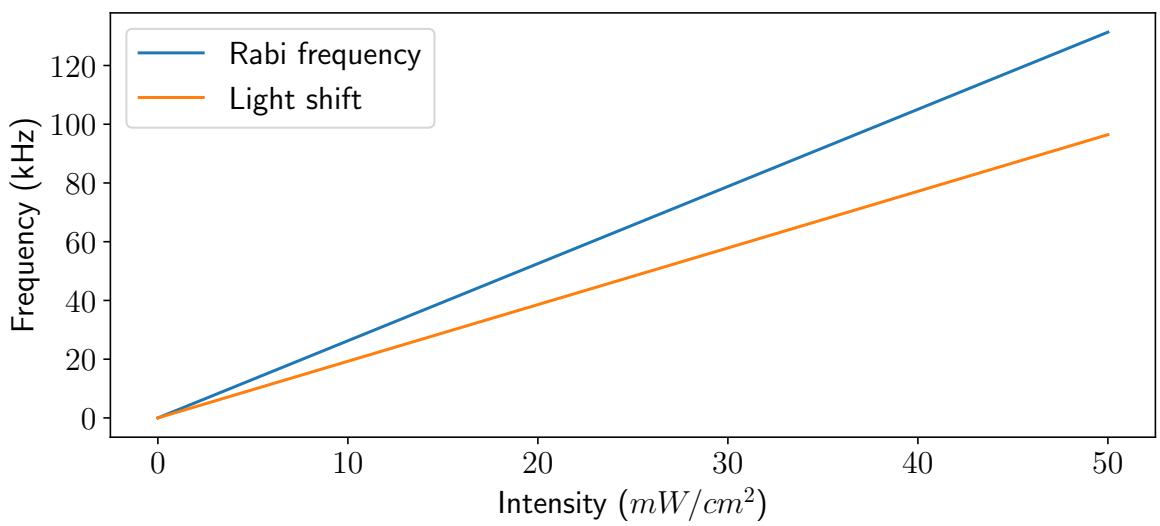


Figure 3.20: **The dependence of the scalar light shift on the intensity:** A comparison of the light shift and the Raman-Rabi frequency at the optimum point ($252MHz$) for different intensities ($I_+ = I_-$). The modulus of the Rabi frequency and the light shift is shown to allow for direct comparison, the value of the light shift is negative.

The experimental set-up is shown in figure 3.21. The two Raman beams were oppositely circularly polarised and the power and relative frequencies of the beams was controlled using acoustic optical modulators (AOMs). The 795nm laser was locked using a heated dichroic atom vapour laser lock (DAVLL) that allowed locking to the large detunings required. Phase coherence between the Raman beams was maintained by deriving the Raman beams from the same laser.

In more detail the beam generated by the laser was initially split with a small intensity going to the DAVLL lock. The beam was then further split using a half wave plate and a polarising beam cube which allowed control of the relative intensity of the $\sigma_+$ and $\sigma_-$ beams. Each of the beams was then passed though a double pass AOM arrangement that increased the frequency of the beams by $\approx 160MHz$ and allowed the frequency difference between the two beams to be set. The two beams were then overlapped on another polarising beam cube. After this point the two beams were linearly polarised at 90 degrees to each other. This overlapped beam was then coupled into the two polarisation axes of a fibre optic cable. At the output of the cable there was a quarter wave plate (QWP) that produced the required circularly polarised light. The resultant beam was parallel to the bias field that acted as the quantisation axis of the system causing the circularly polarised Raman beams to interact with the atoms as $\sigma_+$ and $\sigma_-$ beams.

Figure 3.22 shows a preliminary result for Raman coupling between the $m_F = 1$ and $m_F = -1$ states. The Raman laser frequency was set at the midpoint of the $F' = 1$ and $F' = 2$ excited states. The intensity of the $\sigma_+$ and $\sigma_-$ beams were both set to $5mW$. The detuning between the Raman beams was set to be twice the resonant frequency of the nearest neighbour coupling RF field. The Raman coupling time was varied and a $5kHz$ Raman-Rabi oscillation was recorded that had a small amplitude of population inversion. The population transfer was observed to be only between the $m_F = -1$ and $m_F = +1$ states

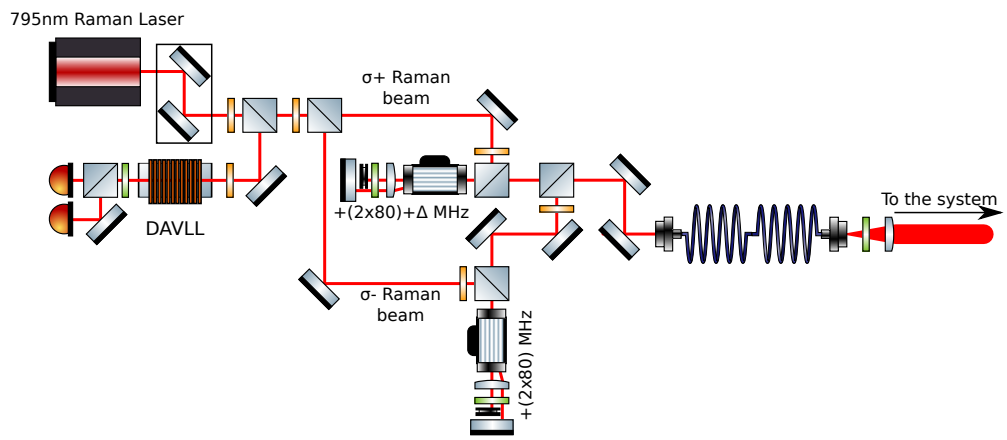


Figure 3.21: **Schematic for the Raman transition experimental set-up:** Two beams were generated with opposite circular polarisation and shifted by the frequency splitting between the $m_F = 1$ and $m_F = -1$ states. The laser was locked using a DAVLL lock.

and no population was observed in the central cloud ($m_F = 0$). The lack of population in the central state suggested that the scattering rate was negligible. The limited population inversion suggested that either the Raman coupling field was off-resonance or inhomogeneous broadening was present. The observed Raman-Rabi oscillation was also significantly damped and this may have been due to the decoherence caused by the Gaussian intensity profile of the Raman beams producing a spatially varying Rabi frequency across the atomic cloud.

Based on the preliminary data, it was concluded that the Raman-Rabi frequency would have to be increased and the decoherence reduced. This was so that future experiments could investigate interference effects, that require the Raman-Rabi frequency to be comparable to the on-resonance RF Rabi frequency, in a fully connected network.

## 3.7 Perturbation generation

The energy levels of the magnetic substates are set using an external bias field. The perturbations of the energy levels are introduced by modulating the bias field using the

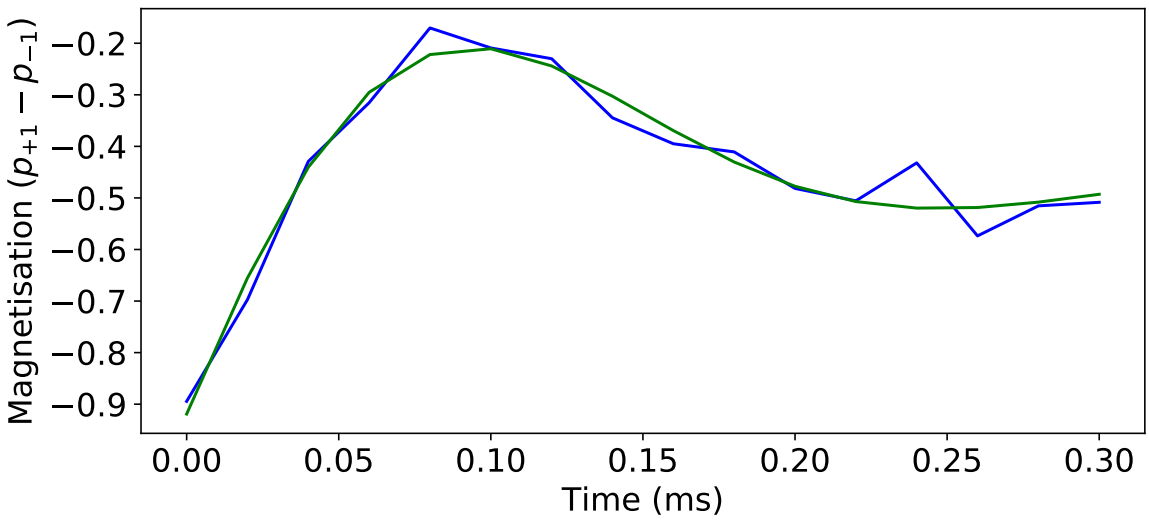


Figure 3.22: **Raman-Rabi oscillation:** A damped Rabi oscillation (frequency=3.25 ± 0.32$kHz$, amplitude=0.66 ± 0.10 and damping rate=0.11 ± 0.01$ms$) was observed for different Raman pulse times.

perturbation coil (shown in figure 3.4). Full control of the perturbation wave forms is achieved using a python script that is linked to an arbitrary waveform generator (AWG). The spectrum of the noise can then be shaped using software filters. The output of the AWG is connected to a voltage-to-current converter that maps the waveform directly onto the magnetic field using the perturbation coil.

To characterise the perturbation coil the voltage amplitude of a $50kHz$ waveform was varied and the corresponding current through the perturbation coil was measured, as shown in figure 3.23a. There was a linear relationship, bounded by $0V$ and $\approx 2.5V$, between the amplitude of the applied voltage and the current until at $\approx 4A$ the system saturated, corresponding to a perturbation amplitude of $\approx 180kHz$. The saturation arises because of a combination of the maximum voltage that can be applied to the power amplifier (that drives the perturbation coil) and the resistance of the coil.

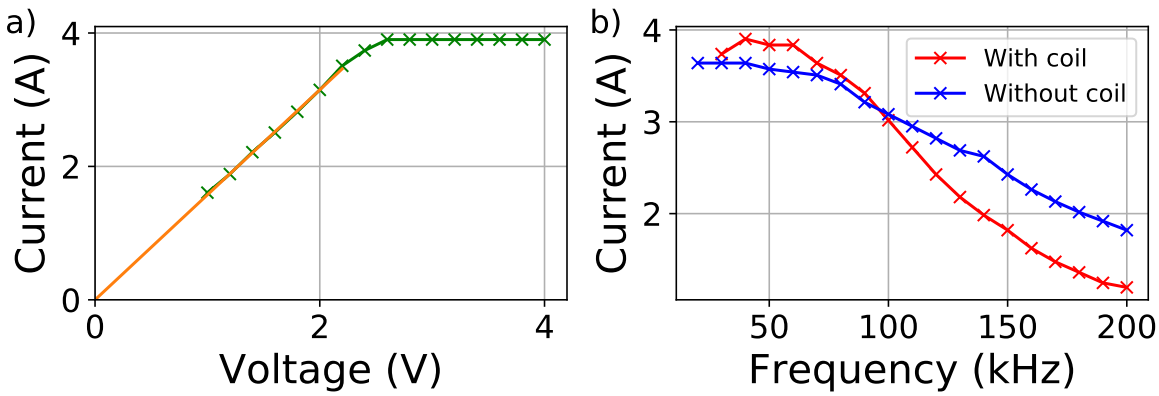


Figure 3.23: **Characterisation of the response of the perturbation coil driver:** a) shows the response of the current for a 50kHz sine wave, b) shows the response to changing frequency.

The frequency response of the perturbation coil was characterised by varying the frequency of a $2.5V$ waveform and recording the current through the coil, as shown in figure 3.23b. In addition, to determine what part of the perturbation coil system was limiting the response current, two configurations were tried, with the coil and without. The current in the circuit with the coil reduced rapidly for frequencies above $50kHz$ whereas without the coil there was a slow reduction in the current as the frequency was increased. The rapid reduction was due to the inductance and resistance of the coil, limiting the bandwidth. The slow reduction came from the limitations of the voltage-to-current converter. To increase the maximum amplitude the resistance of the perturbation coil circuit could be reduced however this would also reduce the bandwidth of the system.

## 3.8 Analysis

A typical absorption image of the three clouds, which were generated using the Stern-Gerlach measurement, is shown in figure 3.24. The populations of the three clouds can be determined from fitting the absorption images using three overlapping 2D Gaussians. For

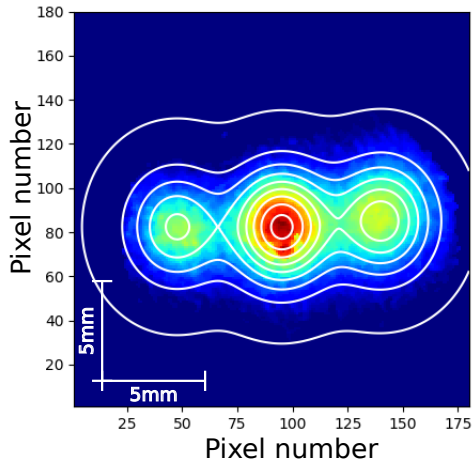


Figure 3.24: **Example absorption image:** An example image of the calibration shot, showing the three fitted 2D Gaussians.

every sequence of data a calibration image is used to provide the initial guesses for the fitting parameters used in the rest of the data sequence and determine the positions of the centres of the three clouds. The calibration image must have population in every state in order to give reliable fitting parameters for all three clouds even if the population in any of the clouds varies to zero during the data sequence.

Several fitting routines were tried in this study but the most successful was found to be the limited memory Broyden-Fletcher-Goldfarb-Shanno algorithm with bounds (L-BFGS-B). This algorithm was chosen from the available algorithms in the "minimize function" from the python library scipy.optimize. It is the only algorithm that both supports bounds and is optimised for problems where there is a large number of variables (as is the case in this study). It is based on calculating the gradient of the minimisation problem [120] in multiple dimensions. It is faster than other Newton optimisation methods because it uses multiple previous measurements of the gradient and variables to improve the directionality of the minimisation search. A fitting routine that incorporates bounds is necessary because

it makes the fitting routine faster and produces more reliable results, particularly for the case where there is likely to be a high variation of the amplitude of the clouds in the data-set.

## 3.9 Summary

A quantum network has been formed from the three magnetic substates of the $F = 1$ ground state of laser-cooled Rubidium 87 with the energy levels determined by the Zeeman effect (energy separation $\approx 1MHz$). The experimental system to cool 10 million atoms to $10\mu K$ has been described and the pumping procedure has been extensively characterised. The initial excitation has been prepared in the $F = 1$ $m_F = +1$ state with a purity of $> 95\%$, where purity is defined as the population of the atoms in the $F = 1$ $m_F = +1$ state relative to the total population in the $F = 1$ state. A Stern-Gerlach measurement system has been used to determine the transport through the network, and has been demonstrated as an accurate and reliable method to determine the population distribution. Nearest-neighbour coupling with an on-resonance frequency of $\approx 40kHz$ has been achieved and experimental imperfections such as adiabatic following and inhomogeneous broadening have been investigated experimentally and theoretically. The system can generate a perturbation that has an amplitude of up to $180kHz$ with a bandwidth of $0 - 100kHz$. This perturbation has the required amplitude to investigate the localisation, ENAQT and Zeno regimes discussed in the introductory chapter. Future improvements with next-nearest neighbour Raman coupling have been investigated and the required experimental realisation has been determined with preliminary results illustrating the requirement to reduce dephasing.

# CHAPTER 4

# SINGLE FREQUENCY MODULATION: EXPERIMENTAL RESULTS AND DISCUSSION

## 4.1 Introduction

As discussed in the introductory chapter the environment can be modelled as a noisy perturbation composed of many spectral components. To understand the effect of the noisy frequency distribution on transport through the network it is useful to investigate the response of the system to single frequency modulations, this will be experimentally investigated in this chapter. The resulting observations of multiphoton resonances and Bloch-Siegert shifts will be discussed and interpreted using Floquet theory. Finally an alternative interpretation using the sideband model will be discussed.

## 4.2 Theory of coupling between the dressed states

To model the influence of the modulation on the system, the Hamiltonian that determines the evolution of the state of the system will be first defined and then the effect of modulation will be investigated in the dressed state basis.

The system under investigation is a coupled three level system, as defined in equation 2.4, with the addition of a perturbation of the energy levels. Thus the Hamiltonian acting on the system, after the rotating wave approximation has been applied, with the addition of the perturbation of the system's energies $\delta(t)$ is

$$H = \hbar \begin{pmatrix} +\Delta + \delta(t) & \frac{\Omega_{RF}}{\sqrt{2}} & 0 \\ \frac{\Omega_{RF}}{\sqrt{2}} & 0 & \frac{\Omega_{RF}}{\sqrt{2}} \\ 0 & \frac{\Omega_{RF}}{\sqrt{2}} & -\Delta - \delta(t) \end{pmatrix} \tag{4.1}$$

For the case currently under investigation the perturbation is of the form $\delta(t) = \delta_0 \cos(\omega_m t)$, where $\delta_0$ is the modulation amplitude and $\omega_m$ is the angular frequency of the modulation.

To understand the effect of the modulation it is examined in the dressed state basis derived in section 2.2, where, in the absence of a perturbation, the Hamiltonian of the system is diagonal. The unitary matrix that performs this change of basis, equation 2.11, is applied to the modulated Hamiltonian, equation 4.1. This results in the Hamiltonian in the dressed state basis becoming

$$u^{-1}Hu = H' = \hbar \begin{pmatrix} \tilde{\Omega} + \cos\theta\delta_0\cos(\omega_m t) & \frac{\sin\theta}{\sqrt{2}}\delta_0\cos(\omega_m t) & 0 \\ \frac{\sin\theta}{\sqrt{2}}\delta_0\cos(\omega_m t) & 0 & \frac{\sin\theta}{\sqrt{2}}\delta_0\cos(\omega_m t) \\ 0 & \frac{\sin\theta}{\sqrt{2}}\delta_0\cos(\omega_m t) & -\tilde{\Omega} - \cos\theta\delta_0\cos(\omega_m t) \end{pmatrix}, \tag{4.2}$$

which directly shows the couplings between the dressed states due to the modulation field (the off-diagonal components of the Hamiltonian). Where $\hbar\tilde{\Omega}$ is the energy splitting of the dressed states and is equal to $\hbar\sqrt{\Delta^2 + \Omega_{RF}^2}$. In the absence of modulation ($\delta_0 = 0$) there is no coupling between the dressed states and the system state will oscillate around a rotated precession axis due to the coupling from the application of the RF field in the base state basis, as shown in figure 4.1a. Applying the modulation, however, results in both diagonal

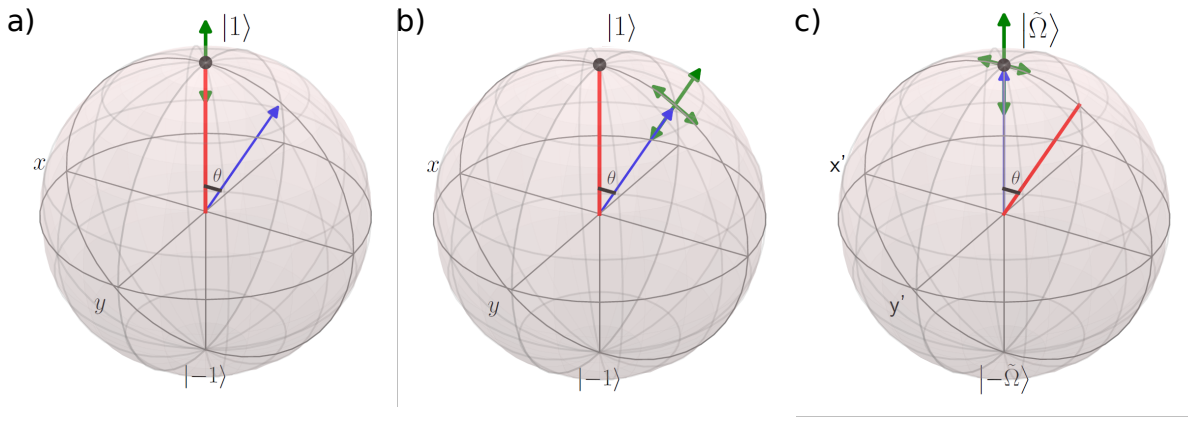


Figure 4.1: **Modulation on the Bloch sphere:** a) Oscillation of the bias field in the base state basis due to the modulation, showing the modulation (green), the precession axis (blue) and the quantisation axis (red) b) the oscillating bias field is decomposed into both a perpendicular and parallel modulation on the precession axis, and c) the resulting perpendicular and parallel coupling in the dressed basis arising from the modulation.

and off-diagonal oscillating components in the Hamiltonian in the dressed state basis, figure 4.1b,c and equation 4.2. The off-diagonal terms couple the dressed states together and consequently lead to oscillation of the populations of the base states. In this chapter the influence of these diagonal and off-diagonal coupling terms on the evolution of the system will be experimentally investigated.

## 4.3 Single frequency coupling between dressed states

This following discussion details the experimental procedure including the calibration of the modulation field. The evolution of the state for the fundamental resonance is then discussed and finally experimental results for the effect of varying the generalised Rabi frequency are presented.

### 4.3.1 Experimental procedure

The dressing of the states was experimentally achieved by detuning the frequency of the RF coupling relative to the transition frequency between the magnetic sub-levels. For the following series of experiments the detuning was set so that the energy of the dressed states ($\tilde{\Omega}$) was $\approx$ 60kHz (the on-resonance Rabi frequency was $\approx 40kHz$ and the detuning was $\approx 45kHz$). The RF field, that dresses the state, was initially ramped up for $0.02ms$ to reach it's maximum strength (to avoid any transient effects) and then the single frequency modulation was applied. A new calibration measurement was made for each data run in order to verify that the generalised Rabi frequency was in the range $58 - 60kHz$.

**Calibration of the modulation field** The modulation field was generated by the perturbation coil that was driven by a voltage-to-current converter that in turn was driven by an arbitrary waveform generator (AWG). As the output voltage of the AWG was set for each data run a calibration between this and the modulation field strength was required. The strength of the modulation field was calibrated using the experimental relationship between the amplitude of the modulation field and the on-resonance Rabi frequency of the fundamental ($\omega_m = \tilde{\Omega}$) resonance, discussed in section 4.6.2, and was determined to be $73.2 \pm 2.4kHz/V$. This gave a relative, as opposed to an absolute, measurement of the strength of the perturbation coil.

An absolute DC calibration of the modulation field was performed by realising the RF spectroscopy of the Zeeman splitting of the magnetic sub-levels. Since the modulation field was aligned with the bias field a change in the DC modulation field directly translated into a shift of the resonant RF frequency. This absolute calibration resulted in an inexplicably poor correlation between all the experimental data and the commonly accepted theory, therefore the previous relative calibration, using the experimentally obtained result, was adopted for

all the analysis. The difference between the two calibrations may be the result of either misalignment of the coil or a difference between the static and dynamic amplitude, possibly resulting from eddy currents in the chamber shielding the atoms at high frequencies.

### 4.3.2 Evolution under resonant modulation

To understand the effect of the off-diagonal coupling in equation 4.2 the frequency of the modulation was set to the resonance frequency of the energy splitting of the dressed states ($\omega_m = \tilde{\Omega}$). The time the modulation and the RF coupling fields was applied for was varied and the response of the magnetisation, $(p_1 - p_{-1})$, of the system is shown in figure 4.2.

As with the case of a single dressing by the RF coupling, low frequency full amplitude Rabi oscillations were observed due to the modulation of the system. The magnetisation response was fitted using a combination of a single low frequency ($Freq_{low}$) sinusoidally varying waveform (representing the coupling between the dressed states) and a much higher frequency ($Freq_{high}$) oscillation (corresponding to the frequency of the modulation) with the latter having symmetric sidebands at $\pm$ the low frequency. The experimental data was thus fitted using four components with the frequencies, $Freq_{low}$, $Freq_{high}$, $Freq_{high} - Freq_{low}$ and $Freq_{high} + Freq_{low}$. The physical origin of the modulation of the high frequency waveform that results in the sidebands is unknown, but has been observed both experimentally and in computational simulations and is therefore a topic for further study.

This response of the system can be theoretically understood by considering the effect of just the off-diagonal coupling terms in the Hamiltonian, as shown in figure 4.1c and represented in equation 4.2. The Hamiltonian in the dressed state basis used in the rest of this section is

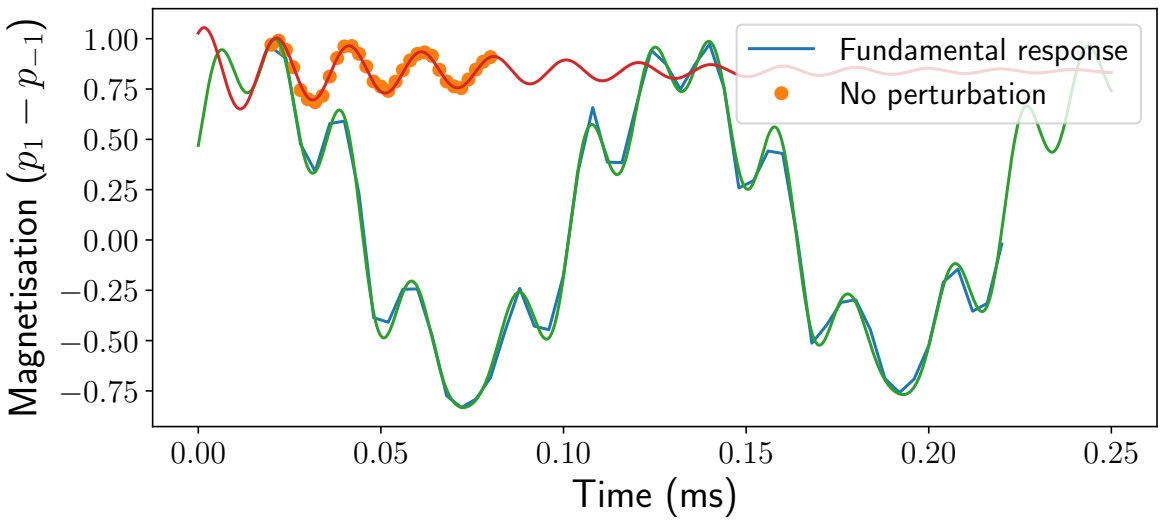


Figure 4.2: **Fundamental on-resonance response:** Experimental results showing an $8kHz$ ($Freq_{low}$) Rabi oscillation for the fundamental response, where the modulation frequency was equal to the generalised Rabi frequency ($\omega_m = \tilde{\Omega}$).

therefore

$$H = \hbar \begin{pmatrix} \tilde{\Omega} & \frac{2c}{\sqrt{2}}\cos(\omega_m t) & 0 \\ \frac{2c}{\sqrt{2}}\cos(\omega_m t) & 0 & \frac{2c}{\sqrt{2}}\cos(\omega_m t) \\ 0 & \frac{2c}{\sqrt{2}}\cos(\omega_m t) & -\tilde{\Omega} \end{pmatrix}, \tag{4.3}$$

where the diagonal modulation, shown in figure 4.1, has been ignored and $c$ is equal to $\frac{\delta_0 \sin(\theta)}{2}$. The coupling is dependent upon the angle of the precession axis, $\theta$, (where $\tan(\theta) = \Omega_{RF}/\Delta$) determined by the dressing by the RF coupling field. Without the initial RF coupling $\theta$ would equal zero and there would be no off-diagonal coupling between the dressed states.

The same treatment used in section 2.2 can be applied to equation 4.3 to remove the time dependence, resulting in

$$H = \hbar \begin{pmatrix} \Delta' & \frac{c}{\sqrt{2}} & 0 \\ \frac{c}{\sqrt{2}} & 0 & \frac{c}{\sqrt{2}} \\ 0 & \frac{c}{\sqrt{2}} & -\Delta' \end{pmatrix} = \hbar\Delta' J_z + \hbar c J_x \tag{4.4}$$

where $\Delta'$ is the detuning in the rotating dressed basis and equal to $\tilde{\Omega} - \omega_m$. The use of the rotating wave approximation is less valid in this case than when it was applied to the coupling arising from the RF field, because the coupling due to the modulation can be of the same order of magnitude as the resonance frequency of the modulation. Finally the Hamiltonian can be diagonalised, as in section 2.2, by transferring the system to a doubly dressed frame [121] and from this the characteristics of the doubly dressed Rabi oscillations can be determined. The Rabi oscillation between the dressed states is thus equal to

$$p_{+\tilde{\Omega}} - p_{-\tilde{\Omega}} = 1 - \frac{2\Omega_c^2}{\Delta'^2 + c^2} \sin^2(\sqrt{\Delta'^2 + c^2} t/2) \tag{4.5}$$

where $p_{+\tilde{\Omega}} - p_{-\tilde{\Omega}}$ is the magnetisation in the dressed basis. The oscillation of the population in the dressed states leads to oscillation of the population of the base states. When the system is transformed from the dressed state basis to the base state basis the frequency of the coupling between the dressed states is also present in the oscillation of the population of the base states and therefore the coupling frequency resulting from the dressed states can be inferred. The coupling between the dressed states is observed as the low frequency oscillation between the base states in figure 4.2.

The high frequency oscillation in figure 4.2 was observed to be in-phase with the frequency of the modulation applied to the system. Simulations have suggested that changing the phase

of the modulation may result in a change of the shape of the system resonances when the driving frequency becomes comparable with that of the Rabi frequency associated with the modulation.

### 4.3.3 Varying the generalised Rabi frequency

To understand the influence of the angle ($\theta$) on the on-resonance ($\omega_m = \tilde{\Omega}$) system dynamics, the generalised Rabi frequency ($\tilde{\Omega}$) was varied. The generalised Rabi frequency was controlled by altering the detuning of the frequency of the RF coupling field relative to the resonance frequency corresponding to the energy splitting resulting from the application of the bias field. The frequency of the modulation was kept equal to the altered generalised Rabi frequency and the amplitude of the modulation was kept constant. The dependence of the measured on-resonance Rabi frequency, which results from the application of the modulation, on the generalised Rabi frequency of the RF coupling is presented in figure 4.3. As discussed previously, the Rabi frequency of the response was found to be equal to $\sqrt{\Delta'^2 + c^2}$, therefore the on-resonance ($\Delta' = 0$) Rabi frequency of the response is equal to $c$ which is equal to $\frac{\delta_0 \sin(\theta)}{2}$ where $\sin(\theta) = \frac{\Omega_{RF}}{\tilde{\Omega}}$. The theoretical response therefore should be $\frac{\delta_0 \Omega_{RF}}{2\tilde{\Omega}}$. The experimental data was thus fitted using the relationship $y = (a/x)$ where $a$ was found to be $436 \pm 5kHz^2$. A theoretically based value for this was also determined using typical experimental measurements of the relevant parameters. The result was $\frac{\delta_0 \Omega_{RF}}{2} = 430 \pm 15kHz^2$ ($\Omega_{RF} = 39.2 \pm 0.3kHz$, $\delta_0 = 22.0 \pm 0.7kHz$) and this is in excellent agreement with the experimentally determined value.

For low generalised Rabi frequencies the Rabi frequency of the response diverges from the above relationship. This could be due to beating between the low frequency Rabi oscillation and the high frequency oscillation causing difficulties in fitting the experimental data. In this regime the application of the RWA for the modulation is also less valid because the Rabi

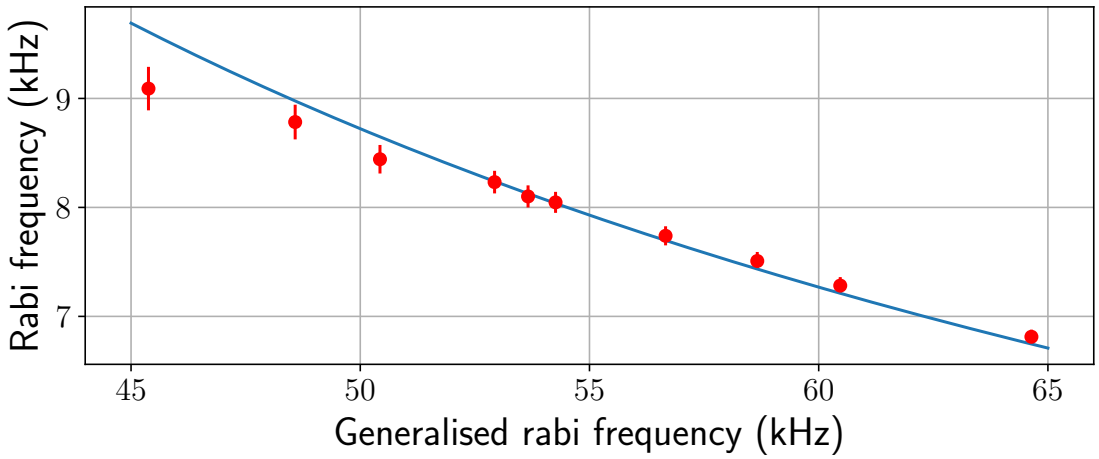


Figure 4.3: **The effect of varying the generalised Rabi frequency:** The frequency of the measured Rabi oscillations plotted against the generalised Rabi frequency.

frequency is of the same order as the on-resonance modulation frequency. Discrepancies may also result from the lack of stability of the bias field that alters the generalised Rabi frequency over the measurement time.

## 4.4 Sub-harmonic resonances

Besides the main resonance at $\omega_m = \tilde{\Omega}$, further resonances were observed when the modulation frequency was equal to integer fractions of the generalised Rabi frequency, as shown in figure 4.4. The additional resonances are interpreted as multiphoton resonances using the Floquet formalism [82, 83]. The Floquet formalism incorporates the parallel component in the dressed basis of the modulation, as defined in figure 4.1, and the impact of the breakdown of the rotating wave approximation (that was applied to the modulation in the Hamiltonian).

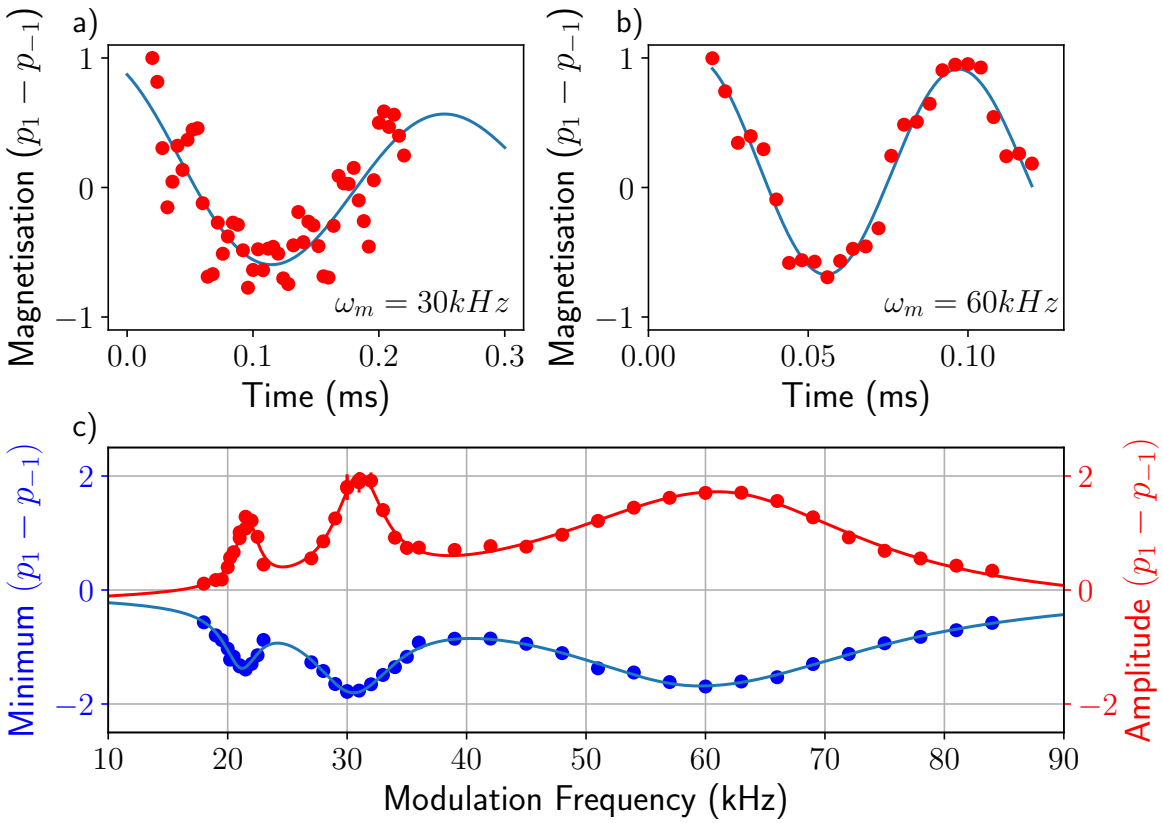


Figure 4.4: **Spectroscopy:** a) Rabi oscillation for $\omega_m = 30kHz$, b) Rabi oscillation for $\omega_m = 60kHz$, c) experimental results for the dependence of the amplitude of the Rabi oscillations on the modulation frequency, showing the fundamental and sub-resonances.

The experimental data, figure 4.4c, that shows the sub-resonance response of the system, was taken by scanning the frequency of the modulation. The modulation amplitude was kept constant ($\delta_0 = 37kHz$), and the amplitude of the low frequency Rabi oscillations of the system response was measured. The minimum of the magnetisation ($P_1 - P_{-1}$) was used as a measure of the amplitude of the resonances and to check the accuracy of the fitted amplitude. The fitting was achieved by fitting only the low frequency oscillations, as shown in figure 4.4a and b, as there were a large number of high frequency contributions for the higher order resonances that made the full fitting routine unreliable.

At lower modulation frequencies (less than 18kHz) Landau-Stuckelberg interference, as discussed in section 1.6.2, was observed. This obscured the features of the higher order resonances. The Rabi frequency of the fundamental ($\omega_m = \tilde{\Omega}$) resonance was larger than that of the 1st mode ($\omega_m = \tilde{\Omega}/2$), which itself was larger than that of the 2nd mode for a given modulation amplitude. The width of the sub-resonances was also smaller as the mode number increased.

Figure 4.5 illustrates the Floquet multiphoton interpretation of the resonances [82, 83]. The fundamental resonance ($\omega_m = \tilde{\Omega}$) is modelled as single photon coupling arising from the off-diagonal coupling terms in equation 4.2, figure 4.5a. The 1st mode response ($\omega_m = \tilde{\Omega}/2$) is a two photon coupling that arises from the combination of the off-diagonal ($\sigma^+$) and the diagonal ($\pi$) coupling, figure 4.5b. There are two transfer paths for the 3 photon 2nd mode resonance ($\omega_m = \tilde{\Omega}/3$), figure 4.5c and d. Figure 4.5c pictorially represents the 3 photon resonance that arises due to two photons from the diagonal coupling ($\pi$) and one photon from the off-diagonal coupling ($\sigma^+$). Figure 4.5d shows the other 3 photon contribution arising from just the off-diagonal terms ($\sigma^+$ and $\sigma^-$); the state absorbs a $\sigma^+$ photon exciting the state, followed by a $\sigma^-$ counter-rotating photon that de-excites the state and then finally another $\sigma^+$ photon re-excites the state. In the following section we shall investigate the

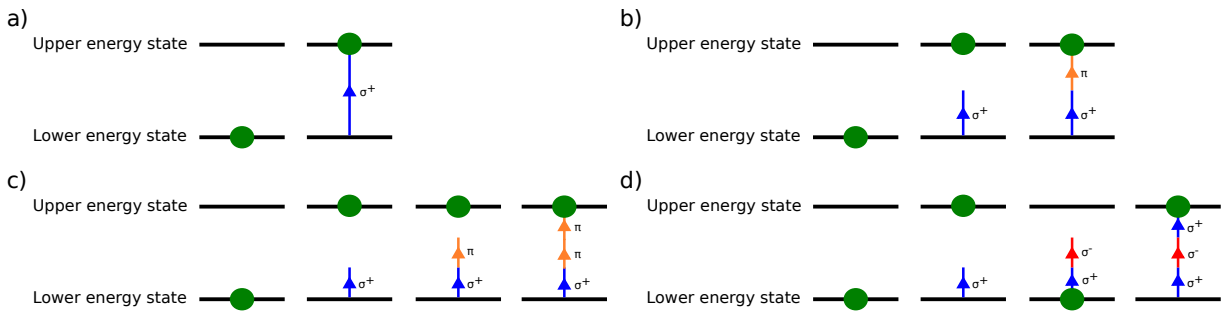


Figure 4.5: **Possible photon transition paths:** a) a 1 photon transition resulting from the absorption of a $\sigma^+$ photon, b) a 2 photon transition resulting from the absorption of a $\sigma^+$ and $\pi$ photon, c) a 3 photon transition resulting from the absorption of a $\sigma^+$, and two $\pi$ photons, d) a 3 photon transition can also result from the absorption of a $\sigma^+$, $\sigma^-$ and $\sigma^+$ photon.

experimental behaviour of these resonances and explain the calculations underpinning the Floquet theorem.

## 4.5 Floquet theory

To fully characterise and understand the behaviour of the multiphoton resonances experimentally observed in figure 4.5c, Floquet formalism was used. The photon interpretation of the Floquet theory is discussed in Shirleys' thesis [83] and the following derivation is adapted from this. Initially to simplify the derivation the system is generalised from a three-level to a two-level system, following this the Floquet formalism is applied and finally construction of the infinite Floquet matrix is discussed.

Using equation 4.2 the Hamiltonian in the dressed state basis can be expressed as

$$H = \hbar \begin{pmatrix} \tilde{\Omega} + 2g\cos(\omega_m t) & \frac{2c\cos(\omega_m t)}{\sqrt{2}} & 0 \\ \frac{2c\cos(\omega_m t)}{\sqrt{2}} & 0 & \frac{2c\cos(\omega_m t)}{\sqrt{2}} \\ 0 & \frac{2c\cos(\omega_m t)}{\sqrt{2}} & -\tilde{\Omega} - 2g\cos(\omega_m t) \end{pmatrix} = \hbar(\tilde{\Omega} + 2g\cos(\omega_m t))J_z + 2\hbar c\cos(\omega_m t)J_x \tag{4.6}$$

where the off-diagonal and diagonal terms, as defined in figure 4.1, have been redefined as g=$\cos\theta\delta_0/2$ and c=$\sin\theta\delta_0/2$ respectively. Observing that the generalised Rabi frequency is equal to $\sqrt{a^2+b^2}$ for both the $aJ_z + bJ_x$ three-level system and the $\frac{a}{2}\sigma_z + \frac{b}{2}\sigma_x$ two-level system, the mathematical derivation for the evolution of the system can be simplified to a two-level system which evolves according to the Hamiltonian

$$H = (\tilde{\Omega}/2 + g\cos(\omega_m t))\sigma_z + c\cos(\omega_m t)\sigma_x = \hbar \begin{bmatrix} \frac{\tilde{\Omega}}{2} + g\cos(\omega_m t) & c\cos(\omega_m t) \\ c\cos(\omega_m t) & -\frac{\tilde{\Omega}}{2} - g\cos(\omega_m t) \end{bmatrix} \tag{4.7}$$

which when expanded using the Euler relation results in

$$H = \hbar \begin{bmatrix} \frac{\tilde{\Omega}}{2} + \frac{g}{2}e^{i\omega_m t} + \frac{g}{2}e^{-i\omega_m t} & \frac{c}{2}e^{i\omega_m t} + \frac{c}{2}e^{-i\omega_m t} \\ \frac{c}{2}e^{i\omega_m t} + \frac{c}{2}e^{-i\omega_m t} & -\tilde{\omega_m} - \frac{g}{2}e^{i\omega_m t} - ge^{-i\omega_m t} \end{bmatrix} \tag{4.8}$$

Finally a phase transformation is applied to simplify the diagonal components, corresponding to a change in the zero energy reference

$$H = \hbar \begin{bmatrix} \tilde{\Omega} + ge^{i\omega_m t} + ge^{-i\omega_m t} & \frac{c}{2}e^{i\omega_m t} + \frac{c}{2}e^{-i\omega_m t} \\ \frac{c}{2}e^{i\omega_m t} + \frac{c}{2}e^{-i\omega_m t} & 0 \end{bmatrix} \tag{4.9}$$

The next part of the discussion will demonstrate how the evolution under this time dependent Hamiltonian can be represented equivalently using an infinite Floquet matrix and time repeating Floquet modes.

The Hamiltonian described by equation 4.9 is periodic with respect to time with period $T = \frac{2\pi}{\omega_m}$ ($H(t) = H(t+T)$), therefore Floquet formalism can be applied [76]. Floquet theory treats the modulation as a perturbation of the dressed states and is therefore only valid in cases where the modulation amplitude is small compared with the energy splitting of the dressed states ($\delta_0 < \tilde{\Omega}$). The system states evolve according to a unitary transformation that

is also periodic with the same time interval, $T$. The wave function, $\psi(t)$, that describes the system, evolves according to $\psi(t) = u(t,0)\psi(0)$, derived from the Schrodinger (equation 2.1), where

$$u(t,0) = e^{\frac{-i\int_0^t H(t)\ dt}{\hbar}} \tag{4.10}$$

As the unitary transformation is periodic, the wave function, $\psi(t) = \psi(t+T)$, is also periodic and can be reduced to solutions of the form [83]

$$\psi_\gamma = Ae^{(\frac{-i\epsilon_\gamma t}{\hbar})}\phi_\gamma(t) \tag{4.11}$$

where $\epsilon_\gamma$ is the energy of the corresponding dressed state $\gamma$ ($\epsilon_\alpha = \tilde{\Omega}$ and $\epsilon_\beta = 0$). The periodicity has been included into the Floquet modes $\phi_\gamma(t)$ that are eigenvectors of the Floquet Hamiltonian

$$H_F\phi_\gamma(t) = \epsilon_\gamma\phi_\gamma(t) \tag{4.12}$$

where

$$H_F = H(t) - i\hbar\frac{\delta}{\delta t} \tag{4.13}$$

The Floquet mode is periodic with time and the relationship between Floquet modes is

$$\phi_{\gamma,n}(t) = e^{\frac{int}{T}}\phi_\gamma(t) \tag{4.14}$$

which for every Floquet mode gives a physically equivalent state but with shifted energy $\epsilon_{\gamma,n} = \epsilon_\gamma + \hbar n/T$. The components of $\hat{H}_F$ and $\epsilon_{\gamma,n}$ are time-independent and are represented as an infinite dimensional time independent Hamiltonian with infinitely repeating energy structure. This will now be calculated.

The Floquet mode, $\phi_\gamma(t) = \phi_\gamma(t+T)$, is periodic and can be decomposed into a Fourier series that is infinite [82, 83] as shown in

$$\phi_\gamma(t) = \sum_n F_{xy}^n e^{in\omega_m t} \tag{4.15}$$

where

$$F_{xy}^n = \frac{\omega_m}{2\pi} \int_{-\pi/\omega_m}^{\pi/\omega_m} H_{xy} e^{-in\omega_m t}\ dt \tag{4.16}$$

where n denotes the Fourier mode and $x$ and $y$ are the system dressed states. $H_{xy}$ is the component of the Hamiltonian in the dressed state basis. The Floquet modes can be individually defined by an energy level of the dressed states and a photon number (n). The energies of the Floquet modes and the couplings between the Floquet modes are represented in an infinite Hamiltonian matrix. The matrix elements of the infinite Hamiltonian can be calculated from

$$\langle x_n | H_F | y_m \rangle = F_{xy}^{n-m} + n\omega_m \delta_{xy} \delta_{nm} \tag{4.17}$$

where $n - m$ is the difference in photon number between the Floquet modes. For example, the coupling between the Floquet states $\alpha_{-1}$ ($m = -1$) and $\alpha_0$ (n=0) is $\langle \alpha_0 | H_F | \alpha_{-1} \rangle = F_{00}^1$ where the equation is solved thus

$$\begin{aligned}
F_{00}^1 &= \frac{\omega_m}{2\pi} \int_{-\pi/\omega_m}^{\pi/\omega_m} H_{00} e^{-i\omega_m t}\ dt \\
F_{00}^1 &= \frac{\omega_m}{2\pi} \int_{-\pi/\omega_m}^{\pi/\omega_m} (\tilde{\omega_m} + g e^{i\omega_m t} + g e^{-i\omega_m t}) e^{-i\omega_m t}\ dt \\
F_{00}^1 &= \frac{\omega_m}{2\pi} \int_{-\pi/\omega_m}^{\pi/\omega_m} (\tilde{\Omega} e^{-i\omega t} + g + g e^{-2i\omega t})\ dt = g
\end{aligned} \tag{4.18}$$

Using equation 4.17 the infinite Hamiltonian for the Floquet modes is derived as

$$
\begin{array}{cc}
 & \begin{array}{cccccccccc} . & \alpha & \beta & \alpha & \beta & \alpha & \beta & \alpha & \beta & . \\ . & -1 & -1 & 0 & 0 & 1 & 1 & 2 & 2 & . \end{array} \\
\begin{array}{cc} . & . \\ \alpha & -1 \\ \beta & -1 \\ \alpha & 0 \\ \beta & 0 \\ \alpha & 1 \\ \beta & 1 \\ \alpha & 2 \\ \beta & 2 \\ . & . \end{array}
&
\begin{bmatrix}
. & . & . & . & . & . & . & . & . & . \\
. & -\omega_m + \tilde{\Omega} & 0 & g & c/2 & 0 & 0 & 0 & 0 & . \\
. & 0 & -\omega_m & c/2 & 0 & 0 & 0 & 0 & 0 & . \\
. & g & c/2 & \tilde{\Omega} & 0 & g & c/2 & 0 & 0 & . \\
. & c/2 & 0 & 0 & 0 & c/2 & 0 & 0 & 0 & . \\
. & 0 & 0 & g & c/2 & \omega_m + \tilde{\Omega} & 0 & g & c/2 & . \\
. & 0 & 0 & c/2 & 0 & 0 & \omega_m & c/2 & 0 & . \\
. & 0 & 0 & 0 & 0 & g & c/2 & 2\omega_m + \tilde{\Omega} & 0 & . \\
. & 0 & 0 & 0 & 0 & c/2 & 0 & 0 & 2\omega_m & . \\
. & . & . & . & . & . & . & . & . & .
\end{bmatrix}
\end{array}
\tag{4.19}
$$

where the header column and row represent the Floquet mode in terms of the associated base state energy level and the photon number. The $g$ terms in Shirley's theory are interpreted as $\pi$ photons, and the $c$ terms as $\sigma_-$ and $\sigma_+$ polarised photons [82, 83]. In the next section this infinite matrix will be used to understand the experimental response of the resonances.

## 4.6 The dependence of the fundamental and 1st mode resonances on the modulation amplitude

This section details the experimental investigation into the effect of the modulation amplitude on the 1st mode and fundamental resonances. The modulation amplitude was varied and the frequency of the modulation was scanned around both the fundamental and 1st

mode resonances. The results were then used to determine the dependence on the modulation amplitude of the Rabi frequency, width of the resonances, amplitude of the response and central frequencies of the resonances. The latter two relationships provide insights into inhomogeneous broadening and the Bloch-Siegert shift.

### 4.6.1 Experimental procedure

The frequency of the modulation was scanned around the fundamental and 1st mode resonances to determine the on-resonance response of the system for a set modulation amplitude. The low frequency responses of the magnetisation of the system for a set modulation amplitude and frequency were fitted using the equation

$$p_{+1} - p_{-1} = j - k \sin^2(\omega t/2) \tag{4.20}$$

where $j$ is the offset, $k$ is the amplitude and $\omega$ is the Rabi frequency of the response. This equation is based on the theoretical relationships derived in section 2.2.

### 4.6.2 On-resonance Rabi frequency dependence on modulation amplitude

The on-resonance Rabi frequency of the fundamental and first mode resonance is determined from the measurements discussed in section 4.6.1 and is shown in figure 4.6. The Rabi frequency of the response follows the theoretical dependence on the modulation frequency given by $\sqrt{(\omega_m - \omega_{res})^2 + b^2}$, where $\omega_{res}$ is the resonance modulation frequency of the mode (n) and $b$ is the on-resonance Rabi frequency. The experimentally determined on-resonance Rabi frequency ($b$), for a set modulation amplitude, was therefore determined by scanning the modulation frequency and fitting the result to this relationship.

As discussed in section 4.3.1 the fundamental resonance frequency response was used to calibrate the modulation amplitude. The fundamental resonance frequency response had a linear dependence on the modulation amplitude ($y = mx$, m=0.334 $\pm$ 0.002) and the 1st mode had a quadratic response ($y = ax^2$, a=(2.67 $\pm$ 0.01) $\times 10^{-3} kHz^{-1}$). The inclusion of all the experimental results of the frequency scan in the fitting procedure reduced the effect that an unstable bias field might have had on the results.

The experimental relationships between the modulation amplitude and the on-resonance Rabi frequency can be derived using the infinite Floquet matrix. The transition rates ($V_{pq}$) between Floquet states and the energies of the Floquet states ($V_{pp}$) can be calculated using the equations [82]

$$V_{pp}(E) = V_{pp} + \sum_i \frac{V_{pi}V_{ip}}{E - E_i^0} + \sum_i \sum_j \frac{V_{pi}V_{ij}V_{jp}}{(E - E_i^0)(E - E_j^0)} \tag{4.21}$$

$$V_{pq}(E) = V_{pq} + \sum_i \frac{V_{pi}V_{iq}}{E - E_i^0} + \sum_i \sum_j \frac{V_{pi}V_{ij}V_{jq}}{(E - E_i^0)(E - E_j^0)} \tag{4.22}$$

where the energy ($E$) is the energy of the final state and $V_{xy}$ is the matrix element of the infinite Floquet matrix. Multiphoton resonances can occur via intermediate Floquet states and can therefore be used to calculate the behaviour of the multiphoton transitions between the base states observed in the experimental data. The first term in equation 4.22 describes direct coupling due to one photon with no intermediate state. The second term describes two photon coupling with one intermediate state and the third term describes three photon coupling with two intermediate states. The first three resonances will now be discussed in detail.

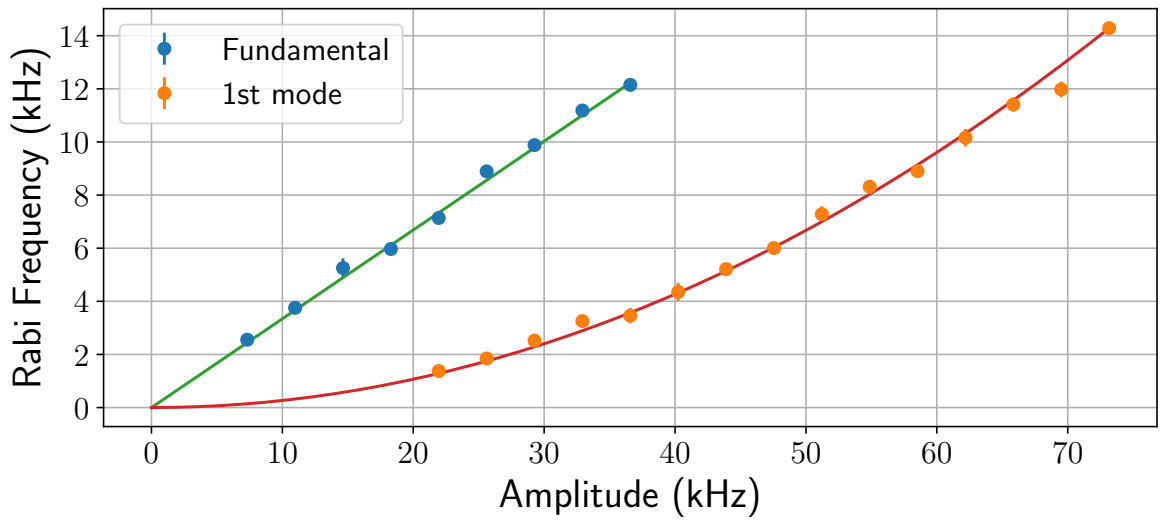


Figure 4.6: **Rabi frequency for the fundamental and 1st mode:** The coupling frequency dependence on the modulation amplitude for the fundamental and 1st mode.

### Fundamental single photon coupling

The theoretical response of the fundamental single photon Rabi frequency, derived from Floquet theory, has the same relationship as that of the doubly dressed Hamiltonian discussed previously (ignoring for the moment the higher order $V_{pp}$ Bloch-Siegert shift terms that will be discussed later). The two-state matrix determined from the Floquet equations 4.21 and 4.22 is

$$H = \hbar \begin{bmatrix} \omega_m - \tilde{\Omega} & c/2 \\ c/2 & 0 \end{bmatrix} \tag{4.23}$$

Theoretically the on-resonance Rabi frequency for the single photon resonance should be equal to $c$, which has the value $\delta_0 sin(\theta)/2$; this is consistent with previous experimental results in this study, section 4.3.2. Using typical experimental values, $c$ approximates to $\delta_0(0.334 \pm 0.002)kHz$ ($\Omega_{RF} = 39.2 \pm 0.3kHz$, $\tilde{\Omega} = 58.5 \pm 1.3kHz$). This value has been used for the calibration of the amplitude of the modulation field. The fitted data is in good agreement with the expected linear response.

### 1st mode two-photon coupling

The 1st mode two photon coupling can be derived by considering the infinite Floquet matrix, equation 4.24, where the blue pathway describes two photon coupling between the $\alpha_{-1}$ and the $\beta_{+1}$ Floquet states, via the $\alpha_0$ intermediate state that has energy $\tilde{\Omega}$

$$
\begin{array}{cc}
. & . \\
\alpha & -1 \\
\beta & -1 \\
\alpha & 0 \\
\beta & 0 \\
\alpha & 1 \\
\beta & 1 \\
\alpha & 2 \\
\beta & 2 \\
. & .
\end{array}
\begin{bmatrix}
. & . & . & . & . & . & . & . & . & . \\
. & -\omega_n + \tilde{\Omega} & 0 & g & c/2 & 0 & 0 & 0 & 0 & . \\
. & 0 & -\omega_n & c/2 & 0 & 0 & 0 & 0 & 0 & . \\
. & g & c/2 & \Omega & 0 & g & c/2 & 0 & 0 & . \\
. & c/2 & 0 & 0 & 0 & c/2 & 0 & 0 & 0 & . \\
. & 0 & 0 & g & c/2 & \omega_n + \tilde{\Omega} & 0 & g & c/2 & . \\
. & 0 & 0 & c/2 & 0 & 0 & \omega_n & c/2 & 0 & . \\
. & 0 & 0 & 0 & 0 & g & c/2 & 2\omega_n + \tilde{\Omega} & 0 & . \\
. & 0 & 0 & 0 & 0 & c/2 & 0 & 0 & 2\omega_n & . \\
. & . & . & . & . & . & . & . & . & .
\end{bmatrix}
\tag{4.24}
$$

This matrix shows the only path that couples the states via the $\alpha_0$ Floquet state. The coupling is physically understood to arise from the absorption of a $\pi$ photon followed by the absorption of a $\sigma_+$ photon, as shown and discussed in figure 4.5. Applying equation 4.22, with the energy of the intermediate state equal to $+\tilde{\Omega}$, the two photon coupling rate is equal to $V_{pi} = \frac{gc}{2(\omega_m - \tilde{\Omega})}$, where $\tilde{\Omega}$ is equal to $2\omega_m$, if the Bloch-Siegert shifts are not included. The Hamiltonian matrix for the two photon case is therefore

$$
H = \hbar \begin{bmatrix} -\omega_m + \tilde{\Omega} & -cg/2\omega_m \\ -cg/2\omega_m & +\omega_m \end{bmatrix}
\tag{4.25}
$$

and thus the on-resonance Rabi frequency is $cg/\omega_m$ for the two photon transition. Using $c = \delta_0 \sin(\theta)/2$ and $g = \delta_0 \cos(\theta)/2$ this results in a coupling of $\frac{\Omega_{RF}\Delta}{4\tilde{\Omega}^2\omega_m}\delta_0^2$. Using typical experimental values this approximates to $a\delta_0^2$, where $a = (4.3 \pm 0.1) \times 10^{-3} kHz^{-1}$ (using $\Omega_{RF} = 39.2 \pm 0.3kHz$, $\tilde{\Omega} = 58.5 \pm 1.3kHz$). This is 50% higher than the experimentally determined value of $a = (2.67 \pm 0.01) \times 10^{-3} kHz^{-1}$ obtained by fitting the response of the 1st mode on-resonance Rabi frequency, shown in figure 4.6. This discrepancy could be caused by the modulation no longer being considered as a perturbation of the RF dressed system for the high amplitude modulations associated with observing the 1st mode resonance, and therefore the Floquet theory breaking down. In addition the Floquet formalism is only valid for cases where ($2\omega_m \approx \tilde{\Omega}$), however in these results the shift of the energy level due to the Bloch-Siegert effect is significant and thus this relationship is no longer valid. Also at higher modulation amplitudes, as the Rabi frequency approached that of the driving frequencies, significant beating between the frequency components was observed and this could have distorted the fit.

### 2nd mode three photon coupling

The three photon case is more complex than the one and two photon cases as there are two paths that can connect the two Floquet states that have a three photon energy difference (for example $\alpha_{-1}$ and $\beta_2$ via the intermediate states [$\beta_0$ and $\alpha_{+1}$] and [$\alpha_0$ and $\alpha_{+1}$]). This corresponds to either the absorption of two $\pi$ photons and a $\sigma_-$ photon or the absorption of

a $\sigma_-$, followed by a $\sigma_+$ and finally a $\sigma_-$ photon as shown in

$$
\begin{array}{cc}
\cdot & \cdot \\
\alpha & -1 \\
\beta & -1 \\
\alpha & 0 \\
\beta & 0 \\
\alpha & 1 \\
\beta & 1 \\
\alpha & 2 \\
\beta & 2 \\
\cdot & \cdot
\end{array}
\begin{bmatrix}
\cdot & \cdot & \cdot & \cdot & \cdot & \cdot & \cdot & \cdot & \cdot & \cdot \\
\cdot & -\omega_n + \tilde{\Omega} & 0 & g & c/2 & 0 & 0 & 0 & 0 & \cdot \\
\cdot & 0 & -\omega_n & c/2 & 0 & 0 & 0 & 0 & 0 & \cdot \\
\cdot & g & c/2 & \tilde{\Omega} & 0 & g & c/2 & 0 & 0 & \cdot \\
\cdot & c/2 & 0 & 0 & 0 & c/2 & 0 & 0 & 0 & \cdot \\
\cdot & 0 & 0 & g & c/2 & \omega_n + \tilde{\Omega} & 0 & g & c/2 & \cdot \\
\cdot & 0 & 0 & c/2 & 0 & 0 & \omega_n & c/2 & 0 & \cdot \\
\cdot & 0 & 0 & 0 & 0 & g & c/2 & 2\omega_n + \tilde{\Omega} & 0 & \cdot \\
\cdot & 0 & 0 & 0 & 0 & c/2 & 0 & 0 & 2\omega_n & \cdot \\
\cdot & \cdot & \cdot & \cdot & \cdot & \cdot & \cdot & \cdot & \cdot & \cdot
\end{bmatrix}
\tag{4.26}
$$

The three photon coupling arising from the three off-diagonal photons (ccc) involves the intermediate states, $E_i = \omega_m + \tilde{\Omega}$, and $E_j = 0$ hence the transition rate is $ccc/[8(\omega_m - \tilde{\Omega})(2\omega_m)]$. For the case of two $\pi$ photons and a $\sigma_-$ photon the intermediate states are $Ei = \omega_m + \tilde{\Omega}$ and $Ej = \tilde{\Omega}$ resulting in a transition rate contribution of $ggc/[2(\omega_m - \tilde{\Omega})(2\omega_m - \tilde{\Omega})]$. These transition rates due to the two paths are summed resulting in the Hamiltonian

$$
H = \hbar \begin{bmatrix} -\omega_m + \tilde{\Omega} & \frac{ccc}{-32\omega_m^2} + \frac{gcg}{4\omega_m^2} \\ \frac{ccc}{-32\omega_m^2} + \frac{gcg}{4\omega_m^2} & +2\omega_m \end{bmatrix}
\tag{4.27}
$$

Experimental results for the three photon case could not be determined as there was significant interference caused by Landau-Stuckelberg resonances at high amplitudes. In addition the 2nd mode response was difficult to fit as the 1st mode response overlapped with the 2nd mode resonance at high amplitudes. The response amplitude of the 3 photon case is also small due to the inhomogeneous broadening present in the system and this makes

determining the fitting parameters difficult.

### 4.6.3 Widths of the Fundamental and Sub-resonances

The dependence of the spectral widths of the fundamental and sub-resonances on the amplitude of the modulation was experimentally determined. As discussed previously the modulation frequency for a set modulation amplitude was scanned in the vicinity of the fundamental and 1st mode resonances and the amplitude of the low frequency Rabi oscillations determined. The amplitude of the Rabi frequency response had a Lorentzian dependence on the frequency of the modulation centred at the resonance frequency, as shown in figure 4.4, therefore the width of the resonance dependence can be determined from

$$Amplitude(\omega_m) = \frac{k\frac{width}{2}^2}{(\omega_m - \frac{\tilde{\Omega}}{n})^2 + \frac{width}{2}^2} \tag{4.28}$$

where $n$ is the photon number of the transition and k is the on-resonance amplitude. The width of the response for the fundamental and 1st mode response is presented in figure 4.7. As the amplitude of the perturbation field was increased the spectral width of both the resonances increased and the resonances overlapped as shown in figure 4.4. The low amplitude response was dominated by the 5kHz inhomogeneous broadening that also acted to reduce the on-resonance amplitude, this is discussed in section 4.6.4. The fitted values for the fundamental resonance width dependence on amplitude were $y = mx$ where $m = 0.76 \pm 0.03$ and, for the 1st mode, $y = ax^2$ where $a = (3.9 \pm 0.2) \times 10^{-3} kHz^{-1}$.

The width of the resonances has been shown previously to be theoretically dependent on the on-resonance Rabi frequency, therefore the expected dependence of the width on the modulation amplitude is linear for the fundamental resonance and quadratic for the 1st mode. This agrees with the experimentally determined relationships. The theoretical

value of the width of the fundamental resonance is $2c$, where c is equal to $\delta_0\Omega_{RF}/2\tilde{\Omega}$, and thus is linear with respect to the modulation amplitude. Using typical experimental values the linear relationship can be determined as $a\delta_0$ (where $a = 0.67 \pm 0.03$, calculated from $\Omega_{RF} = 39.2 \pm 0.3kHz$, $\tilde{\Omega} = 58.5 \pm 1.3kHz$). The experimentally determined value of $a$ was $0.76 \pm 0.03$. This was greater than the theoretically determined value, possibly because of an errors associated with either the $\approx 5kHz$ inhomogeneous broadening or difficulties with fitting the data at high modulation amplitudes because of the overlap of the resonances.

The theoretically determined width of the 1st mode is $\frac{cg}{\omega_m}$, where c is equal to $\delta_0\Omega_{RF}/2\tilde{\Omega}$ and g is equal to $\delta_0\Delta/2\tilde{\Omega}$. Therefore the dependence on the modulation amplitude is $a\delta_0^2$, where a is equal to $\frac{\Omega_{RF}\Delta}{4\tilde{\Omega}^2\omega_m}$, which for typical experimental values ($\Omega_{RF} = 39.2 \pm 0.3kHz$, $\tilde{\Omega} = 58.5 \pm 1.3kHz$) yields a value for $a$ of $(4.3 \pm 0.1) \times 10^{-3}kHz^{-1}$. The experimental dependence of the width on the modulation amplitude was found to be $y = ax^2$ where $a = (3.9 \pm 0.2) \times 10^{-3}kHz^{-1}$. This is in good agreement with the theoretically determined value, however, it is not fully consistent with the experimental results for the 1st mode on-resonance Rabi frequency dependence on modulation amplitude. This could possibly be due to the width of the 1st mode being less sensitive than the on-resonance response frequency to the effect of the Bloch-Siegert shift.

### 4.6.4 Inhomogeneous broadening

The dependence of the amplitude of the on-resonance Rabi oscillation on modulation amplitude can be determined from the measurement of the response of the system in the vicinity of both the 1st mode and the fundamental resonances for fixed modulation amplitudes. Theoretically the maximum of the oscillation amplitude should not have a dependency on the amplitude of the modulation field, as discussed in section 2.2. However this is experimentally not the case due to inhomogeneous broadening of the frequencies at which the atoms resonate

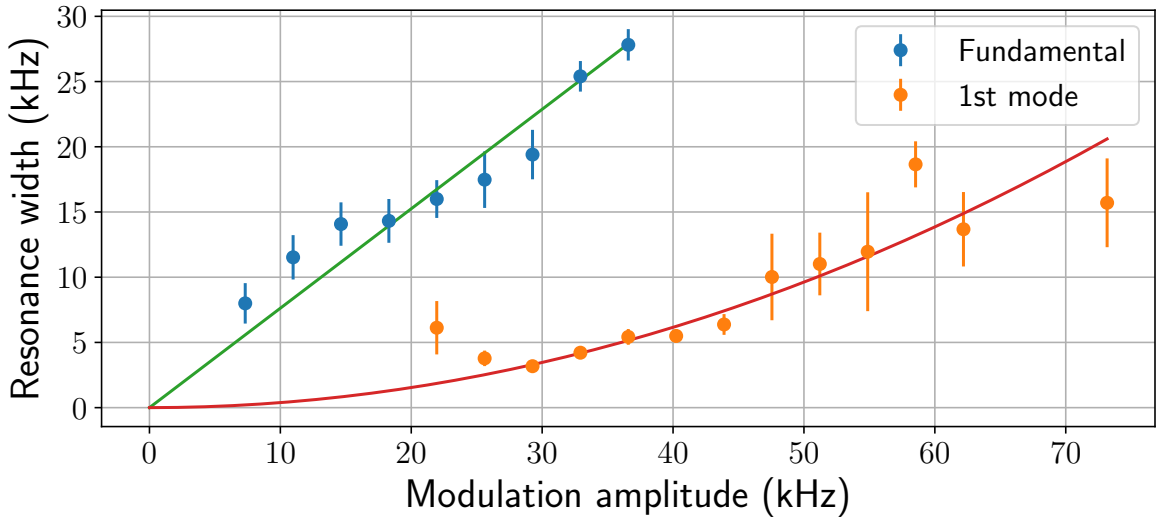


Figure 4.7: **Resonance width:** The dependence of the width of the resonance of the fundamental and 1st mode on the modulation amplitude. The width of the fundamental had a linear response, whereas the width of the 1st mode was smaller and had a quadratic response.

in the atomic cloud.

The dependence of the on-resonance minimum magnetisation (that is related to the amplitude of the Rabi response) on the modulation amplitude is shown in figure 4.8. To determine the on-resonance minimum magnetisation for a set modulation amplitude the dependence of the minimum of the Rabi oscillation on modulation frequency, for the fundamental and 1st mode resonances, for a set modulation amplitude was fitted using a Lorentzian. As shown in figure 4.8 the on-resonance minimum magnetisation increased with modulation amplitude and then saturated. The 1st mode resonance saturated at a higher modulation amplitude than the fundamental resonance.

This behaviour can be understood by considering that there was a spatial variation in the magnetic bias field and thus a variation in the resonance frequency of atoms across the atomic cloud. This results in only part of the cloud being on-resonance for a low modulation

amplitude and consequently a lower on-resonance minimum magnetisation. As the amplitude increases the width of the response increases, as shown in figure 4.7, and the power broadening dominates over the inhomogeneous broadening (caused by the variation of the magnetic bias field). At high amplitude the full cloud will be on-resonance and the minimum of the magnetisation of the response will be maximised.

The reason why the 1st mode resonance required a larger amplitude than the fundamental resonance to reach saturation can be understood by considering that the amplitude of the response is dependent on the degree of overlap between the inhomogeneous broadening and the power broadening. The power broadening of the resonance is dependent upon the on-resonance Rabi frequency and, for the range under investigation, the on-resonance Rabi frequency is smaller for the 1st mode than for the fundamental, as shown in figure 4.6, therefore a larger amplitude for the 1st mode is required to have sufficient power broadening to overcome the effect of inhomogeneous broadening. The inhomogeneous broadening can be utilised to investigate models that have static disorder, this will be discussed in section 5.8.

### 4.6.5 Bloch-Siegert effect

As discussed previously, the modulation frequency was scanned in the vicinity of the fundamental and 1st mode resonances. From the fitting of the data to determine the amplitude of the Rabi response the resonance frequency $\frac{\tilde{\Omega}}{n}$ was also determined. Figure 4.9 shows the dependence of the shift of the resonance frequency of the fundamental and 1st mode resonances on the amplitude of the modulation. For the fundamental resonance no correlation was observed between the amplitude of the modulation and the resonance frequency. For the 1st mode the resonance frequency was observed to have a quadratic dependence on the modulation amplitude, $y = ax^2$, where $a = (1.5 \pm 0.1) \times 10^{-3} kHz^{-1}$. The rest of this section will discuss the theoretical explanation of this observation and compare the experimentally

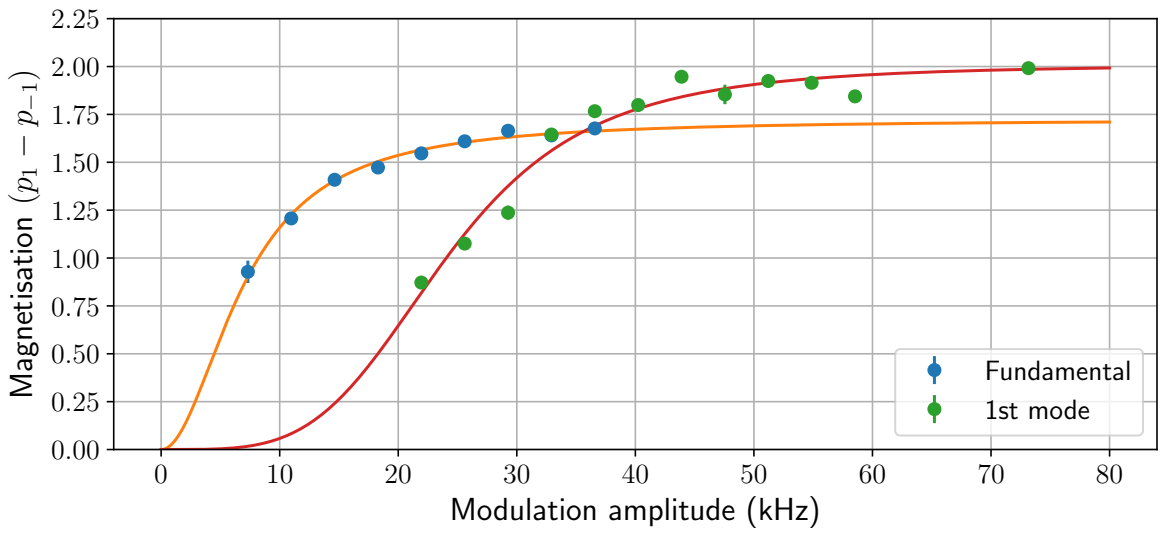


Figure 4.8: **The on-resonance minimum magnetisation response of the atoms:** The dependence of the on-resonance minimum of the magnetisation (that is related to the amplitude of the Rabi response) on the modulation amplitude.

and theoretically determined values of the Bloch-Siegert shift.

The shift of the resonance frequency was determined theoretically by considering the second term in equation 4.21. The shift results from the non-resonant components in the Floquet Hamiltonian, weakly dressing the Floquet states. In the literature this shift is referred to as the Bloch-Siegert shift. The Bloch-Siegert shift is commonly a small correction, however becomes larger as the rotating wave approximation breaks down at high modulation amplitudes. The difference in detuning between the counter-rotating and co-rotating terms becomes smaller as the modulation frequency is reduced and this results in the ratio of the Bloch-Siegert effect to the coupling being larger for higher photon transitions and hence producing a larger shift.

To provide an understanding of how the Bloch-Siegert shift originates, the shift of the resonant frequency of a simple two level off-resonantly coupled system will be discussed. The

Hamiltonian for this simple system is defined as

$$H = \hbar \begin{bmatrix} \omega_0/2 & \Omega \\ \Omega & -\omega_0/2 \end{bmatrix}$$

The shift can be calculated from this Hamiltonian by transforming the system into the dressed basis where the energies of the states are $\pm\sqrt{\Omega^2 + (\omega_0/2)^2}$. For the case of high detuning ($\omega_0 \gg \Omega$), where the state evolution is not significantly perturbed, the shift of the resonant frequency between the states is equal to $\omega_0 + 2(\Omega)^2/\omega_0$ or equivalently a shift of $+\omega_0/2+(\Omega)^2/\omega_0$ for the upper state and $-\omega_0/2-(\Omega)^2/\omega_0$ for the lower state. As the coupling is far off-resonance the base states and dressed states have a large overlap and therefore the interaction of the off-resonant coupling can be simplified to a shift of the energies of the base states. To derive the Bloch-Siegert shift the off-resonant single photon coupling with nearest neighbour Floquet states will be considered for the single photon and multiphoton cases.

**Single photon**

To calculate the Bloch-Siegert shift for the fundamental single photon ($\omega_m = \tilde{\Omega}$) resonance, only the off-resonant coupling terms need to be considered in the infinite matrix in equation 4.19. For single photons the Bloch-Siegert shift is

$$V_{pp} = g^2/(\omega_m) + c^2/4(\omega_0 + \omega_m) + g^2/(-\omega_m) = c^2/(8\omega_m) \tag{4.29}$$

calculated from equation 4.21. It should be noted that the shift due to parallel coupling terms, $\pi$(g), always cancel each other out as the difference in energy between the states (that the parallel coupling terms act between) have opposite sign energy differences. For typical experimental parameters the Bloch-Siegert shift in this case is equal to $y = a\delta_0^2$ where a=$2\frac{\Omega_{RF}^2\delta_0^2}{32\tilde{\Omega}^3}$ =$(4.8\pm0.3)\times10^{-4}kHz^{-1}$, based on $\Omega_{RF} = 39.2\pm0.3kHz$, $\tilde{\Omega} = 58.5\pm1.3kHz$. The

factor of two results from the energy of the upper state increasing by $V_{pp}$ and the energy of the lower state reducing by $V_{pp}$. The maximum frequency shift, therefore, over the experimental range of $\approx 0 - 40kHz$ is predicted to be $0.77 \pm 0.05kHz$, this is much smaller than could be experimentally determined in this study and is comparable to the error associated with the measurement of the generalised Rabi frequency. This explains why the shift cannot be experimentally observed for the fundamental resonance shown in figure 4.9.

### Multiple photons

For multiphoton resonances there is no contribution to the transition rate from on-resonance single photon terms and therefore all the single photon nearest neighbour coupling terms have to be considered in order to calculate the Bloch-Siegert shift, as shown in

$$
\begin{array}{cc}
\cdot & \cdot \\
\alpha & -1 \\
\beta & -1 \\
\alpha & 0 \\
\beta & 0 \\
\alpha & 1 \\
\beta & 1 \\
\alpha & 2 \\
\beta & 2 \\
\cdot & \cdot
\end{array}
\begin{bmatrix}
\cdot & \cdot & \cdot & \cdot & \cdot & \cdot & \cdot & \cdot & \cdot & \cdot \\
\cdot & -\omega_n + \tilde{\Omega} & 0 & g & c/2 & 0 & 0 & 0 & 0 & \cdot \\
\cdot & 0 & -\omega_n & c/2 & 0 & 0 & 0 & 0 & 0 & \cdot \\
\cdot & g & c/2 & \tilde{\Omega} & 0 & g & c/2 & 0 & 0 & \cdot \\
\cdot & c/2 & 0 & 0 & 0 & c/2 & 0 & 0 & 0 & \cdot \\
\cdot & 0 & 0 & g & c/2 & \omega_n + \tilde{\Omega} & 0 & g & c/2 & \cdot \\
\cdot & 0 & 0 & c/2 & 0 & 0 & \omega_n & c/2 & 0 & \cdot \\
\cdot & 0 & 0 & 0 & 0 & g & c/2 & 2\omega_n + \tilde{\Omega} & 0 & \cdot \\
\cdot & 0 & 0 & 0 & 0 & c/2 & 0 & 0 & 2\omega_n & \cdot \\
\cdot & \cdot & \cdot & \cdot & \cdot & \cdot & \cdot & \cdot & \cdot & \cdot
\end{bmatrix}
\tag{4.30}
$$

where there are four components to the Bloch-Siegert shift due to four nearest-neighbour single photon interactions. The shifts, due to these off-resonant couplings, are calculated

using equation 4.21 and are detailed below.

The counter-rotating contribution (red and blue in the matrix in equation 4.30) are

$$v_{pp} = g^2/(\tilde{\Omega} - (\tilde{\Omega} - \omega_m)) + c^2/4(\tilde{\Omega} + \omega_m) \tag{4.31}$$

and the co-rotating contributions (orange and purple) are

$$v_{pp} = g^2/(\tilde{\Omega} - (\omega_m + \tilde{\Omega})) + c^2/4(\tilde{\Omega} - \omega_m) \tag{4.32}$$

The total shift of the energy separation is therefore

$$v_{pp} = g^2/(\omega_m) + c^2/4(\tilde{\Omega} + \omega_m) + g^2/(-\omega_m) + c^2/4(\tilde{\Omega} - \omega_m) \tag{4.33}$$

The contribution from the diagonal (g) terms cancel, as in the single photon case. Finally, to determine the multiphoton Bloch-Siegert shift, the relationship $\tilde{\Omega} = n\omega_m$ is used. In the case of $n > 1$, therefore, the Bloch-Siegert shift is defined by

$$v_{pp} = (c)^2/4\omega_m(n+1) + (c)^2/4\omega_m(n-1) = \frac{c^2}{4\omega_m}\frac{2n}{(n+1)(n-1)} \tag{4.34}$$

and thus the resonance frequencies of the higher order resonances (n) are given by

$$\omega_m = \frac{\tilde{\Omega} + 2v_{pp}}{n} = \frac{\tilde{\Omega}}{n} + \frac{c^2}{\tilde{\Omega}}\frac{n}{(n+1)(n-1)} \tag{4.35}$$

For the 1st mode ($2\omega_m = \tilde{\Omega}$) this results in a theoretical frequency shift of $a\delta_0^2$ where $a = \frac{2c^2}{3\tilde{\Omega}}$. For typical experimental values this is equal to $(1.3 \pm 0.1) \times 10^{-3} kHz^{-1}$. The experimentally determined value was equal to $(1.5 \pm 0.1) \times 10^{-3}$ and is greater than the theoretically calculated value. This may be the result of a fitting error associated with the

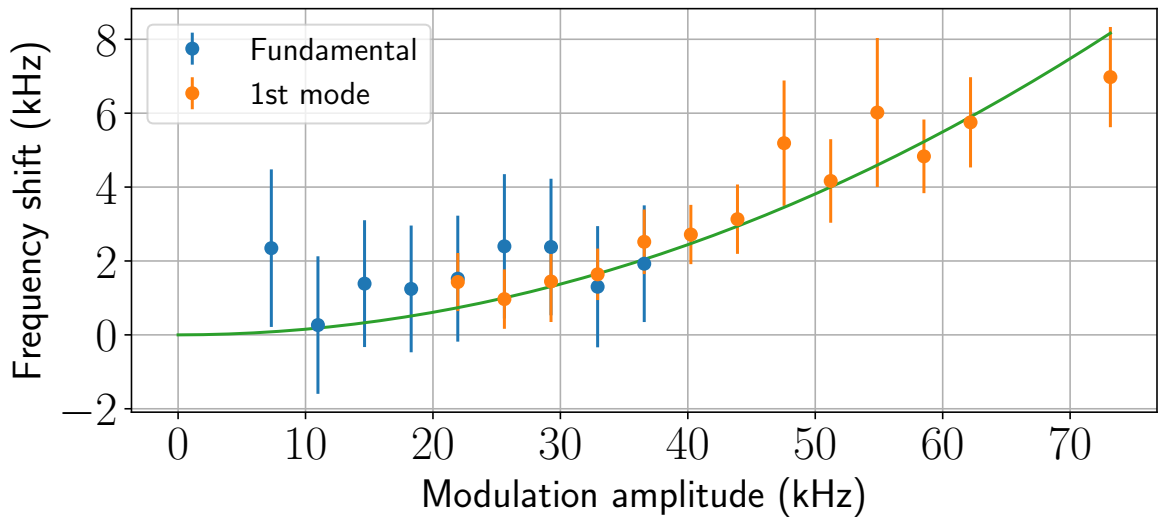


Figure 4.9: **Bloch-Siegert shift:** Experimental data showing the dependence of the shift of the fundamental and 1st mode resonance frequencies on the modulation amplitude.

difficulty in experimentally locating the resonant frequency due to the large widths (and thus overlap) of the resonances. Also as the Bloch-Siegert shift can only be observed at high modulation amplitudes, there may be an effect that for large modulation amplitudes the modulation can no longer be treated as a perturbation of the RF dressed system, and therefore Floquet theory breaks down.

### 4.6.6 Summary

In summary Floquet theory can explain the effect of the modulation amplitude on; 1) the fundamental on-resonance Rabi frequency, 2) the widths of the fundamental and 1st mode resonances, and 3) the observed Bloch-Siegert shift for the fundamental and 1st mode resonances. However, it only partially accounts for the behaviour of the on-resonance Rabi frequency of the 1st mode resonance, predicting the quadratic dependence but not the quadratic coefficient. This is probably caused because at large modulation amplitudes the modulation can no longer be treated as a perturbation of the RF dressed system, and therefore Floquet

theory breaks down. In the next section the response of the system at high modulation amplitudes will be considered.

## 4.7 High amplitude modulation: the sideband model

The resonance response of the system to high modulation amplitudes was investigated by setting the modulation frequency to the generalised Rabi frequency and varying the amplitude of the modulation. The results of this experiment are shown in figure 4.10. The Rabi frequency of the response was initially proportional to the amplitude of the modulation however as the amplitude increased the frequency reached a maximum and then decreased. The data was fitted using a Bessel function of the first kind, $aJ_1(x/b)$, where the fitting parameters were determined as $a = 38.6 \pm 0.1kHz$ and $b = (54.4 \pm 0.2) \times 10^{-2}kHz^{-1}$. The fit with the experimental data was exceedingly good, as shown in figure 4.10. It was not possible to take data for the response of the 1st mode ($\omega_m = \tilde{\Omega}/2$) as the Bloch-Siegert shift at higher amplitudes moved the system entirely off resonance making fitting difficult. This result may have consequences for the response of the system to noisy perturbations and this will be discussed in the next chapter.

In order to understand the Bessel function response of the data the sideband model [76] is required. The theories used to explain the low amplitude response of the system are no longer valid at high amplitudes. This is because at high amplitude modulations the Rabi frequency becomes comparable to the generalised Rabi frequency ($\tilde{\Omega} = \sqrt{\Omega_{RF}^2 + \Delta^2}$). In this regime the first dressing by the RF field breaks down and the RWA applied to the modulation in the dressed basis is no longer valid. This also leads to the photon interpretation of the Floquet theory breaking down and therefore a different theory is required to explain the response of the system over the full amplitude range used in this study. The next section begins by deriving the sideband model, then discusses the implications and then finally the model is

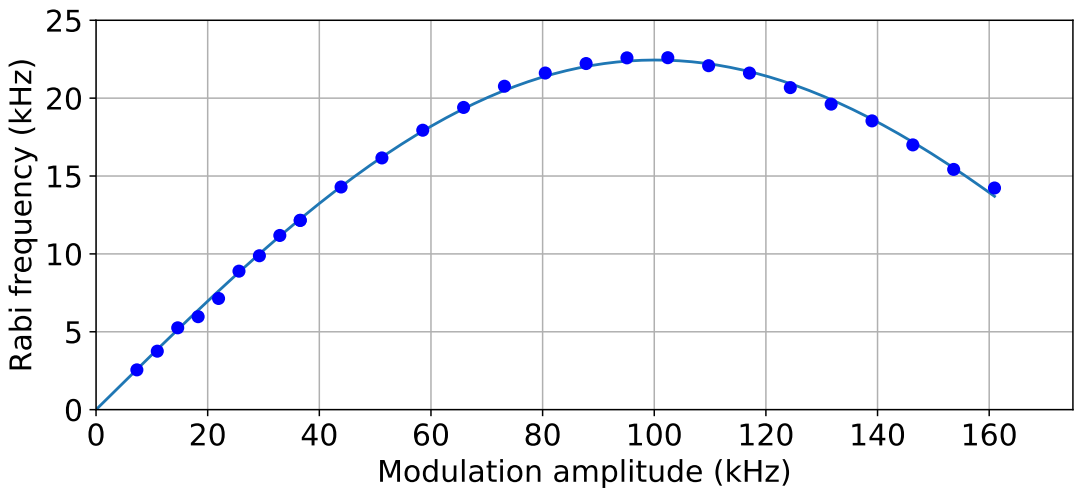


Figure 4.10: **High amplitude response:** The dependence of the fundamental frequency response on the amplitude of the modulation.

compared with Floquet theory.

The sideband model treats the modulation as altering the rotating frame dynamically. As before, the Hamiltonian, in the base state basis, with the modulation is given by

$$H = \hbar \begin{pmatrix} +\omega_0 + \delta(t) & \sqrt{2}\Omega_{RF}\cos(\omega_{RF}t) & 0 \\ \sqrt{2}\Omega_{RF}\cos(\omega_{RF}t) & 0 & \sqrt{2}\Omega_{RF}\cos(\omega_{RF}t) \\ 0 & \sqrt{2}\Omega_{RF}\cos(\omega_{RF}t) & -\omega_0 - \delta(t) \end{pmatrix} \tag{4.36}$$

The system is transferred to a frame that rotates at the energy separation, $\omega_0 + \delta(t)$, using the unitary transformation

$$\hat{U}(t) = e^{-\sigma_z[\omega_0 + \xi(t)]/2} \tag{4.37}$$

where

$$\xi(t) = \int_0^t \delta(t)\ dt \tag{4.38}$$

is the integral of the modulation with respect to time. This unitary transformation only changes the evolution of the phase of the states and does not mix the base states. In this rotating frame the RF coupling is modulated by $A(t)$, as shown in

$$H = \sqrt{2}\hbar\Omega_{RF}\cos(\omega_{RF}t)A(t)e^{i\omega_0 t}\begin{pmatrix} 0 & 1 & 0 \\ 1 & 0 & 1 \\ 0 & 1 & 0 \end{pmatrix} \tag{4.39}$$

where

$$A(t) = e^{i\xi(t)} \tag{4.40}$$

The time dependence of the diagonal terms has now been transferred to the off-diagonal terms. $A(t)$ is periodic with time and therefore can be reduced to its Fourier components

$$A(t) = \sum_{n=-\infty}^{n=-\infty} \Delta_n e^{2\pi int/T} \tag{4.41}$$

where $T$ is the periodicity of the modulation and

$$\Delta_n = \frac{1}{T}\int_0^T e^{-in2\pi t/T} e^{i\xi(t)}\, dt \tag{4.42}$$

the Hamiltonian in the rotating basis is thus

$$H = \frac{\Omega_{RF}}{\sqrt{2}} \sum_{n=-\infty}^{n=-\infty} \Delta_n (e^{i(n2\pi/T+\omega_0+\omega_{RF})t} + e^{i(n2\pi/T+\omega_0-\omega_{RF})t})\mathbf{J}_x \tag{4.43}$$

If only the terms that are near resonance and thus have a major effect on the system evolution are considered, the fast oscillating terms $(\omega_0 + \omega_{RF})$ can be ignored (applying the RWA) and

the Hamiltonian simplifies to

$$H = \frac{\hbar\Omega_{RF}}{\sqrt{2}}\Delta_n \begin{pmatrix} 0 & e^{i(n2\pi/T+\omega_0-\omega_{RF})t} & 0 \\ e^{-i(n2\pi/T+\omega_0-\omega_{RF})t} & 0 & e^{i(n2\pi/T+\omega_0-\omega_{RF})t} \\ 0 & e^{-i(n2\pi/T+\omega_0-\omega_{RF})t} & 0 \end{pmatrix} \tag{4.44}$$

For a perturbation of the form $\delta(t) = \delta_0 \cos(\omega_m t)$, as has been investigated experimentally in this chapter, the periodicity, $T$, is equal to $2\pi/\omega_m$ and the Fourier coefficients [76] are

$$\Delta_n = J_n(\delta_0/\omega_m) \tag{4.45}$$

where $J_n$ are the Bessel functions for the different Fourier components

$$J_\alpha(x) = \sum_{m=0}^{\infty} \frac{(-1)^m}{m!(m+\alpha)!}(\frac{x}{2})^{2m+\alpha} \tag{4.46}$$

The order $(n)$ of the Bessel function can be understood to correspond to the number of photons involved in the transition [76]. For the fundamental resonance ($\omega_m = \tilde{\Omega}$) the Bessel function, $n = 1$, has a related coupling of

$$\frac{\Omega_{RF}}{\sqrt{2}}\Delta_n \tag{4.47}$$

Using typical experimental parameters the response of the Rabi frequency of the fundamental is equal to $aJ_1(\delta_0/b)$ where $a = 39.2 \pm 0.3kHz$ and $b = \tilde{\Omega} = 59.9 \pm 0.8kHz$. Comparing this with the experimentally determined values of $a = 38.6 \pm 0.1kHz$ and $b = 54.4 \pm 0.2kHz$ the results are in excellent agreement, supporting the validity of the sideband theory. An error might result from the Bloch-Siegert shift moving the system off-resonance, however this would only result in an increase in the frequency response and cannot therefore explain the decrease seen at high amplitudes. At high amplitudes the low frequency of the Rabi oscillations also

becomes comparable to the high frequency, low amplitude, oscillations observed in figure 4.2. This leads to beating behaviour that makes the fitting unreliable.

The sideband model should be equivalent to the Floquet theory at low modulation amplitudes. At these amplitudes only the lowest order expansion of equation 4.46 is relevant and thus the theoretical Rabi frequency is given by

$$\Omega_{RF} J_1(\delta_0/\omega) \approx \Omega_{RF}(\frac{\delta_0}{2\omega_m}) \tag{4.48}$$

this is linear with increasing modulation amplitude. Equation 4.48 is equal to the response determined from Floquet theory

$$c = \frac{sin(\theta)}{2}\delta_0 \tag{4.49}$$

when $\omega_m$ is equal to $\tilde{\Omega}$. The sideband theory thus agrees with the Floquet formalism in the low modulation amplitude regime.

The 1st (2 photon) and 2nd (3 photon) mode transition rates can be calculated from the higher order Bessel functions. The lowest order expansion of the Bessel function $J_2$ is a quadratic expression that corresponds to the 2 photon 1st mode resonance. The $J_3$ Bessel function has a cubic response that corresponds to the 3 photon 2nd mode resonance. These relationships are in agreement with Floquet theory and the experimental results, further confirming the applicability of the sideband model.

It should however be noted that the fundamental resonance modulation frequency predicted by the sideband model and that of the Floquet theory disagree. This is because the shift of the resonance frequency due to the off-resonant un-modulated dressing by the RF field is not considered in the sideband model. This is because the off-resonant Bessel function terms were ignored in the derivation of the sideband model. If however all the off-resonant Bessel

function terms are considered, every Bessel function can be understood as corresponding to a different Bloch vector on the Bloch sphere around which the system precesses, as shown in figure 4.11. For low modulation amplitudes the $J_0$ Bessel function term (that corresponds to the un-modulated dressing by the RF field) has the highest strength, as shown in figure 4.12, and shifts the on-resonance frequency $\omega_0$, to $\omega_{RF} + \tilde{\Omega}$. As the modulation amplitude increases the magnitude of the Bloch vector corresponding to the un-modulated dressing (n=0) is reduced. This has the result that there is no longer a shift of resonant frequency due to the $J_0$ Bessel function and as such the resonant modulation frequency, $\omega_0$, becomes equal to $\omega_{RF} + \Delta$.

In conclusion, for low amplitudes the Floquet theory predicts the resonant frequency correctly, and the sideband model does not. As the amplitude increases the sideband model becomes more valid, and the Floquet theory less valid. The modulation amplitude where the Bessel function equals zero is referred to as the phenomenon of "coherent destruction of tunnelling" [81, 122, 123], at this point the system does not evolve and is localised in the original state.

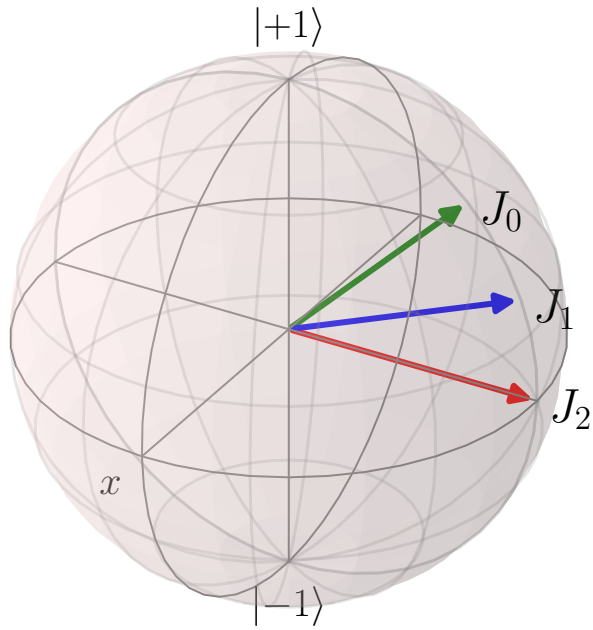


Figure 4.11: **Sidebands on the Bloch sphere:** Green is the Bloch vector that corresponds to the un-modulated dressing of the system by the RF (detuning of $\Delta$), blue is the Bloch vector for the 1st order sideband (detuning of $\Delta - \omega_m$), and red is the Bloch vector for the 2nd order sideband that is on-resonance ($\Delta - 2\omega_m = 0$).

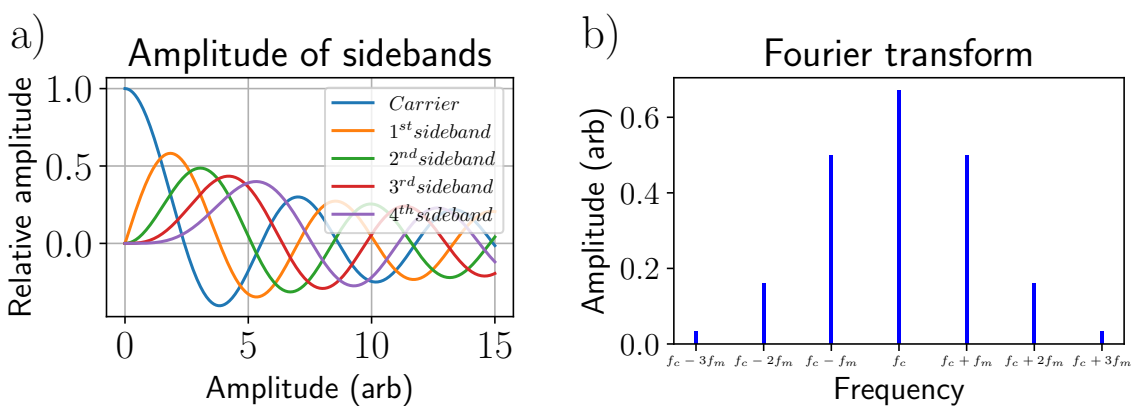


Figure 4.12: **Sidebands:** a) The dependence of the strength of the different sidebands on the modulation amplitude. As in the case of the Floquet theory, the 1st sideband frequency increases linearly, the 2nd quadratically and the 3rd cubically. b) An example of the Fourier transform of the coupling frequencies. The 1st sideband frequency corresponds to the single photon, the 2nd to the two photon and the 3rd to the three photon transition.

CHAPTER 5

# EXPERIMENTAL INVESTIGATION INTO NOISY PERTURBATION

## 5.1 Introduction

As discussed in the introductory chapter, transport through a network of weakly coupled sites can be theoretically enhanced by the interplay between the weak coherent coupling and the environmental perturbation of the site energies. The noise spectrum of the FMO environment has been experimentally observed to have a flat background (linked to dephasing assisted transport mechanisms) and vibrational resonances (which may enhance transport through the operation of vibration assisted transport mechanisms [5]). To experimentally investigate dephasing assisted transport mechanisms an incoherent white noise perturbation field was applied to the weakly coupled system used in this study. Different shapes of the noisy perturbation spectrum were used to investigate dephasing and vibration-assisted transport models. By altering the shape of the perturbation spectrum the effect of the resonance response, including the sub-resonances, on transport through the system was investigated. The resultant observations were interpreted by reference to the sideband model and similarities with incoherent transport processes highlighted.

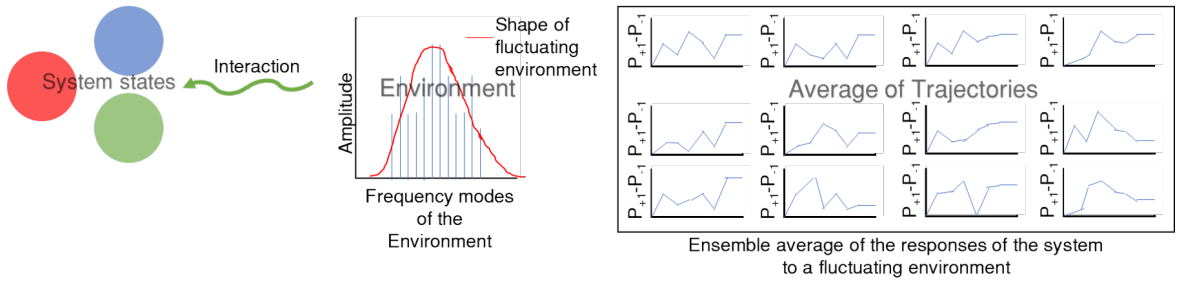


Figure 5.1: **Average of the system response to a fluctuating environment:** To determine the response of the system to a fluctuating environment the distribution of the population between the system states was measured for different realisations that had the same spectral shape but different individual components.

## 5.2 Experimental modelling of the environment

The protein scaffolding supporting the FMO complex introduces environmental noise into the FMO system. In the simplest FMO models the source of the environmental noise is classical and random, hence it is modelled as a fluctuating environment composed of multiple frequencies. The frequency composition of the environment is incoherent (i.e. random phase relationship between the different frequency components). Theoretical models assume that the environment only perturbs the state energies, and consequently the current experimental set-up can accurately model features of the environment by perturbing the bias field. The influence of the spectral shape of the environmental noise can be modelled by shaping the frequency composition of the perturbation. To model the fluctuating part of the environment the response of the system is averaged over multiple realisations of the noisy spectrum, as shown in figure 5.1. Each of the individual realisations evolves unitarily, but the ensemble average can evolve non-unitarily [53]. The classical perturbations that were experimentally generated were composed of discrete frequencies, however, because the discrete frequency separation was less than the broadening ($1/T$), due to the limited simulation time ($T$), the discrete nature of the background was a good approximation of a continuous environment.

## 5.3 Measurement of population transport

Ideally the dependence of the population transported though the system on the applied perturbation could be effectively characterised by modelling the sink feature of the FMO in the experimental set-up. The initial excitation (polarisation of the population) would be transferred through the system until it is irreversibly transferred from the target state to the sink state. In the current system, however, there is no sink state and therefore the observed magnetisation of the system (the population in the target state minus the population in the initial state) has been used to calculate the rate of transport through the system, similar to the approach taken by Maier et.al [52].

## 5.4 Experimental method

The method to experimentally generate shaped perturbations that are able to simulate the environment under investigation will be initially discussed. Following this the number of realisations to accurately determine the response of the system to the noisy perturbations under investigation will be examined.

### 5.4.1 Generation of the perturbation

The effect of a fluctuating perturbation was characterised by averaging the effect of many independent realisations with the same spectral form. A random value, that had a Gaussian probability distribution of width normalised to one centred at zero, was computationally generated for each time in the series, as shown in figure 5.2a. The series was then Fourier transformed in order to reveal the white noise spectrum of the frequency components, as shown in figure 5.2b. This spectrum was then shaped using the filter function under investigation and then inversely Fourier transformed to produce an independent realisation with the

desired spectral features. The series was then normalised and amplified by the experimentally required rms noise amplitude. It should be noted that, because the series was normalised to one and then amplified, if the spectral width of the band was halved the amplitude density of the modes would be doubled for the same rms noise amplitude. These operations were repeated in order to generate multiple realisations that were then applied to the system. The resultant average and distribution of the populations of the system states, for the multiple realisations of a particular spectral shape, was then experimentally determined.

### 5.4.2 Determining the required number of realisations

In order to evaluate the number of realisations required to accurately determine the system response, 100 realisations of a white noise ($0-100kHz$) perturbation for the same time ($60\mu s$) and rms noise amplitude ($59kHz$) were applied to the system and the distribution of the population between the three sites was measured. The most sensitive response of the system was expected to be where the selected time and rms noise amplitude led to states where the three $m_F$ sites are nearly equally populated. Figure 5.3 shows the moving average of the 100 measurements as a function of the moving average bin size (number of realisations). The distribution of the moving average values reduced with the increasing number of realisations until at above $\approx 25$ realisations the system stabilised and there was no further benefit of an increase in the number of realisations. At this number of realisations the distribution of the average was no longer dominated by statistical fluctuations, associated with the number of realisations, and was dominated by the stability of the experiment. A standard of 25 realisations was therefore chosen for the following experimental investigations of the system response to noisy perturbations.

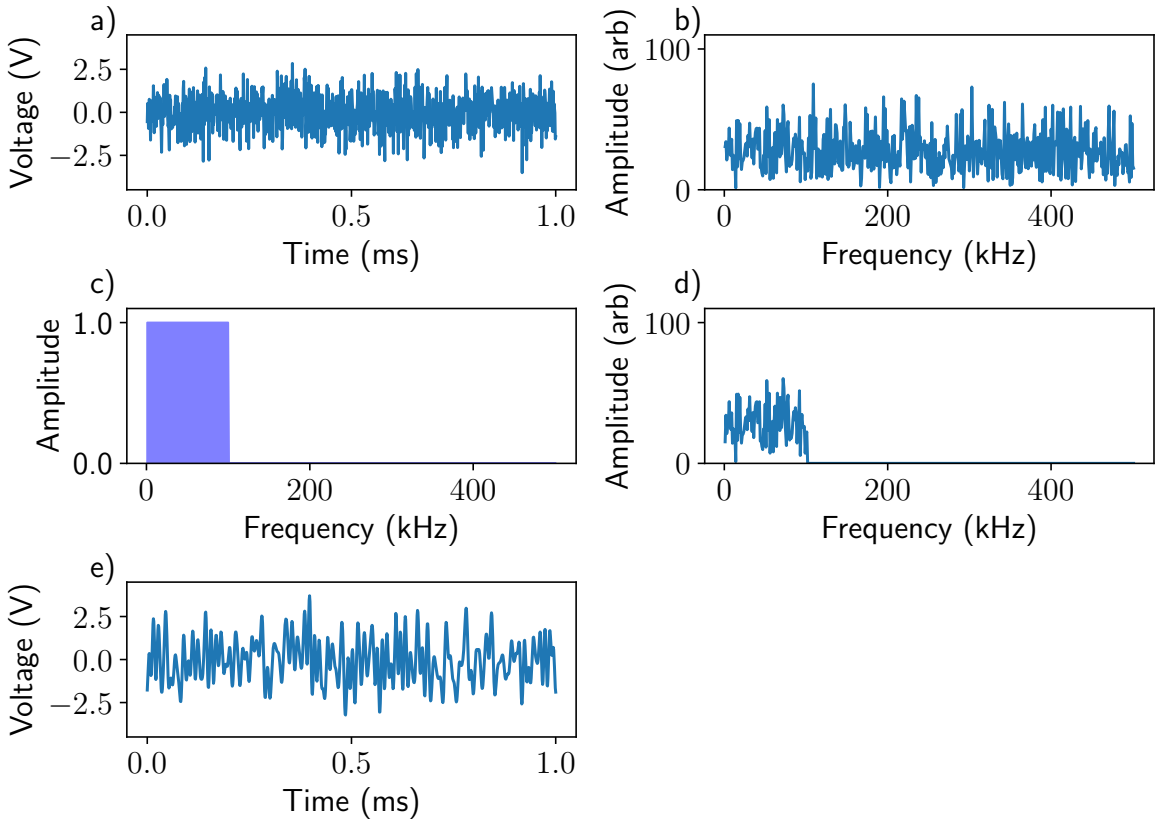


Figure 5.2: **Generating and shaping the perturbation** (sequential processing is shown in a) to e)): a) Randomly distributed points that have a Gaussian distribution of width 1.00 are generated at discrete points in time, b) this signal is Fourier transformed and has a flat white noise spectrum, c) the spectrum is then shaped by multiplying the spectrum by a filter function that has the desired spectral feature, d) the final shaped white noise spectrum, and e) the normalised realisation is generated by applying the inverse Fourier transform to the shaped spectrum, and normalising the resultant signal. This normalised signal (that contains the desired spectral features) is amplified to produce the final signal.

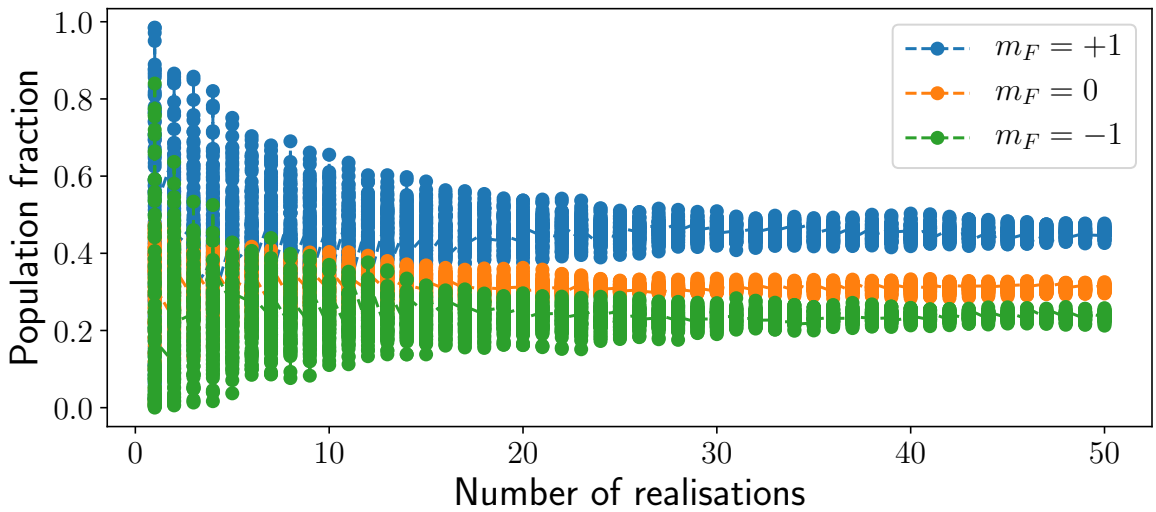


Figure 5.3: **The dependence of the distribution of the moving average on the numbers of realisations:** 100 realisations of a white noise ($0-100kHz$, noise rms $= 59kHz$) perturbation were applied to the system for $60\mu s$ and the resultant responses averaged using the moving average method where the number of realisations (bin size) was altered.

## 5.5 The system response to white noise perturbation

To understand the influence of an incoherent perturbation on the evolution of the weakly coupled system the effect of the rms amplitude of the perturbation was examined. Initially the experimental method is outlined and then the experimental results are presented. Finally the results are discussed with reference to the density of states interpretation, perturbation theory and the effect of the resonant structure.

### 5.5.1 Experimental method

Experiments were conducted by initially setting the generalised Rabi frequency ($\tilde{\Omega}$) to $30kHz$ ($\Omega_{RF} \approx 16kHz$, $\Delta \approx 25kHz$), so that the ratio between the rms amplitude of the noisy perturbation and the generalised Rabi frequency could be varied by up to a factor of $\approx 10$. An independent realisation of the noisy perturbation field was then generated with

the desired spectral features and rms amplitude, as outlined in section 5.4.1. Following this the noisy perturbation and the RF field were simultaneously applied to the system (that had been prepared as outlined in section 3) for the evolution time under investigation and the resultant distribution of the population between the three states measured using the procedure discussed in section 3.4. This process was repeated for 25 realisations. Figure 5.4 shows the response of the system to varying rms amplitude for a noise spectrum of bandwidth $0 - 50kHz$ for 25 realisations and an evolution time of $60\mu s$. A histogram of the final magnetisation was plotted in order to show the distribution of the final state of the system. The mean of the distribution was also plotted to show the trend of the relationship between the rms amplitude of the perturbation and the magnetisation of the system.

It should be noted that for this data the resistance of the perturbation electronic circuit, discussed in section 3.7, was reduced by 50%. This increased the maximum perturbation field from $180kHz$ to $360kHz$ by increasing the maximum current through the circuit. The reduction of transport, observed in figure 5.4, cannot therefore be due to an effect associated with the field being 'clipped' (where any noise points above the maximum are outputted as the maximum value). Changing the circuit also had the effect of reducing the bandwidth to $50khz$, which we do not believe will had a significant effect on the results, because the generalised Rabi frequency was $30kHz$ for all the experiments discussed in this section. The original circuit, discussed in section 3.7, with the greater bandwidth and lower maximum perturbation field, was used for the shaped noise results. In addition the optimal rms amplitude was below this saturation regime and therefore the effect of 'clipping' should not have had an effect on the rate of transport measurements in figure 5.14.

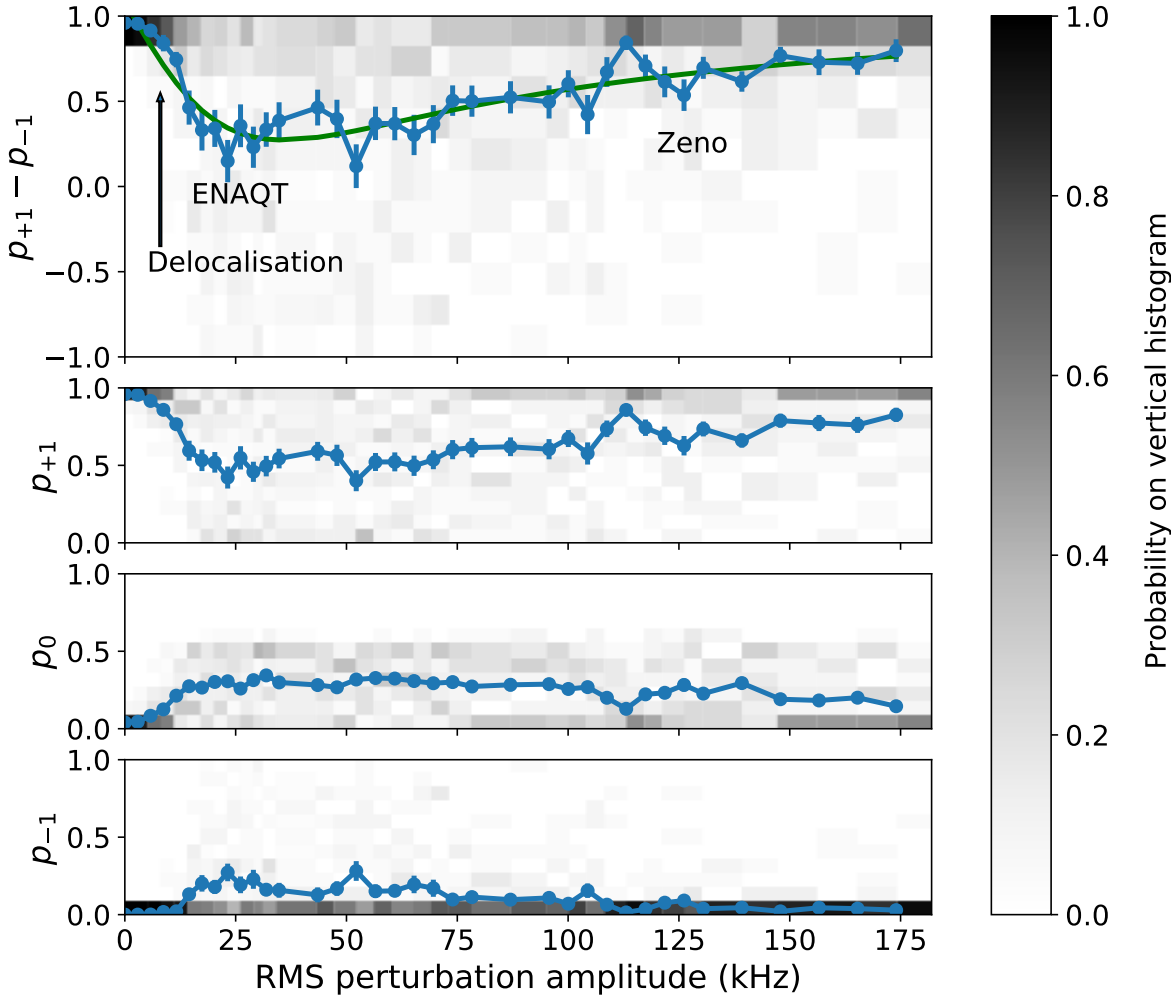


Figure 5.4: **The dependence of the final state on the rms noise amplitude:** The rms amplitude of the noisy perturbation ($0 - 50kHz$ flat spectral shape) was varied for a $60\mu s$ evolution time and the average of the population in the different $m_F$ states for 25 realisations measured. The rms amplitude is in units of frequency in order to provide comparison with the energy separation of the magnetic sub-states ($\approx 1MHz$). The vertical histograms show the population distribution of the 25 realisations for each value of the noise field amplitude. The colour in the key corresponds to the fraction of the 25 realisations that were in the final state (e.g for an amplitude of $0kHz$ the probability that the magnetisation ($p_{+1} - p_{-1}$) of the final state will have a value of between 0.8 and 1.0 is 100%).

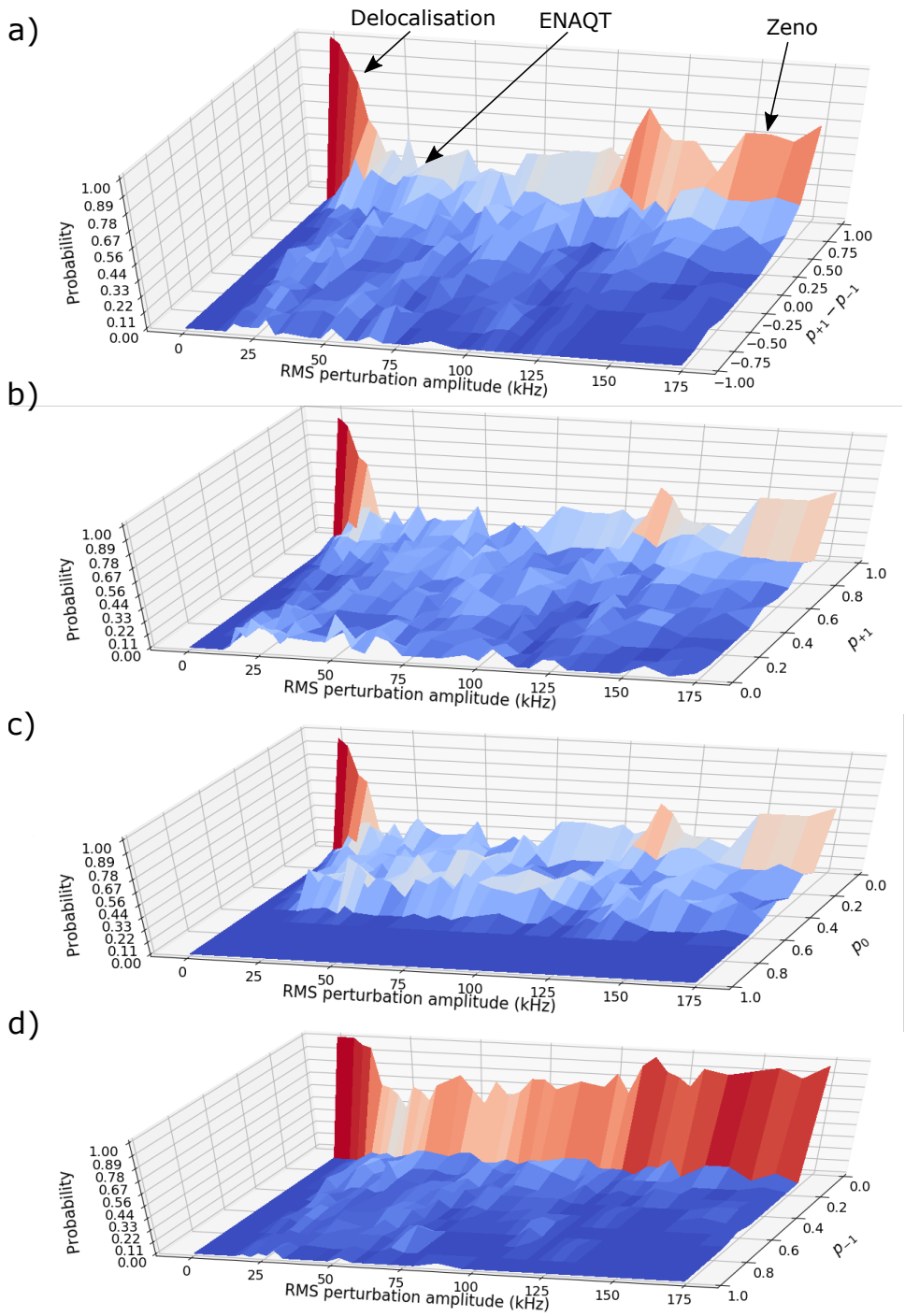


Figure 5.5: **3D representation of the dependence of the probability distribution on the rms perturbation amplitude:** 3D representation of the vertical histograms in figure 5.4 showing the dependence of the probability distribution on the rms perturbation amplitude.

### 5.5.2 The response of the system to rms noise amplitude

The dependence of the magnetisation of the system on the rms noise amplitude, figure 5.4, showed the initial theoretically predicted delocalisation of the population from the initial state due to the application of the noise field. As the rms amplitude increased the transport also increased to a maximum value that approached the fully thermalised state, this regime is referred to as environment-assisted quantum transport (ENAQT). At higher rms amplitudes the transport was observed to reduce and this is identified as the Zeno-like regime. The "optimum" rms noise amplitude to maximise transport for 60$\mu$s was $\approx 25kHz$, that is of the same order as the detuning and the generalised Rabi frequency. It can also be seen that the population of the $m_F = 0$ state increased at approximately twice the rate of the population of the $m_F = -1$ state. In the rest of this section the different response regimes will be discussed in detail and reference will be made to the influence of the resonant structure that was experimentally observed in section 4.

### 5.5.3 The density of states interpretation

The density of states interpretation outlined in the introduction is supported by the data presented in figure 5.4. This interpretation models the noisy perturbation as increasing the width of the distribution of the state energy, as shown in figure 1.4. The result of this is to increase the overlap between the energy distribution of the states and the detuned frequency of the coherent coupling field, shown in figure 5.6, and thus increase the strength of coupling and the population transported. For very large state energy widths, however, the overlap is reduced as a result of the state being more diffuse, resulting in a reduction in transport.

This overlap interpretation can be investigated by calculating the overlap integral between a delta function representing the detuned coupling field and the distribution of the energy

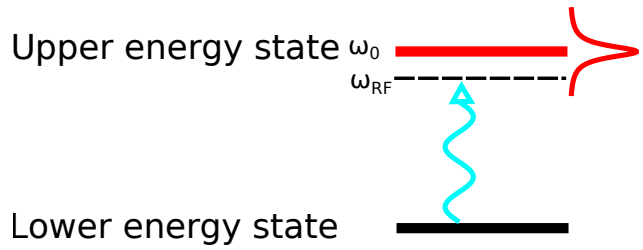


Figure 5.6: **Overlap of the RF field and the energy distribution of the state:** Pictorial representation of the overlap between two adjacent energy levels, where the distribution of the energy of the upper state has a broadening of its energy distribution, overlapping with the frequency of the coherent coupling field.

of the system states that is increased by the application of the perturbation, this is shown pictorially for a two level system in figure 5.6. The data in figure 5.4 is fitted using the equation

$$p_{+1} - p_{-1} = \frac{-0.25 \times x \times p}{(x/2)^2 + (k/2)^2} + c = \int_0^t \int_{-\infty}^{+\infty} \frac{-0.25 \times x \times \frac{dp}{dt}}{(x/2)^2 + (f)^2} \delta(f - k/2)\ df\ dt \tag{5.1}$$

where $x$ is the energy width of the state and is dependent on the rms noise amplitude, k is equal to twice the detuning (and the rms amplitude where the maximum magnetisation occurs), p is a constant that relates the overlap to the population transport, and c is the offset that is related to the magnetisation of the initial state. Values of $k = 36 \pm 2kHz$, $c = 1.09 \pm 0.05$ and $p = 58 \pm 6kHz$ were obtained by fitting this equation to the experimental data shown in figure 5.4 for the dependence of the average magnetisation on the rms noise amplitude. The value of the detuning determined from the fitting is $18 \pm 1kHz$ (k/2) and this is less than the detuning determined from the measurement of the generalised Rabi frequency ($25kHz$). This discrepancy is believed to result from the power broadening, due to the RF coupling, being ignored and therefore the use of a delta function in the overlap integral is invalid. Nevertheless the fit to the data supports the density of states interpretation apart from in the low rms amplitude regime that will be discussed shortly.

The reduction of transport seen at high rms amplitudes can also be interpreted as a "quantum Zeno-like" effect by relating the width of the state to the inverse of the measurement rate. In this interpretation a large energy width is equivalent to the state being measured rapidly and thus transport is suppressed as discussed in chapter 2. Both these interpretations, however, fail to take into account the effect of the frequency distribution of the perturbation on the system. This will be investigated later in this chapter.

### 5.5.4 System behaviour at low rms amplitudes

At low rms amplitudes a quadratic dependence of the population transported on the perturbation rms amplitude was observed. This can be understood with reference to the commonly known Fermi's golden rule that applies to evolution times greater than the inverse of the energy of the state, derived from perturbation theory (as outlined in section 2) and shown in

$$p_k = 2\pi \frac{|\langle k| H_{amp} |n\rangle|^2 t}{\hbar} = \Gamma t \tag{5.2}$$

where $p_k$ is the population transported, $t$ is the evolution time, $|\langle k| H_{amp} |n\rangle|$ is the coupling between the dressed states and is dependent on the rms amplitude of the perturbation. The rate of population transfer $\Gamma$ can be equivalently represented as

$$\Gamma = 2\pi g(\omega)|\kappa(\omega)|^2 \tag{5.3}$$

where $g(\omega)$ is the frequency distribution (controlled by shaping the perturbation), and $|\kappa(\omega)|^2$ is the coupling strength (dependent upon the rms amplitude of the perturbation and the resonant structure).

### 5.5.5 The effect of the resonances

As discussed in the previous chapter, the response of the experimental system has been found to be dependent upon the frequency of the perturbation, chapter 4. The response of the system to the perturbation frequency has resonance behaviour. The effect of the perturbation was interpreted as causing coupling between the dressed states of the system and hence inducing transitions between the base states. The resonant structure of the system was also found to be strongly dependent upon the perturbation amplitude, and the width of the resonances was dependent upon the amplitude of the perturbation (power broadening). Thus, for the case of a noisy perturbation with frequency components that cover the resonances, incoherent-like transport processes could arise from the broader range of frequencies that would contribute to the dynamics of the system at large rms amplitudes. There is an additional complexity arising from more than one coupling channel, caused by the presence of the fundamental and sub-resonances, that may cause interference effects. The effect of the resonances will be investigated in this chapter by shaping the distribution of the perturbation frequencies. This allows the effect of the different resonances and the interplay between them to be characterised, as shown in figure 5.7.

### 5.5.6 Distribution and spread of the resultant magnetisation

The population distribution of the state of the system after the application of the 25 realisations is shown on the vertical histograms in figure 5.4 and in the 3D representation in figure 5.5. At low rms amplitudes the distribution of the magnetisation of the system had a low variation and did not significantly evolve from the initial state. As the rms amplitude increased the distribution still remained skewed towards a magnetisation of one, but the width of the distribution was increased and discontinuities appeared in the distribution that moved the average of the magnetisation towards zero. At higher rms amplitudes the distribution of

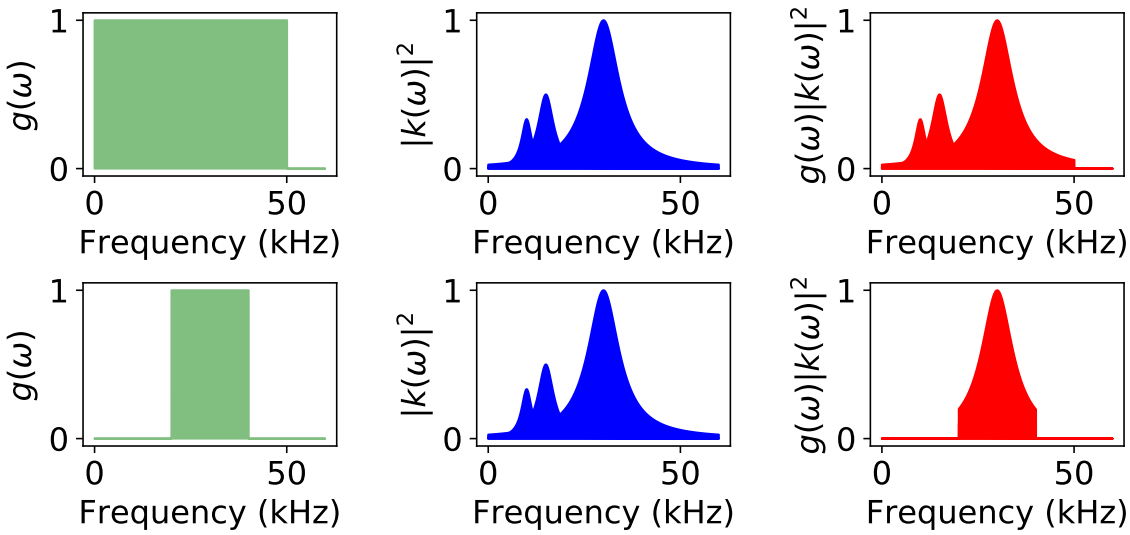


Figure 5.7: **Shaping the perturbation:** Shaping the spectrum of the perturbation allows different resonances to be targeted. For the $0-50kHz$ band the system response is dependent on the contributions from all the resonances. For the $20-40kHz$ band only the fundamental resonance contributes toward the system response.

the state of the system re-localised towards the initial state (magnetisation=1.0).

For the case of the population of the $m_F = +1$ ($p_{+1}$) state, the distribution of the fraction of the population was localised to one for low rms amplitudes and then as the rms amplitude increased the system had a more even distribution. Finally at high rms amplitudes the system re-localised towards the initial state ($p_{+1} = 1.0$).

The distribution of the population of the $m_F = 0$ response mostly did not exceed 0.5. This confirmed that the system evolves on the Bloch sphere, as the maximum population that the central state can reach corresponds to the state on the equator of the Bloch sphere and a population fraction of 0.5. The few cases where the population fraction was higher than 0.5 may be the result of system drift leading to imperfect initial state preparation or fitting errors. The distribution at low rms amplitudes peaked at 0.0 and as the rms amplitude increased an even distribution of final states was observed (between 0.0 and 0.5). At higher

rms amplitudes the system began to re-localise ($p_0 = 0$) but at a slower rate than for the case of the $m_F = +1$ state.

For the $m_F = -1$ state, the population was initially localised at zero for low rms amplitudes. As the rms amplitude increased the state still remained peaked at zero but there were discontinuities in the distribution that increased the average of the distribution. In conclusion the response of the system was noisy and non-Gaussian, however, the average of the response of the system followed the expected theoretical behaviour.

### 5.5.7 Summary of the system response to white noise perturbation

The localisation, environment-assisted quantum transport and Zeno like regimes have been observed in the dependence of the magnetisation response on the white noise amplitude. The response of the system was noisy and non-Gaussian, however, the model of the density of states interpretation was found to predict the average shape of the response. Fermi's golden rule was used to explain the low amplitude dependence of the magnetisation on the rms noise amplitude. The effect of the resonant structure was discussed and will be investigated further in the next section.

## 5.6 The response of the system to spectrally shaped perturbations

As discussed previously the system response contains multiple resonances that result from the different coupling paths discussed in section 4. By changing the shape of the perturbation spectrum, different resonances and therefore different transport paths can be targeted and the interplay between them investigated. This section will outline the spectral shapes of the

perturbations that were used to investigate the effect of the different transport paths and the experimental procedure used to determine the rate of transfer for the different spectral shapes of the perturbations. The results are then discussed and compared with reference to the theoretical models outlined in section 2. Finally the results will be discussed with reference to the sideband model.

### 5.6.1 Experimental procedure

Filter functions were generated that contained the features of the spectrum required to investigate a particular perturbation spectrum shape. Figure 5.8 shows the shapes of the filter functions used in this series of experiments. The selected perturbations were: 1) a wide frequency band ($0-100kHz$) that covered all the resonances, 2) a reduced band ($0-50kHz$) also covered all the resonances and was used to understand the influence of the off-resonant high frequency components in the $50-100kHz$ range, 3) a band ($0-20kHz$) that was used to investigate just the effect of the sub-resonances, 4) a band ($20-40kHz$) that only covered the fundamental resonance of the system and finally 5) a $10kHz$ wide band that had a Lorentzian shape centred at the generalised Rabi frequency and was used to investigate the influence of a more complex spectral structure.

For each perturbation shape, the evolution time was initially kept constant and the rms amplitude of the perturbation was varied, as in section 5.5.1. From this measurement the optimum rms amplitude at which the transport was maximised for a fixed evolution time could be determined. For every time and rms amplitude 25 realisations of the perturbation were applied. The evolution time was varied for the optimum rms amplitude to determine the rate of transport (the time derivative of the magnetisation). The rate of transport was determined at rms amplitudes slightly greater and less than the optimum in order to verify that the response at the optimum rms amplitude corresponded to the fastest rate of transport.

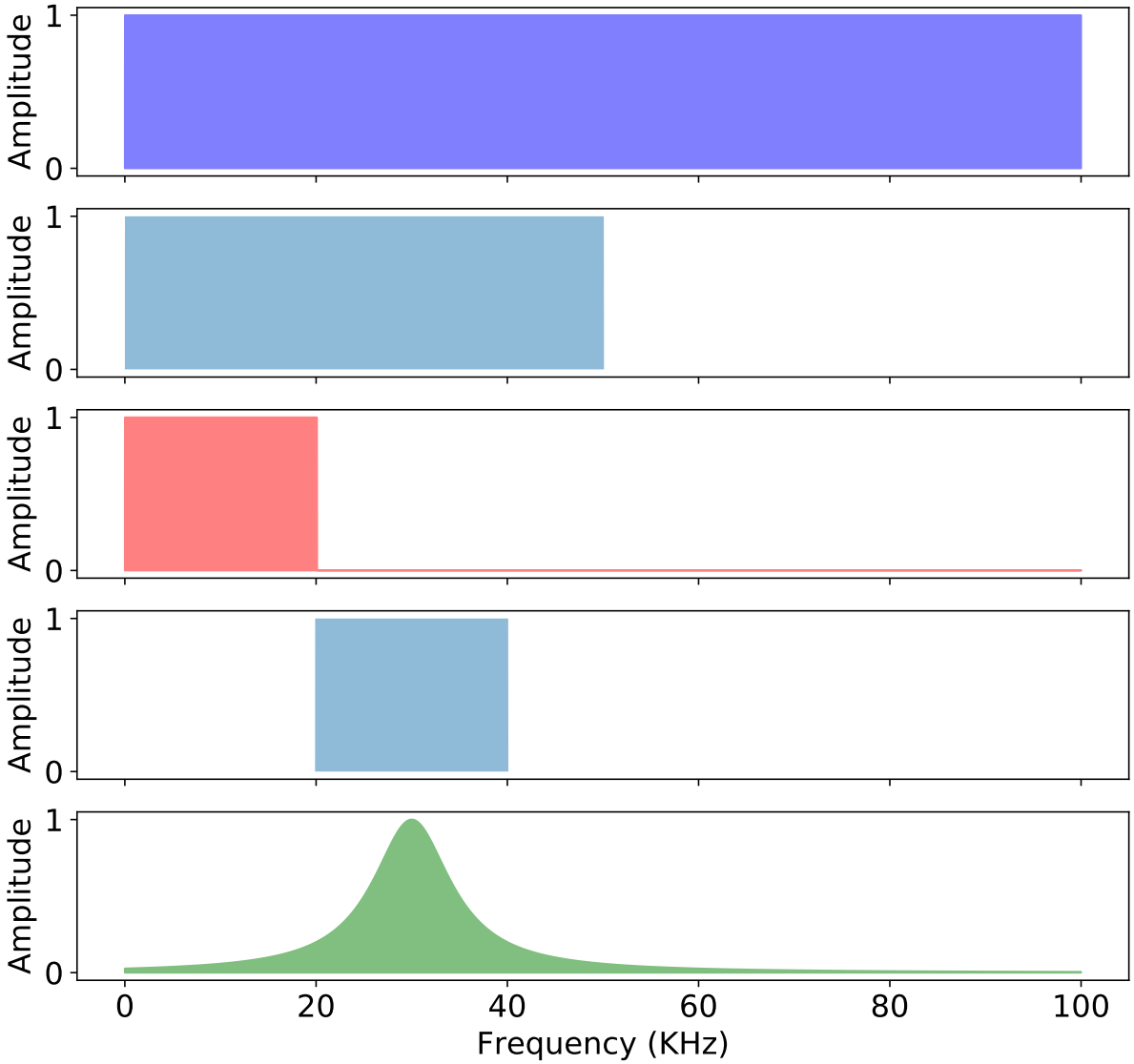


Figure 5.8: **Filter functions used in this study:** The shape of the filter functions used to generate the perturbations in this study (from top to bottom); $0-100kHz$ band, $0-50kHz$ band, $0-20kHz$ band, $20-40kHz$ band and Lorentzian band of width $10kHz$ centred at the generalised Rabi frequency.

| Band | Optimum rms amplitude |
|---|---|
| 0-100kHz | $58 \pm 4kHz$ |
| 0-50kHz | $45 \pm 2kHz$ |
| 0-20kHz | $57 \pm 4kHz$ |
| 20-40kHz | $39 \pm 2kHz$ |
| Lorentz 10kHz | $37 \pm 2kHz$ |

Table 5.1: **Summary of the optimum rms amplitudes:** The optimum rms amplitudes for the different perturbations under investigation.

The experiments were based on the assumption that the rms amplitude of the environmental perturbations was not the limiting factor affecting the optimisation of transport in biological systems and that the systems naturally evolve to maximise the influence of the environmental perturbations. The rate of transport at the optimum rms amplitude for each perturbation shape was therefore taken as the appropriate condition to use to compare the effect of different perturbation shapes.

### 5.6.2 Experimental results for shaped perturbations

#### The dependence of the optimum rms amplitude on the spectral shape

The rms amplitude of each shaped perturbation was varied for a fixed evolution time. The dependence of the magnetisation of the system on rms amplitude for all the shaped perturbations, figures 5.9 to 5.13, shows the typical localisation, ENAQT and quantum Zeno-like regimes that were discussed in the previous section. The theoretical relationship between the magnetisation and the rms perturbation amplitude, equation 5.1 (from the density of states interpretation in section 5.5.3), was used to determine the optimum rms amplitude for each of the shaped perturbations. A summary of the optimum rms amplitudes for the different spectral shapes is presented in table 5.1.

The optimum rms amplitudes were dependent upon the spectrum of the perturbation and therefore, based on this observation, the optimum rms amplitude does not have a simple

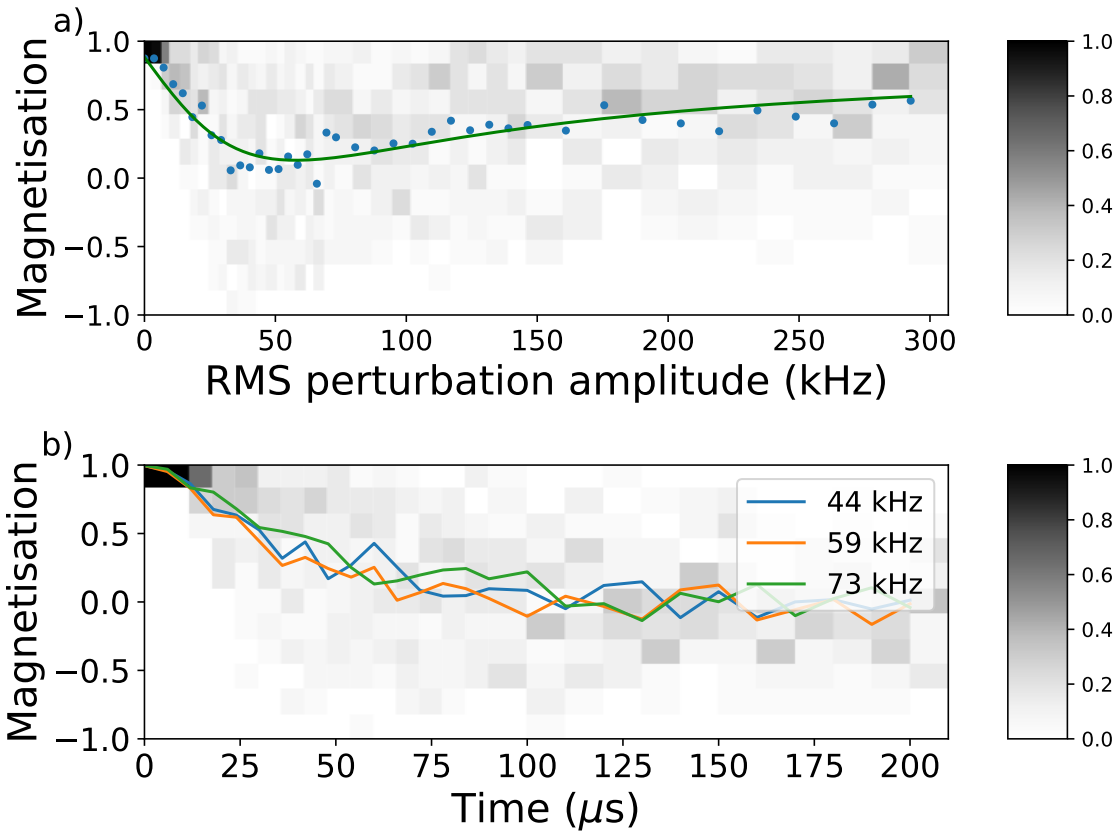


Figure 5.9: **The magnetisation of the system in response to the $0 - 100kHz$ perturbation:** a) The dependence of the system magnetisation on the rms amplitude applied for an evolution time of $60\mu s$ (the rms amplitude is in units of frequency in order to provide comparison with the energy separation of the magnetic sub-states ($\approx 1MHz$)). b) The dependence of the system magnetisation on evolution time for fixed rms amplitudes of $44kHz$, $59kHz$ and $73kHz$. The vertical histograms show the population distribution of the 25 realisations and the colour in the key corresponds to the fraction of the 25 realisations that were in the final state. The histogram in b) only displays data from the $59kHz$ response.

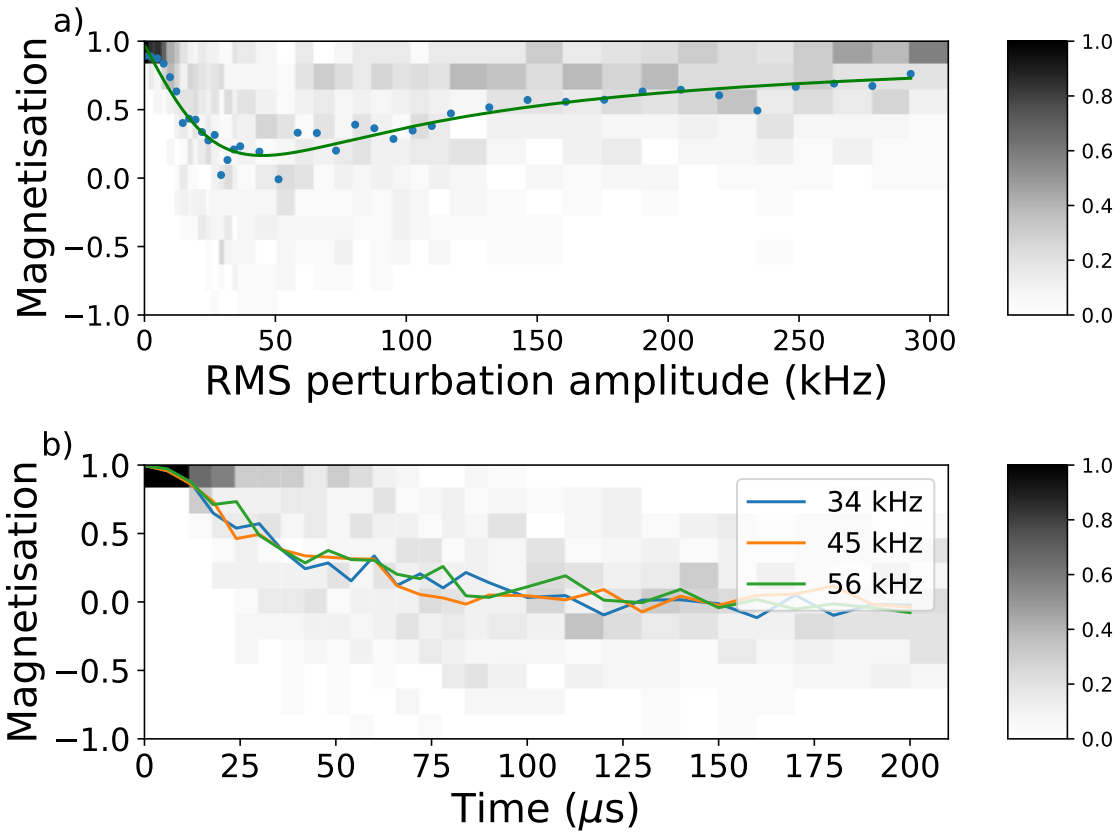


Figure 5.10: **The magnetisation of the system in response to the $0 - 50kHz$ perturbation:** a) The dependence of the system magnetisation on the rms amplitude applied for an evolution time of $60\mu s$ (the rms amplitude is in units of frequency in order to provide comparison with the energy separation of the magnetic sub-states ($\approx 1MHz$)). b) The dependence of the system magnetisation on evolution time for fixed rms amplitudes of $34kHz$, $45kHz$ and $56kHz$. The vertical histograms show the population distribution of the 25 realisations and the colour in the key corresponds to the fraction of the 25 realisations that were in the final state. The histogram in b) only displays data from the $45kHz$ response.

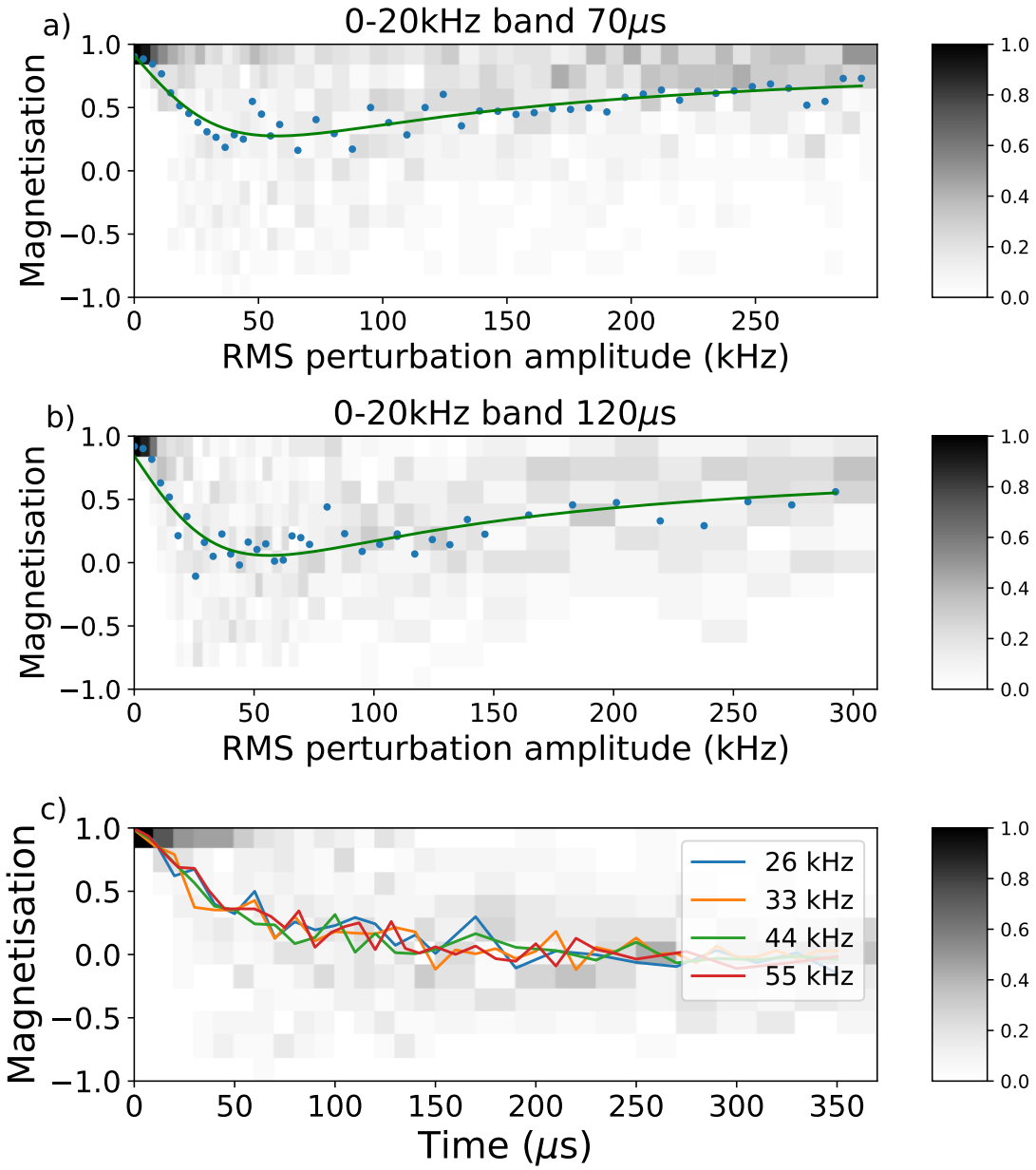


Figure 5.11: **The magnetisation of the system in response to the $0 - 20kHz$ perturbation:** a) and b) The dependence of the system magnetisation on the rms amplitude applied for an evolution time of $70\mu s$ and $120\mu s$ respectively (the rms amplitude is in units of frequency in order to provide comparison with the energy separation of the magnetic substates ($\approx 1MHz$)). c) The dependence of the system magnetisation on evolution time for fixed rms amplitudes of $26kHz$, $33kHz$, $44kHz$ and $55kHz$. The vertical histograms show the population distribution of the 25 realisations and the colour in the key corresponds to the fraction of the 25 realisations that were in the final state. The histogram in c) only displays data from the $44kHz$ response.

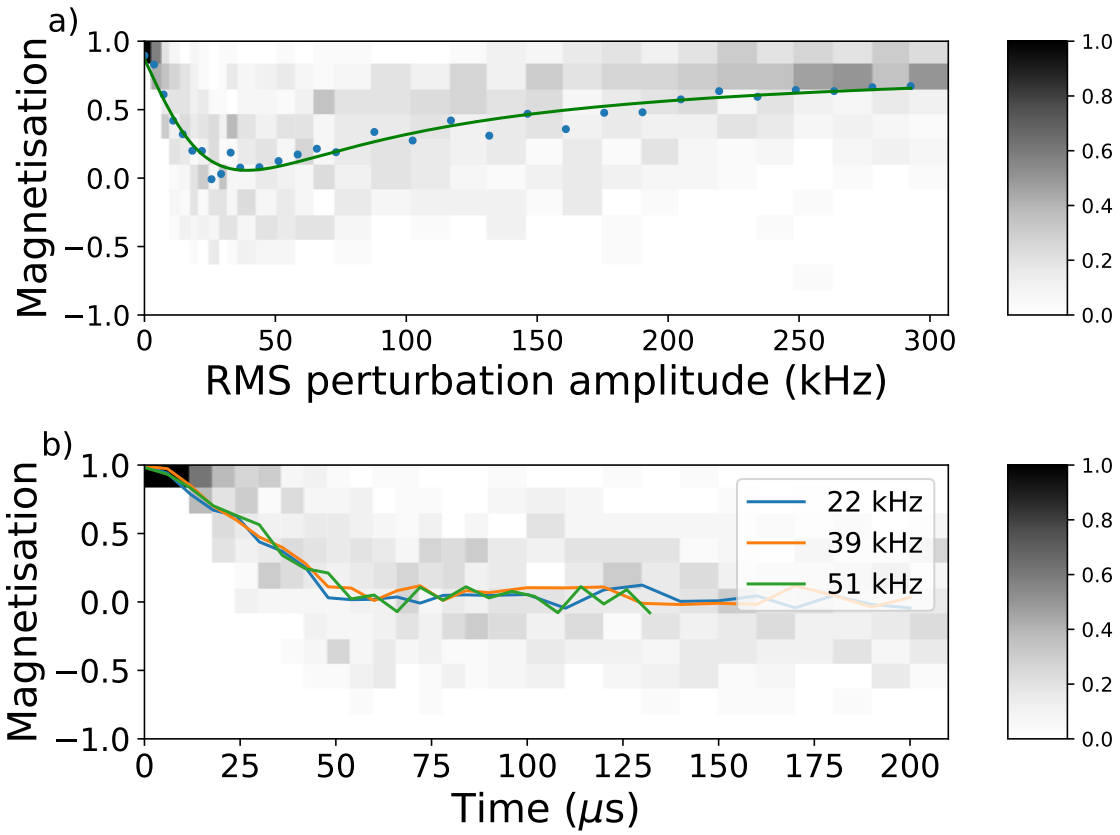


Figure 5.12: **The magnetisation of the system in response to the** $20 - 40kHz$ **perturbation:** a) The dependence of the system magnetisation on the rms amplitude applied for an evolution time of $70\mu s$ (the rms amplitude is in units of frequency in order to provide comparison with the energy separation of the magnetic sub-states ($\approx 1MHz$)). b) The dependence of the system magnetisation on evolution time for fixed rms amplitudes of $22kHz$, $39kHz$ and $51kHz$. The vertical histograms show the population distribution of the 25 realisations and the colour in the key corresponds to the fraction of the 25 realisations that were in the final state. The histogram in b) only displays data from the $39kHz$ response.

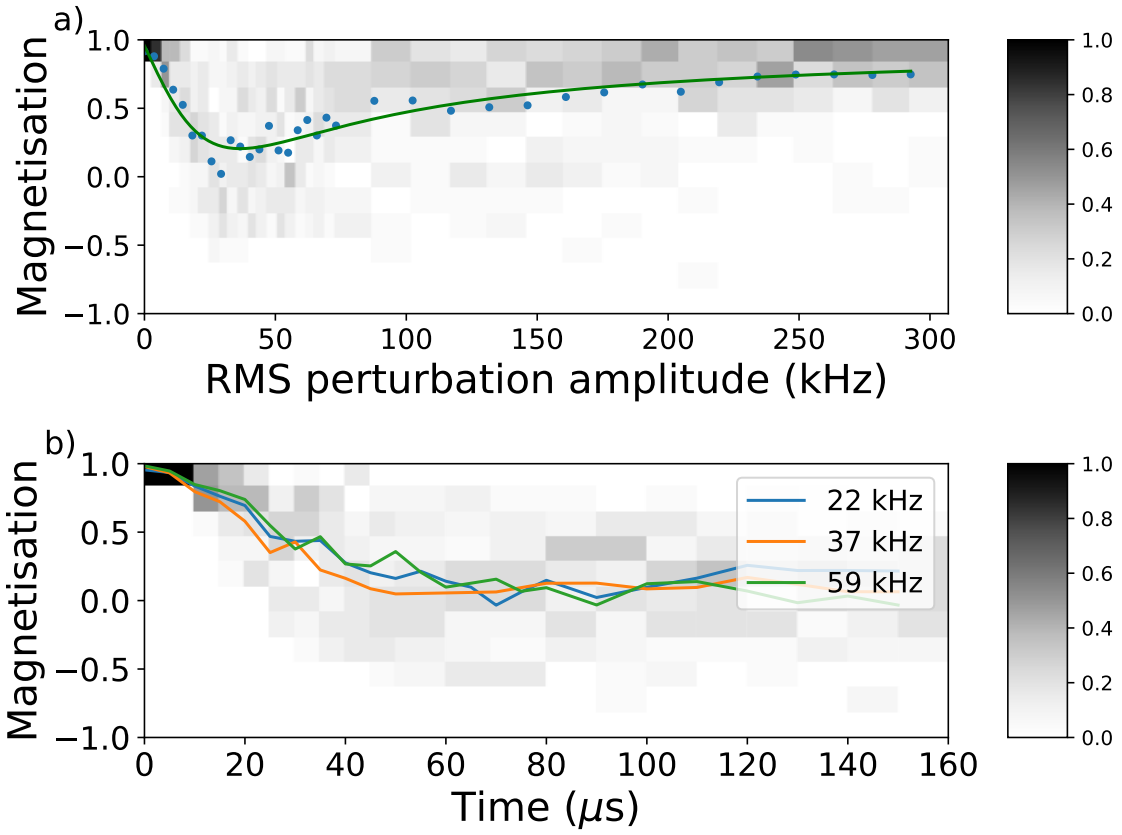


Figure 5.13: **The magnetisation of the system in response to the $10kHz$ width Lorentzian perturbation:** a) The dependence of the system magnetisation on the rms amplitude applied for an evolution time of $40\mu s$ (the rms amplitude is in units of frequency in order to provide comparison with the energy separation of the magnetic sub-states ($\approx 1MHz$)). b) The dependence of the system magnetisation on evolution time for fixed rms amplitudes of $22kHz$, $37kHz$ and $59kHz$. The vertical histograms show the population distribution of the 25 realisations and the colour in the key corresponds to the fraction of the 25 realisations that were in the final state. The histogram in b) only displays data from the $37kHz$ response.

relationship to the detuning or the generalised Rabi frequency. The Lorentzian shaped perturbation of width $10kHz$, centred at the fundamental resonance, required the lowest rms amplitude to maximise transport. This suggests that the path corresponding to the fundamental resonance induced the most efficient optimal transport and therefore could have the largest contribution to the transport in the case of a wideband perturbation. The optimum rms amplitude for the $20 - 40kHz$ band was the next smallest and was followed by the $0 - 50kHz$ band. Finally the rms amplitude of the $0 - 100kHz$ and that of the $0 - 20kHz$ were similar to each other, despite the amplitude density of the $0 - 20kHz$ band being much greater than the $0 - 100kHz$ band, see section 5.4.1. In addition the observation that the $20 - 40kHz$ band required an optimum rms amplitude less than the $0 - 20kHz$ band leads to the conclusion that the sub-resonance transport channel was weaker than the fundamental channel.

### Determining the transport rate

As discussed previously the perturbation rms amplitudes were fixed at values close to the optimum and then the evolution time was varied. As can been seen in figures 5.9 to 5.13 the system was robust in response to variations of the perturbation rms amplitude near the optimum for all the spectrally shaped perturbations under investigation. This may explain why the noise assisted transport mechanism could operate in natural systems that exist in strongly varying environments. Figure 5.14 shows a summary of the effect of changing the evolution time at the optimum rms amplitudes for the different perturbation spectra under investigation. Three regimes with respect to time were generally observed, 1) a quadratic response at short times, 2) a linear response at intermediate times, and 3) an exponential dependence at longer times. These regimes will be discussed in the rest of this section.

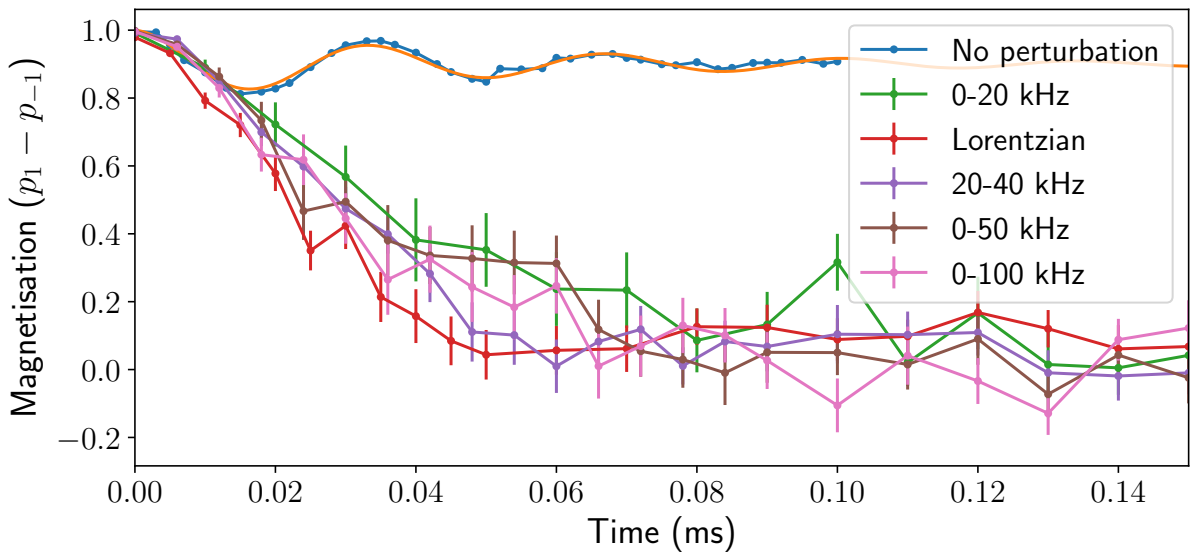


Figure 5.14: **Response of the magnetisation of the system to different perturbation spectral shapes:** The response of the magnetisation to the different spectral shapes is shown. The behaviour of the system for no perturbation is included in order to provide comparison.

The initial quadratic dependency for all the responses was similar to the response of the fast oscillating ($\tilde{\Omega} = 30kHz$) waveform that corresponded to the dressing of the base states by the RF field, shown as the response of the system for no perturbation in figure 5.14. The Lorentzian response had a slightly larger quadratic coefficient than the rest of the responses, however, due to the limited number of measurements at short times this could be accounted for by statistical fluctuations.

A linear response at intermediate times can clearly be observed for the $20 - 40kHz$ and Lorentzian band results. This is similar to the results for Fermi's golden rule, discussed in 2.6, where the transfer rate between dressed states is predicted to be constant, however the exact mapping between transfer in the dressed state basis to transfer in the base state basis (which is the basis that is measured in) is complex and therefore can only provide an indication of the expected behaviour. For $20 - 40kHz$ the gradient of the linear response was $17 \pm 1kHz^{-1}$

and the Lorentzian was greater at $21 \pm 2kHz^{-1}$ which supports the hypothesis that the higher the density of the frequency components close to the fundamental resonance the faster the transport rate. For the other shaped perturbations a linear fit was attempted, but with less confidence as the data sets have a significant non-linear component. The measured linear response of the $0 - 20kHz$ band was $14 \pm 2kHz^{-1}$, the $0 - 50kHz$ band was $14 \pm 2kHz^{-1}$ and the $0 - 100kHz$ band was $16 \pm 2kHz^{-1}$. These were all similar and lower than the Lorentzian and the $20 - 40kHz$ bands, further supporting the conclusion that transport was driven faster by frequencies near the fundamental resonance.

At longer times the $0-20kHz$, $0-50kHz$ and $0-100kHz$ bands showed a clear exponential response consistent with the operation of an incoherent transfer process between the dressed states and were modelled using the rate equations discussed in section 2.6. The $0 - 20kHz$ band had the slowest exponential decay time with a time constant of $(44 \pm 8)\mu s$, this was consistent with the experimental results from section 4, namely that the sub-resonances evolved at a slower rate than the fundamental resonance, but could still induce transport. The response of the system to the $0 - 50kHz$ and $0 - 100kHz$ perturbation shapes were similar to each other and were measured as $(31 \pm 4)\mu s$ and $(32 \pm 5)\mu s$ respectively. This led to the conclusion that the effect of frequencies in the range $50 - 100kHz$ on the transport rate was minimal. The $20 - 40kHz$ band had a response time of $(23 \pm 3)\mu s$ and the fastest response overall was the Lorentzian band at $(16 \pm 2)\mu s$. This further reinforces the conclusion that the transport was most enhanced by frequencies close to the fundamental resonance.

Considering these results a further conclusion can be reached that, based on the $20-40kHz$ band producing a faster rate of transport than the $0-50kHz$ band, the effect of the different transfer paths (sub-resonances and fundamental) were not additive and the combined effect of the $20 - 40kHz$ and $0 - 20kHz$ bands was actually to suppress transport relative to the $20 - 40kHz$ band. An explanation of this behaviour may be that the combination opened

up more paths for transport (with hugely different Rabi frequencies) and thus higher levels of dephasing (and interference) compared with the case of a frequency band that covers a single resonance.

### 5.6.3 Conclusions

In conclusion perturbation frequencies from $50 - 100kHz$ were shown to have very little effect on the evolution of the system. This conclusion results from a negligible difference in the rate of transport observed between the $0 - 50kHz$ and $0 - 100kHz$ bands. In addition, based on the $20 - 40kHz$ band producing a faster rate of transport than the $0 - 50kHz$ band, the combined effect of the different transfer paths (sub-resonances and fundamental) was found to suppress transport. Furthermore the responses of the system had quadratic, linear and exponential time regimes which are indicative of incoherent transfer processes between the dressed states, as shown in section 2.6.

The results additionally support the conclusion that frequencies applied at the frequency corresponding to the dressed state splitting (fundamental resonance) had the greatest contribution to transport. Dephasing assisted transport, whereby low frequency noise dephases the state, was studied using the $0 - 100kHz$ and the $0 - 50kHz$ perturbations, as discussed in the introductory chapter. The Lorentzian band, centred at the generalised Rabi frequency, was used to model a vibrational environment that induces transport between the dressed states, as also discussed in the introductory chapter. The Lorentzian band resulted in a faster transport rate than the $0 - 100kHz$ and the $0 - 50kHz$ bands and this implies that vibrational assisted transport may be a faster transport mechanism than dephasing assisted transport.

### 5.6.4 Sideband interpretation of the effect of shaped perturbations

The sideband interpretation used in section 4.7 to explain the effect of single frequency perturbations on the system can also be applied to the incoherent perturbation spectra investigated in this series of experiments. From section 4.7 the effect of an incoherent perturbation can be investigated theoretically by transforming to a rotating frame that has a rotation frequency that varies dynamically with the energy level splitting, thus removing the oscillating components of the modulation field. This modulates the coupling between the states due to the RF field by a factor of A(t) as shown in the Hamiltonian

$$H = \sqrt{2}\hbar\Omega_{RF}\cos(\omega_{RF}t)A(t)e^{i\omega_0 t}\begin{pmatrix} 0 & 1 & 0 \\ 1 & 0 & 1 \\ 0 & 1 & 0 \end{pmatrix} \tag{5.4}$$

where A(t) is

$$A(t) = e^{i\xi(t)} \tag{5.5}$$

and

$$\xi(t) = \int_0^t \delta(t).dt \tag{5.6}$$

and $\delta(t)$ is the incoherent perturbation composed of multiple frequencies [76]. The static component of the coupling matrix element, c=$\langle\Omega_{RF}\cos(\omega_{RF}t)A(t)e^{i\omega_0 t}\rangle$, is referred to as the strength of the on-resonant coupling, and is related to the rate of transport.

The strength of the static component, $c$, can be determined by taking the Fourier transform of $A(t)e^{i\omega_0 t}$, an example of this is shown in figure 5.15. In figure 5.15 the average of the modulus of the Fourier transform of $A(t)e^{i\omega_0 t}$ for $\omega_0 = 1000kHz$ and $\omega_{RF} = 1030kHz$ for

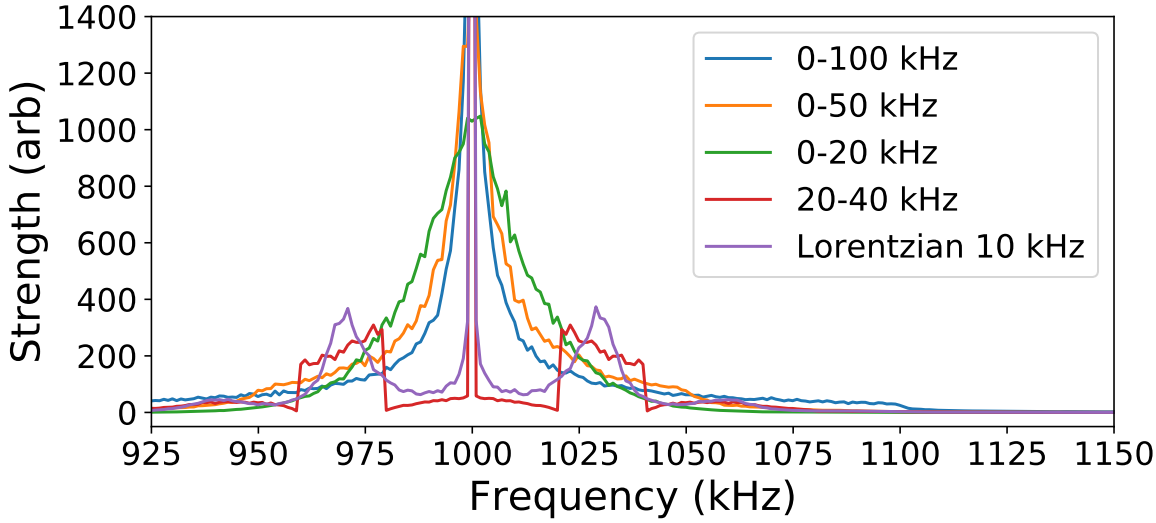


Figure 5.15: **An example of the modulus of the Fourier transform of $A(t)e^{i\omega_0 t}$:** The Fourier transform of $A(t)e^{i\omega_0 t}$ plotted for a rms perturbation amplitude of $50kHz$ for different perturbation shapes.

100 realisations of the noise field is plotted. The amplitude of the frequency component which is on-resonance, $c$, is the frequency components corresponding to $\omega_{RF}$ ($1030kHz$). The dependence of the strength, c, of the on-resonance frequency component on the rms perturbation amplitude is plotted in figure 5.16 for the different perturbation shapes. The graph has a similar shape to the experimental plots of the dependence of the magnetisation on the rms perturbation amplitude. An example of a experimental graph is shown in figure 5.4. At high rms perturbation amplitudes the strength of the coupling is reduced due to the power being dissipated across higher order sidebands.

The results in figure 5.16 broadly agree with the experimental measurements of the rate of transport for the different perturbations, figure 5.14. Analysis using the sideband model determined that the Lorentzian shaped perturbation had the highest strength and this may be why it had experimentally the fastest rate of transport. The rms perturbation amplitude for which the maximum strength occurs for the $0-50kHz$ band is less than the $0-100kHz$

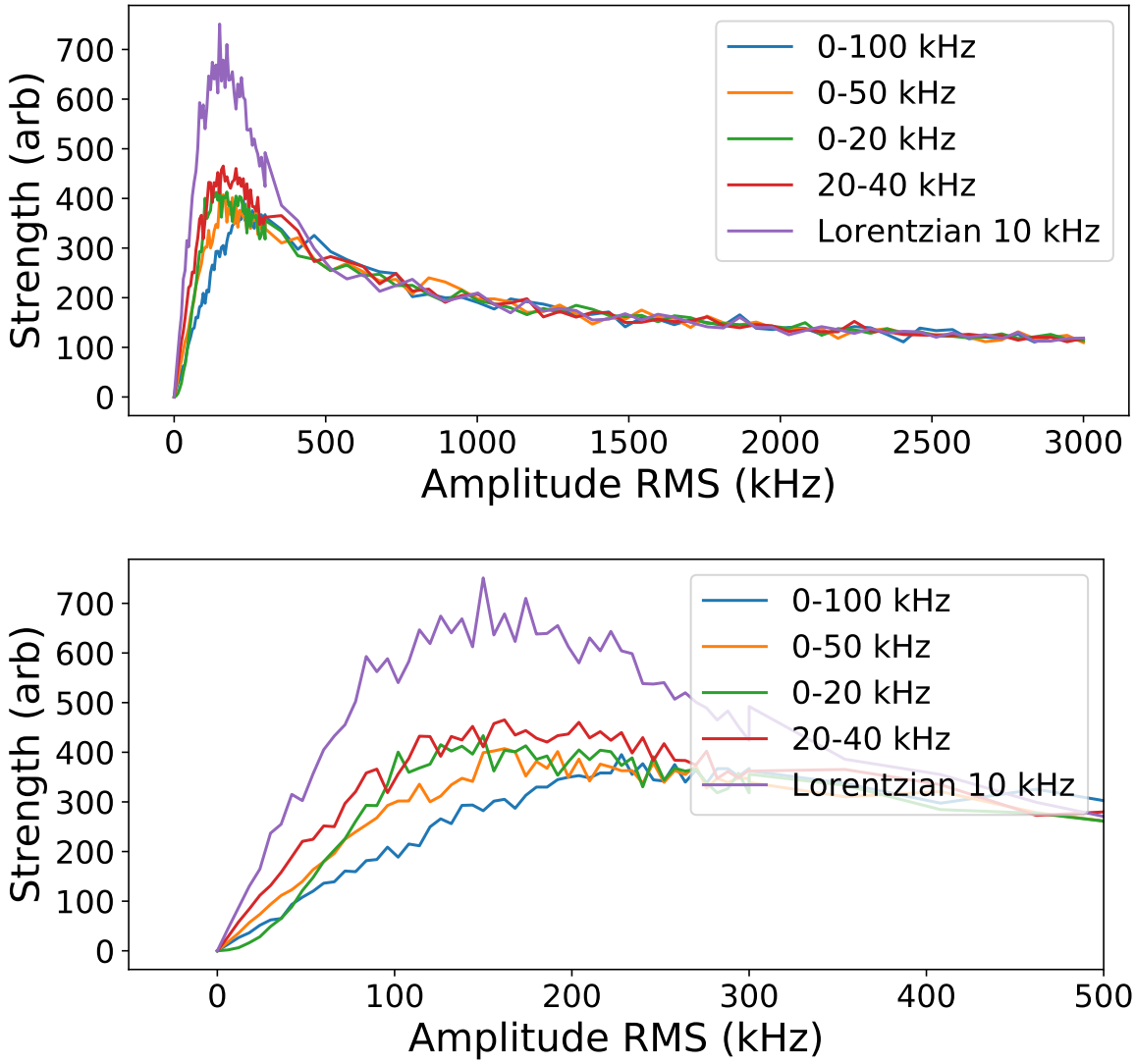


Figure 5.16: **The dependence of the strength of the on-resonance Fourier component, $c$, on the rms amplitude of the perturbation of different perturbation shapes:** The strength of the on-resonance Fourier component, $c$, is in arbitrary units.

band, agreeing with the experimental results for the optimum rms amplitude. The only anomaly is the $0-20kHz$ band, this had a transport rate experimentally less than the other bands, but a similar maximum strength to that determined from the sideband model. This may be because the 1st mode resonance experimentally has a large Bloch-Siegert shift that moves the resonance to higher frequencies where the coupling strength, c, is theoretically lower. Finally the $0-20kHz$ band had a quadratic dependence at low rms amplitudes consistent with the 2nd order Bessel function discussed in section 4.7.

In conclusion the sideband model broadly agrees with the experimental results and provides a good explanation of the relative rates of transport produced by the perturbation shapes used in this study.

## 5.7 Effect of the spectral width of the noisy Lorentzian perturbation

In the previous section it was experimentally demonstrated that the Lorentzian band of width $10kHz$ centred at the generalised Rabi frequency ($30kHz$) produced the fastest rate of transport. This band isolated the effect of the fundamental resonance on the population transfer rate. In this section the effect that the width of the Lorentzian band has on transport will be experimentally investigated.

The $10kHz$ width Lorentzian band was compared with a Lorentzian band where the width was restricted to $5kHz$. To provide a direct comparison with the $10kHz$ width Lorentzian band the optimum rms amplitude, previously determined for the 10kHz band, was also used for the $5kHz$ width Lorentzian band. The evolution time was varied and figure 5.17 shows the dependence of the magnetisation on evolution time. Evidence of coherent transport was

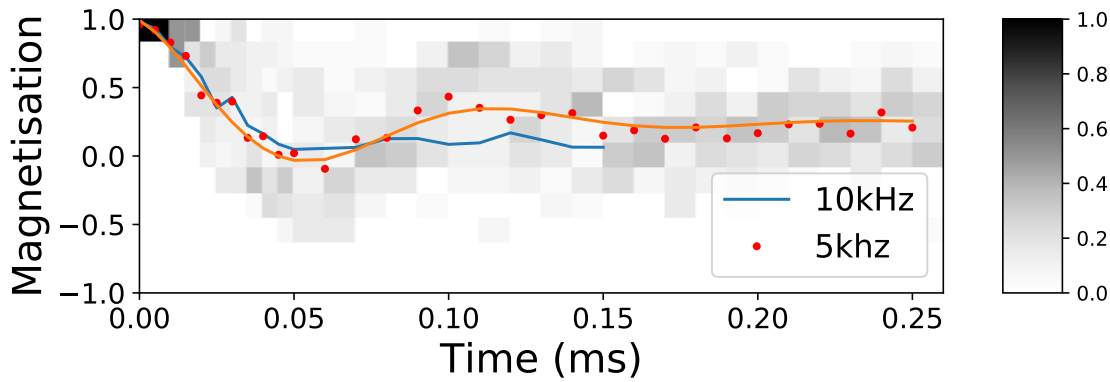


Figure 5.17: **The response of the magnetisation of the system to the $5kHz$ width Lorentzian perturbation frequency band:** The dependence of the magnetisation of the system on the evolution time for a fixed rms amplitude of $36kHz$.

clearly observed as a damped oscillation of the magnetisation of the system over the evolution time range (frequency $8.3 \pm 0.3kHz$, amplitude $0.75 \pm 0.05$ and damping constant $(59 \pm 8)\mu s$). The distribution of the 25 realisations showed clustering around the average behaviour, which is also typical of deterministic coherent transfer processes. This result suggests that, as the width of the frequency distribution of the noise reduces, the dephasing of the response of the system will reduce until the response approaches that of the single modulation frequency case discussed in chapter 4. The width, therefore, acts to introduce dephasing into the system and thus the $10kHz$ width Lorentzian band could be the critically damped single frequency case. This may support the hypothesis that the fastest rate of transport will be seen for responses that have a coherent component to their evolution.

## 5.8 The effect of Static Disorder

In a large biological system composed of many photosynthetic complexes there is often static variation of the resonant absorption frequencies between the components of the system, referred to as "static disorder". If a single frequency perturbation, therefore, is applied to

the system only a limited number of the complexes will be able to absorb the perturbation energy resulting in low transport through the overall system. The static disorder could be overcome by increasing the power of the perturbation and therefore broadening the resonant response of each individual complex (power broadening [103]) and hence increasing the overall transport. In the experimental system currently under investigation, however, it has been observed that there was a maximum power of the perturbation that could be applied using a single frequency. This is because the un-modulated dressing of the system by the RF coupling field breaks down at high power (section 4.7) reducing the strength of the response. In some cases it may therefore be beneficial to broaden the spectral composition of the perturbation in order to resonate with a greater number of the components of the system.

The effect of static disorder can be understood by considering the average response of a two level system with a coupling of $\Omega_{RF}\cos(\omega_{RF}t)\sigma_x$ where the splitting of the energy levels, $\omega_0(n)$, follows a Lorentzian distribution (figure 5.18a). In this case the average evolution of an excitation in the lower energy state due to the application of the Hamiltonian

$$H = \begin{pmatrix} \omega_0(n) & \Omega_{RF}\cos(\omega_{RF}t) \\ \Omega_{RF}\cos(\omega_{RF}t) & 0 \end{pmatrix} \tag{5.7}$$

can be used to model the effect of the static disorder.

Figure 5.18 shows the results of a computational simulation of the response of an ensemble of systems that have a Lorentzian distribution of detunings centred around zero for an on-resonance coupling frequency of $40kHz$. As the width of the distribution, the static disorder, increases the probability that an individual system will have a detuning of zero is reduced, as shown in figure 5.18b. The response of a large collection of systems that have detunings that follow the probability distribution has been averaged and is shown in figure 5.18c. Dephasing

behaviour and reduced amplitude of the oscillation of the population in the lower state is observed as the frequency range increases. This is because higher detunings have a lower response amplitude than systems that are on-resonance. The probability distribution of the generalised Rabi frequencies of the ensemble of systems is shown in figure 5.18 d,e and f. The Rabi frequency of $40kHz$ is the resonance frequency of the system for all the distributions, but as the width increases the distribution spreads and the probability at $40kHz$ reduces, increasing the spread of the frequency components and also the magnitude of the dephasing.

The reduction of the amplitude of the oscillation is shown experimentally in section 4.6.4, where the atoms have a range of different resonant frequencies due to the inhomogeneity of the bias field. The static disorder was determined in this experimental system from the relationship between the on-resonance amplitude and the applied RF coupling power. It was estimated to be approximately $5kHz$ determined from the overlap of the energy of the state and the power broadening.

For the case of an ensemble where the average of the detuning of the coupling field relative to the transition frequency is not zero, the presence of static disorder increases the overlap between the ensemble and the coupling field. This slightly increases the overall transport rate because for intermediate detunings there is a non-linear dependence of the amplitude response on the detuning. Some systems that make up the ensemble consequently become more on-resonant as a result of the static disorder and this has a larger positive effect on the transport than the reduction due to an equal number of systems becoming more off-resonant. This, however, only has a very small effect on increasing the overlap and thus the transport.

In conclusion static disorder generally reduces the transport except in cases where the system is detuned. In this case the static disorder makes some systems more resonant thus increasing the overall transport, however this effect is small compared with the effect of

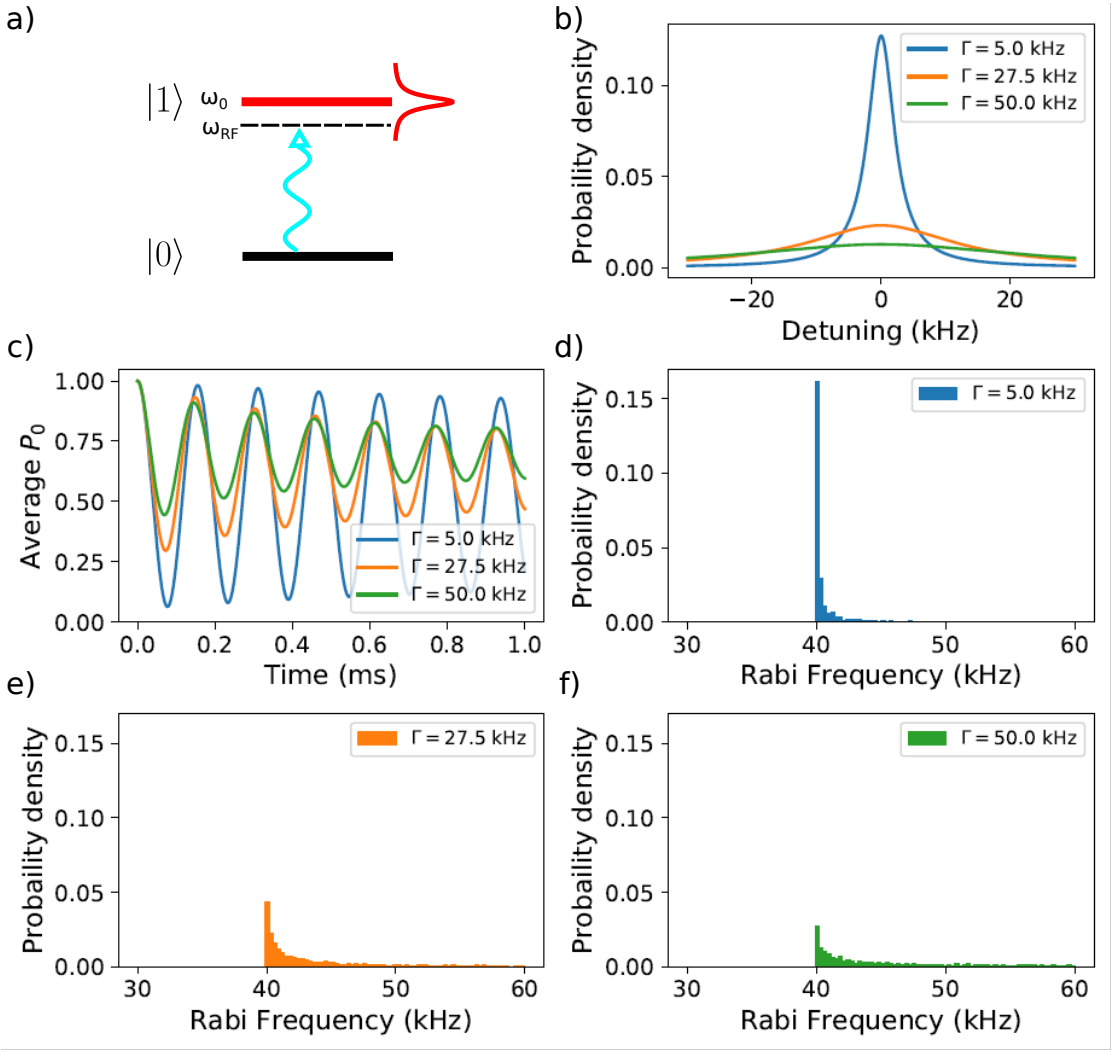


Figure 5.18: **Computational simulation of static disorder:** a) pictorial representation of the two level system under investigation. The distribution of the energy of the upper state has static disorder. The coupling between the states is resonant when $\omega_{RF}$ is equal to $\omega_0$. b) The probability distribution of the detunings for different widths of static disorder. c) The average population response in the lower energy state for different static disorder widths. d),e) and f) the frequency components of the average population response in the lower energy state for the $5kHz$, $28kHz$ and $50kHz$ width bands respectively.

a dynamic perturbation (as discussed earlier in this chapter). The negative effect static disorder has on transport could be minimised by broadening the frequency composition of the perturbation and this may explain why transport in natural systems, that have static disorder, may be enhanced by environmental interactions that have a broadened spectrum.

# CHAPTER 6

# CONCLUSIONS AND FURTHER WORK

## 6.1 Principal conclusions

This study has developed the experimental set-up required to investigate transport through a three site network interacting with a weak coherent coupling field and a classical pure dephasing incoherent noise field. Molasses cooled rubidium 87 atoms were successfully pumped to the $F = 1$ $m_F = +1$ state to form the initial state of the system with $> 95\%$ purity, where purity is defined as the population of the atoms in the $F = 1$ $m_F = +1$ state relative to the total population in the $F = 1$ state. The coupling and noise under investigation has then been applied and the resultant population distribution between the $m_F$ states has been accurately recorded using a Stern-Gerlach magnetic gradient and absorption imaging measurement system.

Work has progressed on the implementation of a multiply connected network using Raman coupling between the $m_F = \pm 1$ states. Initial results have determined the need to increase the frequency of the Raman Rabi oscillations and also to reduce the effect of decoherence caused by inhomogeneous coupling across the atoms induced by distortion of the Raman beams.

The effects of single frequency pure dephasing perturbations of the site energies on the weakly coupled system have been investigated. Full coherent transfer between the base states has been observed when the perturbation frequency was at integer fractions of the generalised Rabi frequency. These resonances were interpreted as photon transitions between the dressed states using Floquet theory. The dependence of the Bloch-Siegert shift, Rabi frequency and the width of the resonances on the modulation amplitude have been characterised and found to be in good agreement with Floquet theory for low perturbation amplitudes. The only discrepancy found was in the resonant Rabi frequency response of the two photon ($1^{st}$ mode, $\omega_m = \Omega_{gen}/2$) resonance that had a measured coefficient of the quadratic dependency which was significantly less than the theoretically predicted value. This discrepancy most likely originated from a combination of the large Bloch-Siegert shift and that the modulation can no longer be treated as a perturbation of the RF dressed system for the large modulation amplitudes associated with the 1st mode resonance.

The response of the Rabi frequency of the fundamental resonance at high perturbation amplitudes was partially explained using the sideband model. The sideband model allows the dynamics of the system to be determined by calculating the system dynamics in a rotating frame that has dynamic variation of its rotation rate depending on the modulation of the energy levels. This leads to a modulation of the RF coupling in the rotating frame. The Bessel function response of the Rabi frequency of the fundamental resonance was characterised using this method and discussed with reference to coherent destruction of tunnelling. Differences from Floquet theory were interpreted as resulting from the non-resonance coupling frequency components dressing the system.

Mechanisms of transport resulting from the fluctuating environment in the FMO have been modelled, giving insights into the equivalent biological processes. The effect of a noisy pure dephasing classical field perturbation of the energy levels on the weakly coupled system has

been investigated. An optimum noise amplitude for transport was observed by measuring the dependence of the magnetisation of the system on the amplitude of the noisy perturbation for a fixed evolution time. This showed localisation of the state of the system at low amplitude noise, environmental assisted quantum transport (ENAQT) behaviour at intermediate amplitude noise and Zeno-like behaviour at high amplitude noise. This replicated the observations made in the experiments based on alternative approaches discussed in section 1.5 that was a key aim of this study. In addition this study found a good agreement between this response and the density of states interpretation. Finally transport through the system was observed to be strongly dependent upon the frequency components of the noisy perturbation. This led to the conclusion that because there is not a simple relationship between the optimum noise amplitude and the detuning or generalised Rabi frequency the density of states interpretation cannot fully explain the behaviour of the system.

Vibrational assisted transport (VAT) was modelled using a noisy perturbation field that had a frequency distribution centred at the generalised Rabi frequency. The typical dependence on noise amplitude was observed with localisation at low amplitude noise, environmental assisted quantum transport (ENAQT) behaviour at intermediate amplitude noise and Zeno-like behaviour at high amplitude noise. This verifies and builds on experiments results obtained from superconducting qubit experiments [18] where this same dependence using Lorentzian shaped noise was observed. The conclusion of this part of the study was that VAT transferred the population at a faster rate than dephasing assisted transport (DAT), for the case where the power was optimised. DAT was modelled in this case using a wide-band noisy perturbation field. It was also found that perturbations consisting of only low frequency components, below the generalised Rabi frequency (the frequency corresponding to the energy difference of the dressed states), which cover the resonant frequencies of the sub-resonances, can produce transport.

Finally, the presence of low frequency noise in the perturbation that covers the sub-resonances can reduce the transport rate compared with a frequency band that only covers the fundamental resonance. This may arise from interference effects between different coherent paths. Coherent transfer resulting from a noisy field, that has frequency components centred at the generalised Rabi frequency, was also observed.

## 6.2 Future work

The system could be extended to more realistically model an FMO system. These possible improvements will be discussed in this next section and include 1) implementing a multiply connected network using Raman transitions in order to investigate the effect of interference between competing paths, 2) modelling the reaction centre of the FMO using a sink state, 3) breaking the degeneracy of the energy level splitting between the sites using the non-linear Zeeman effect to model a 'genuine' three level system, 4) implementing perturbations of the energies of the base states that are independent of one another, 5) increasing the number of sites in the system through the use of alternative atomic energy levels, 6) utilising a glass cell in order to reduce the effect of eddy currents and improve the homogeneity of the Raman beams, and 7) investigating non-Markovian dynamics where the environment is dependent upon the state of the system. All of these improvements will help to emulate more features that may play important roles in the transport of the exciton through the FMO complex and thus increase the understanding of how these different features can combine to produce fast and highly efficient transport.

### 6.2.1 Implementing a multiply connected network

As previously discussed, next nearest neighbour Raman coupling has been used to couple $m_F = \pm 1$ states to each other. When combined with next neighbour RF coupling, this forms

a multiply connected network similar to an FMO. A multiply connected network exhibits interference effects between the multiple coherent transfer paths which can result in destructive interference of the transfer from the initial state to the target state and thus limits transport through the network. In this case the role of noise would be to reduce the destructive interference by randomising the phase of the base states and thus increasing the rate of transport through the network.

For destructive interference to occur the frequency of the Raman and RF couplings must be similar. Experimentally this means increasing the frequency of the two-photon Raman Rabi coupling by amplifying the power of the Raman beams, this can be done using a tapered amplifier. The decoherence of the Raman Rabi oscillation will have to be reduced at the same time in order to ensure that the system behaves quantum mechanically over the evolution time of the measurement. In conclusion a multiply connected network will allow the effect of multi-path interference on transport to be investigated.

### 6.2.2 Implementing a sink

The reaction centre is a key feature of FMO systems that could be incorporated into the experimental set-up. Theoretically the reaction centre can be modelled as a population sink that irreversibly transfers population from a site in the network to a sink state. A sink state is a state that is isolated from the rest of the system to which only one-way transfer is possible. The $F = 2$ ground state of the current system could be employed as a sink state. A spontaneous emission process could be used to transfer population from the $F = 1$ $m_F = -1$ site of the system to the $F = 2$ sink state. This could be accomplished using an $F = 1$ to $F' = 2$ $\sigma_+$ polarised beam at high magnetic fields, as shown in figure 6.1. In this case the population would be excited to the $F' = 2$ state, from which it spontaneously decays either back to the $F = 1$ $m_F = -1$ state or more likely to the $F = 2$ sink state due to the higher

branching ratio. The population that returns to the original state will no longer have a phase relationship with the other base states that compose the system and this will therefore lead to decoherence. A higher magnetic field is required if the $F = 1$ to $F' = 2$ $\sigma_+$ polarised beam is to strongly address only the $F = 1$ $m_F = -1$ state. The ratio of the sinking rates between states $F = 1$ $m_F = -1$ and $F = 1$ $m_F = 0$ as a function of the detuning of the excitation beam with the $F = 1$ $m_F = -1$ to $F = 2$ $m_F = 2$ transition is shown in figure 6.2. The higher the magnetic field, the larger the ratio of the scattering and the more the beam will only address the $F = 1$ $m_F = -1$ state and thus the purer the sink.

The incoherent transition to the sink state broadens the energy level of the target state, and thus in some cases can increase the amount of transport through a network by increasing the overlap of the target state with a detuned dressed state. However, for a very high non-adiabatic coupling strength, transport to the target state is suppressed because the energy spread of the target state becomes too diffuse and consequently the transport to the sink state is reduced. In conclusion the use of a sink would greatly increase the complexity of the system and allow more realistic models of FMO systems to be investigated.

### 6.2.3 Realising a 'genuine' three-level system

As discussed in section 2.3 the current system comprises a three-level system that has behaviour similar to a two-level system. A worthwhile extension to this work would be to implement a 'genuine' three-level system where the energies of the levels and coupling strengths are fully independent. This could be achieved by using a large magnetic field where the non-linear Zeeman effect breaks the symmetry of the resonant transition frequency between the $m_F = +1$ & $m_F = +0$ states, and the $m_F = -1$ & $m_F = +1$ states, as shown in figure 6.3. The dependence of the energy of the magnetic sub-states is determined using the Breit-Rabi formula [10]

a)

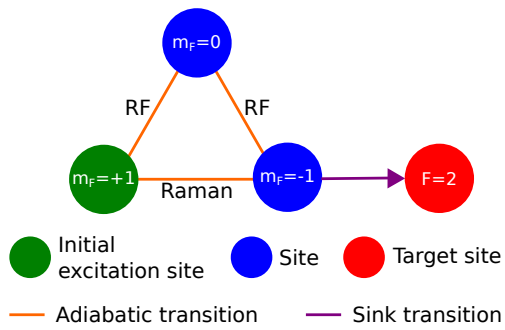


b)

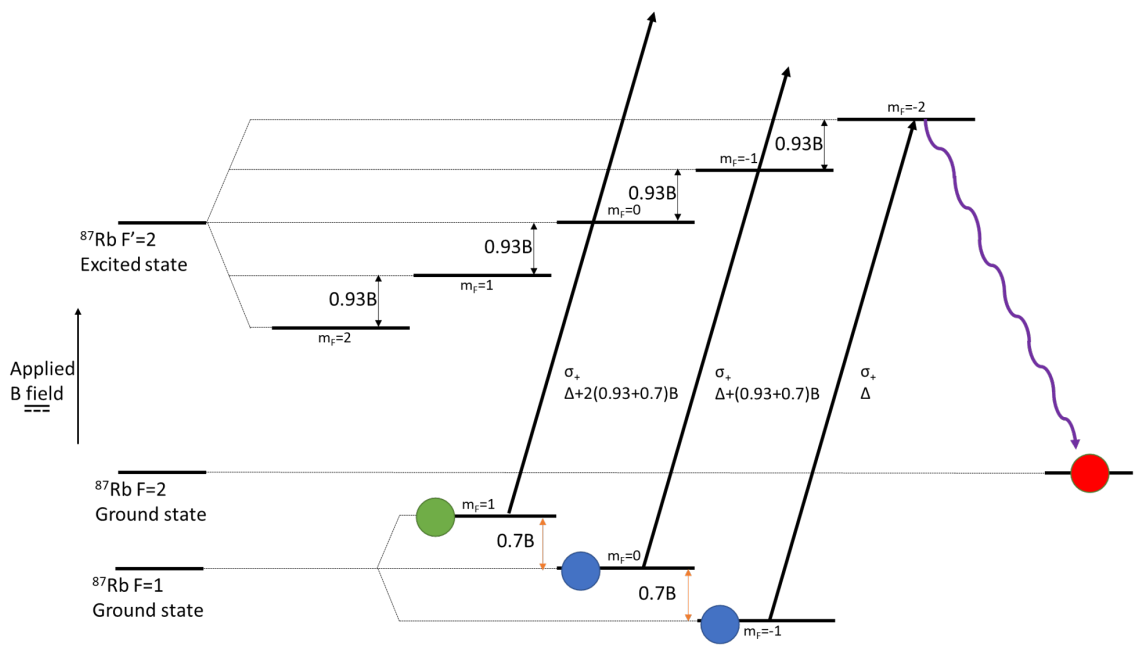


Figure 6.1: **The transitions require to implement a sink state:** a) diagram of the multiply connected network showing the three sites (composed of the magnetic sub-states) and the target state (sink state) that is connected to the network by an irreversible transition, b) the energy level structure and the transitions required to implement a sink state; atoms are excited from the $F = 1$ $m_F = -1$ state to the $F = 2$ $m_F = -2$ where they spontaneously decay to the sink state.

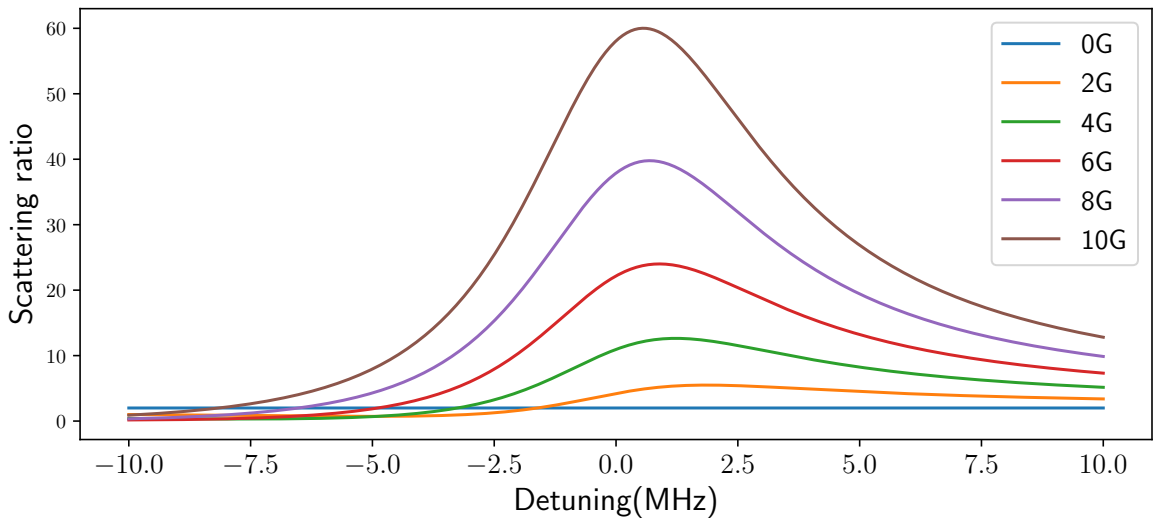


Figure 6.2: **Scattering ratio:** The dependence of the ratio of the scattering of the transition, $F = 1$ $m_F = -1$ to $F = 2$ $m_F = -2$, relative to the transition, $F = 1$ $m_F = 0$ to $F = 2$ $m_F = -1$, on the detuning of the sink beam for magnetic fields from 0-10 Gauss. The detuning is taken relative to the transition $F = 1$ $m_F = -1$ to $F = 2$ $m_F = -2$.

$$E_{m_F} = -\frac{\mathrm{E_{hfs}}}{2(2I+1)} + g_I \mu_B m_F B - \frac{\mathrm{E_{hfs}}}{2}\sqrt{1 + \frac{4m_F x}{2I+1} + x^2} \tag{6.1}$$

where

$$x = \frac{(g_J - g_I)\mu_B B}{\mathrm{E_{hfs}}} \tag{6.2}$$

and

$$\mathrm{E_{hfs}} = \mathrm{A_{hfs}}(I + \frac{1}{2}) \tag{6.3}$$

where $E_{hfs}$ is the hyperfine energy level splitting, $A_{hfs}$ is the magnetic dipole constant, $g_I$ is the nuclear g factor, g is the Lande g factor, $\mu_B$ is the Bohr magneton and I is the nuclear spin. The state energies are initially linear with respect to the magnetic field, as shown in figure 6.3b, but for high magnetic fields the state energies all reduce at the same rate, as shown in figure 6.3a. The theoretical difference between the resonant splitting frequencies of the central state and the two outer states is plotted in figure 6.3c. This difference is quadratically

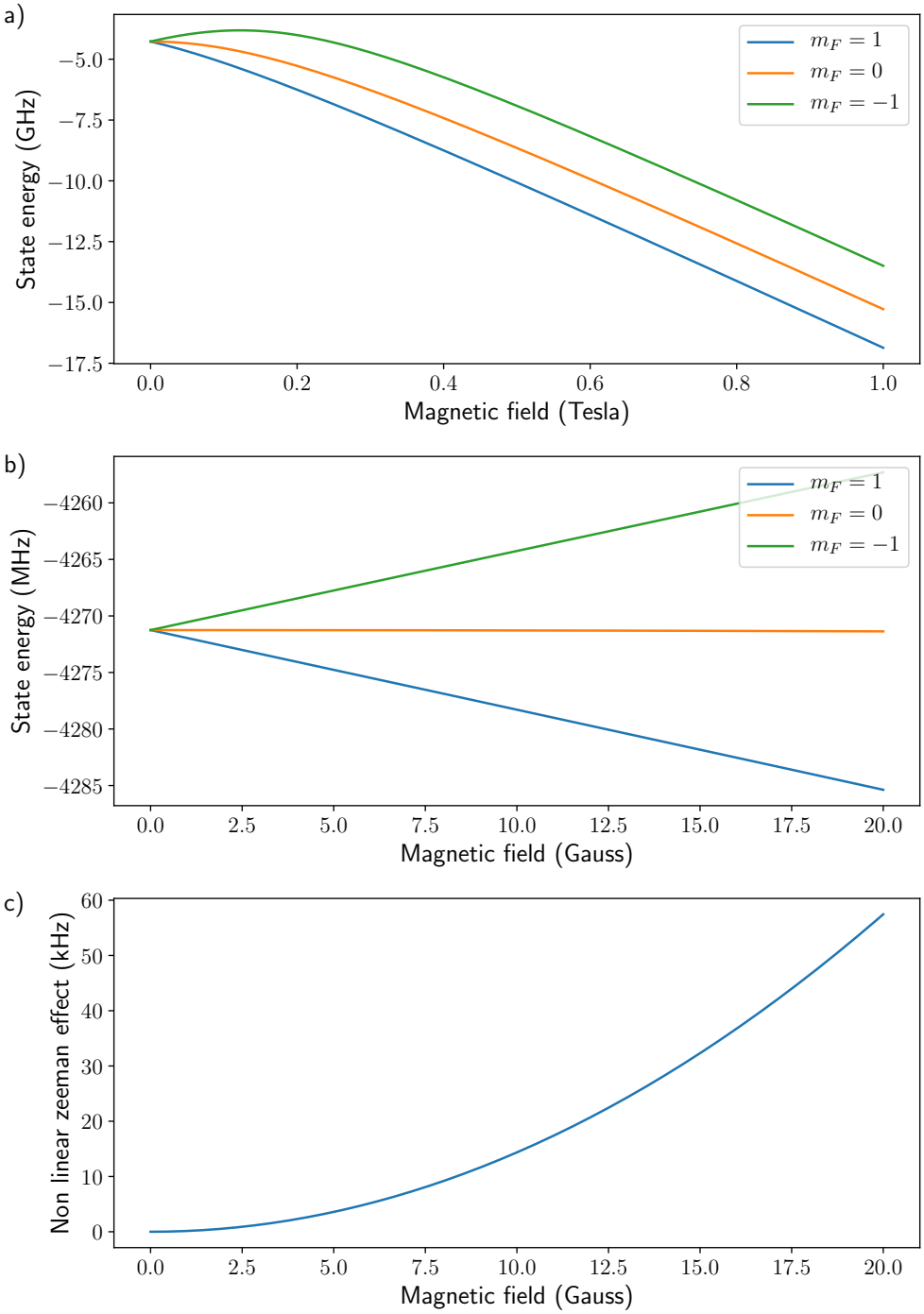


Figure 6.3: **The non-linear Zeeman effect:** a) The dependence of the energy of the $m_F$ states on the magnetic field for the range $0 - 1T$, b) The dependence of the energy of the $m_F$ states on the magnetic field for the range $0 - 20G$, c) the dependence of the difference in the resonant frequencies between adjacent $m_F$ states on the magnetic field.

dependent upon the magnetic field. For the states to be considered independent a difference in the splitting resonant frequency between the states of the order of the on-resonance coupling Rabi frequency is required. To achieve this, fields of the order of 10 Gauss will be needed. A functioning experimental three-level system will enable the effect that unequal coupling between the states has on transport to be investigated.

### 6.2.4 Making the perturbation of the energy levels independent

The current system can be approximated by a two-level system due to the symmetries discussed in section 2.3. Therefore if the system is extended to a 'genuine' three-level system using the non-linear Zeeman effect, as described in section 6.2.3, the scope of the study can be increased further by making the perturbation for each of the levels fully independent.

In the system currently under investigation the bias magnetic field is modulated to generate the noisy perturbation of the energy of the outer two states and therefore the energies of these states have equal and opposite shifts. The energy of the central state is not dependent upon the applied magnetic field. The relationship between the energy differences between the two outer states and the central state could be removed by using a beam that affects the energies of the magnetic sub-states non-linearly through the AC stark shift [124], effectively changing the energy of the central state. The non-linear AC stark shift could be modulated, by varying power of the beam, and would, when combined with the perturbation of the magnetic field, be able to induce independent noise between the three $F = 1$ magnetic sub-states. However, to have a large non-linear effect of the AC stark shift the beam would have to be close to a resonance and therefore cause a significant amount of scattering that would decohere the state.

It has been suggested that the protection of coherent transport in biological systems may arise as a result of the correlation of the environmental perturbation between different sites [4] (overlap of vibrational modes between sites). This could be investigated by introducing correlations between frequency components of the different sites and observing the effect on coherent transport.

### 6.2.5 Implementation of the glass cell

In order to implement the previously mentioned enhancements the vacuum chamber was upgraded to a glass cell. This is the most important upgrade of the existing experimental set-up because eddy currents, present in the metal vacuum chamber used in the present study, significantly reduced the strength of the RF field that could be applied to the atomic cloud, section 3. The implementation of a sink state and accessing the non-linear Zeeman regime would require an increase in the frequency of the coupling field (RF) by a factor of $\approx 10$. This would require an increase in power by over 100 which is not possible using the current experimental set-up. This is because the attenuation due to eddy currents was $\approx 50\%$ at $1MHz$ and has a quadratic dependence on the frequency of the field. A glass cell, however, does not promote the formation of eddy currents and thus is capable of supporting high-frequency coupling fields without strong attenuation. Initial tests have shown that the RF Rabi frequency for the glass cell was a factor of $\approx 2.5\times$ larger than that achieved with the metal chamber, which supports the hypothesis that the eddy currents were reducing the strength of the RF field.

As discussed in section 3 the coupling due to the Raman beams had a large amount of decoherence. This decoherence is believed to be due to the beam intensity profile of the Raman coupling beams distorting as it passes through an uncoated window. The distortions led to a spatial variation of the Raman Rabi frequency across the atomic cloud that resulted

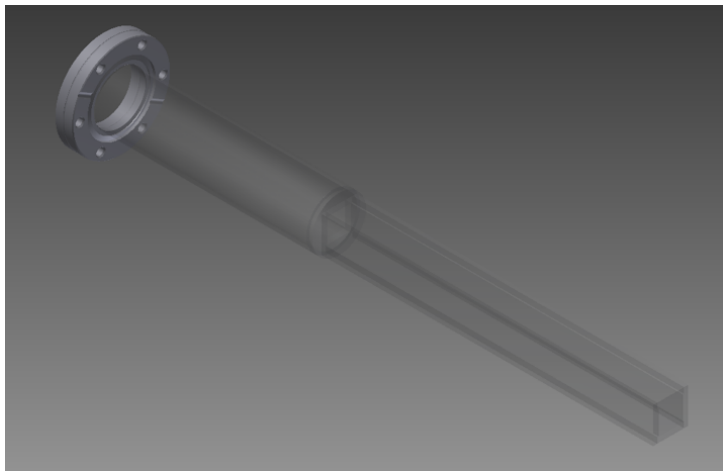

Figure 6.4: **Glass cell:** The glass cell that is used in the enhanced set-up to remove the influence of eddy currents and provide more optical access. The cold atomic cloud is formed in the square part of the chamber and the flat surfaces of the cell (windows) have an anti-reflection coating.

in decoherence of the overall Rabi response of the ensemble of atoms. The glass cell has coated windows that will significantly reduce this effect and result in less decoherence of the Rabi oscillations that result from the Raman coupling.

A glass cell will additionally increase the optical access to the atomic cloud making the system more usable and versatile. The need for a reducing flange in the metal chamber restricted the maximum Stern-Gerlach separation distance as discussed in section 3. A glass cell with increased optical access does not require this flange and also allows the measurement axis to be rotated by 90 degrees, increasing the available space for the Stern-Gerlach cloud separation by aligning it along the non-bounded axis of the glass cell.

In conclusion, the use of a glass cell will permit the necessary alterations to the system to be implemented that will allow Raman coupling and a sink to be studied.

### 6.2.6 Expanding the system to more sites

Biological systems have a more complex structure with more sites than the experimental network used in this study. Increasing the number of sites will allow the effect of a range of coupling strengths between sites and the influence of static disorder of the energies of the sites to be investigated. These effects will also produce a more complex perturbation spectrum structure because the different coupling strengths and detunings between the sites will result in a range of dressed states with different energy splittings and thus a richer resonance structure with which the pure dephasing perturbation can interact.

Extending the system to 5 sites could be achieved by using the $F = 2$ $m_F$ states of rubidium 87 as the system sites and to a 7 site system using the $F = 3$ $m_F$ states of rubidium 85. Beyond this, microwaves could be used to couple the $F = 1$ magnetic sub-states to the sub-states of the $F = 2$ ground state thus increasing the complexity of the system to 8 sites and introducing differential coupling rates between the sites. In conclusion, expanding the system to more sites will more realistically model an FMO-like system and allow the investigation of more complex perturbation structures.

### 6.2.7 Non-Markovian dynamics

As discussed in the introductory chapter the Markov approximation is where the evolution of the system is dependent only upon the current state of the system and not on past interactions, thus correlations do not build up with the environment (descibed as the environment having no memory). However, non-Markovian dynamics may operate in biological systems resulting from the environment being affected by the presence of an excitation. In the current system this could be simulated by changing the environment dynamically during the evolution, depending on the changing state of the system. In this case the state of the system

would have to be measured non-destructively by using a weak measurement process [125,126] and fed back to the perturbation using fast electronics. Alternatively, without any change to the current experimental set-up, the system could be left to evolve for a set time under the influence of the perturbation. Then, depending on the state of the system, the perturbation could be altered for the next phase of the evolution. An example of this is shown in figure 6.5, for the case of non-markovian scaling of the noise field dependent on the base state populations. Finally, it is still an open question whether an environment (that is essentially deterministic) can effectively model a bath, including features such as entanglement. This is a topic for future theoretical and experimental research.

## 6.3 Final Conclusions

In order to study and model environmentally assisted transport mechanisms in biological systems this study has developed an experimental set-up using the $F = 1$ $m_F$ sub-states of rubidium 87 as sites in a network. It has been found that transport through the network has a strong dependence on the frequency composition of the pure dephasing perturbation of the network sites. Further work is required to improve the experimental set-up and incorporate additional features of FMO-like systems including a reaction centre and multi-path interference effects.

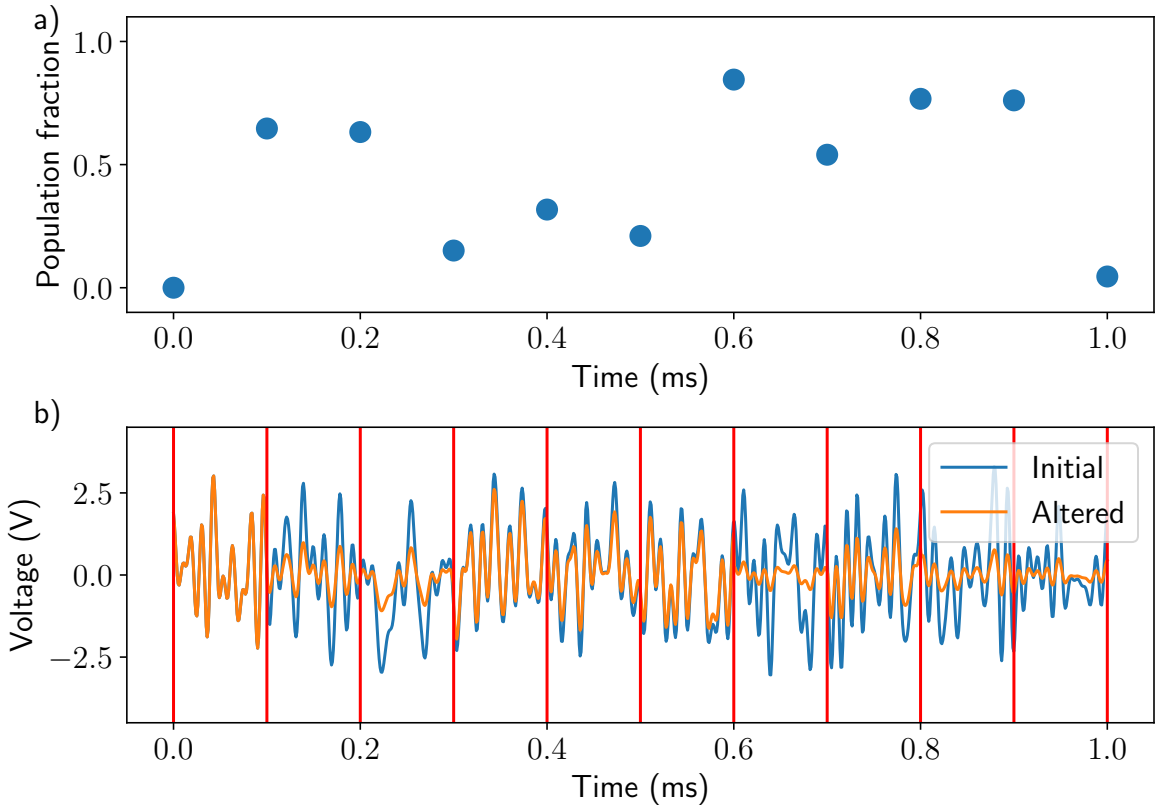


Figure 6.5: **An example of non-Markovian feedback to the noisy perturbation:** a) the evolution of the population in the target state, b) the amplitude of the noise is altered for the next stage of the evolution depending on the measurement of the population in the target state (the multiplier in this case is one minus the population fraction in the target state).

# LIST OF REFERENCES


[1] X. Jia, Y. Mei, J. Z. Zhang, and Y. Mo, "Hybrid QM/MM study of FMO complex with polarized protein-specific charge," *Scientific Reports*, vol. 5, pp. 1–10, 2015.

[2] N. Lambert, Y.-N. Chen, Y.-C. Cheng, C.-M. Li, G.-Y. Chen, and F. Nori, "Quantum biology," *Nature Physics*, vol. 9, pp. 10–18, 2013.

[3] G. D. Scholes, G. R. Fleming, L. X. Chen, A. Aspuru-Guzik, A. Buchleitner, D. F. Coker, G. S. Engel, R. Van Grondelle, A. Ishizaki, D. M. Jonas, J. S. Lundeen, J. K. McCusker, S. Mukamel, J. P. Ogilvie, A. Olaya-Castro, M. A. Ratner, F. C. Spano, K. B. Whaley, and X. Zhu, "Using coherence to enhance function in chemical and biophysical systems," *Nature*, vol. 543, pp. 647–656, 2017.

[4] F. Caruso, A. W. Chin, A. Datta, S. F. Huelga, and M. B. Plenio, "Highly efficient energy excitation transfer in light-harvesting complexes: The fundamental role of noise-assisted transport," *The Journal of Chemical Physics*, vol. 131, p. 105106, 2009.

[5] S. F. Huelga and M. B. Plenio, "Vibrations, quanta and biology," *Contemporary Physics*, vol. 54, pp. 181–207, 2013.

[6] S. Viciani, M. Lima, M. Bellini, and F. Caruso, "Observation of noise-assisted transport in an all-optical cavity-based network," *Phys. Rev. Lett.*, vol. 115, p. 083601, 2015.

[7] S. N. Shevchenko, S. Ashhab, and F. Nori, "Landau-Zener-Stückelberg interferometry," *Physics Reports*, vol. 492, no. 1, pp. 1–30, 2010.

[8] J. R. Johansson, P. D. Nation, and F. Nori, "QuTiP 2: A Python framework for the dynamics of open quantum systems," *Computer Physics Communications*, vol. 184, pp. 1234–1240, 2013.

[9] ——, "QuTiP: An open-source Python framework for the dynamics of open quantum systems," *Computer Physics Communications*, vol. 183, pp. 1760–1772, 2012.

[10] D. A. Steck, "Rubidium 87 D Line Data," 2019. [Online]. Available: http://steck.us/alkalidata

[11] K. C. Wright, L. S. Leslie, and N. P. Bigelow, "Raman coupling of zeeman sublevels in an alkali-metal bose-einstein condensate," *Phys. Rev. A*, vol. 78, p. 053412, 2008.

[12] K. Yasushi, N. Mikio, T. Shogo, K. Sachiko, U. Chikako, and S. Fumiaki, "Generation and Suppression of Decoherence in Artificial Environment for Qubit System," *Journal of the Physical Society of Japan*, vol. 76, no. 7, p. 74002, 2007.

[13] D. de Falco and D. Tamascelli, "Noise-assisted quantum transport and computation," *Journal of Physics A: Mathematical and Theoretical*, vol. 46, no. 22, p. 225301, 2013.

[14] G. S. Engel, T. R. Calhoun, E. L. Read, T. K. Ahn, T. Mančal, Y. C. Cheng, R. E. Blankenship, and G. R. Fleming, "Evidence for wavelike energy transfer through quantum coherence in photosynthetic systems," *Nature*, vol. 446, pp. 782–786, 2007.

[15] Y. Zur and S. Vega, "Two-photon NMR on spins with I=1 in solids," *The Journal of Chemical Physics*, vol. 79, no. 2, pp. 548–558, 1983.

[16] Y. Zur, M. H. Levitt, and S. Vega, "Multiphoton NMR spectroscopy on a spin system with I=1/2," *The Journal of Chemical Physics*, vol. 78, no. 9, pp. 5293–5310, 1983.

[17] W. A. Anderson, "Nuclear magnetic resonance spectra of some hydrocarbons," *Phys. Rev.*, vol. 102, pp. 151–167, 1956.

[18] A. Potočnik, A. Bargerbos, F. A. Y. N. Schröder, S. A. Khan, M. C. Collodo, S. Gasparinetti, Y. Salathé, C. Creatore, C. Eichler, H. E. Türeci, A. W. Chin, and A. Wallraff, "Studying light-harvesting models with superconducting circuits," *Nature Communications*, vol. 9, p. 904, 2018.

[19] L. Childress and J. McIntyre, "Multifrequency spin resonance in diamond," *Phys. Rev. A*, vol. 82, p. 033839, 2010.

[20] A. Marais, B. Adams, A. K. Ringsmuth, M. Ferretti, J. M. Gruber, R. Hendrikx, M. Schuld, S. L. Smith, I. Sinayskiy, T. P. J. Krüger, F. Petruccione, and R. van Grondelle, "The future of quantum biology," *Journal of The Royal Society Interface*, vol. 15, no. 148, 2018.

[21] M. Allen, "Birds measure magnetic fields using long-lived quantum coherence," 2016. [Online]. Available: https://www.physicsworld.com/a/birds-measure-magnetic-fields-using-long-lived-quantum-coherence/

[22] L. Turin, "A Spectroscopic Mechanism for Primary Olfactory Reception," *Chemical Senses*, vol. 21, no. 6, pp. 773–791, 1996.

[23] M. Schmidt Am Busch, F. Müh, M. El-Amine Madjet, and T. Renger, "The eighth bacteriochlorophyll completes the excitation energy funnel in the FMO protein," *Journal of Physical Chemistry Letters*, vol. 2, no. 2, pp. 93–98, 2011.

[24] M. B. Plenio and S. F. Huelga, "Dephasing-assisted transport: quantum networks and biomolecules," *New Journal of Physics*, vol. 10, 2008.

[25] F. Levi, S. Mostarda, F. Rao, and F. Mintert, "Quantum mechanics of excitation transport in photosynthetic complexes: a key issues review," *Reports on Progress in Physics*, vol. 78, no. 8, 2015.

[26] P. Rebentrost, M. Mohseni, I. Kassal, S. Lloyd, and A. Aspuru-Guzik, "Environment-assisted quantum transport," *New Journal of Physics*, vol. 11, 2009.

[27] W. M. Zhang, T. Meier, V. Chernyak, and S. Mukamel, "Exciton-migration and three-pulse femtosecond optical spectroscopies of photosynthetic antenna complexes," *The Journal of Chemical Physics*, vol. 108, no. 18, pp. 7763–7774, 1998.

[28] F. Segatta, L. Cupellini, S. Jurinovich, S. Mukamel, M. Dapor, S. Taioli, M. Garavelli, and B. Mennucci, "A Quantum Chemical Interpretation of Two-Dimensional Electronic Spectroscopy of Light-Harvesting Complexes," *Journal of the American Chemical Society*, vol. 139, no. 22, pp. 7558–7567, 2017.

[29] T. Brixner, T. Mančal, I. V. Stiopkin, and G. R. Fleming, "Phase-stabilized two-dimensional electronic spectroscopy," *The Journal of Chemical Physics*, vol. 121, no. 9, pp. 4221–4236, 2004.

[30] D. M. Jonas, "Two-Dimensional Femtosecond Spectroscopy," *Annual Review of Physical Chemistry*, vol. 54, no. 1, pp. 425–463, 2003.

[31] T. Brixner, I. V. Stiopkin, and G. R. Fleming, "Tunable two-dimensional femtosecond spectroscopy," *Opt. Lett.*, vol. 29, no. 8, pp. 884–886, 2004.

[32] V. Čápek, "Generalized Haken-Strobl-Reineker model of excitation transfer," *Zeitschrift für Physik B Condensed Matter*, vol. 60, no. 1, pp. 101–105, 1985.

[33] A. Ishizaki and G. R. Fleming, "Theoretical examination of quantum coherence in a photosynthetic system at physiological temperature," *Proceedings of the National Academy of Sciences*, vol. 106, no. 41, pp. 17 255–17 260, 2009.

[34] M. Yang and G. R. Fleming, "Influence of phonons on exciton transfer dynamics: Comparison of the Redfield, Förster, and modified Redfield equations," *Chemical Physics*, vol. 275, no. 1-3, pp. 355–372, 2002.

[35] A. Ishizaki and G. R. Fleming, "Unified treatment of quantum coherent and incoherent hopping dynamics in electronic energy transfer: Reduced hierarchy equation approach," *The Journal of Chemical Physics*, vol. 130, p. 234111, 2009.

[36] O.-P. Saira, V. Bergholm, T. Ojanen, and M. Möttönen, "Equivalent qubit dynamics under classical and quantum noise," *Physical Review A - Atomic, Molecular, and Optical Physics*, vol. 75, no. 1, pp. 1–5, 2007.

[37] M. Mohseni, P. Rebentrost, S. Lloyd, and A. Aspuru-Guzik, "Environment-assisted quantum walks in photosynthetic energy transfer," *Journal of Chemical Physics*, vol. 129, no. 17, 2008.

[38] H.-P. Breuer and F. Petruccione, *The Theory of Open Quantum Systems.* Oxford: Oxford University Press, 2007.

[39] A. Chenu, M. Beau, J. Cao, and A. del Campo, "Quantum simulation of generic many-body open system dynamics using classical noise," *Phys. Rev. Lett.*, vol. 118, p. 140403, 2017.

[40] M. Rossi, "Dynamics and characterization of quantum systems interacting with classical noise," Ph.D. dissertation, University of Milan, 2017.

[41] A. Eisfeld and J. S. Briggs, "Classical master equation for excitonic transport under the influence of an environment," *Phys. Rev. E*, vol. 85, p. 046118, 2012.

[42] D. Hsu and J. L. Skinner, "General quantum mechanical theory of pure dephasing," *Journal of Luminescence*, vol. 37, no. 6, pp. 331–337, 1987.

[43] J. L. Skinner and D. Hsu, "Pure dephasing of a two-level system," *The Journal of Physical Chemistry*, vol. 90, no. 21, pp. 4931–4938, 1986.

[44] L. D. Contreras-Pulido, M. Bruderer, S. F. Huelga, and M. B. Plenio, "Dephasing-assisted transport in linear triple quantum dots," *New Journal of Physics*, vol. 16, p. 113061, 2014.

[45] C. A. Brasil, F. F. Fanchini, and R. d. J. Napolitano, "A simple derivation of the Lindblad equation," *Revista Brasileira de Ensino de Fisica*, vol. 35, no. 1, 2013.

[46] S. A. Gurvitz, "Rate equations for quantum transport in multidot systems," *Phys. Rev. B*, vol. 57, pp. 6602–6611, 1998.

[47] H.-P. Breuer, "Non-markovian generalization of the lindblad theory of open quantum systems," *Phys. Rev. A*, vol. 75, p. 022103, 2007.

[48] L. Diósi, "Hybrid quantum-classical master equations," *Physica Scripta*, vol. T163, p. 014004, 2014.

[49] P. Pearle, "Simple derivation of the Lindblad equation," *European Journal of Physics*, vol. 33, no. 4, 2012.

[50] Z.-X. Man, N. B. An, and Y.-J. Xia, "Non-markovian dynamics of a two-level system in the presence of hierarchical environments," *Opt. Express*, vol. 23, no. 5, pp. 5763–5776, 2015.

[51] K. Fujii, "Introduction to the Rotating Wave Approximation (RWA): Two Coherent Oscillations," *Journal of Modern Physics*, vol. 08, no. 12, pp. 2042–2058, 2017.

[52] C. Maier, T. Brydges, P. Jurcevic, N. Trautmann, C. Hempel, B. P. Lanyon, P. Hauke, R. Blatt, and C. F. Roos, "Environment-Assisted Quantum Transport in a 10-qubit Network," *Physical Review Letters*, vol. 122, p. 50501, 2019.

[53] G. Falci, A. D'Arrigo, A. Mastellone, and E. Paladino, "Initial decoherence in solid state qubits," *Phys. Rev. Lett.*, vol. 94, p. 167002, 2005.

[54] V. Weisskopf and E. Wigner, "Berechnung der natürlichen Linienbreite auf Grund der Diracschen Lichttheorie," *Zeitschrift für Physik*, vol. 63, no. 1, pp. 54–73, 1930.

[55] A. Rudavskyi, "Influence of environment on spontaneous emission." [Online]. Available: www.rug.nl/research/zernike/education/topmasternanoscience/ns190rudavskyi.pdf

[56] J. S. Lee, M. A. Rohrdanz, and A. K. Khitrin, "Controlled spontaneous emission," *Journal of Physics B: Atomic, Molecular and Optical Physics*, vol. 41, no. 4, 2008.

[57] A. Olaya-Castro, C. F. Lee, F. F. Olsen, and N. F. Johnson, "Efficiency of energy transfer in a light-harvesting system under quantum coherence," *Physical Review B*, vol. 78, p. 085115, 2008.

[58] F. Caruso, N. Spagnolo, C. Vitelli, F. Sciarrino, and M. B. Plenio, "Simulation of noise-assisted transport via optical cavity networks," *Phys. Rev. A*, vol. 83, p. 013811, 2011.

[59] M. Rätsep, Z.-L. Cai, J. R. Reimers, and A. Freiberg, "Demonstration and interpretation of significant asymmetry in the low-resolution and high-resolution Qy fluorescence and absorption spectra of bacteriochlorophyll a," *The Journal of Chemical Physics*, vol. 134, no. 2, p. 24506, 2011.

[60] F. Caycedo-Soler, A. W. Chin, J. Almeida, S. F. Huelga, and M. B. Plenio, "The nature of the low energy band of the Fenna-Matthews-Olson complex: Vibronic signatures," *The Journal of Chemical Physics*, vol. 136, no. 15, p. 155102, 2012.

[61] O. Goldberg, Y. Meir, and Y. Dubi, "Vibration-Assisted and Vibration-Hampered Excitonic Quantum Transport," *The Journal of Physical Chemistry Letters*, vol. 9, no. 11, pp. 3143–3148, 2018.

[62] F. L. Semião, K. Furuya, and G. J. Milburn, "Vibration-enhanced quantum transport," *New Journal of Physics*, vol. 12, p. 083033, 2010.

[63] B. Misra and E. C. G. Sudarshan, "The Zeno's paradox in quantum theory," *Journal of Mathematical Physics*, vol. 18, no. 4, pp. 756–763, 1977.

[64] S. Pascazio, "All You Ever Wanted to Know About the Quantum Zeno Effect in 70 Minutes," *Open Systems & Information Dynamics*, vol. 21, no. 01n02, p. 1440007, 2014.

[65] A. Z. Chaudhry, "The quantum Zeno and anti-Zeno effects with strong system-environment coupling," *Scientific Reports*, vol. 7, p. 1741, 2017.

[66] Y.-R. Zhang and H. Fan, "Zeno dynamics in quantum open systems," *Scientific Reports*, vol. 5, p. 11509, 2015.

[67] E. W. Streed, J. Mun, M. Boyd, G. K. Campbell, P. Medley, W. Ketterle, and D. E. Pritchard, "Continuous and pulsed quantum zeno effect," *Phys. Rev. Lett.*, vol. 97, p. 260402, 2006.

[68] A. Iwakura, Y. Matsuzaki, and Y. Kondo, "Engineered noisy environment for studying decoherence," *Phys. Rev. A*, vol. 96, p. 032303, 2017.

[69] E. M. Purcell, "Spontaneous Emission Probabilities at Radio Frequencies," *Phys. Rev.*, vol. 69, p. 681, 1946.

[70] Z. Jacob, I. I. Smolyaninov, and E. E. Narimanov, "Broadband Purcell effect: Radiative decay engineering with metamaterials," *Applied Physics Letters*, vol. 100, no. 18, p. 181105, 2012.

[71] J. R. Rubbmark, M. M. Kash, M. G. Littman, and D. Kleppner, "Dynamical effects at avoided level crossings: A study of the Landau-Zener effect using Rydberg atoms," *Physical Review A*, vol. 23, no. 6, pp. 3107–3117, 1981.

[72] W. D. Oliver, Y. Yu, J. C. Lee, K. K. Berggren, L. S. Levitov, and T. P. Orlando, "Mach-Zehnder Interferometry in a Strongly Driven Superconducting Qubit," *Science*, vol. 310, no. 5754, pp. 1653–1657, 2005.

[73] M. Wubs, K. Saito, S. Kohler, Y. Kayanuma, and P. Hänggi, "Landau–Zener transitions in qubits controlled by electromagnetic fields," *New Journal of Physics*, vol. 7, p. 218, 2005.

[74] D. M. Berns, W. D. Oliver, S. O. Valenzuela, A. V. Shytov, K. K. Berggren, L. S. Levitov, and T. P. Orlando, "Coherent quasiclassical dynamics of a persistent current qubit," *Phys. Rev. Lett.*, vol. 97, p. 150502, 2006.

[75] S. N. Shevchenko, A. I. Ryzhov, and F. Nori, "Low-frequency spectroscopy for quantum multilevel systems," *Phys. Rev. B*, vol. 98, p. 195434, 2018.

[76] M. P. Silveri, J. A. Tuorila, E. V. Thuneberg, and G. S. Paraoanu, "Quantum systems under frequency modulation," *Reports on Progress in Physics*, vol. 80, no. 5, 2017.

[77] L. Du, D. Lan, and Y. Yu, "Low-frequency Landau–Zener–Stückelberg interference in dissipative superconducting qubits," *Low Temperature Physics*, vol. 39, pp. 665–679, 2013.

[78] S. Ashhab, "Landau Zener Stueckelberg interferometry with driving fields in the quantum regime," *Journal of Physics A: Mathematical and Theoretical*, vol. 50, p. 134002, 2017.

[79] S. Ashhab, J. R. Johansson, A. M. Zagoskin, and F. Nori, "Two-level systems driven by large-amplitude fields," *Phys. Rev. A*, vol. 75, p. 063414, 2007.

[80] V. Novičenko, E. Anisimovas, and G. Juzeliūnas, "Floquet analysis of a quantum system with modulated periodic driving," *Phys. Rev. A*, vol. 95, p. 023615, 2017.

[81] S.-K. Son, S. Han, and S.-I. Chu, "Floquet formulation for the investigation of multiphoton quantum interference in a superconducting qubit driven by a strong ac field," *Physical Review A - Atomic, Molecular, and Optical Physics*, vol. 79, no. 032301, 2009.

[82] J. H. Shirley, "Solution of the schrödinger equation with a hamiltonian periodic in time," *Phys. Rev.*, vol. 138, p. B979, 1965.

[83] ——, "Interaction of a quantum system with a strong oscillating field," Ph.D. dissertation, Caltech, 1963.

[84] K. R. K. Rao and D. Suter, "Nonlinear dynamics of a two-level system of a single spin driven beyond the rotating-wave approximation," *Phys. Rev. A*, vol. 95, p. 053804, 2017.

[85] S. Kohler, "Dispersive readout: Universal theory beyond the rotating-wave approximation," *Phys. Rev. A*, vol. 98, p. 023849, 2018.

[86] M. Allegrini, E. Arimondo, and A. Bambini, "Matrix continued-fraction solution for saturation effects in spin-1/2 radio-frequency spectroscopy," *Phys. Rev. A*, vol. 15, pp. 718–726, 1977.

[87] A. G. Redfield, "Nuclear magnetic resonance saturation and rotary saturation in solids," *Phys. Rev.*, vol. 98, pp. 1787–1809, 1955.

[88] E. Arimondo and G. Moruzzi, "Bloch-Siegert shift in optically oriented $^{199}$Hg vapour," *Journal of Physics B: Atomic and Molecular Physics*, vol. 6, no. 11, pp. 2382–2389, 1973.

[89] A. Schmidt and S. Vega, "The Floquet theory of nuclear magnetic resonance spectroscopy of single spins and dipolar coupled spin pairs in rotating solids," *The Journal of Chemical Physics*, vol. 96, no. 4, pp. 2655–2680, 1992.

[90] P. Bucci, M. Martinelli, and S. Santucci, "Response to Double Irradiation of a Nuclear Spin System: General Treatment and New Multiple Quantum Transitions," *The Journal of Chemical Physics*, vol. 53, pp. 4524–4531, 1970.

[91] J. Winter, "Étude théorique et expérimentale des transitions à plusieurs quanta entre les sous-niveaux Zeeman d'un atome," *J. Phys. Radium*, vol. 19, no. 11, pp. 802–805, 1958.

[92] F. Bloch and A. Siegert, "Magnetic resonance for nonrotating fields," *Physical Review*, vol. 57, no. 6, pp. 522–527, 1940.

[93] F. Ahmad and R. K. Bullough, "Theory of the Bloch-Siegert shift," *Journal of Physics B: Atomic and Molecular Physics*, vol. 7, no. 9, pp. L275–L280, 1974.

[94] J. Tuorila, M. Silveri, M. Sillanpää, E. Thuneberg, Y. Makhlin, and P. Hakonen, "Stark effect and generalized bloch-siegert shift in a strongly driven two-level system," *Phys. Rev. Lett.*, vol. 105, p. 257003, 2010.

[95] S. Yeh and P. Stehle, "Atomic level shifts and transition amplitudes in incoming radiation fields," *Phys. Rev. A*, vol. 15, pp. 213–222, 1977.

[96] P. Forn-Díaz, J. Lisenfeld, D. Marcos, J. J. García-Ripoll, E. Solano, C. J. P. M. Harmans, and J. E. Mooij, "Observation of the bloch-siegert shift in a qubit-oscillator system in the ultrastrong coupling regime," *Phys. Rev. Lett.*, vol. 105, p. 237001, 2010.

[97] A. P. Saiko, G. G. Fedoruk, and S. A. Markevich, "Effective field and the Bloch-Siegert shift at bichromatic excitation of multiphoton EPR," *JETP Letters*, vol. 84, no. 3, pp. 130–135, 2006.

[98] S. Vinjanampathy and J. Anders, "Quantum thermodynamics," *Contemporary Physics*, vol. 57, no. 4, pp. 545–579, 2016.

[99] B. Karimi and J. P. Pekola, "Otto refrigerator based on a superconducting qubit: Classical and quantum performance," *Phys. Rev. B*, vol. 94, p. 184503, 2016.

[100] J. Millen and A. Xuereb, "Perspective on quantum thermodynamics," *New Journal of Physics*, vol. 18, no. 1, p. 11002, 2016.

[101] J. P. Garrahan and I. Lesanovsky, "Thermodynamics of quantum jump trajectories," *Phys. Rev. Lett.*, vol. 104, p. 160601, 2010.

[102] S. Haywood, *Symmetries and Conservation Laws in Particle Physics.* Imperial college press, 2010.

[103] C.J.Foot, *Atomic Physics.* Oxford University Press, 2005.

[104] V. Debierre, I. Goessens, E. Brainis, and T. Durt, "Fermi's golden rule beyond the Zeno regime," *Physical Review A - Atomic, Molecular, and Optical Physics*, vol. 92, no. 023825, 2015.

[105] M. B. Plenio and P. L. Knight, "The quantum-jump approach to dissipative dynamics in quantum optics," *Rev. Mod. Phys.*, vol. 70, pp. 101–144, 1998.

[106] J. Dalibard, Y. Castin, and K. Mølmer, "Wave-function approach to dissipative processes in quantum optics," *Physical Review Letters*, vol. 68, pp. 580–583, 1992.

[107] C. Gill, "Simulating transport through quantum networks in the presence of classical noise using cold atoms," Ph.D. dissertation, University of Birmingham, 2017.

[108] C. E. Wieman, D. E. Pritchard, and D. J. Wineland, "Atom cooling, trapping, and quantum manipulation," *Rev. Mod. Phys.*, vol. 71, pp. S253–S262, 1999.

[109] W. D. Phillips, "Nobel lecture: Laser cooling and trapping of neutral atoms," *Rev. Mod. Phys.*, vol. 70, pp. 721–741, 1998.

[110] H. J. Metcalf and P. van der Straten, *Laser Cooling and Trapping.* Springer-Verlag New York, 1999.

[111] P. J. Ungar, D. S. Weiss, E. Riis, and S. Chu, "Optical molasses and multilevel atoms: theory," *J. Opt. Soc. Am. B*, vol. 6, no. 11, pp. 2058–2071, 1989.

[112] J. Dalibard and C. Cohen-Tannoudji, "Laser cooling below the doppler limit by polarization gradients: simple theoretical models," *J. Opt. Soc. Am. B*, vol. 6, no. 11, pp. 2023–2045, 1989.

[113] T. M. Brzozowski, M. Maczynska, M. Zawada, J. Zachorowski, and W. Gawlik, "Time-of-flight measurement of the temperature of cold atoms for short trap-probe beam distances," *Journal of Optics B: Quantum and Semiclassical Optics*, vol. 4, no. 1, pp. 62–66, 2002.

[114] C. P. Pearman, C. S. Adams, S. G. Cox, P. F. Griffin, D. A. Smith, and I. G. Hughes, "Polarization spectroscopy of a closed atomic transition: applications to laser frequency locking," *Journal of Physics B: Atomic, Molecular and Optical Physics*, vol. 35, no. 24, pp. 5141–5151, 2002.

[115] U. Schünemann, H. Engler, R. Grimm, M. Weidemüller, and M. Zielonkowski, "Simple scheme for tunable frequency offset locking of two lasers," *Review of Scientific Instruments*, vol. 70, no. 1, pp. 242–243, 1999.

[116] "Analysis of laser frequency stability using beat-note measurement," Photonics, N K T, Tech. Rep., 2013.

[117] W. Gerlach and O. Stern, "über die richtungsquantelung im magnetfeld," *Annalen der Physik*, vol. 379, no. 16, pp. 673–699, 1924.

[118] M. Born and V. Fock, "Beweis des Adiabatensatzes," *Zeitschrift für Physik*, vol. 51, no. 3, pp. 165–180, 1928.

[119] M. P. Fewell, "Adiabatic elimination, the rotating-wave approximation and two-photon transitions," *Optics Communications*, vol. 253, no. 1, pp. 125–137, 2005.

[120] R. H. Byrd, P. Lu, J. Nocedal, and C. Zhu, "A Limited Memory Algorithm for Bound Constrained Optimization," *SIAM Journal on Scientific Computing*, vol. 16, no. 5, pp. 1190–1208, 2005.

[121] I. Cohen, S. Weidt, W. K. Hensinger, and A. Retzker, "Multi-qubit gate with trapped ions for microwave and laser-based implementation," *New Journal of Physics*, vol. 17, p. 043008, 2015.

[122] H. Lignier, C. Sias, D. Ciampini, Y. Singh, A. Zenesini, O. Morsch, and E. Arimondo, "Dynamical control of matter-wave tunneling in periodic potentials," *Physical Review Letters*, vol. 99, no. 22, pp. 1–4, 2007.

[123] F. Grossmann, T. Dittrich, P. Jung, and P. Hänggi, "Coherent destruction of tunneling," *Physical Review Letters*, vol. 67, no. 4, pp. 516–519, 1991.

[124] K. Jensen, V. M. Acosta, J. M. Higbie, M. P. Ledbetter, S. M. Rochester, and D. Budker, "Cancellation of nonlinear zeeman shifts with light shifts," *Phys. Rev. A*, vol. 79, p. 023406, 2009.

[125] S. Lloyd and J.-J. E. Slotine, "Quantum feedback with weak measurements," *Phys. Rev. A*, vol. 62, p. 012307, 2000.

[126] G. G. Gillett, R. B. Dalton, B. P. Lanyon, M. P. Almeida, M. Barbieri, G. J. Pryde, J. L. O'Brien, K. J. Resch, S. D. Bartlett, and A. G. White, "Experimental feedback control of quantum systems using weak measurements," *Phys. Rev. Lett.*, vol. 104, p. 080503, 2010.